Meridional movement of Pacific winds and their role in ENSO event onset and termination

Author:
Abellan Villardon, Esteban

Publication Date:
2017

DOI:
https://doi.org/10.26190/unsworks/3212

Climate Change Research Centre

University of New South Wales

Meridional movement of Pacific winds and their role in ENSO event onset and termination

Esteban Abellán

June 2017

Supervisors: Dr. Shayne McGregor and
Prof. Matthew H. England.

A thesis submitted in fulfillment of the requirements for the degree of
Doctor of Philosophy.

ORIGINALITY STATEMENT

'I hereby declare that this submission is my own work and to the best of my knowledge it contains no materials previously published or written by another person, or substantial proportions of material which have been accepted for the award of any other degree or diploma at UNSW or any other educational institution, except where due acknowledgement is made in the thesis. Any contribution made to the research by others, with whom I have worked at UNSW or elsewhere, is explicitly acknowledged in the thesis. I also declare that the intellectual content of this thesis is the product of my own work, except to the extent that assistance from others in the project's design and conception or in style, presentation and linguistic expression is acknowledged.'

Signed ....

Date ....29/ 03/ 2017..

Abstract

During the mature phase of El Niño-Southern Oscillation (ENSO) events, near the end of the calendar year, there is a southward shift of the zonal wind anomalies, which are centred around the equator prior to the event peak. This thesis investigates the role of this meridional wind movement in the termination of ENSO events by using simple and complex climate models.

Previous studies have shown that ENSO's anomalous wind stresses, including this southward shift (SWS), can be reconstructed with the two leading Empirical Orthogonal Functions (EOFs) of wind stresses over the tropical Pacific. Here a hybrid coupled model is developed, featuring a statistical atmosphere based on these first two EOFs coupled to a shallow water model ocean. The addition of the SWS enhances the termination of El Niño events, making the events shorter, while it does not appear to play an important role on the duration of La Niña events. Thus, the SWS is partly responsible for seasonal synchronization of ENSO events.

This thesis also examines the representation of the SWS in phase 5 of the Coupled Model Intercomparison Project (CMIP5). Although the models that capture the SWS also simulate many more strong El Niño and La Niña events peaking at the correct time of the year, the overall seasonal synchronization is still underestimated. This is attributed to underestimated changes in warm water volume during moderate El Niño events, so that these events display relatively poor seasonal synchronization. Several significant differences between the models with and without the SWS are identified including biases in the magnitude and spatial distribution of precipitation and sea surface temperature anomalies during ENSO.

Aiming to understand the physical mechanisms leading up to the extreme 2015–16 El Niño in relation to the two previous extreme events (1997–98 and 1982–83), we found a persistent location of the westerly wind stress anomalies north of the equator during the two years prior to the event peak. As a result of this meridional asymmetry, the anomalous southward ocean flow during this period, in cooperation with warmer subsurface water over the central equatorial Pacific, led to the large event magnitude.

4

Acknowledgements

My sincerest thanks to my two supervisors, Shayne McGregor and Matthew H. England. Actually, I can only find nice words when I try to express my thoughts. I feel very lucky to have worked with them, not only because of their help and enthusiasm over the duration of my PhD but more importantly because they are good people. Shayne, I will be forever grateful for your huge patience when I was just getting started. I must also mention your fast readings of every draft and prompt responses, even when you were extremely busy. Matt, you have been absolutely sympathetic with all the issues along this journey. Thank you for giving me very good advice and guidance. You both have always been there when I have needed help and definitely, this PhD would not have been possible without you. I would also like to thank Agus Santoso for providing brilliant ideas and much insight into Part 3 and the two examiners (Dr Jong-Seong Kug and anonymous) for the constructive comments and suggestions, which improved the presentation of this thesis.

I am very grateful to Shayne McGregor's *Australian Research Council* (ARC) *Discovery Early Career Researcher Award* (DECRA) Fellowship, which supported this PhD scholarship. Thanks also to the ARC Centre of Excellence for Climate System Science, who have provided financial support and very well organized winter schools. I also acknowledge the *Climate Change Research Centre* (CCRC) for giving me a top-up scholarship and, particularly, the professional staff for all their assistance.

Special thanks should go to my colleagues, past and present, at the CCRC. You guys are amazing! It has been a pleasure to spend so much time together over the past three years and a half at lunch time, afternoon tea breaks, winter schools, conferences and outside of work. Thank you to all of you for your company and making the CCRC a great place to work.

Finally, I give a heartfelt "thank you" to my family; especially, my mum Mariluz, dad Lázaro, sister Mònica, brother-in-law David and naughty little nephew Pol, for their motivation, support, and video chats, making me feel closer during my stay in Australia. I am also deeply indebted to my friends, both near and far, for their encouragement and being part of my life. Last but not least, I would like to thank my partner, Carles, for his unconditional love and always believing in me. This whole adventure would not have been possible without you.

Contents

List of Figures

List of Tables

Supporting Publications

Abellán, E. and S. McGregor, 2016. The role of the southward wind shift in both, the seasonal synchronization and duration of ENSO events. *Climate Dynamics*, **47**, 509-527, doi: 10.1007/s00382-015-2853-1

Abellán, E., S. McGregor and M. H. England, 2017. Analysis of the southward wind shift of ENSO in CMIP5 models. *Journal of Climate*, **30**, 2415–2435, doi: 10.1175/JCLI-D-16-0326.1

Abellán, E., S. McGregor, M. H. England and A. Santoso, 2017. Distinctive role of ocean advection anomalies in the development of the extreme 2015–16 El Niño. *Climate Dynamics, under review*

Preface

El Niño-Southern Oscillation

The El Niño-Southern Oscillation (ENSO) phenomenon is the most important source of natural climatic variability worldwide on interannual time scales (e.g. Rasmusson and Carpenter 1982). ENSO is characterized by two main states, depending on the anomalous sign of sea surface temperature (SST) over the eastern and central tropical: El Niño (warming, positive SST anomalies) and La Niña (cooling, negative SST anomalies) (Fig. 0.1), which occur about every 2-7 years (Fig. 0.2).

Associated with these fluctuations in SST, El Niño events feature above normal sea level pressure (SLP) over Indonesia-northern Australia and below normal SLP over central and eastern tropical Pacific whereas the opposite is observed for La Niña events (Fig. 0.1). This large-scale seesaw in surface pressure between the western Pacific warm pool and the eastern tropical Pacific cold tongue regions is known as the Southern Oscillation. Consistently, the low-level equatorial easterlies or trade winds weaken or even reverse during El Niño and atmospheric convection is enhanced in the central and eastern tropical Pacific. Conversely, La Niña events are marked by stronger trade winds, which pile up warm water in the western Pacific enhancing atmospheric convection and rainfall in this region (Fig. 0.3). However, ENSO's impacts are not restricted to the surrounding region with weather impacts often observed across most of the globe (e.g. Ropelewski and Halpert 1987; McPhaden et al. 2006) and almost every aspect of human life such as disease outbreaks (e.g. Bouma and Dye 1997), agriculture (e.g. Hansen et al. 1998), natural disasters (e.g. Dilley and Heyman 1995; Goddard and Dilley 2005), animal movements (e.g. Saba et al. 2008; Quiños et al. 2010), water resources (e.g. Benson and Clay 1998; Twine et al. 2005), energy demand and price fluctuations (Voisin et al. 2006), and others.

It is generally accepted that the generation of an ENSO event requires a positive ocean-atmosphere feedback to amplify the original anomalous zonal equatorial SST gradient. This feedback, hypothesized by Bjerkness (1969) consists of weakened (strengthened) easterly winds during El Niño (La Niña), which deepen (shoal) the thermocline depth in the eastern equatorial Pacific, reduce (enhance) the eastern cooling and hence the zonal SST gradient which in turns reduces (enhances)

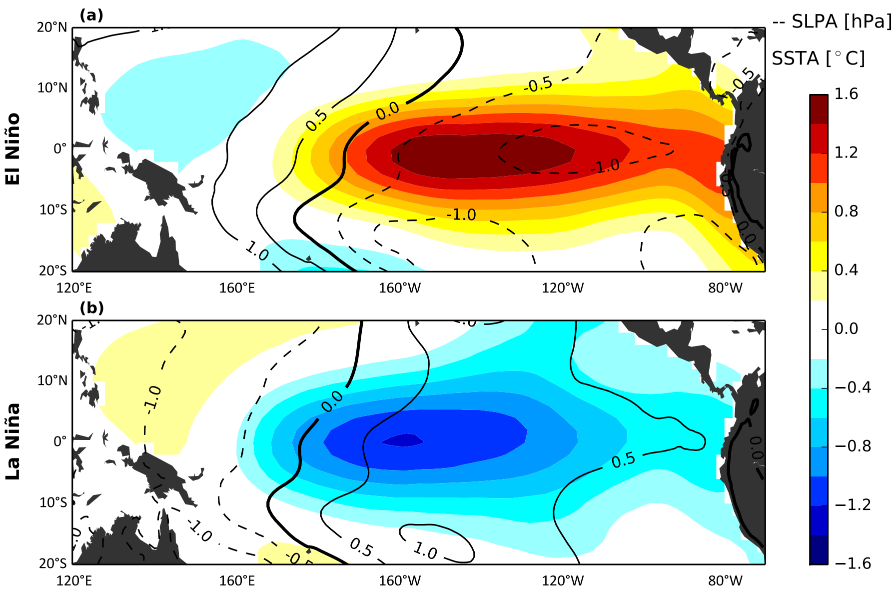

Figure 0.1: Sea surface temperature anomaly composites during DJF (shading) and sea level pressure anomaly (contours) for El Niño (a) and La Niña (b) events. Note that the contour interval is 0.5 hPa, dashed contours indicate negative values and bold line zero SLP anomaly. El Niño years: 1982–83, 1986–87, 1991–92, 1994–95, 1997–98, 2002–03, 2004–05, 2006–07, 2009–10, 2015–16. La Niña years: 1983–84, 1984–85, 1988–89, 1995–96, 1998–99, 2000–01, 2007–08, 2010–11, 2011–12. Dataset: ERSST (SST) and ERA-Interim (SLP).

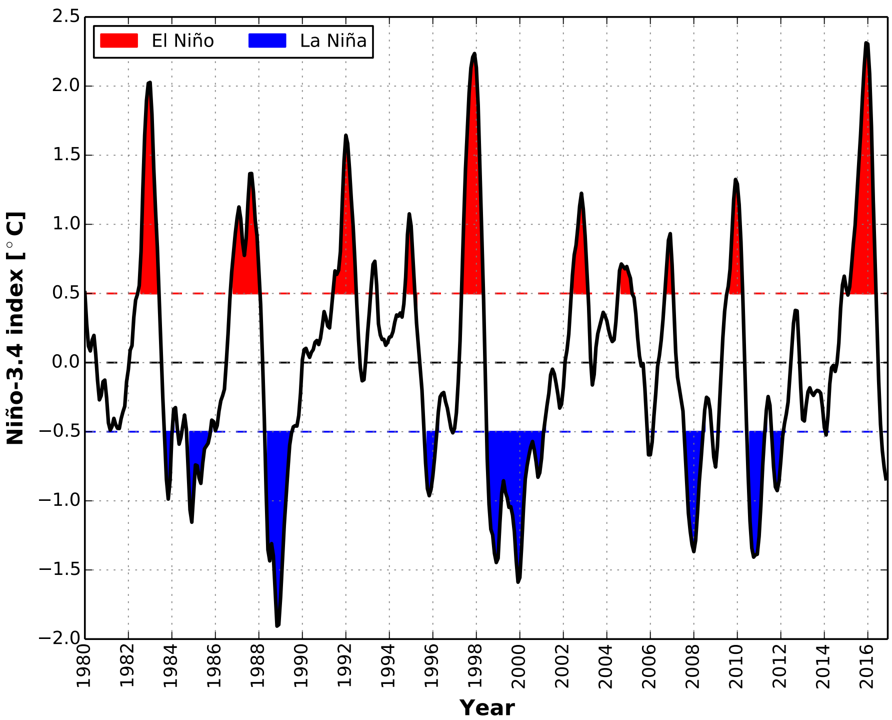

Figure 0.2: Time series of sea surface temperature anomalies in the Niño-3.4 region (5°S–5°N, 170°W–120°W) during 1980–2016. Dataset: ERSST

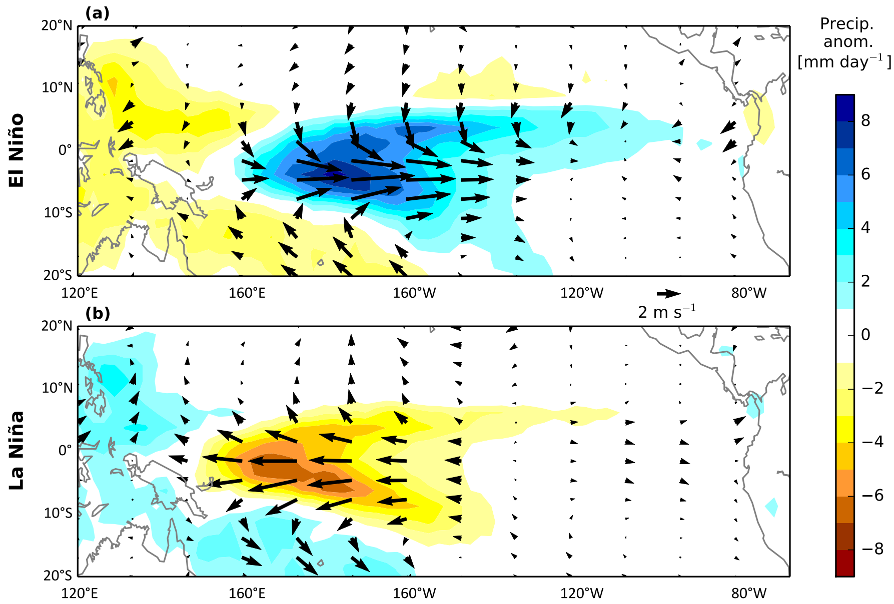

Figure 0.3: Rainfall anomaly composites during DJF (shading) and 925-hPa wind (vectors) for El Niño (a) and La Niña (b) events. See figure 0.1 for ENSO years. Dataset: CMAP (rainfall) and ERA-Interim (wind).

the wind stress. Thus, in this coupled atmosphere-ocean feedback loop, any small perturbation in either the strength of the trades or the SST gradient will grow (positive feedback). On the other hand, after an ENSO event reaches its mature phase, negative feedbacks are required to terminate growth.

The most influential conceptual theories explaining ENSO's underlying dynamics are: the Recharge-Discharge Oscillator (Jin 1997); the Delayed-Action Oscillator(Schopf and Suarez 1988); the Western Pacific Oscillator (Weisberg and Wang 1997). All of these oscillator models assume a positive ocean-atmosphere feedback in the eastern and central equatorial Pacific. Each, however, has different negative feedback that turns the warm (cold) phase into the cold (warm) phase. The Recharge-Discharge Oscillator paradigm consists of variations in warm water volume and sea level and views ENSO as an east-west-tilting mode of the equatorial thermocline, which leads to the development of SST anomalies in the eastern equatorial Pacific (Jin 1997). The Delayed-Action Oscillator model considers the excitation of off-equatorial upwelling Rossby wave propagating westward which eventually are reflected at the western boundary as upwelling Kelvin waves that shut down the instability on arrival to the eastern basin, reversing the phase of the ENSO cycle (Schopf and Suarez 1988). The Western Pacific Oscillator paradigm takes into account the off-equatorial anomalous anticyclones over the western Pacific, which trigger easterly wind anomalies in this region generating upwelling and cooling that travel eastward (Weisberg and Wang 1997).

Although the above simple paradigms take the linear view that La Niña events are the mirror of El Niño events, several studies reveal that warm and cold ENSO events are not a simple mirror image (e.g. Hoerling et al. 1997; Kessler 2002; Larkin and Harrison 2002; Choi et al. 2013; Dommenget et al. 2013). Instead, El Niño and La Niña exhibit significant asymmetries. For instance, cool La Niña SST anomalies extend about 10 ° further west than those warm El Niño events (Okumura and Deser 2010). Apart from this asymmetry in their spatial structure, many La Niña events persist into the following year and often reintensify in boreal winter (e.g. Larkin and Harrison 2002; McPhaden and Zhang 2009; Okumura and Deser 2010; Ohba and Ueda 2009; Ohba et al. 2010; Okumura et al. 2011; DiNezio and Deser 2014), whereas most El Niño events terminate rapidly during boreal spring. Furthermore, the SST anomalies associated with El Niño events are larger than those with La Niña, generating a positive (negative) SST skewness in the eastern (central) equatorial Pacific (Burgers and Stephenson 1999). It has been suggested that non-linear SST-wind feedback (Choi et al. 2013; Frauen and Dommenget 2010) might be the source of ENSO asymmetry.

It has been increasingly recognized that ENSO events come in many different flavours (Wang and Weisberg 2000; Trenberth and Stepaniak 2001; Larkin and Harrison 2005; Weng et al. 2007; Yu and Kao 2007; Ashok et al. 2007; Kao and Yu 2009; Kug et al. 2009; Lee and McPhaden 2010) with two main types of El Niño events: Eastern-Pacific El Niño, characterized by relatively large SST anomalies in the eastern equatorial Pacific, and Central-Pacific El Niño associated with anomalous SST mostly confined to the central equatorial Pacific near the edge of the western Pacific warm pool. The former is also known as canonical El Niño, whereas the latter has different names: El Niño-Modoki (Ashok et al. 2007); Warm Pool El Niño (Kug et al. 2009), Date Line El Niño (Larkin and Harrison 2005).

Despite these differences between events mentioned above, one of the unique features of ENSO events is their tendency to peak mostly toward the end of the calendar year (Rasmusson and Carpenter 1982; Harrison and Larkin 1998; Deser and Wallace 1987; Galanti and Tziperman 2000; An and Wang 2001) (Fig. 0.4). This synchronization to the annual cycle suggests a strong interaction between ENSO's dynamics and the annual cycle (Tziperman et al. 1998; Zhang et al. 2015). The onset of ENSO events commonly occurs in boreal spring (MAM) or summer (JJA) and the events usually terminate in boreal spring of the following year (Larkin and Harrison 2002; Chang et al. 2006). Figure 0.4 also displays the duration and magnitude asymmetries between El Niño and La Niña events mentioned above.

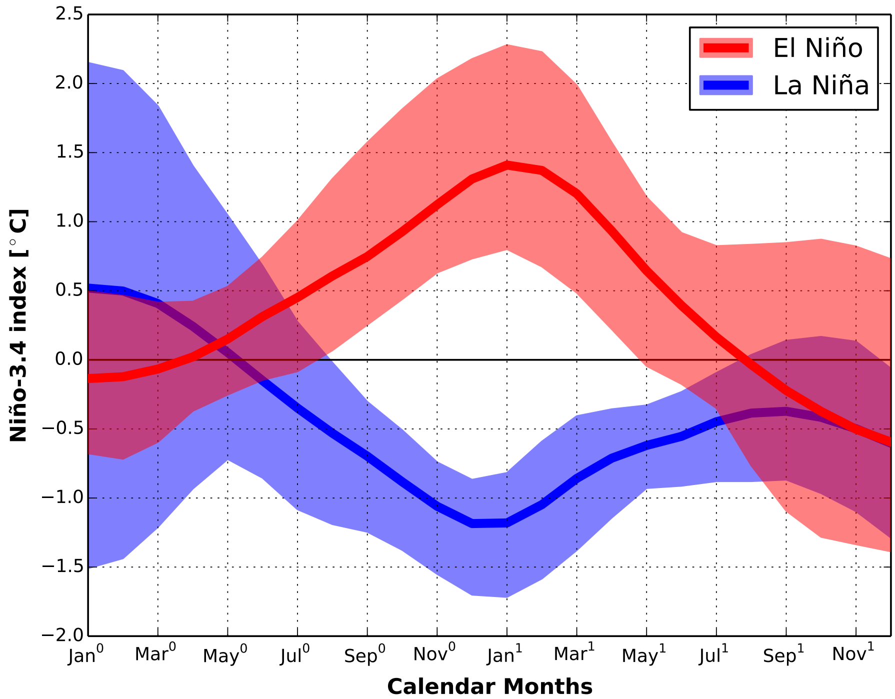

Figure 0.4: Sea surface temperature anomaly composites during ENSO years (see Fig. 0.1 for ENSO years) over the Niño-3.4 region. The shaded area shows fits the 5^{th} and 95^{th} percentile of all composite years.

Wind stress and oceanic response

As mentioned before, ENSO can be explained by the strong coupling between the Walker circulation, the zonal gradient of SST and the longitudinal tilt of the thermocline (Bjerknes 1969; Wyrtki 1975). The most important forcing of the ocean circulation is due to the transfer of the momentum from the atmosphere to the ocean by ocean surface wind stress (hereafter wind stress). At large scales and at low frequencies, the equatorial ocean is driven by the zonal wind stress (Clarke 2008). The ocean response is a sum of forced long equatorial Rossby waves and a forced equatorial Kelvin wave (Matsuno 1966).

Previous research (e.g Kirtman 1997; Wang et al. 1999; An and Wang 2000; Capotondi et al. 2006; Neale et al. 2008; Kug et al. 2009) has shown that the spatial distribution of anomalous wind stress during ENSO events is crucial for their time scale. In the delayed oscillator theory, mentioned above, when the amplitude of the Kelvin waves reflecting off the western boundary is reduced, the period of the oscillation is increased (Kirtman 1997). Further, a shift in the location of the SST anomalies can lead to different patterns of wind stress. For instance, the zonal wind anomalies associated with CP El Niño are shifted to the west compared to those associated with the EP El Niño (Kug et al. 2009).

The role of the winds in ENSO onset

A link between westerly wind bursts (WWB) and the onset and development of every significant El Niño event has been observed (Luther et al. 1983; Kerr 1999; Fasullo and Webster 2000; McPhaden 2004). A WWB can be defined as all instances of westerly wind anomalies above 7 m s^{-1} and sustained above 4 m s^{-1} for 5 or more days (Eisenman et al. 2005; Gebbie et al. 2007). These westerly gusts cause downwelling thermocline depth anomaly in the central Pacific, which travels to the eastern Pacific as a set of Kelvin waves (Zelle et al. 2004), with the subsequent warming in the eastern equatorial Pacific (e.g. Vecchi and Harrison 2000). Thus, WWB have been shown to play an important role triggering El Niño events (Latif et al. 1988; Lengaigne et al. 2004), whereas the buildup of the warm water volume (WWV) in the equatorial Pacific is considered a necessary precondition for the development of an El Niño (Wyrtki 1985; Meinen and McPhaden 2000; An and Kang 2001).

Similar to the duration, amplitude (in wind stress anomaly), and zonal extent of WWBs, their counterparts are easterly wind surges (EWSs; Chiodi and Harrison 2015). It is shown that EWS events lead to decrease in SST that occur in ENSO-neutral conditions during the months of the year associated with La Niña onset and growth. Thus, this peak at subseasonal (3-60 day) time scales of the zonal wind field due to WWBs and EWSs in the equatorial Pacific (Harrison and Luther 1990) plays a key role in the initiation of ENSO events (e.g. Luther et al. 1983; Harrison and Giese 1991; Hartten 1996; Harrison and Vecchi 1997; Vecchi and Harrison 2000; Harrison and Chiodi 2009; Chiodi et al. 2014). In association with this, a lower frequency and large-scale Bjerkness feedback component (westerly for El Niño and easterly for La Niña) is fundamental to the maintenance of ENSO events.

The role of the winds in ENSO termination

The observed westerly (easterly) wind anomalies during El Niño (La Niña) events prior to their peaks (SON) exhibit the largest magnitude located at the equator (Fig. 0.5). However, the maximum of these westerly anomalies shift south of the equator during the mature phase (DJF) (Fig. 0.5). Previous studies have associated this movement of the westerly to the southern hemisphere, described in the late 80's by Harrison (1987), with the ENSO peak season (Harrison and Vecchi 1999; Vecchi and Harrison 2003) and, therefore, as an indicator of the ENSO termination. This southward wind shift has been shown to drive: (1) strong thermocline shoaling in the

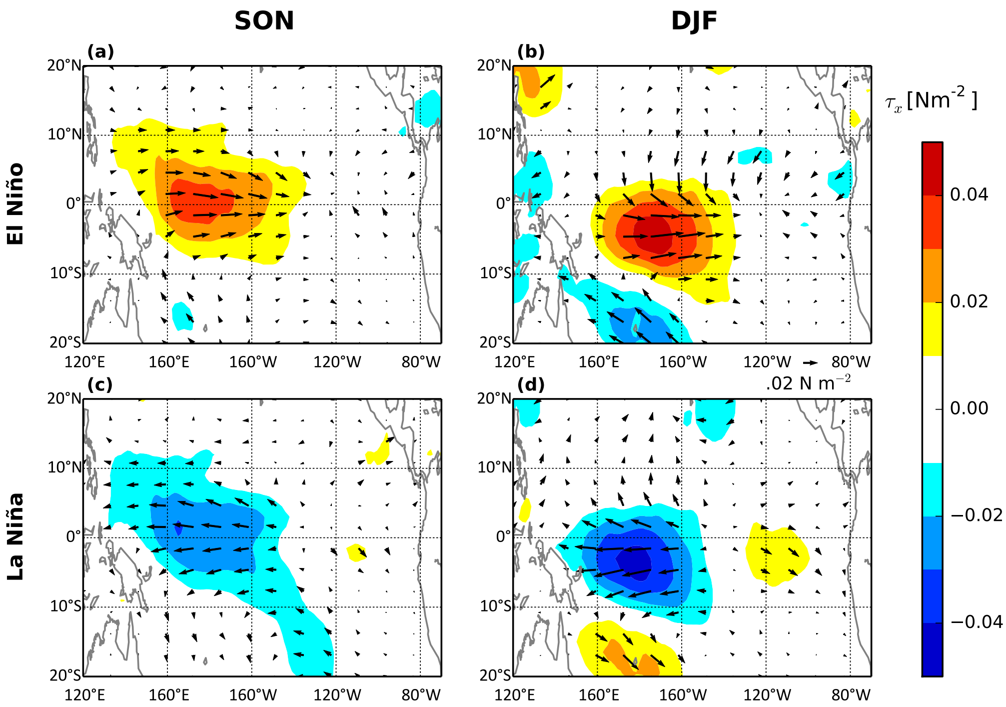

Figure 0.5: Composites of wind stress anomalies during El Niño events (top), and La Niña events (bottom). The anomalies are averaged from September to November during year 0 (left), and from December to February during year +1 (right). Shading indicates zonal components. See Fig. 0.1 for ENSO years. Dataset: ERA-Interim

eastern equatorial Pacific (e.g. Harrison and Vecchi 1999; Vecchi and Harrison 2003, 2006; Lengaigne et al. 2006; Lengaigne and Vecchi 2010); (2) changes in equatorial warm water volume (WWV) (McGregor et al. 2012b, 2013) and (3) interhemispheric exchanges of upper ocean mass (McGregor et al. 2014). The link with the seasonal cycle is thought to be related to seasonal changes in insolation (Vecchi and Harrison 2003; Spencer 2004; Lengaigne et al. 2006; Vecchi 2006; Xiao and Mechoso 2009), which drives southward displacement of the warmest SST and convection during DJF (Lengaigne et al. 2006; Vecchi 2006), and the associated minimal surface momentum damping of wind anomalies (McGregor et al. 2012b).

Objectives and Thesis Outline

This thesis seeks to better understand the role of the meridional movement of wind stress anomalies during ENSO events in their evolution. In particular, we examine the consequences of the meridional location of the winds and its movement. This includes the wind shift observed during the mature phase of ENSO events on their termination and the effect of the westerly wind anomalies located north of the equator during 2014 in the large magnitude of the 2015–16 El Niño.

This thesis is divided into three main parts, corresponding to the three lead-authored publications listed in the Supporting Publications. Therefore, each part consists of a complete scientific article, including an abstract, an introduction, methods, results, discussion and conclusion sections. The aims of each part are introduced below:

Part 1 examines the role of the southward wind shift in the seasonal synchronization and, thus, the termination of ENSO events. We construct a hybrid coupled model capable of reproducing ENSO and this late-year meridional wind movement and carry out some experiments with and without this shift. This allows us to compare the events between these two settings in terms of the synchronization to the seasonal cycle of the events and their duration in addition to the asymmetry between El Niño and La Niña events. This work was published in *Climate Dynamics*.

Part 2 continues the analysis of the southward wind shift but focuses on state-of-the-art coupled general circulation models participating in the CMIP5 (Taylor et al. 2012). The aim of Part 2 is to address the following questions: (1) Do the CMIP5 models reproduce a realistic southward wind shift? (2) what variables are related to this shift in CMIP5 models? and, linked to Part 1 with a simple model, (3) what is the role of this meridional movement in the seasonal synchronization of modeled ENSO events? This work was published in *Journal of Climate*.

Part 3 explores the physical mechanisms that controlled the development of the most recent extreme El Niño event of 2015–16, and how they differed from the past two strongest El Niño events observed since the satellite era began in 1979 (1982–83 and 1997–98 events). This is a done through a detailed analysis of wind stress, SST, sea surface height anomalies in the lead up to these El Niño events. We then perform a heat budget analysis focusing on the ocean advective terms to further reveal the distinction among the events. This work has been submitted for publication to *Climate Dynamics*.

As each of these parts contains a specific discussion and conclusion section, the chapter "Concluding Remarks" provides a brief summary of the key findings of the thesis and contains recommendations for future research.

Part 1

The role of the southward wind shift in both, the seasonal synchronisation and duration of ENSO events

---

The material in this Part is based around the work published as:

Abellán, E. and S. McGregor, 2016. The role of the southward wind shift in both, the seasonal synchronization and duration of ENSO events. *Climate Dynamics*, **47**, 509-527, doi: 10.1007/s00382-015-2853-1

See Appendix A for the publication.

Abstract

Near the end of the calendar year, when El Niño events typically reach their peak amplitude, there is a southward shift of the zonal wind anomalies, which were centred around the equator prior to the event peak. Previous studies have shown that ENSO's anomalous wind stresses, including this southward shift, can be reconstructed with the two leading EOFs of wind stresses over the tropical Pacific. Here a hybrid coupled model is developed, featuring a statistical atmosphere that utilises these first two EOFs along with a linear shallow water model ocean, and a stochastic westerly wind burst model. This hybrid coupled model is then used to assess the role of this meridional wind movement on both the seasonal synchronization as well as the duration of the events. It is found that the addition of the southward wind shift in the model leads to a Christmas peak in variance, similar to the observed timing, although with weaker amplitude. We also find that the added meridional wind movement enhances the termination of El Niño events, making the events shorter, while this movement does not appear to play an important role on the duration of La Niña events. Thus, our results strongly suggest that the meridional movement of ENSO zonal wind anomalies is at least partly responsible for seasonal synchronization of ENSO events and the duration asymmetry between the warm (El Niño) and cool (La Niña) phases.

1.1 Introduction

The El Niño-Southern Oscillation (ENSO) phenomenon is the main driver of Earth's interannual climate variability (Neelin et al. 1998; McPhaden et al. 2006), leading to significant changes in the global atmospheric circulation (Ropelewski and Halpert 1989; Philander 1990; Trenberth et al. 1998; Wang et al. 2003). ENSO refers to a year-to-year recurring warming (El Niño) and cooling (La Niña) of the eastern and central tropical Pacific sea surface temperature (hereafter SST), and a related large-scale seesaw in atmospheric sea level pressure between the Australia-Indonesian region and the south-central tropical Pacific (Bjerkness 1969; Wyrtki 1975; Cane and Zebiak 1985; Graham and White 1988).

El Niño and La Niña events typically last for about a year and have an irregular period ranging between 2 and 7 yr. As every winter or summer is different in the extratropics, ENSO events come in many different flavours (Trenberth and Stepaniak 2001). However, they generally follow a similar pattern of developing during boreal spring (MAM), peaking in boreal winter (DJF) and decay during boreal spring of the following year (Rasmusson and Carpenter 1982; Larkin and Harrison 2002; Chang et al. 2006). Understanding the physical processes responsible of such seasonal synchronization is of central importance to predictions (Balmaseda et al. 1995; Torrence and Webster 1998), simulations (Ham et al. 2013) as well as impacts of ENSO, which depend on the characteristics of the events (Trenberth 1997).

However, the dynamics underlying ENSO synchronization to the annual cycle is not yet understood. Recently, Stein et al. (2014) classified existing theories into two possible categories: (i) frequency locking of ENSO, as a nonlinear oscillator, to periodic forcing by the annual cycle (e.g., Jin et al. 1994; Tziperman et al. 1994); or (ii) the modulation of the stability of ENSO due to the seasonal variation of the background state of the equatorial Pacific (Philander et al. 1984; Hirst 1986). Their results suggest that the annual modulation of the coupled stability of the equatorial Pacific ocean-atmosphere system is by far the more likely mechanism generating the synchronization of ENSO events to the annual cycle (Stein et al. 2014). Thus, below we will provide a brief description of the main theories that fall into this category.

One of the earliest suggestions about the tendency of ENSO seasonal synchronization was reported by Philander (1983), who suggested the seasonal movement of the Pacific intertropical convergence zone (ITCZ), and its effect on the atmospheric heating, (i.e. the coupled instability strength) as the responsible for ENSO's onset, hence for such seasonal synchronization. Furthermore, Hirst (1986) noted that other seasonal climatological factors that might enhance the coupled instability of the system are strong zonal wind in July–August, shallow thermocline in September–October, large zonal equatorial SST gradient in September, and high SST over the central equatorial Pacific in May. Subsequently, Battisti (1988) added to the previous list the influence of some weakening of oceanic upwelling in the central Pacific during March–May and some strengthening of the coastal upwelling in the eastern Pacific during August–September. Tziperman et al. (1997) found that the dominant factor in determining the strength of the ocean-atmosphere instability to be due to the seasonal wind convergence (i.e., the ITCZ location), while Yan and Wu (2007) work suggested that the seasonal change in the mean SST is the predominating factor. The results of Galanti et al. (2002) were partly consistent with those of Hirst (1986), suggesting that the seasonal ocean-atmosphere coupling strength is influenced by the outcropping of the east Pacific thermocline during the second half of the year. Inter-basin teleconnections have also recently been implicated in the termination of ENSO events. As one example, some studies indicate that the basin warming of the tropical Indian Ocean is responsible for the weakening or reversal of equatorial westerly wind anomalies over the western Pacific at the mature phase of

El Niño (Annamalai et al. 2005; Kug and Kang 2006; Obha and Ueda 2007, 2009; Yamanaka et al. 2009; Yoo et al. 2010). Finally, another mechanism, which involves meridional changes in the coupled ocean-atmosphere wind system and thought as a major negative feedback playing a role in the decay of El Niño events, will be emphasized below.

This study focuses on the southward wind shift theory proposed by Harrison and Vecchi (1999) and Vecchi and Harrison (2003) as a major negative feedback involved in the phase synchronization between ENSO and the annual cycle. During El Niño events, the associated westerly wind anomalies are centred quite symmetric about the equator prior to the event peak (SON) whereas there is a shift of these anomalies towards south of the equator during the mature phase (DJF), with anomalous northerly winds developing north of the equator (Fig. 1.1). The magnitude of this southward wind shift appears to be dependent on the magnitude of the ENSO event, as suggested by Lengaigne et al. (2006). For instance, during DJF of strong El Niño events there is a strong southward movement along with movement towards east, with the maximum amplitude of the anomalous westerly winds shifting from date line in SON, to 160 °W in DJF (Fig. 1.1a, b). In contrast, during DJF of moderate El Niño events there is a much smaller southward wind shift, consistent with the findings of McGregor et al. (2013) who utilised multiple reanalysis products, and virtually no zonal movement of the anomalous westerlies (Fig. 1.1c, d). The zonal and meridional movement observed with easterly wind anomalies during La Niña events largely mirror for moderate El Niño events (Fig. 1.1e, f), although with southerly winds developing north of the equator. These composite analyses shown in Fig. 1.1 are in broad agreement with those reported by Okumura and Deser (2010), where a different atmospheric reanalysis product was used.

This shift in wind anomalies has been studied by Harrison (1987); Harrison and Larkin (1998); Harrison and Vecchi (1999); Vecchi and Harrison (2003); and more recently it has been proposed to explain the seasonal synchronization since the resulting reduction of equatorial westerly wind anomalies has been shown to drive: i) strong thermocline shoaling in the eastern equatorial Pacific (e.g., Harrison and Vecchi 1999; Vecchi and Harrison 2003, 2006; Lengaigne et al. 2006; Lengaigne and Vecchi 2010); ii) changes in equatorial warm water volume (WWV) (McGregor et al. 2012b, 2013) and iii) interhemispheric exchanges of upper ocean mass (McGregor et al. 2014). This shift has been linked to the southward displacement of the warmest SSTs and convection during DJF (Lengaigne et al. 2006; Vecchi 2006), and the associated minimal surface momentum damping of wind anomalies (McGregor et al. 2012b), both of which are due to the seasonal evolution of solar insolation. McGregor et al. (2013) also show that the discharging effect of the southward wind

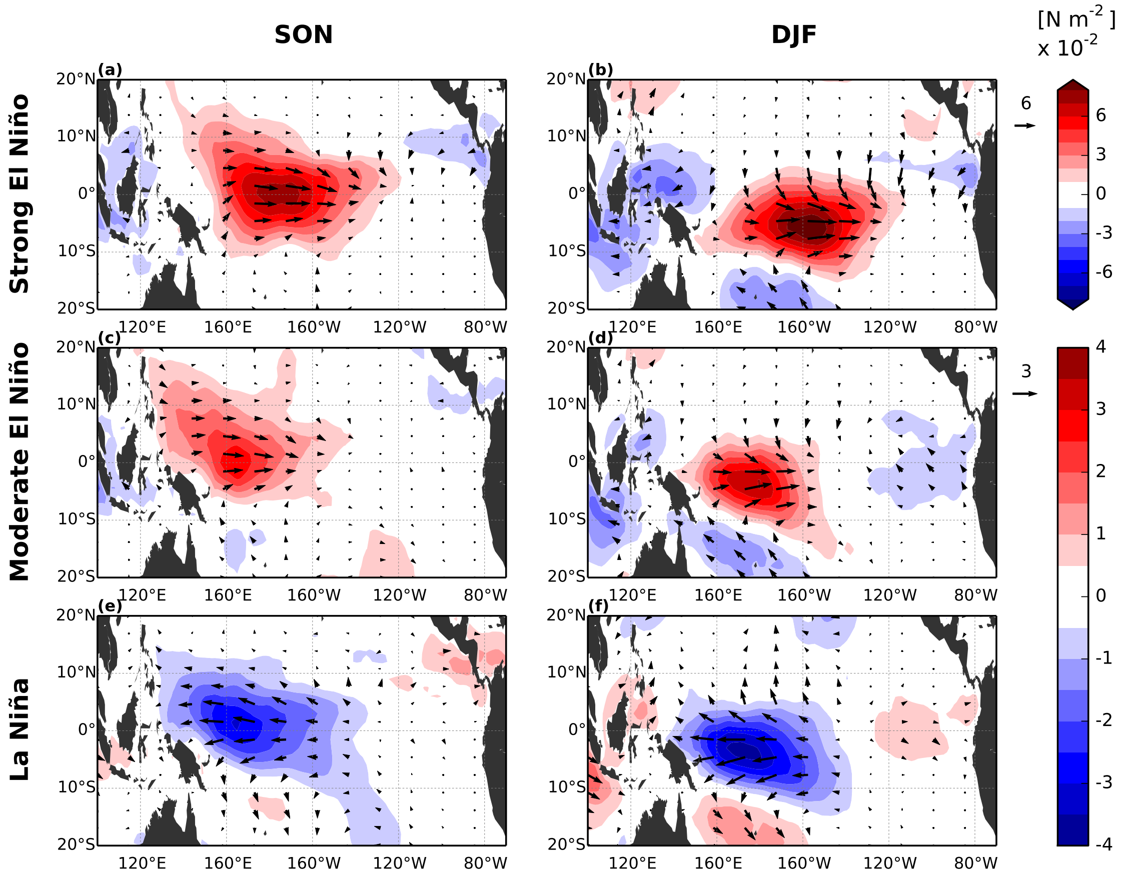

Figure 1.1: Composites of wind stress anomalies during strong El Niño (a, b), moderate-weak El Niño (c, d), and La Niña events (e, f). The anomalies are averaged from September to November during year 0 (a, c, e), and from December to February during year +1 (b, d, f). Shading indicates zonal components. Strong El Niño years: 1982–83 and 1997–98. Moderate-weak El Niño years: 1987–88, 1991–92, 1994–95, 2002–03, 2004–05, 2006–07 and 2009–10. La Niña years: 1984–85, 1988–89, 1995–96,1999–00, 2000–01, 2007–08, 2010–11 and 2011–12. See section 1.2.1 for the ENSO definition.

shift increases with increasing El Niño amplitude, while remaining relatively small regardless of La Niña amplitude. They suggest that this aspect may also help explain the ENSO phase duration asymmetry (i.e., why El Niño events have a shorter duration than La Niña events).

The purpose of this study is to single out the meridional wind movement of ENSO winds from the other possible mechanisms detailed above, and identify its role in the synchronization of ENSO events to the seasonal cycle. We also examine whether the ENSO phase asymmetry observed in this shift can account for the fact that La Niña events tend to persist for longer periods than El Niño (Okumura et al. 2011). Specifically, a simple hybrid coupled model (HCM), which utilises a statistical atmospheric that is able to function with and without the southward wind shift, is developed. We find that this meridional wind movement plays a crucial role in the seasonality of ENSO events since its inclusion in the model results in a moderate synchronization of modelled ENSO events to the seasonal cycle with maximum of SST anomalies (SSTA hereafter) in November–January. Additionally, we show that the duration of warm events is influenced by this shift, with the meridional wind movement favouring the early termination, while the duration of cool events appears to be marginally dependent on whether and how the shift is included in the model.

The rest of the chapter is organised as follows. In the next section we shall present the SST dataset used and the two leading Empirical Orthogonal Functions (EOFs) of wind stresses over the tropical Pacific, Sect. 1.3 describes the 3-component hybrid coupled model developed in this study. Section 1.4 and 1.5 present our experiment results, with the large 1997–98 El Niño and 4-member ensemble of 100-yr runs respectively, carried out with and without this southward wind shift and how sensitive the response of thermocline depth and, consequently, SSTA result. Finally, a discussion of the major findings is presented in Sect. 1.6.

1.2 Data

This study employs the monthly Niño-3.4 and Niño-3 indexes (namely SSTA averaged in the region 5 °S–5 °N, 170 °W–120 °W, and 5 °S–5 °N, 150 °W–90 °W, respectively) derived from Extended Reconstructed SST (ERSST v3b) dataset (Smith et al. 2008) for the period 1979–2013 when wind stress data are required (Sect. 1.1 and 1.2) and for the period 1880–2013 when wind stresses are not required (Sect. 1.5). It is important to mention that the anomalies were computed with respect to a 1971–2000 monthly climatology. Here, we define an ENSO event when Niño-3.4 index is either above 0.5 °C (warm events) or below -0.5 °C (cool events) for at least 5 consecutive months after a 3-month binomial filter applied, as in Deser et al. (2012) to reduce month-to-month noise. Strong El Niño events are identified when their peak magnitudes are greater than 2.0 °C, as Lengaigne et al. (2006). Further, this El Niño classification according to their magnitudes has been used in numerous other studies (e.g., Lengaigne and Vecchi 2010; Takahashi et al. 2011; Chen et al. 2015)

It is also worth noting that the results of the southward wind shift during ENSO events are qualitatively similar if we instead differentiate between Eastern Pacific (EP) and Central Pacific (CP) type ENSO events rather than event magnitude, consistent with McGregor et al. (2013).

1.2.1 Wind stress decomposition

In order to determine the dominant patterns associated with interannual wind changes, an Empirical Orthogonal Function (EOF) analysis of wind stresses over the tropical Pacific (10 °S–10 °N and 100 °E–70 °W) is performed. Observational wind data is taken from the European Centre for Medium-Range Weather Forecasts (ECMWF) Interim Reanalysis (ERA-interim) (Dee and Uppala 2009). We first obtain the daily average wind data that span the period 1979–2013, the surface winds are then converted to wind stresses using the quadratic stress law (Wyrtki and Meyers 1976):

$$(\tau_x, \tau_y) = C_D \rho_a W(U, V) \tag{1.1}$$

where U and V are the zonal and meridional surface winds (m s^{-1}) respectively; W denotes the surface wind speed (m s^{-1}), $C_D = 1.5 \times 10^{-3}$ is the dimensionless drag coefficient; and $\rho_a = 1.2$ kg m^{-3} represents the atmospheric density at the surface. The monthly mean wind stresses are calculated from the daily wind stresses and wind stress anomalies are computed by removing the monthly climatology of the entire 35-yr of record.

As in previous studies (McGregor et al. 2012b, 2013; Stuecker et al. 2013), the global spatial patterns of the first two EOFs (calculated over all seasons) are obtained by regressing the associated principal component (PC) time series onto the anomalous wind stress at each spatial location. The first EOF (EOF1), which accounts for 33 % of the equatorial region variance, features positive zonal wind anomalies in the western-central tropical Pacific (i.e., anomalous Walker circulation) that have their maximum amplitude south of the equator (Fig. 1.2a). It is clear that EOF1 represents ENSO variability since the correlation coefficient between this leading PC time series and SSTA averaged over the Niño-3 region (5 °S–5 °N and 150 °–90 °W)

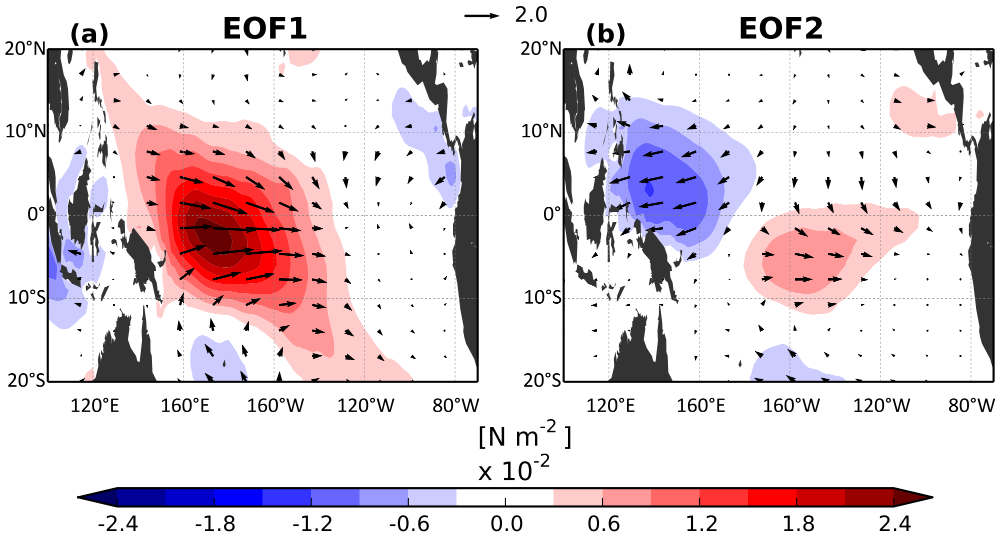

Figure 1.2: The spatial pattern of surface wind stresses from (a) EOF1 and (b) and EOF2, which account for approximately 33 % and 16 % of the total variance over the tropical Pacific region, respectively. The shading contours represent the zonal components.

is 0.76. Regarding the second mode (EOF2), which explains 16 % of the equatorial region variance, the associated regression patterns are largely meridionally asymmetric featuring a prominent anticyclonic circulation in the western north Pacific region (Fig. 1.2b) consistent with the Philippine Anticyclone (e.g., Wang et al. 1999). Furthermore, EOF2 captures westerlies located south of the equator, around the same region as the maximum anomalies during DJF of El Niño events (Fig. 1.1b). As it will be shown later in this section, this second mode is related to the southward wind shift, although as expected by the definition of the EOF analysis (e.g., Lorenz 1956), there is only a weak linear relationship (r = 0.20) between the EOF2 time series (PC2) and ENSO (Niño-3 index). Interestingly however, PC2 has been linked to ENSO (McGregor et al. 2012b) as well as shown to play a prominent role in the recharge/discharge of equatorial region WWV (McGregor et al. 2013) and interhemispheric exchanges (McGregor et al. 2014).

Composites of PC1 around ENSO events reveal that event development occurs from Mar^0–May^0, and reaches the maximum amplitude near the end of the calendar year (Fig. 1.3). It is worthwhile to note the subtle differences between strong and moderate or weak El Niño events, where the maximum PC1 amplitudes in strong warm events tend to be stronger that seen during moderate events and zero values during moderate events are reached around 3 months before in strong events.

The composite of PC2 for warm events reveals a striking difference between the two types magnitudes of El Niño. For instance, PC2 during strong events changes

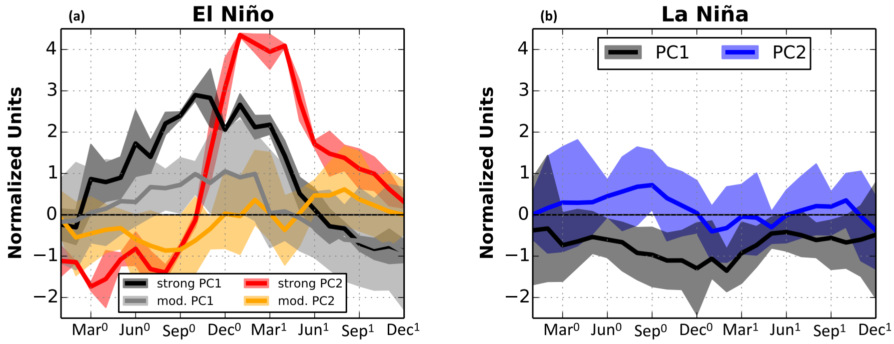

Figure 1.3: Time series of the wind stresses PC1 and PC2 from Jan^0 to Dec^1 for (a) El Niño and (b) La Niña during 1979–2013. The shaded areas show the 5th and 95th percentiles across all events, and the thick lines represent the mean values.

sign dramatically around the mature phase (moderate negative prior and strong positive after), while PC2 values during moderate events tend to be negative prior to the mature phase and remain roughly zero thereafter (Fig. 1.3a). The evolution of PC2 during La Niña events roughly mirrors that of moderate El Niño events, displaying positive values prior to event peak, which remain approximately zero thereafter (Fig. 1.3b).

These EOF results are consistent with the composites of wind stress anomalies shown in Fig. 1.1. For instance, PC1 (PC2) is positive (negative) during SON for El Niño events leading to westerly anomalies that are quasi-symmetric around the equator since the EOF2 anomalies of wind stress are positive over the Philippine region. If we analyse what occurs during DJF, we find that the maximum westerly anomalies in strong El Niño events are shifted south-eastward towards the same area represented by the westerlies in the EOF2 pattern (Fig. 2b), consistent with the high positive values of PC2. During SON in both moderate El Niño and all La Niña events, PC1 and PC2 display anomalies of the same sign which ensures that the anomalies are largely symmetric about the equator, consistent with the observed composites (Fig. 1.1). The pattern observed for both moderate El Niño and all La Niña events during DJF (Fig. 1.1) is quite similar to EOF1 (Fig. 1.2a), which is in good agreement with PC2 values shown to be close to zero (Fig. 1.3). Therefore, in agreement with the previous studies of McGregor et al. (2012b, 2013) the combination of these two leading EOFs can be viewed to represent this southward shift of zonal wind stress anomalies during both El Niño and La Niña. It is worth emphasizing that McGregor et al. (2013) utilised eight global wind products, ERA-interim among others, finding a very similar spatial patterns and temporal variability for the two leading EOF modes amongst all data sets (see their Fig. S1 and Table S1).

1.3 Coupled model description

In this section, we describe the components of the hybrid coupled model which has been developed in this project with the objective of exploring the role of the southward wind shift in the synchronization of ENSO events to the seasonal cycle.

1.3.1 Ocean model

The ocean model utilised here is a shallow-water model (SWM), whose name refers to the fact that the horizontal scale of the planetary scale waves (100–1000 km) is much larger than the vertical scale (ocean depth ~4 km), which allows the Navier-Stokes equations to be simplified considerably. It is a linear reduced-gravity model resolved on a 1 ° × 1 ° spatial grid for the low- to mid-latitude global ocean between 57 °S–57 °N and 0 °–360 °E. The density structure of the 1½-layer baroclinic system consists of a well mixed active upper layer of uniform density overlaying a deep motionless lower layer of larger uniform density. These ocean density layers are separated by an interface (the pycnocline) that provides a good approximation of the thermocline. This is a crucial consequence as it allows us to quantify the upper-ocean heat content (e.g. Rebert et al. 1985), i.e., the warm-water volume (Meinen and McPhaden 2000), and provide an estimate of equatorial SSTA (e.g., Kleeman 1993; Zelle et al. 2004).

The ocean dynamics are described by the linear reduced-gravity form of the shallow-water equations detailed below (Eqs. (2) – (4)):

$$u_t - fv + g'\eta_x = \frac{\tau^x}{\rho H} + F_m \tag{1.2}$$

$$v_t + fu + g'\eta_y = \frac{\tau^y}{\rho H} + F_m \tag{1.3}$$

$$g'\eta_t + c_1^2(u_x + v_y) = 0 \tag{1.4}$$

where u and v are the eastward and northward components of velocity respectively (m s^{-1}), t is time (s), H represents the mean pycnocline depth, $H = 300$ m (Tomczak and Godfrey 1994, p. 37), f (s^{-1}) is the Coriolis parameter, ρ is the ocean water density, $\rho = 1000$ kg m^{-3}, and F_m the bottom friction per unit mass. The reduced gravity, g', reflects the density difference between the upper and lower layers. We use the typical value of $g' = 0.026$ m s^{-2} (Tomczak and Godfrey 1994, p. 37). The corresponding first baroclinic mode gravity wave speed, $c_1 = \sqrt{g'H}$), is

2.8 m s^{-1}. The long Rossby wave speed C_R (m s^{-1}) is given by the equation, $C_R = \beta(c_1^2/f^2)$, where β (m^{-1} s^{-1}) is the derivative of f northward.

The model time step is 2 h and Fischer's (1965) numerical scheme is utilized for model time stepping. Motion in the upper layer is driven by the applied wind stresses (per unit density), τ (m^2 s^{-2}), which are anomalies from long-term monthly means (i.e., seasonal cycle removed). The associated response of the ocean is displayed by the vertical displacement of the thermocline, η (m), and the horizontal velocity components (u and v) of the flow velocity. This model formulation permits Ekman pumping and both Rossby and Kelvin wave propagation along the thermocline to be generated with appropriate large-scale wind stress forcing. It also includes realistic continental boundaries that were calculated as the location where the bathymetric dataset of Smith and Sandwell (1997) has a depth of less than the model mean thermocline depth of 300 m.

Regarding the calculation eastern-central Pacific SSTA, we utilise a simplified version Kleeman's (1993) SST equation by applying the thermocline anomaly term only. Kleeman (1993) shows that this single term is primarily responsible for hindcast skill in ENSO predictions. Thus, while being the simplest scheme, it contains the essential physics required to produce realistic SSTA. Hence, the equatorial SSTA depends only on the thermocline depth anomaly. Changes in the SSTA on the equator are modelled by the equation

$$T_t = \alpha(x)\eta(x) - \epsilon T \tag{1.5}$$

where T is the SSTA at time t, ϵ is the Newtonian cooling coefficient, $\epsilon = 2.72 \times 10^{-7}$ s^{-1}, x is the longitude and α is a longitude-dependent parameter that relates the modeled oceanic thermocline depth displacement η along the equator to the SSTA, being α= 3.4 $\times$ 10^{-8} °C m^{-1}s^{-1} in the eastern Pacific and reducing linearly west of 140 °W to a minimum of $\alpha/5$ at the western equatorial boundary at 120 °E. Such a difference reflects the fact that the equatorial thermocline depth anomalies display a tighter connection with SSTA in the east than the west (Zelle et al. 2004). For the rest of latitudes, a fixed meridional structure that decays away from the equator with an e-folding radius of 10 ° is assumed. Taking into account the non-linear relationship between central Pacific zonal wind stress anomalies and Niño-3 index as reported by Frauen and Dommenget (2010), the parameter α is reduced by 20 % for negative SSTA in Niño-3 region. In addition, a threshold of 37.5 m is set on the maximum absolute depth of equatorial thermocline anomalies in order to prevent runaway coupled instability.

It is also worthwhile to mention that the use of this simplified SST equation implies that each of these HCMs can generate only EP El Niño and La Niña events, i.e. only one EOF of SSTA. Therefore, the results of these HCM simulations will not distinguish between EP-CP event differences. It has been documented in several studies that this ocean model can produce observed variations of ocean heat content and sea surface heights reasonably well (e.g., McGregor et al. 2012b,a). Furthermore, a validation of this ocean model was carried out by simply forcing the model with ERA-interim monthly wind stress anomalies over 1979–2013. The modelled Niño-3 and Niño-3.4 indexes were then compared with those observed during the same period revealing correlation coefficients of 0.83 and 0.82, respectively (statistically significant above the 99 % level).

1.3.2 Statistical atmospheric model

The statistical atmosphere has been constructed by the two leading EOFs of wind stresses over the tropical Pacific. It has been shown above that the linear combination of both EOFs can reproduce quite well the southward shift of the maximum westerly wind anomalies and its related seasonal weakening of equatorial westerly wind anomalies, both of which have been proposed to contribute to the transition between El Niño and La Niña (e.g., Harrison and Vecchi 1999; Vecchi and Harrison 2003, 2006; Lengaigne et al. 2006; McGregor et al. 2012b, 2013).

The statistical atmospheric model is coupled to the ocean SWM to produce three Hybrid Coupled Models (HCM): HCM1 consists of EOF1 only (i.e., no meridional wind movement); HCM1+2 and HCM1+2_S include both EOF1 and EOF2 (i.e., they both produce meridional wind movement). In all cases, the EOF1 coupling is achieved by modelling the EOF1 surface wind stress response by:

$$(\tau_1^x, \tau_1^y) = PC1(t) \times (EOF1^x, EOF1^y) \tag{1.6}$$

where $PC1$ is approximated by the modelled Niño-3 index. The close relationship between these two variables was noted earlier.

The method used to calculate PC2 in HCM1+2 is a least squares second-order polynomial fit from PC1 for each calendar month (month),

$$(\tau_2^x, \tau_2^y) = PC2(PC1, month) \times (EOF2^x, EOF2^y) \tag{1.7}$$

where we use the two closest months to our month of interest (e.g., data taken for February, includes January and March also) in order to obtain a smooth transition

Table 1.1: Polynomial parameters of $PC2 = a \cdot PC1^2 + b \cdot PC1$ used in HCM1+2 simulations for each calendar month as well as correlation coefficient and root mean squared error (RMSE) of HCM1+2 and HCM1+2_S. Note that the highest (lowest) values of RMSE are obtained around March (September) in both simulations, with differences roughly 30 % between HCM1+2 and HCM1+2_S during January–February, being the former with lower values for all calendar months, although no significant difference is seen between the two HCMs during May–August. However, the strongest (weakest) relationship between PC2 and PC1 are obtained during boreal winter and summer (spring and autumn) for both HCMs.

Parameter	Jan	Feb	Mar	Apr	May	Jun	Jul	Aug	Sep	Oct	Nov	Dec
a	0.38	0.46	0.49	0.53	0.30	0.13	0.13	0.09	0.14	0.18	0.17	0.27
b	0.22	0.17	0.11	-0.06	-0.19	-0.47	-0.68	-0.70	-0.62	-0.48	-0.20	0.03
r(HCM1+2)	0.70	0.71	0.58	0.46	0.24	0.36	0.61	0.69	0.71	0.61	0.40	0.56
RMSE(HCM1+2)	0.83	0.89	1.05	1.05	0.98	0.79	0.66	0.61	0.56	0.61	0.77	0.85
r(HCM1+2_S)	0.42	0.45	0.33	0.18	-0.01	0.34	0.59	0.68	0.66	0.47	0.14	0.24
RMSE(HCM1+2_S)	1.20	1.27	1.30	1.18	1.00	0.80	0.70	0.69	0.69	0.71	0.84	1.05

of PC2 values from one month to another (Fig. 1.4). The second-degree polynomial function is of the form,

$$PC2 = a \cdot PC1^2 + b \cdot PC1 \tag{1.8}$$

where a and b depend on calendar month. The small independent term is set to zero in order to remove any seasonal cycle in EOF2. A full list of quadratic polynomial coefficients as well as their correlation coefficients and RMSE for each calendar month are given in Table 1.1. We point out that the non-linear term leads to a non-zero trend of zonal winds, which might impact on the results presented in Sect. 1.5 for the long-term integrations. However, as these trends over the tropical Pacific (0.003 N m^{-2} decade^{-1}) are one order of magnitude smaller than their standard deviations, we believe that these results should be very similar without a trend.

The method used to calculate PC2 in HCM1+2_S, on the other hand, is based on a climate mode that emerges through the atmospheric non-linear interaction between ENSO and the annual cycle known as C-mode (Stuecker et al. 2013, 2015). Here PC2 wind stresses are calculated by,

$$(\tau_2^x, \tau_2^y) = PC2_S \times (EOF2^x, EOF2^y) \tag{1.9}$$

where $PC2_S = PC1(t) \times \cos(\omega_a month - \varphi)$ refers to PC2 simple, which comes from the lowest-order term of the atmospheric nonlinearity. Here ω_a denotes the angular frequency of the annual cycle, $\omega_a = 2\pi/12$ rad month^{-1} and φ represents a one-month phase shift, $\varphi = 2\pi/12$ rad. How well observed data fit this HCM for each calendar month is indicated by RMSE and correlation coefficients in Table 1.1.

It is clear that the relationship between PC1 and PC2 values depends strongly on calendar month (Fig. 1.4). The relationship between the pair is quasi-linear during JJA, with increasing values of PC1 being related to decreasing values of PC2. The relationship during DJF, on the other hand, displays a clear non-linearity with PC2 values increasing for increasing positive values of PC1, while the PC2 amplitude also appears to increase for decreasing negative values of PC1. Thus, the seasonal difference between the relationship between PC1 and PC2 is most pronounced for strong El Niño events (high values of PC1). Such behaviour is represented reasonably well by the HCM1+2 configuration (Fig. 1.4); for instance, for strong El Niño events ($2<PC1<3$), PC2 prior to the event peak (JJA) has values around minus unity, while around the event peak (DJF) PC2 is between two and three, which is consistent with the sign change shown in Fig. 1.3a. Interestingly, however, such a strong seasonal change is not observed in moderate El Niño events ($PC1\sim1$) and La Niña events ($PC1<0$), which is consistent with the ENSO phase and type asymmetry reported by Lengaigne et al. (2006). This ENSO phase and type non-linearity is not represented, however, in HCM1+2_S where the relationship between PC2 and PC1 is linear regardless the calendar month (Fig. 1.4). Thus, the HCM1+2 simulations only have a weak southward wind shift during La Niña events, while the HCM1+2_S simulations have a strong southward wind shift and the magnitude of the easterlies are also stronger.

Reconstructing PC2 with the polynomial fit of HCM1+2 and comparing with PC2 from the observations reveals a correlation coefficient of 0.61, while doing the same analysis for the HCM1+2_S reconstructed PC2, reveals a correlation coefficient of 0.42. Thus, here we consider HCM1+2 as the more realistic experimental set up and HCM1+2_S as the idealized southward wind shift, with RMSE 0.66 and 0.70 in JJA; and 0.83 and 1.20 in DJF, respectively (see Table 1.1 for the rest of calendar months). However, due to lack of data for strong negative SSTA over the eastern equatorial Pacific for our analysis period, we take both methods into consideration in order to examine the sensitivity of the HCM results.

1.3.3 Westerly wind burst model

Westerly wind activity has been shown to play an important role in the onset of El Niño events (Luther et al. 1983; Latif et al. 1988; Kerr 1999; Lengaigne et al. 2004; McPhaden 2004). These wind events, known as westerly wind bursts (WWB), force downwelling Kelvin waves, which propagate to the eastern equatorial Pacific and ultimately act to warm SST there, potentially initiating the event (e.g., Giese and Harrison 1990, 1991). Equatorial westerly wind activity has been associated with tropical cyclones (Keen 1982), cold surges from midlatitudes (Chu 1988), the

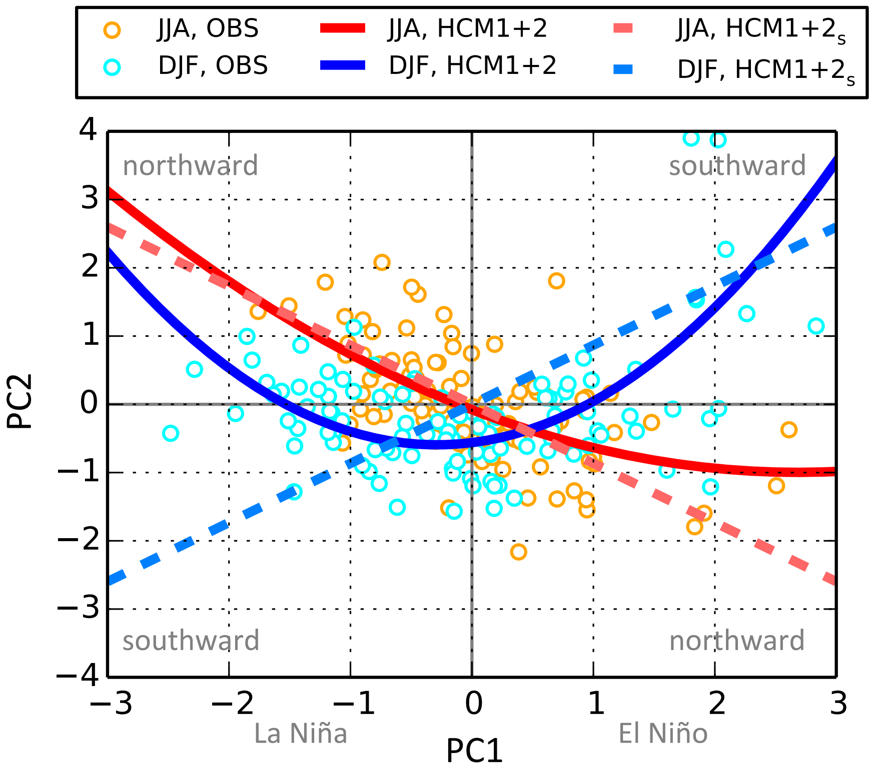

Figure 1.4: Scatter plot of the wind stresses PC2 against PC1 based on the observations (1979–2013) for two 3-month periods: June–August (orange dots); and December–February (light blue dots). The underlying solid (dashed) lines represent the regression used in HCM1+2 (HCM1+2$_S$). See text for the description of the two hybrid coupled model represented in this panel. The directions indicated on the corners in gray mark the direction of the meridional movement of ENSO wind anomalies.

convectively active phase of the Madden-Julian oscillation (Chen et al. 1996; Zhang 1996), or a combination of all three (Yu and Rienecker 1998).

Although different definitions have been proposed to diagnose WWB from observations (e.g., Harrison and Vecchi 1997; Yu et al. 2003; Eisenman et al. 2005), there is a broad agreement that it can be represented roughly by a Gaussian shape in both space and time,

$$u_{\mathrm{wwb}}(x, y, t) = Aexp(-\frac{(t-T_0)^2}{T^2} - \frac{(x-x_0)^2}{L_x^2} - \frac{(y-y_0)^2}{L_y^2}) \qquad (1.10)$$

where x_0 (160 °) and y_0 (0 °) are the central longitude and latitude of the wind event, T_0 (10 days) is the time of peak wind, A is the peak wind speed, T (10 days) represents the event duration, and L_x (20 °) and L_y (9 °) are the spatial scales. The values of these parameters are set here to obtain realistic values of wind stresses over the western Pacific (Niño-4 region). In regards to their frequency, Eisenman et al. (2005) found and average of 3.1 westerly wind events (WWEs) per year during 1990–2004, Gebbie et al. (2007) identified an average of 3.6 WWEs per year during 1979–2002 and Verbickas (1998) found 3.8 WWEs per year during 1979–1997.

In Sect. 1.5 we incorporate WWB into the HCM by utilising the WWB equation above, and having the probability of a WWB beginning on any given day set a fixed parameter which depends on the simulation set up. This means that we have WWBs that are purely stochastic, with the different parameter choice simply modulating the rate of WWB occurrence and their magnitude. Although it has been increasingly recognized that WWB are partially modulated by the SST field and partially dependent upon stochastic processes in the atmosphere (e.g., Kessler and Kleeman 2000; Eisenman et al. 2005; Gebbie et al. 2007), here WWB are represented by purely stochastic way due to the simplicity of our SSTA formulation (Gebbie and Tziperman 2009). Nevertheless, this study is not about the response of El Niño events to different flavours of WWB. Rather, the intent of this work is to focus on the role of the southward wind shift on the termination of ENSO events.

1.4 Response of the Hybrid Coupled Models to observed WWBs

This first experiment is initiated by forcing all three hybrid coupled model versions with ERA-interim wind stress anomalies during the 16-month period (January 1996–April 1997). These are the anomalous wind stresses prior to the 1997–98 extreme El

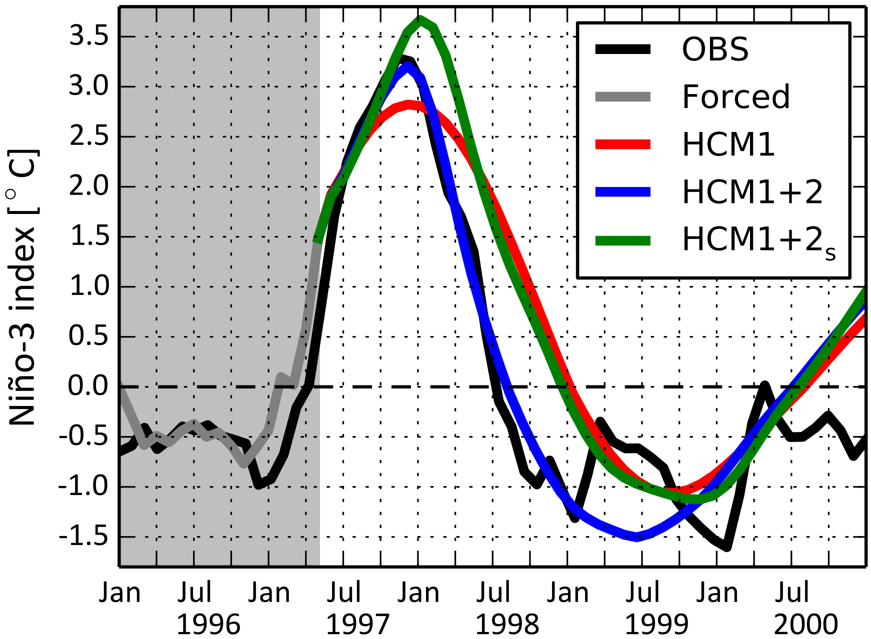

Figure 1.5: Time series of SSTA in the Niño-3 region for the period 1996–2000 in observations (black line), forced run (gray line) with wind stress anomalies observed during 16-month period, and coupled runs to HCM1 (red line), HCM1+2 (blue line), and HCM1+2_S (green line).

Niño, that contain numerous WWBs thought to initiate the event (McPhaden 1999). Each models statistical atmosphere and WWB components are inactive during this initial forcing period, and after this forcing period only the statistical atmospheric component is activated. Each of these simulations is then run for ten years after coupling, although SSTA in Niño-3 region are only plotted until December 2000 in Fig. 1.5 because the remaining evolution lacks importance.

Visual analysis of the model SSTA reveals, i) that in its current configuration all three model versions are in a damped oscillatory state, and ii) that all three model versions do a reasonable job reproducing the 1997–98 El Niño peak. This last point is not noted to suggest predictive skill; it is the difference between each of these three model configurations that is of interest. First of all, the El Niño peak magnitudes in HCM1+2 and HCM1+2_S are stronger than in HCM1. Secondly, normal values (i.e. SSTA = 0 °C) after the warm event are reached up to 3 months earlier in HCM1+2 compared to HCM1 and HCM1+2_S. This suggests that the addition of EOF2 in HCM1+2 allows El Niño events to terminate more abruptly, while it also makes the HCM1+2 temperature evolution more consistent with that observed (Fig. 1.5). Due to the huge growth of the event in HCM1+2_S, its effective termination occurs at similar time to HCM1 although the rate change of the SSTA of HCM1+2_S is as strong as that seen in HCM1+2.

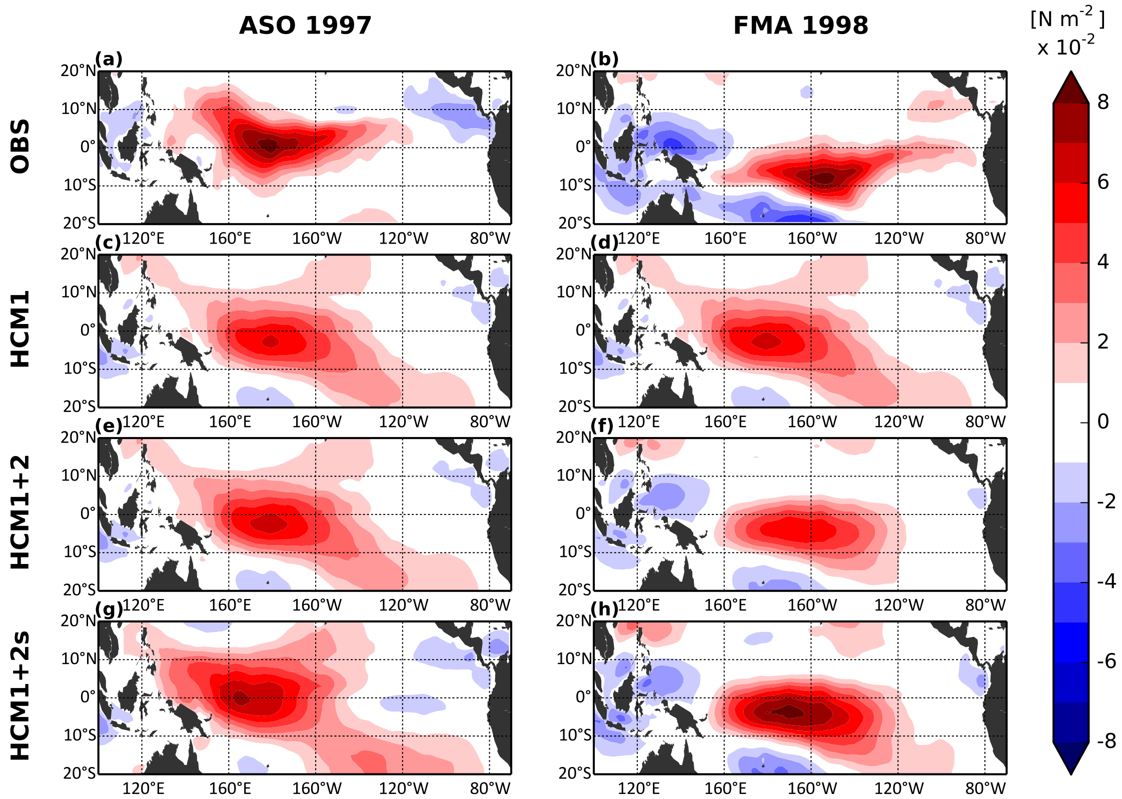

Figure 1.6: Zonal surface wind stress anomalies (N m^{-2}) during ASO in 1997 (a, c, e, g) and FMA in 1998 (b, d, f, h) from observations (a, b), HCM1 (c, d), HCM1+2 (e, f) and HCM1+2$_S$ (g, h).

Such differences among the three HCM time series are due to the fact that the both magnitude and spatial distribution of zonal wind stresses are distinct. Figure 1.6 displays contour maps of zonal wind stress anomalies during ASO of 1997 (left column) and FMA of 1998 (right column) for the observations and the three HCM simulations. The magnitudes of western equatorial Pacific westerlies during the growth phase (ASO) in simulations with EOF2 (HCM1+2 and HCM1+2$_S$) are stronger than in that with EOF1 only (Fig. 1.6), and consistent with expectations the subsequent eastern equatorial Pacific warming is stronger (e.g., Vecchi and Harrison 2000). After the mature of phase of the large 1997–98 El Niño, however, the maximum peaks of westerlies in HCM1+2 and HCM1+2$_S$ are moved to central Pacific as observed (Fig. 1.6) and more importantly shifted south of the equator ($\sim$5 °S). It is worth highlighting that the southward wind shift that occurs within this period is linearly related to the NDJ discharge of heat content (McGregor et al. 2013). Thus, the in HCM1+2 and HCM1+2$_S$ simulations are expected to discharge equatorial heat content much faster than HCM1, which has a fixed structure, ultimately leading to the more abrupt termination of the El Niño event, as shown here.

1.4.1 Perpetual month experiments

Previous literature (e.g., Zebiak and Cane 1987) has suggested that the seasonal changes of the Pacific's background state may be considered as a seasonal modulation of the coupling strength between the ocean and the atmosphere. Here, we will not be considering the changes in background state explicitly, rather we will be considering changes in the surface wind response to ENSO (the southward wind shift) which can be deemed a product of the background state changes (e.g., Vecchi and Harrison 2006; McGregor et al. 2012b). Thus, in order to further examine the variability of the background stability in each calendar month, we have run a series of 12 perpetual month experiments with HCM1+2, in which the relationship between PC1 and PC2 was fixed to a given calendar month (i.e., PC2 is a function of PC1 only, while the coefficients which would vary with month are fixed to the prescribed month regardless the current calendar month of the simulations). Each of these 12 experiments (one for each calendar month) are initiated by forcing with wind stress anomalies observed from ERA-interim during a 16-month period (January 1996–April 1997). As above, each models statistical atmosphere and WWB components are inactive during this initial forcing period, and after this forcing period only the statistical atmospheric component is activated.

Here, as in Tziperman et al. (1997), we think of the amplitude of the resulting El Niño event as a rough measure of the coupling strength, or stability or the background state where a higher amplitude El Niño indicates more unstable background state or stronger coupling strength. In Fig. 1.7a we present the Niño-3 index and WWV anomaly, where WWV is defined as the volume of water above the thermocline between 5 °S–5 °N and 120 °E–80 °W, from the two most extreme calendar months (January and July) of HCM1+2. It is noted that January has the weakest ocean-atmosphere coupling (most stable conditions) and July has the strongest ocean-atmosphere coupling (most unstable conditions) (Fig. 1.7a). As a consequence, the duration of the resulting El Niño event in HCM1+2 is much longer when EOF2 is fixed in July (∼2.5 yr) than in January (∼1 yr) (Fig. 1.7a). It is also interesting to note that upon coupling, the perpetual January HCM1+2 simulation instantaneously begins to discharge WWV, while the perpetual July HCM1+2 simulation after a brief initial adjustment maintains WWV for a further 6–9 months.

These changes in coupling strength are consistent with PC2 and PC1 values in January and July shown in Fig. 1.4, where ENSO's winds (reconstructed with EOF1 and EOF2) are largely symmetric about the equator in July (Fig. 1.6c) and display a strong asymmetry (southward shift) in January (Fig. 1.6d). Further to this, the SSTA and WWV changes displayed are consistent with our expectations based on

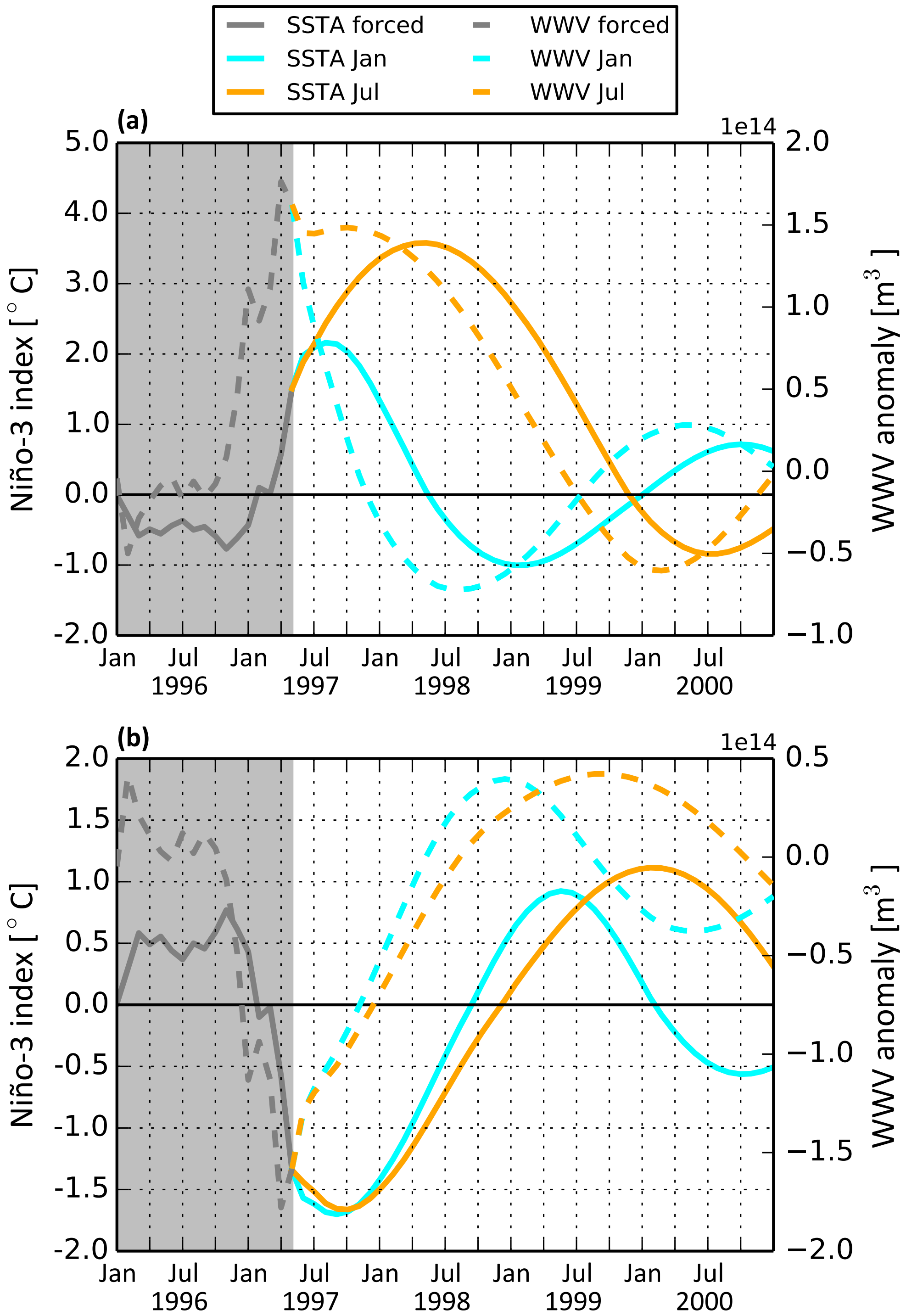

Figure 1.7: a) Time series of the SSTA in the Niño-3 region (solid lines) and warm water volume anomalies integrated over 5 °S–5 °N and 120 °E–80 °W (dashed lines) for the period 1996–2000 in forced run (gray lines) with wind stress anomalies observed during the first 16 months and then coupled to HCM1+2 fixing the configuration of EOF2 at two calendar months, January (light blue) and July (orange). b) The same as a) but multiplying the wind stress anomalies during the forced period by minus one.

previous studies, whereby the southward wind shift acts to enhance the discharge WWV (e.g., McGregor et al. 2014), which is shown to set up conditions favourable for the termination of ENSO warm events (Jin 1997; Meinen and McPhaden 2000).

As a demonstration of the ENSO phase non-linearity of HCM1+2 we repeated the above perpetual month experiments, however, this time simply multiplying the zonal winds forcing by minus one. Using the amplitude of the resulting La Niña event as a rough measure of the coupling strength, we find virtually no difference between the perpetual January and July experiments in SSTA or WWV (Fig. 1.7b). It is also interesting to note that the absolute value of SSTA does not get as large for La Niña events as it does for El Niño events, which is a reflection of the differing relationship between thermocline depth and SST reported in Sect. 1.3.1.

1.4.2 Seasonal synchronization

Previous studies (e.g., Harrison and Vecchi 1999; McGregor et al. 2012b) and the results above suggest that the southward wind should play a prominent role in the synchronization of ENSO events to the seasonal cycle. The goal of this set of experiments is to demonstrate, in an idealised setting, the southward wind shift role in the DJF event peak and, hence, the synchronization of ENSO events to the seasonal cycle.

To this end, four experiments are conducted, all of which are initiated by forcing with wind stress anomalies observed from ERA-interim during the 16-month period between January 1996 and April 1997. As above, each models statistical atmosphere and WWB components are inactive during this initial forcing period, and after this forcing period only the statistical atmospheric component is activated. What differs between each of the experiments, however, is the calendar month each of the two HCMs (HCM1 and HCM1+2) is initialised in when activated. The four runs for each HCM are initiated in February, May, August and November. Also, unlike in the perpetual month experiments, the calendar month is not held fixed at the initialization month, meaning that the month does evolve with time after initialisation. This basically acts as a shift in timing of the applied wind stress forcing, which is representative of El Niño event triggering WWBs occurring at different times of the year.

Figure 1.8 depicts the Niño-3 index time series for the experiment described above. As expected for HCM1, each simulation produces a similar pattern for all runs with the maximum SSTA being reached roughly 7 months after coupling and termination occurring roughly 12 months after that (Fig. 1.8). As the coupling

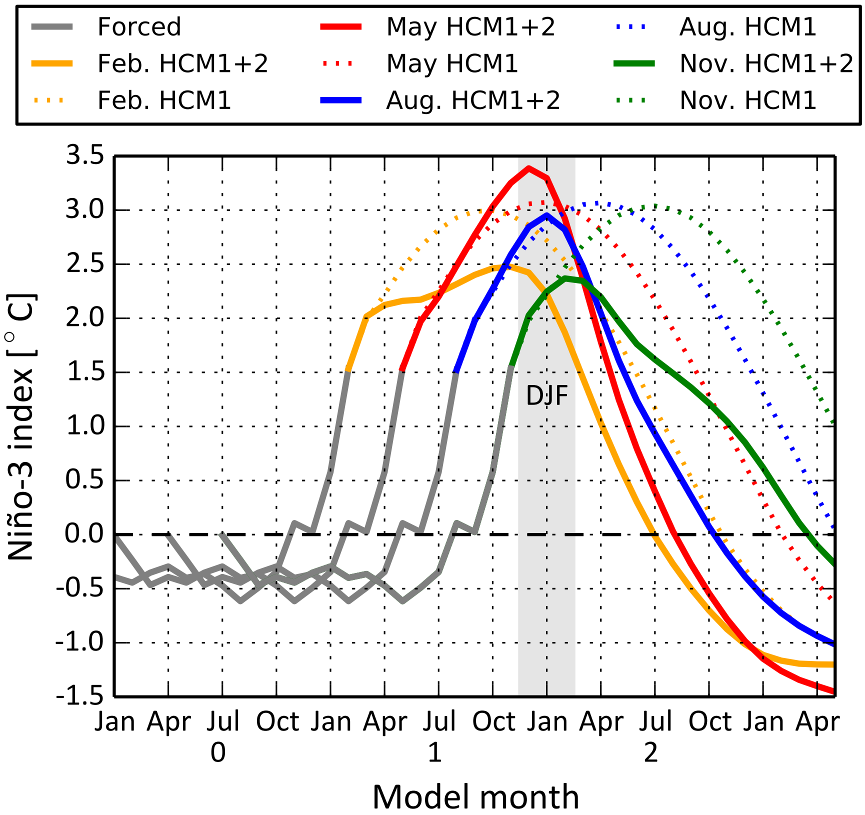

Figure 1.8: Time series of the SSTA in the Niño-3 region forcing the model during a 16-month period (gray lines) and then coupled to HCM1+2 (solid lines) and HCM1 (dotted lines) by starting in different calendar months: February (orange), May (red), August (blue) and November (green).

shifts to later in the calendar year in the HCM1+2 simulations, however, the wind stresses become less symmetric about the equator, thus the maximum amplitude of the events gets smaller. The most significant feature, however, is that each of the simulations reach their SSTA peak during DJF regardless the calendar month when the model coupling is initiated. Thus, this set of experiments demonstrates that the monthly varying coupling strength produced by the southward wind shift acts to synchronise the modelled ENSO event to the seasonal cycle.

1.5 Response of the Hybrid Coupled Models to stochastic WWBs

In this section, we conduct a 4-member ensemble of 100-yr simulations utilising: i) four amplitudes of WWB (8, 10, 12 and 14 m s^{-1}), ii) three probabilities of occurrence of a WWB (2.50, 3.75 and 5.00 WWBs yr^{-1}), and iii) for each of the

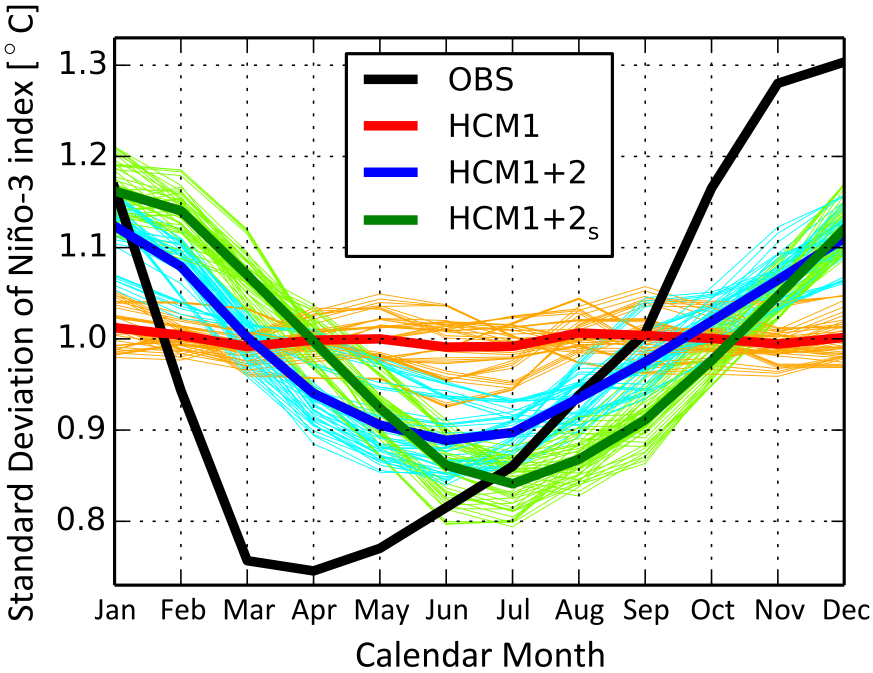

Figure 1.9: Monthly standard deviation of Niño-3 SSTA from observations (black line), and all simulations: HCM1 (red), HCM1+2 (blue) and HCM1+2_S (green). Thin lines represent individual simulations and thick lines indicate the mean of each HCM.

three HCM (HCM1, HCM1+2 and HCM1+2_S), giving 144 ensemble simulations. Each of the four ensemble members for each choice of WWB amplitude, occurrence probability and HCM version differ only in the set of random numbers used to set the timing of occurrence of the WWBs.

1.5.1 Seasonal synchronization

Here we aim too more fully understand the role of the EOF2 (i.e. the southward wind shift during El Niño events) in the synchronization of ENSO to the seasonal cycle. The tendency of seasonal synchronization of ENSO events can be seen in the observations, after normalization of Niño-3 index time series, in maximum peak (1.3 °C) in the standard deviation in December and minimum (0.75 °C) in April (Fig. 1.9). Thus, we present the standard deviation of the SSTA in the central-eastern Pacific (Niño-3 region) for each calendar month and for all runs of the ensemble (Fig. 1.9).

All HCM1 simulations, i.e. without EOF2, have standard deviations that are roughly constant throughout the year. That is, they do not show any synchronization to the annual cycle. The simulations including EOF2, on the other hand, do exhibit seasonal preference in the standard deviation, although there are some differences when compared to that observed. For instance, the HCM1+2 ensemble mean features a boreal winter maximum (1.1 °C) standard deviation and a boreal summer minimum (0.9 °C). Comparing this with observations reveals that the model displays a smaller range, and that the maximum lags that observed by approximately 1 month, while the minimum in June lags that observed by 2 months (Fig. 1.9). The HCM1+2_S ensemble mean displays a boreal winter (January) maximum of 1.2 °C, which lags that observed by one month, and a boreal summer minimum (0.85 °C) that lags by 3 months as that observed, and again exhibiting a weaker range of variability (Fig. 1.9). Therefore, the correlation coefficient between HCM1+2 and observations is higher (r = 0.73) than that between HCM1+2_S and observations (r = 0.45).

To characterize the seasonality of the standard deviation throughout the year, here we use the correlation coefficient between the modelled and observed monthly standard deviation of Niño-3 index, defined as phase-locking performance index (PP) by Ham and Kug (2014), as well as the ratio of the maximum and minimum modelled monthly standard deviation. These two parameters in addition to the standard deviation of SSTA in Niño-3 region are plotted in Fig. 1.10 as a function of the magnitude and probability of WWB.

As expected, the standard deviation increases for both magnitude and number of WWE per year higher for all simulations (Fig. 1.10a–c). However, it is noteworthy that the standard deviations in HCM1 simulations are slightly higher than the others for the same magnitude and probability values as a result of longer duration of warm events, as we shall present in Sec. 5.3. On average, the observed standard deviation (0.84 °C for the period 1880–2013 and 0.87 °C for the period 1979–2013) falls in the bottom left hand corner of the modelled standard deviations (Fig. 1.10a–c).

The PP indices in the HCM1 ensemble are roughly 0 regardless of the WWB parameters (Fig. 1.10d). The HCM1+2 and HCM1+2_S correlation coefficients, however, do appear to depend on both WWB parameters. For instance, the greatest values in both simulations are obtained with the probability of 3.5–4 WWB yr^{-1} and WWB magnitudes between 12–14 m s^{-1} (Fig. 1.10e, f). Regarding the amplitude of the seasonal cycle, i.e. rate of maximum and minimum values of monthly standard deviation, there is a clear increase trend towards few WWE in all simulations (Fig. 1.10g–i), although values in HCM1 are roughly 1. Therefore, the high frequency of WWE might neutralize the role of the southward wind shift and hence the ENSO seasonal synchronization when EOF2 is added in the model. In all cases, the modelled amplitudes are lower than the observed one (1.74 for the period 1880–2013 and

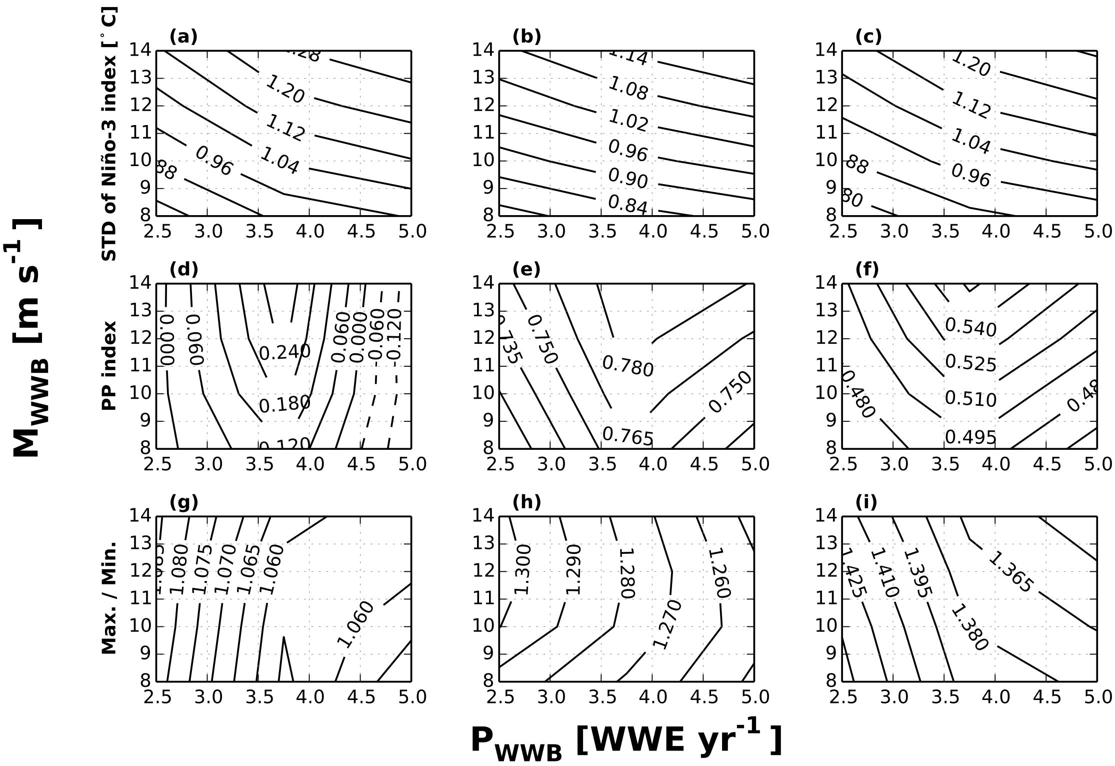

Figure 1.10: Standard deviation of Niño-3 index (a–c), correlation coefficient between monthly standard deviation of Niño-3 index modeled and observed (d–f), and division of maximum by minimum monthly standard deviation of Niño-3 index (g–i) for HCM1 (left), HCM1+2 (middle) and HCM1+2$_S$ (right) simulations as function of magnitude and probability of WWB.

1.97 for the period 1979–2013).

1.5.2 ENSO peak time

To further verify how the addition of EOF2 in HCM1+2 and HCM1+2_S can influence the seasonality of El Niño and La Niña event peaks separately, we construct a histogram displaying the number of El Niño and La Niña event peaks for each calendar month and compare them against those observed and in the HCM1 ensemble (Fig. 1.11). It is worthwhile to mention that the modelled Niño-3.4 data had the long term mean removed and the resulting time series was also smoothed with a 3-month binomial filter to be consistent with the observed. Here we identify ENSO events for which the anomalous Niño-3.4 index exceeds one standard deviation, following Okumura and Deser (2010), however rather than focusing only on the December values our events must exceed this threshold for at least 5 consecutive months.

As expected, most observed peaks of both El Niño and La Niña events tend to occur toward the end of a calendar year from November to January (Fig. 1.11a). In sharp contrast, but not surprisingly, peaks in HCM1 are distributed all year round and there is no marked difference between warm and cold events (Fig. 1.11b) for the entire ensemble. The lack of seasonal synchronization in HCM1 is expected, as it has no mechanism incorporated to link its ENSO phase to the seasonal cycle.

As shown above the simulations including EOF2, HCM1+2 and HCM1+2_S, do display a synchronization to the seasonal cycle which is similar to that observed (Fig. 1.9). Looking at the number of El Niño event peaks for each calendar month in HCM1+2 and HCM1+2_S, both show that most El Niño event peaks occur between November and January (Fig. 1.11c, d) consistent with that seen in the observations (Fig. 1.11a). However, there are some clear differences between HCM1+2 and HCM1+2_S and with the observations, when looking at the number of La Niña event peaks for each calendar month. For instance, while both HCM1+2_S and the observations show that most La Niña event peaks occur between November and January, the HCM1+2 simulations suggest that most La Niña peaks occur during two periods of time in May–August and November–December. This difference helps to explain the weaker range of monthly ENSO variability seen in HCM1+2 compared to that seen in HCM1+2_S (Fig. 1.9).

Bearing in mind that both HCM1+2 and HCM1+2_S incorporate EOF2 (the southward wind shift), their differences must be due to the relationship between PC1 and PC2 for La Niña (negative PC1 values) events (Fig. 1.4). During JJA of

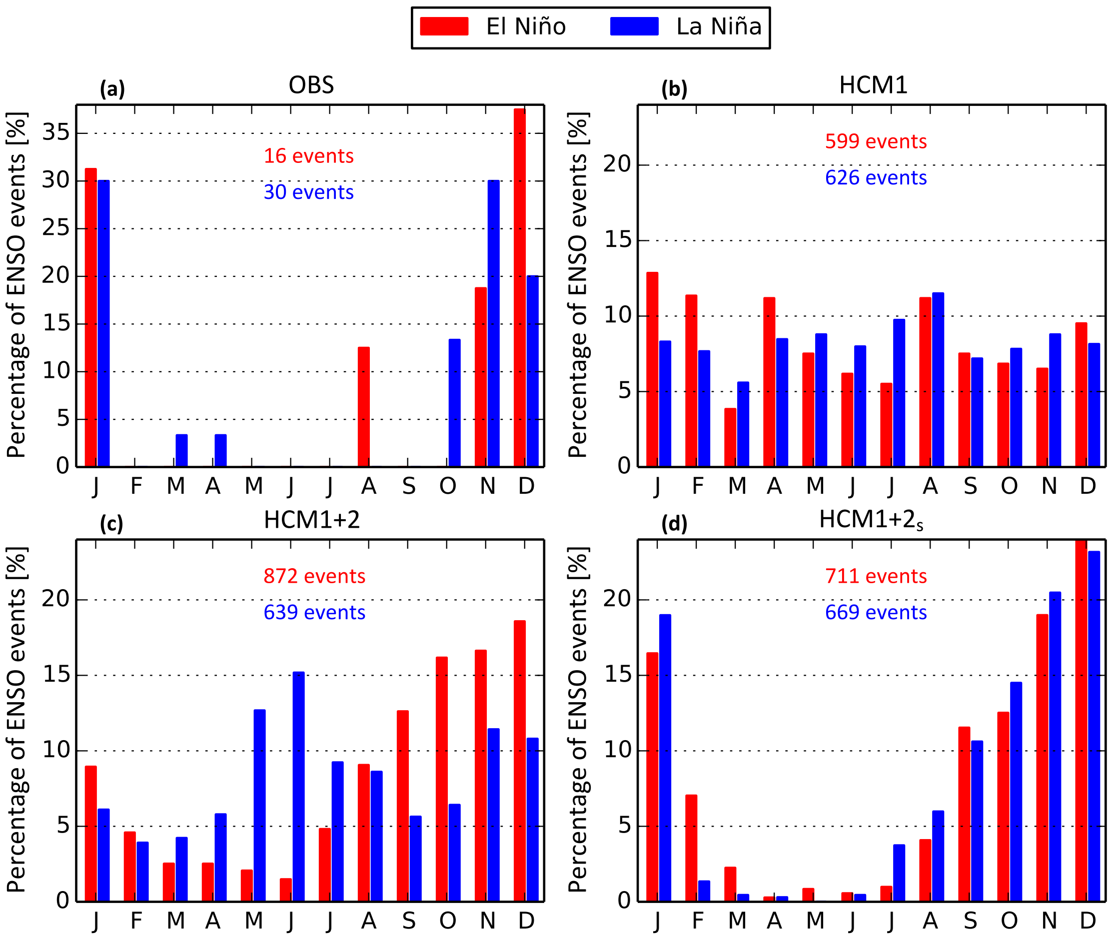

Figure 1.11: Monthly peaks of El Niño (red) and La Niña (blue) events in observations (a) and the three different versions of HCM: HCM1 (b), HCM1+2 (c), and HCM1+2$_S$ (d). Note that number of El Niño and La Niña events is indicated in red and blue, respectively, at the top of each panel.

a moderate La Niña type event (PC1∼-1.5), PC2 from both HCMs display positive PC2 values that indicates the northward location of the related anomalous wind stresses. During DJF, on the other hand, HCM1+2_S displays strong negative values of PC2 (∼-1), which indicates the southward location of the anomalous wind stresses and higher magnitude of these anomalies. As shown above, this southward wind shift would enhance the recharge of heat, acting to terminate the event and leading to its apparent synchronisation with the seasonal cycle. HCM1+2, however, still displays positive values (although smaller than in JJA), indicating that the anomalous wind stresses still remain in a northward location relative to the wind stresses of EOF1 (Fig. 1.2a). Thus, the relatively minor southward wind shift that occurs in HCM1+2 during La Niña events does not act to synchronise the events to the seasonal cycle.

1.5.3 Duration asymmetry

It is generally accepted that there is an asymmetry in the duration of the two phases of ENSO events, with La Niña events lasting longer than El Niño events (Larkin and Harrison 2002; McPhaden and Zhang 2009; Obha and Ueda 2009; Okumura and Deser 2010; Okumura et al. 2011; DiNezio and Deser 2014). Given that McGregor et al. (2013) proposed that the asymmetries in the southward wind shift (e.g., El Niño event magnitude is strongly related to the extent of the meridional wind movement, while the meridional wind movement during La Niña events remains relatively small regardless of the event magnitude) may play a role in this asymmetric duration, here we examine the ensemble of HCM simulations in an attempt to validate this proposal.

The boxplots in Fig. 1.12a and b show the range in durations and magnitudes, respectively, of El Niño and La Niña events, with the event duration defined as the number of months of normalized Niño-3.4 index (Sect. 1.5.2) exceeds one standard deviation, while the magnitude is defined at the event peak which follows the definition of Sect. 1.5.2. To determine whether the mean differences are significant in the duration and magnitude of events amongst the HCMs, we perform a Welch's t-test (Welch 1947), which does not assume equal population variance. We also assess how these duration changes play out temporally by compositing the ensemble Niño-3.4 indexes during the 3-yr period (12 and 24 months before and after the peaks, respectively) around the event peak (Fig. 1.13) for all simulations and those observed for comparison.

The boxplot of El Niño event duration (Fig. 1.12a) and composite of these events for HCM1 (Fig. 13a) reveals events that extend out to over two years and that are on average 6 months longer that observed. This duration difference comes about in spite of HCM1 event magnitudes having no significant differences when compared to observed event amplitude (Fig. 1.12b). Interestingly, the HCM1 composite reveals that a cool state generally follows El Niño events by 18 months (Fig. 1.13a), giving the modelled ENSO a 3-year period. This suggests that the boreal summer peak of La Niña events in the HCM1+2 ensemble could simply reflect that warm events are forced to peak in boreal winter via EOF2, while the trailing cool event peak (which has minimal meridional wind movement) is largely only reliant on the ocean dynamical negative feedbacks of the HCM1 simulation. We also note that all versions of the HCM generate warm events stronger than cold events as observed (Fig. 1.12b) (Hoerling et al. 1997; Burgers and Stephenson 1999; Timmermann and Jin 2002; Jin et al. 2003; Hannachi et al. 2003; An and Jin 2004; Monahan and Dai 2004; Rodgers et al. 2004; Dong 2005).

Comparing the duration of El Niño events of HCM1+2 and HCM1+2_S with those of HCM1, we find that the inclusion of EOF2 in the HCMs (i.e., HCM1+2 and HCM1+2_S) results in warm events having a significantly shorter duration (Fig. 1.12a and Table 1.2). For instance, El Niño events in HCM1+2 are on average 5 months shorter than those of HCM1, while the events of HCM1+2_S are on average 3 months shorter. This result is consistent with the results of Sect. 1.4, shown in Figs. 1.5, 1.8. The HCM1+2 composite on average matches the observed composite very well during event build-up, peak and through the early stages of decay (Fig. 1.13c). In fact, the average El Niño duration in HCM1+2 and observations are not significantly different (Table 1.2). The HCM1+2_S composite also matches the observed composite reasonably well in the months close to the events peak (Fig. 1.13e). It is noticeable, however, that both the average duration and magnitude of the events in HCM1+2_S are significantly longer/larger than those observed (Table 1.2 and Fig. 1.12), which is consistent with the results of Sect. 1.4 (Fig. 1.5). The largest differences between the composites of the HCMs that include EOF2 (HCM1+2 and HCM1+2_S) and the observations come about around the trailing minimum peak, as there is clearly not as strong of a tendency in both of the HCMs for La Niña events to follow 12 months after El Niño events as the La Niña events tend to follow by 18 months (Fig. 1.13c, e).

Unlike warm event duration, the cool event duration response of the HCM simulations which include EOF2 depends on how the southward wind shift (EOF2) has been added. For instance, La Niña events in HCM1+2 (HCM1+2_S) are significantly longer (shorter) than in HCM1. However, the three mean values are only slightly different (10.4, 11.3 and 9.6 months for HCM1, HCM1+2 and HCM1+2_S respectively). In regards to their magnitudes, the inclusion of the southward wind shift

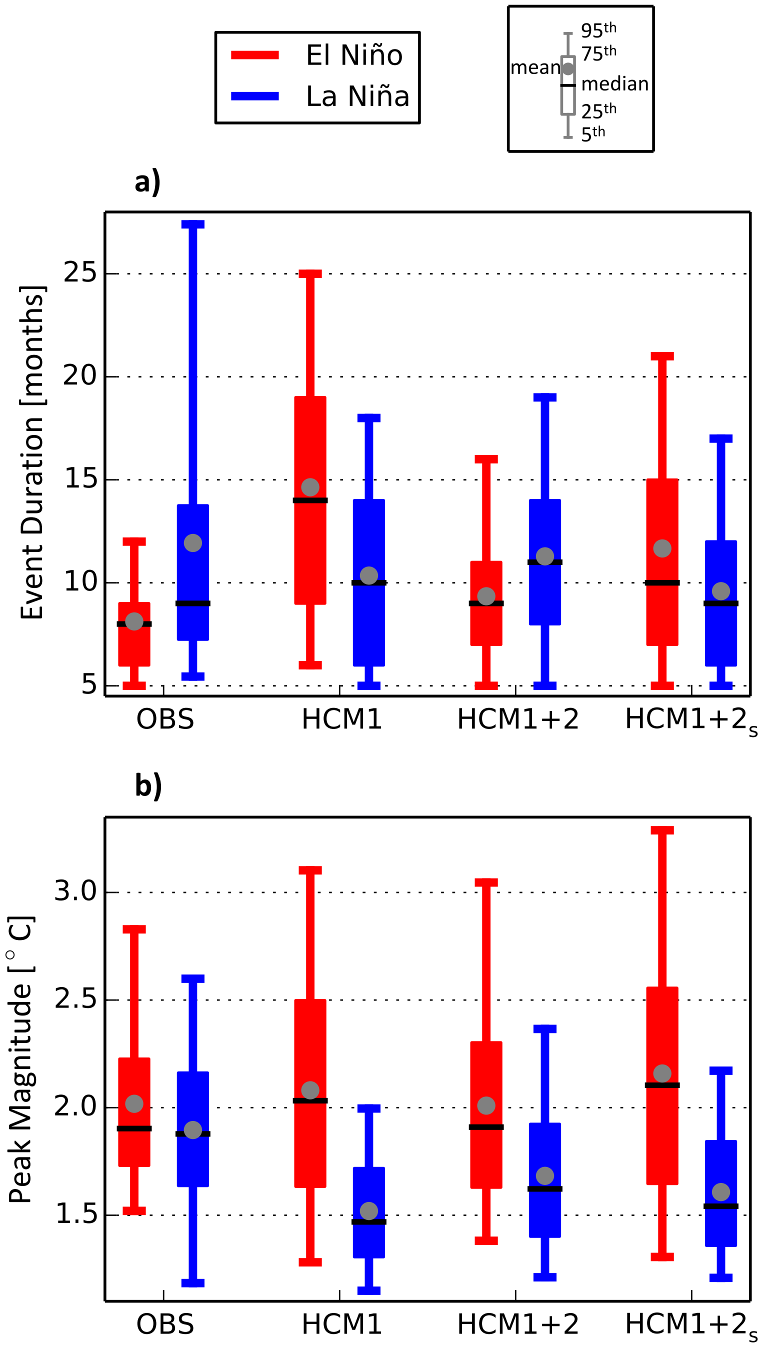

Figure 1.12: Box plots of duration (a) and peak magnitude (b) of El Niño (red) and La Niña (blue) events for observations and the three different versions of HCM (HCM1, HCM1+2 and HCM1+2$_S$). Boxes indicate the 25th and 75th values and caps the 5th and 95th ones. Medians (means) values are highlighted by solid black lines (gray circles). Note that the magnitudes of La Niña peaks are multiplying by minus one.

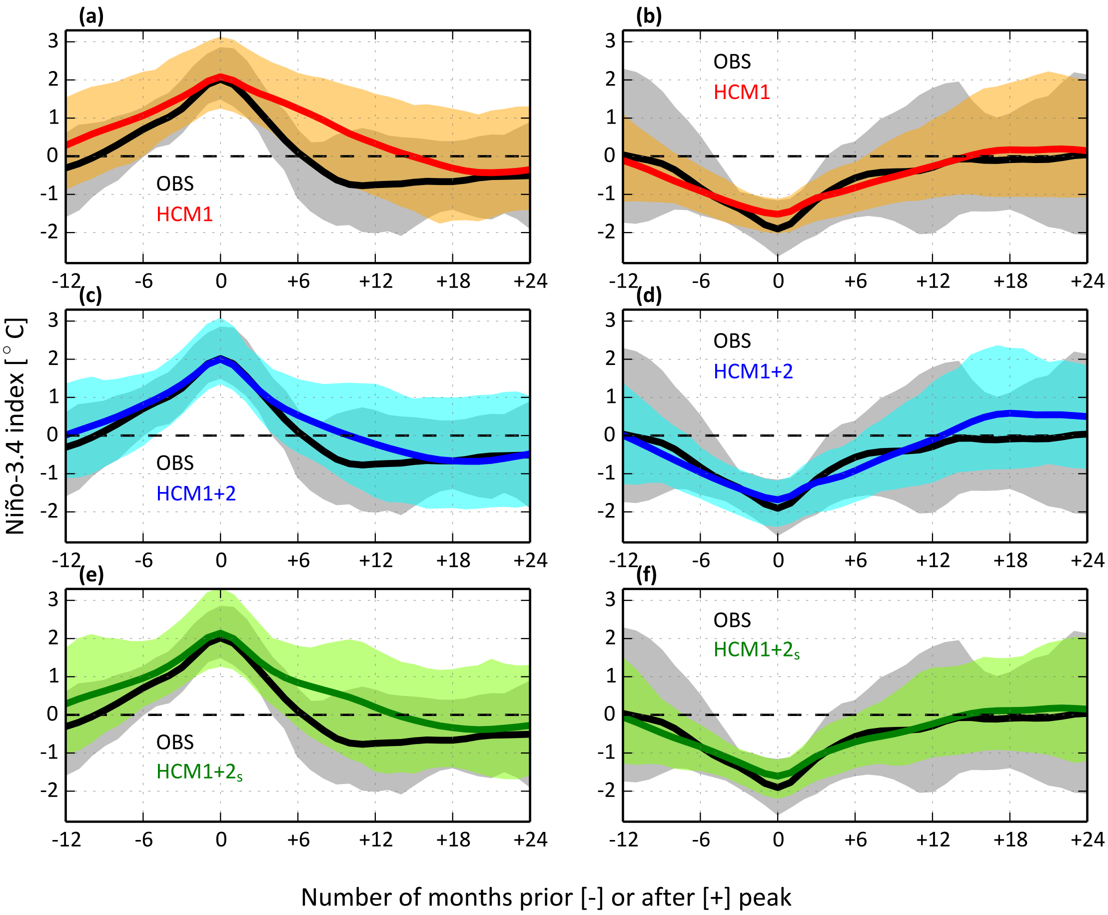

Figure 1.13: Composites of time series of SSTA in Niño-3.4 region during 12 (24) months prior (after) peaks for El Niño (a, c, e) and La Niña (b, d, f). The shaded areas represent the 5th and 95th envelopes of values. Solid lines indicate the mean values.

Table 1.2: Differences between the mean values of ENSO duration (above diagonal) in months and magnitude (below diagonal) in Kelvin amongst observations and all HCMs. Note that values are the result of the subtraction between each column and each row. Bold (italic) values indicate that the difference is significant at the 95 % (90 %) level, as judged by a Welch's *t*-test.

	EN obs	LN obs	EN HCM1	LN HCM1	EN HCM1+2	LN HCM1+2	EN HCM1+2$_S$	LN HCM1+2$_S$
LN HCM1+2$_S$	**-1.5**	*2.3*	**5.1**	**0.8**	*-0.2*	**1.7**	**2.0**	-
EN HCM1+2$_S$	**-3.5**	0.3	**3.0**	**-1.3**	**-2.3**	-0.4	-	**0.6**
LN HCM1+2	**-3.2**	0.7	**3.4**	**-0.9**	-1.9	-	**-0.5**	**0.1**
EN HCM1+2	*-1.2*	*2.6*	**5.3**	**1.0**	-	**0.3**	**-0.2**	**0.4**
LN HCM1	**-2.2**	1.6	**4.3**	-	**-0.5**	**-0.2**	**-0.6**	**-0.1**
EN HCM1	**-6.5**	*-2.7*	-	**0.6**	**0.1**	**0.4**	**-0.1**	**0.5**
LN obs	**-3.8**	-	**-0.2**	**0.4**	-0.1	**0.2**	**-0.3**	**0.3**
EN obs	-	0.1	-0.1	**0.5**	0.0	**0.3**	-0.1	**0.4**

in both HCM1+2 and HCM1+2$_S$ makes La Niña events significantly larger than in HCM1 (Table 1.2).

1.6 Summary and conclusions

In this work we examined the role of the southward movement of ENSO's anomalous zonal winds that occurs near the end of the calendar year, when ENSO events typically reach their peak amplitude. It is shown (Figs. 1.1–1.3) that the combination of the two leading EOF of tropical Pacific wind stresses captures this meridional wind movement, consistent with previous studies (e.g., McGregor et al. 2012b). With the aim of investigating how this meridional wind movement can influence both the seasonal synchronization and duration of ENSO events, a series of Hybrid Coupled Models (HCMs) were constructed: HCM1 (which includes EOF1 only, i.e. no southward wind shift); HCM1+2 and HCM1+2$_S$ (which both including EOF2, while the monthly coefficients are realistic and idealized, respectively).

We found that the variation of the air-sea coupling intensity from month to month, due to the meridional movement of ENSO winds, leads to synchronization of ENSO events with the seasonal cycle. It was shown in Sect. 1.4 (our idealised 1997–98 perturbation experiments) that the strong coupling during boreal summer occurs when ENSO's anomalous wind stresses are largely symmetric about the equator, while the weaker coupling during the boreal winter occurs when ENSO's anomalous wind stresses are largely asymmetric and the wind stress maximum is located between $\sim 5\,°$–$7\,°$S. The strong coupling in boreal summer allows ENSO events to grow rapidly throughout this period. Therefore, as demonstrated in Fig. 1.8, WWB that occur just prior to this strong coupling are the best placed to generate large ENSO events. On the other hand, the weak coupling during boreal winter limits growth and tends to discharge WWV, which enhances the termination of the event. It is worth pointing out that in these idealized experiments no WWB activity occurs after the initial forcing. Thus, this result acts as a theoretical proof of the earlier work of Harrison and Vecchi (1999); Vecchi and Harrison (2003, 2006) and Lengaigne et al. (2006); and is conceptually consistent with the idealised results of Stein et al. (2014). Furthermore, it is in good agreement with that reported by Horii and Hanawa (2004), in which they noted that warm events that do not develop until late summer-fall tend to be weaker and persist longer into the second year.

In Sect. 1.5 we constructed three ensembles of simulations, each using a different version of the HCM, where the ensemble members differ in the timing, magnitude and probabilities of WWB. The purpose of these simulations was to more fully understand the effect of EOF2 in the tendency for ENSO events to be synchronized with the seasonal cycle. As expected, the HCM1 simulations do not exhibit any seasonal preference in the timing of ENSO events; in other words, they do not show any synchronization of ENSO events to the annual cycle. Furthermore, the duration of El Niño events are much longer (up to 6 months on average) that those observed, resulting in higher variability of SSTA over the eastern equatorial Pacific.

The realistic inclusion of EOF2 (HCM1+2), which reproduces strong (weak) southward shift of westerlies (easterlies) in DJF during El Niño (La Niña) years as observations, leads to ENSO seasonal synchronization, although the annual amplitude is weaker than that observed. Such difference (also seen in HCM1+2_S) might be associated with the stochastic WWBs, which were found to reduce the interannual variability compared to semistochastic WWBs (Gebbie et al. 2007). It is shown that El Niño events terminate abruptly in HCM1+2 after peaking near the end of the calendar year, which results in the events being significantly shorter than those of HCM1 ensemble. The minimal meridional wind movement during La Niña phases leaves the termination of these events to rely solely on the modelled oceanic wave adjustment. Therefore, cool events reach their peak amplitude at the wrong time of the year (Fig. 1.11c), while the relative symmetry of the wind stresses about the equator allows the events to grow larger than those of HCM1. The resulting La Niña events are on average also significantly longer than those in HCM1, however the mean difference between these two distributions is less than one month (Table 1.2).

The inclusion of EOF2 with idealised coefficients (HCM1+2_S) also results in synchronization of ENSO to the annual cycle with seasonal amplitude weaker than that observed, but also stronger than that produced in HCM1+2. The minimum variance, however, is lagged by 3 months compared to the observations. The lack of cloud feedbacks in our model might give an explanation of this delayed in the minimum variability found in HCM1+2 and HCM1+2_S configurations compared to the observations (Dommenget and Yu 2016; Rashid and Hirst 2015). More complex climate models, as in phase 5 of the Coupled Model Intercomparison Project (CMIP5, Taylor et al. 2012), which have significant problems in simulating the observed cloud feedback, also show both weaker seasonal phase locking and lag of minimum variance (Bellenger et al. 2014). In the HCM1+2_S configuration, the positive EOF2 values during El Niño years in JJA acts to charge the equatorial region WWV while also making the associated westerlies more symmetric around the equator, which allows the event to grow larger, while the strong southward wind shift in DJF, similar to HCM1+2, enhances the termination of the warm events in the following months. Interestingly, the linearity of the simple southward shift allows this HCM to produce a strong southward shift of anomalous easterlies near the end of the calendar year during La Niña years (Fig. 1.4). This strong shift acts to synchronise the La Niña event peak to the seasonal cycle (Fig. 1.11d), consistent with the observations.

The clear difference between HCM1+2 and HCM1+2$_S$ highlighted above is in the role of the EOF2 in the synchronisation of La Niña events. HCM1+2 suggests that the effect of EOF2 is small during La Niña events, as such it does not act to synchronise the events to the annual cycle and the modelled cool events peak at the wrong time of the year. HCM1+2$_S$, on the other hand, has a strong role making the events peak at the right time of the year. While the resulting La Niña events do have a more realistic end of calendar year peak, it should be noted that the strong role of EOF2 during these events is not consistent with the observations (see Fig. 1.4). This implies that one of the other mechanism discussed in the introduction may be responsible for synchronising the La Niña event peak with the seasonal cycle. However, it is worthwhile to note that there is very little data for large La Niña events so the composites are based largely around smaller magnitude events, thus the role of the southward wind shift in the duration of La Niña events is still unclear.

What has also become apparent from our study, however, is that the characteristics of WWB also have the potential to be incredibly important. In particular, the best correlation coefficients between the monthly standard deviation of Niño-3 index modelled and observed are obtained with 3.5–4.0 WWB yr^{-1} (Fig. 1.10e, f), probabilities consistent with that found in observations (e.g., Gebbie et al. 2007). In relation to the seasonal amplitude, higher values are reached for a lower frequency of WWB (Fig. 1.10h, i), suggesting that higher frequency WWBs (in the absence of any seasonality in the burst themselves) act to damp the seasonal variance changes. This result is in good agreement with previous studies, for instance Neelin et al. (2000), in which it was suggested that the atmospheric stochastic forcing might be a candidate for altering this ENSO's seasonal synchronisation. This importance is perhaps most clearly apparent looking at the peak month of the El Niño event (Fig. 1.11c), as in the absence of WWB around the peak time all events appear to peak in DJF (Fig. 1.8). This suggests that while the meridional movement of winds leads to a rapid termination of El Niño events, as shown here, the effective termination of an event is also reliant on the ocean dynamics of the traditional RDO mechanism (Jin 1997). Thus, the enhanced termination of ENSO events due to the southward shift and its changes in coupling strength might be not enough to overcome poorly timed WWBs. This finding supports the earlier study of Gebbie et al. (2007), where the modelled seasonal synchronisation displays a strong sensitivity of the timing of triggering WWBs.

Thus, despite the simplicity of the HCMs used in this work, we found that the southward shift of El Niño-related westerly plays a key role in having El Niño event peaks in the boreal winter, supporting previous studies (e.g., Harrison and Vecchi 1999; Vecchi and Harrison 2003; McGregor et al. 2012b; Stuecker et al. 2013). This shift also acts to shorten the modelled duration of El Niño events, while our results suggest that it plays a minimal role in the length of La Niña events. Although not mentioned as such, this shift is apparent in the Harrison and Vecchi (1997) analysis of WWEs, where they identified a clear seasonal preference for WWEs to occur north (south) of the equator during July–November (December–March) (see their Figs. 22, 23). This movement of WWBs may have the effect of enhancing the seasonal synchronisation affects of the southward wind shift. Furthermore, in this study it is demonstrated that the effective termination is carried out by two components: i) the ocean dynamics of the traditional RDO mechanism (Jin 1997); and ii) the discharge of WWV due to the southward wind shift, and both must align to some degree to allow for an abrupt event termination.

Part 2

Analysis of the southward wind shift of ENSO in CMIP5 models

The material in this Part is based around the work accepted for publication as:

Abellán, E., S. McGregor, and M. England, 2017. Analysis of the Southward Wind Shift of ENSO in CMIP5 Models. *J. Climate*, **30**, 2415-2435, doi: 10.1175/JCLI-D-16-0326.1

Abstract

During the mature phase of El Niño-Southern Oscillation (ENSO) events there is a southward shift of anomalous zonal winds (SWS), which has been suggested to play a role in the seasonal phase-locking of ENSO. Motivated by the fact that coupled climate models tend to underestimate this feature, this study examines the representation of the SWS in phase 5 of the Coupled Model Intercomparison Project (CMIP5). It is found that most models successfully reproduce the observed SWS, although the magnitude of the zonal wind stress anomaly is underestimated. Several significant differences between the models with and without the SWS are identified including biases in the magnitude and spatial distribution of precipitation and sea surface temperature (SST) anomalies during ENSO. Multiple linear regression analysis suggests that the climatological meridional SST gradient as well as anomalous ENSO-driven convective activity over the northwest Pacific both might play a role in controlling the SWS. While the models that capture the SWS also simulate many more strong El Niño and La Niña events peaking at the correct time of year, the overall seasonal synchronization is still underestimated in these models. This is attributed to underestimated changes in warm water volume (WWV) during moderate El Niño events, so that these events display relatively poor seasonal synchronization. Thus, while the SWS is an important metric, it is ultimately the magnitude and zonal extent of the wind changes that accompany this SWS that drive the changes in WWV and prime the system for termination.

2.1 Introduction

One of the key features of El Niño-Southern Oscillation (ENSO) events is their tendency to mostly peak in boreal winter, i.e. November to January (Rasmusson and Carpenter 1982). It is widely understood that the interaction of ENSO with the annual cycle is the main reason for this apparent seasonal synchronization (e.g., Philander 1983; Zebiak and Cane 1987; Battisti and Hirst 1989; Xie 1995; Tziperman et al. 1997, 1998; Neelin et al. 2000; An and Wang 2000). However, the exact mechanisms are not yet fully understood, with several potential mechanisms proposed linking ENSO and the annual cycle (e.g., Philander 1983; Philander et al. 1984; Zebiak and Cane 1987; Cane et al. 1990; Jin et al. 2003; Dommenget and Yu 2016). Despite this ongoing scientific debate, the southward wind shift (hereafter SWS) has been increasingly recognized as one of the major negative feedbacks involved in ENSO seasonal phase locking and termination (Harrison and Vecchi 1999;

Vecchi and Harrison 2003; Lengaigne et al. 2006; Lengaigne and Vecchi 2010; McGregor et al. 2012b, 2013, 2014; Stuecker et al. 2013; Abellán and McGregor 2016); the climate dynamics linking the SWS to seasonal phase locking will be described below.

During El Niño (La Niña) events, the associated westerly (easterly) wind anomalies are quite symmetric about the equator prior to the event peak (SON); these then move south of the equator (5 °S–10 °S) during the mature phase (DJF). This wind shift has been linked to the southward displacement of the Pacific's warmest sea surface temperatures (hereafter SST) and convection during DJF (Lengaigne et al. 2006; Vecchi 2006), and the associated minimum of wind speed climatology (McGregor et al. 2012b), both of which are due to the seasonal evolution of solar radiation. Recently, the SWS has been ascribed to a climate mode generated in response to nonlinear atmospheric interaction between ENSO SST and the annual cycle of the Pacific warm pool (Stuecker et al. 2013, 2015). This non-linear interaction produced a climate mode, which is characterized as a combination mode (denoted as C-mode), that is responsible for the seasonally synchronized time evolution of the antisymmetric component of the Indo-Pacific atmospheric circulation during ENSO events (Stuecker et al. 2015). In terms of its consequences, the SWS has been shown to: i) make the thermocline depth in the eastern equatorial Pacific return to normal values (e.g., Harrison and Vecchi 1999; Vecchi and Harrison 2003, 2006; Lengaigne et al. 2006); ii) play a crucial role in the discharge process of the warm water volume (hereafter WWV) during El Niño events (McGregor et al. 2012b, 2013); and iii) transfer mass between Northern and Southern Hemisphere during El Niño events (McGregor et al. 2014). Recently, Abellán and McGregor (2016) utilized a simple coupled model to demonstrate that the SWS during El Niño events plays a crucial role in the synchronization of the events with the annual cycle as well as a rapid termination of these events.

Apart from observational analysis (Harrison and Vecchi 1999; Vecchi and Harrison 2003), forced model studies (Spencer 2004; Vecchi and Harrison 2006; Vecchi 2006) and coupled model experiments (Vecchi et al. 2004; Lengaigne et al. 2006; Xiao and Mechoso 2009), the SWS has also been analysed in the Coupled Model Intercomparison Project phase 3 (CMIP3; Meehl et al. 2007). For example, Lengaigne and Vecchi (2010) considered the SWS as a precondition for the termination of El Niño due to a shoaling of the eastern equatorial Pacific thermocline through eastward propagating Kelvin pulses. Recently, Ren et al. (2016) found that the CMIP5 models with better performance in simulating the ENSO mode also tend to simulate a more realistic C-mode, related to the SWS as mentioned before (Stuecker et al. 2013, 2015). Additionally, the seasonal synchronization of ENSO in CMIP5 has been documented in numerous studies, showing a large model spread in this regard (Bellenger et al. 2014) and a clear dependency of this unique feature of ENSO on convective parameter (Ham et al. 2013). However, no study has yet undertaken a thorough evaluation of the representation of the SWS in state-of-the-art coupled general circulation models participating in the CMIP5 (Taylor et al. 2012); this is the overarching goal of the present study. We also investigate the dynamics underlying the SWS in CMIP5 models in addition to elucidating its link with the seasonal synchronization of ENSO events.

The rest of this chapter is organized as follows. We begin in Sect. 2.2 by providing a description of the datasets, CMIP5 models, and analysis method used in this study. In Sect. 2.3, we evaluate how well the zonal wind stress and, in particular, the SWS are captured by CMIP5 models. An analysis of precipitation and SST anomalies during ENSO events as possible drivers of the SWS along with their mean state and multiple linear regression analysis are then carried out in Sect. 2.4. In Sect. 2.5 we examine whether there is a relationship between the SWS, peak time of these events and the WWV changes. The final section presents a summary highlighting the main findings.

2.2 Models and methods

2.2.1 CMIP5 models

We focus our analyses on the historical runs by 34 CMIP5 CGCMs. A list with the official model names utilized is displayed in Fig. 2.1. Further information on individual models is available online (at `http://www-pcmdi.llnl.gov/`; Taylor et al. 2012). Although the exact duration of the simulations varies slightly from model to model, generally the historical run was carried out including solar, volcanic and anthropogenic forcing from 1850 to 2005. Here, to avoid models with large ensemble numbers biasing the results, only one ensemble member ("r1i1p1") run for each model is used.

The models were chosen based on the availability of model output required for this study. However, the CSIRO-Mk3.6 model was excluded due to a poor simulation of equatorial SST through ENSO phases (Brown et al. 2014; Grose et al. 2014) showing more variability in the western than in the eastern Pacific (Guilyardi et al. 2012), in stark contrast to observations.

2.2.2 Observational data

For comparison with the model results, observed atmospheric and oceanic data are used. The SST dataset is the Extended Reconstructed Sea Surface Temperature version 3b (ERSST v3b; Smith et al. 2008) with a $2^\circ \times 2^\circ$ resolution. Both the surface wind stress and mean sea level pressure data are obtained from the European Centre for Medium-Range Weather Forecast (ECMWF) Interim Re-Analysis (ERA-Interim; Dee et al. 2011) with a $1.5^\circ \times 1.5^\circ$ resolution. In light of the large differences seen across observation wind products (e.g. Wittenberg 2004; McGregor et al. 2012a), McGregor et al. (2013) utilized eight global wind products, ERA-Interim among others, finding similar spatial patterns and temporal variability for the meridional wind shift. Precipitation data are taken from the Climate Prediction Center (CPC) Merged Analysis of Precipitation (CMAP; Xie and Arkin 1997) having a horizontal resolution of $2.5^\circ \times 2.5^\circ$.

In this study, we consider the period from 1880 to 2014 for SST and the period 1979–2014 for all other datasets, with a monthly temporal resolution adopted throughout. The anomalies for the observed variables are defined as the deviations from the 1979–2014 climatological mean.

2.2.3 Methodology

Anomalies of all CMIP5 fields are calculated by removing the long-term monthly climatology over the entire period available for each model, whereas the period used to calculate the observed long-term monthly climatology is as discussed above in Sect. 2.2.2. Prior to the calculations, a 3-month binomial filter was applied to all wind stress data (including both the observed and CMIP5 modeled) in order to reduce month-to-month noise, as described in Deser et al. (2012). Both model data and observations were linearly detrended to approximately account for model drift and the impacts of global warming, to first order. Model outputs were examined at native grid resolution and then later interpolated to the same grid as the observations, to facilitate comparison with the measurement record and assessment of the multi-model means.

It has been shown that the dynamics of extreme El Niño events are different from moderate events (e.g. Dommenget et al. 2013; Santoso et al. 2013; Cai et al. 2014, 2015; Capotondi et al. 2015; Takahashi and Dewitte 2015). Therefore, here we classify El Niño events according to the magnitude of SST anomalies within the region 5°S-5°N, 170-120°W (hereafter the Niño-3.4 index), while La Niña events only have the one category. Specifically, (1) strong El Niño events are identified when the Niño-3.4 index exceeds 1.5 °C; (2) moderate El Niño events when the index is greater than 0.5 °C but less than or equal to 1.5 °C; and (3) La Niña events when the index is < -0.5 °C; for at least 5 consecutive months in all three cases. Following this criterion, we find in the observations two strong El Niño events (1982–83, 1997–98), seven moderate El Niño events (1987–88, 1991–92, 1994–95, 2002–03, 2004–05, 2006–07, 2009–10), and eight La Niña events (1984–85, 1988–89, 1995–96, 1999–00, 2000–01, 2007–08, 2010–11, 2011–12) during the period 1979–2014. It is worth pointing out that there are 4 CMIP5 models (GISS-E2-R-CC, inmcm4, MIROC-ESM and MRI-CGCM3) that are not capable of simulating strong El Niño events, according to our definition. We note that as ENSO events typically peak near the end of the calendar year, here we composite during DJF regardless of event peak.

2.3 Wind stress during ENSO

Ocean surface wind stress (hereafter wind stress) is an important variable in the coupled system as it indicates the exchange of momentum between the ocean and atmosphere (Lee et al. 2013). Furthermore, the spatial structure of anomalies during ENSO is considered an important factor in setting the ENSO time scale (e.g. Kirtman 1997; Wang et al. 1999; An and Wang 2000; Capotondi et al. 2006; Neale et al. 2008; Kug et al. 2009). Figure 2.1a-c shows the composite of zonal wind stress anomalies for the period Sep(0) to Feb(1) for observed strong El Niño, moderate El Niño and La Niña events, respectively. The spatial pattern of the observed zonal wind stress anomalies displays westerlies (easterlies) during El Niño (La Niña) with maximum Pacific anomaly located between the equator and 5 °S. However, two distinct features between the strong El Niño events and the other two types of ENSO events can be clearly seen: (1) different magnitude (i.e. twice as strong for strong El Niño events), and (2) westward shift of maximum zonal wind stress anomalies during La Niña and moderate El Niño events (by about 30 ° compared to the strong El Niño pattern); which are almost mirror images. Previous studies have demonstrated that these wind stress differences (i.e., magnitude and location) have been associated with the nonlinear characteristics of the atmospheric response to the SST anomalies of the opposite sign, i.e. via atmospheric convection (Kang and Kug 2002; Ohba and Ueda 2009; Frauen and Dommenget 2010).

Although the zonal distribution of CMIP5 ensemble mean zonal wind stress anomalies are qualitatively similar to those observed, some differences can be seen (Fig. 2.1a-f): i) the magnitude of the CMIP5 ensemble mean anomalous wind stress for each ENSO event type is much weaker (up to 50-60 %) than the observations for its corresponding event type, which is consistent with the results of Bellenger et al. (2014); ii) the multi-model mean CMIP5 simulated equatorial winds are not as broad meridionally as those observed (i.e., the CMIP5 ensemble mean winds only extend to approximately 3 °N and 7 °S; c.f. Fig. 2.1d-f), which can impact the period of ENSO (Capotondi et al. 2006); and iii) the anomalous wind stresses have a larger longitudinal span than the observations, consistent with the earlier study of Lee et al. (2013).

To further assess the skill of the CMIP5 ensemble set in simulating the observed spatial pattern of anomalies of zonal wind stress during ENSO events, we present Taylor diagrams (Taylor 2001) in Fig. 2.1g-i for the three types of ENSO events. Generally speaking, the CMIP5 models produce reasonable correlations when compared with the observations, with average spatial correlation values of 0.58, 0.55 and 0.59 for strong El Niño, moderate El Niño and La Niña events, respectively. In regard to the standard deviation of zonal wind stress patterns, most of the CMIP5 models have less variance (11.0, 4.9 and 4.8 mPa as mean values) than that seen in the observations (16.8, 6.3 and 6.2 mPa for strong El Niño, moderate El Niño and La Niña, respectively). The fact that the magnitude of simulated zonal wind stress is weaker than observed (Fig. 2.1) and with reduced meridional width, might explain the low standard deviation of the associated composite spatial maps.

2.3.1 The southward wind shift

As mentioned in the introduction, the SWS refers to a meridional movement of the anomalous wind stresses during the ENSO event mature phase (i.e., boreal winter). In particular, the maximum of these anomalies is located at (or slightly north of) the equator during August–October (ASO), while the magnitude of the wind stress is increased (decreased) south (north) of the equator during November–January (NDJ), such that the maximum zonal wind stress occurs south of the equator during February–April (FMA) (e.g., Harrison and Vecchi 1999; McGregor et al. 2013). Here we define the SWS as the difference in latitude of the maximum zonal wind stress anomalies between ASO and FMA, averaged over 160 °E-120 °W. It is worth emphasising that other factors, such as the strength and meridional width of the anomalies, also impact the oceanic response to the SWS. However, none of these changes are of interest if the model does not first produce the SWS. Thus, here we have chosen to focus our SWS definition on changes in the latitude of the wind stress anomalies, but we also note that the oceanic impact of the SWS is discussed in Sect. 2.5 of this study. The magnitude of the observed SWS is 9.0 °, 6.0 ° and

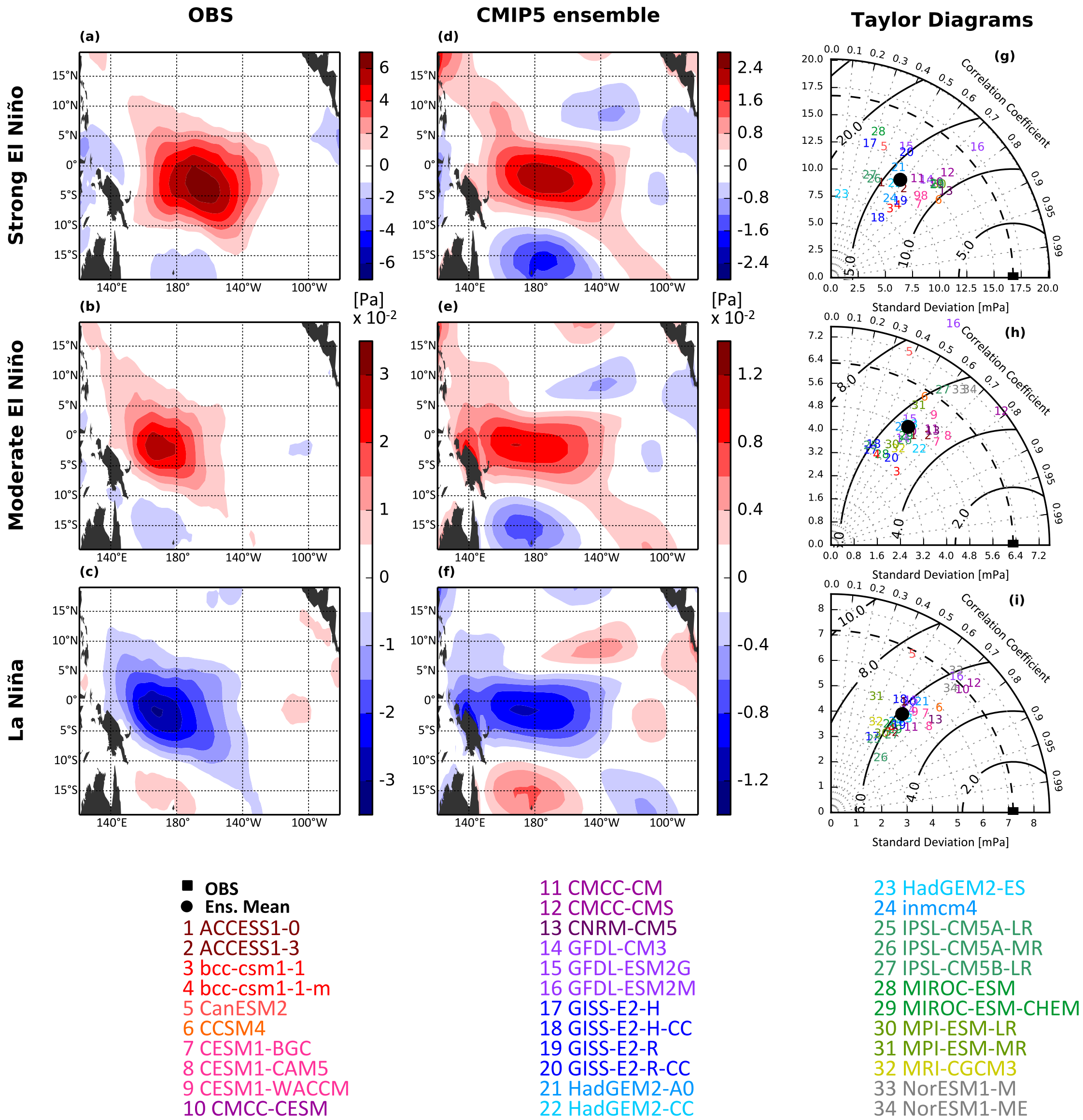

Figure 2.1: Composite mean values of zonal wind stress anomalies during strong El Niño (a, d, g), moderate El Niño (b, e, h) and La Niña (c, f, i) for the period Sep^0-Feb^1, where 0 means the year during which an event develops and 1 means the decaying year, for observations (a-c), ensemble mean (d-f) and all CMIP5 models (g-i). Note the different color bars for the observations and CMIP5 models. Taylor diagrams are obtained by calculating the standard deviation and correlation between each model and observations for the whole domain shown in the left panels.

7.5 ° for strong El Niño, moderate El Niño, and La Niña events, respectively.

Figure 2.2 displays the latitude of the maximum westerly (easterly) anomalies from August to April during El Niño (La Niña) years averaged zonally over the western and central Pacific. We note that these latitudes are calculated based on the composite mean zonal wind stress for each model. Here and in the rest of this work we divide the CMIP5 models into two categories: models with SWS and those without SWS. This classification is based on the ability of each model to realistically reproduce a SWS during the three types of ENSO events, with the magnitude of the shift required to be at least 66.6 % of the observed SWS.

The majority of the models simulate realistic SWS during at least one of the three types of defined ENSO events. In fact, two thirds of the CMIP5 models analyzed (22 out of 34) can reproduce the SWS for all three types of events analyzed. It is also clear that the multi-model ensemble mean of models with SWS (MME-with-SWS) is comparable with observations (Fig. 2.2a-c). It is interesting to note that MME-with-SWS indicate stronger SWS for strong El Niño events (reaching the maximum of westerly anomalies up to 6 °S in March) than that for moderate El Niño or La Niña (located at 4 °S in the same month), which is also seen in observations. There are 4 (out of 30) models that do not capture the SWS during strong El Niño (Fig. 2.2d), while there are 6 and 4 (out of 34) models that do not reproduce the SWS during moderate El Niño and La Niña, respectively (Fig. 2.2e-f). The multi-model ensemble average of these models (i.e., MME-without-SWS) exhibit latitude of maximum zonal wind stress roughly constant (and south of the equator) throughout the 9-month period. It is also worth mentioning that 2 models (IPSL-CM5A-LR and IPSL-CM5A-MR) are not able to simulate the SWS for any type of ENSO event. The study of (Bellenger et al., 2014) analyzes various other ENSO metrics, and also concludes that the ENSO in these last two models exhibits poor agreement with observations.

2.3.2 SWS spatial characteristics

To highlight the SWS we present composite maps of the zonal wind stress and sea level pressure (SLP) anomaly difference between FMA and ASO for the observations and the CMIP5 models with and without SWS, and for the three types of ENSO events (Fig. 2.3). The observational differences during strong El Niño events show several clear structures over the tropics: (1) easterly differences in the western Pacific north of the equator, (2) westerly differences over the central Pacific south of the equator, and (3) high positive anomalous SLP observed over the northwestern Pa-

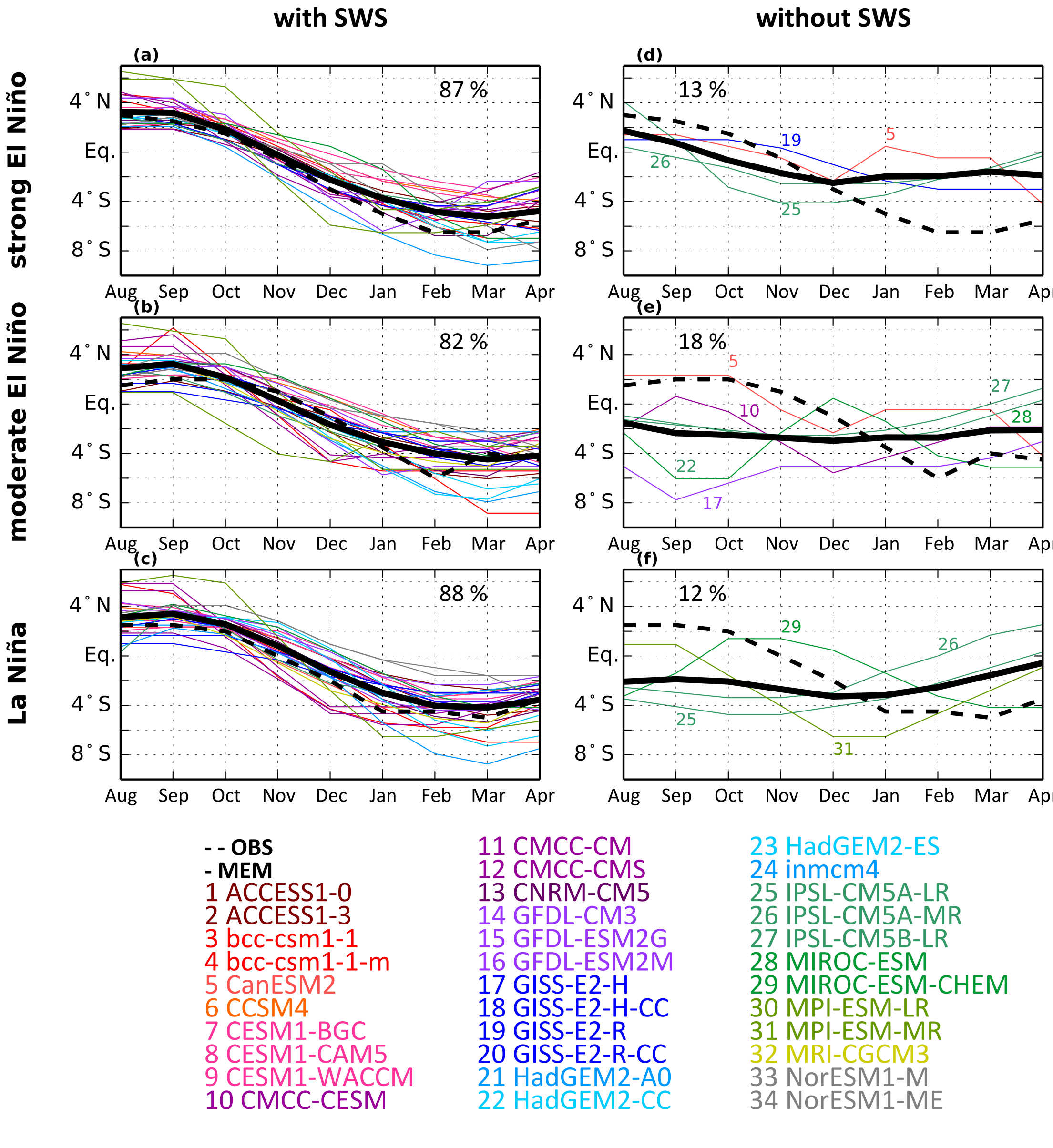

Figure 2.2: Latitude of anomalous zonal wind stress maximum averaged over 160 °E-120 °W during ENSO events, for the period Aug^0-Apr^1). A 3-month running mean is applied: for instance, the value for Aug is the average of July, August and September and so forth. Simulations are divided into models with SWS (a-c) and without SWS (d-f) for strong El Niño (a, d), moderate El Niño (b, e) and La Niña (c, f). See Sect. 2.3.1 for SWS classification.

cific representing a large-scale low-level anticyclone (Fig. 2.3a). All of these features are consistent with the representation of this southward wind shift by an Empirical Orthogonal Function analysis (EOFs) (McGregor et al. 2013), and the combination mode (C-mode), which emerges from the seasonal modulation of ENSO-related atmospheric anomalies (Stuecker et al. 2013). It is noted that the high SLP anomalies in the northwest are generally referred to as the Philippine Sea anticyclone (e.g. Harrison and Larkin 1996; Wang et al. 1999, 2000; Wang and Zhang 2002; Li and Wang 2005). Values in the center of the Philippine Sea anticyclone during strong El Niño years ($\sim$ 3 hPa), as shown in Fig. 2.3a, are larger than the amplitude of the local annual variation ($\sim$ 2 hPa) (Wang and Zhang 2002).

The observed zonal wind stress differences for moderate El Niño show a similar dipole-structure to those for strong El Niño, although both easterly and westerly differences in the tropical Pacific are shifted westward, and their magnitudes are much weaker (Fig. 2.3b). Furthermore, the longitudinal offset of the winds north and south of the equator is reduced. Not surprisingly, the development of the Philippine Sea anticyclone is also more modest due to its link to the El Niño amplitude (Wang and Zhang 2002; Stuecker et al. 2015).

In contrast, the La Niña phase during FMA-ASO leads to an anomalous cyclone developing over the Philippine Sea reversing both its sign and the pattern of zonal wind anomalies (i.e., westerly seasonal difference north of the equator and easterly south of the equator) (Fig. 2.3c). Unlike warm events, these two regions of opposite zonal wind stress anomalies north and south of the equator are centered at roughly the same longitude. Further to this, their magnitudes are weaker than those for moderate El Niño events.

In qualitative agreement with observations, models with SWS display anomaly differences between FMA and ASO with patterns similar to those observed (Fig. 2.3d-f). This includes: (1) positive (negative) anomalous SLP over the Philippine Sea region during El Niño (La Niña) events and pronounced differences zonal wind stresses in the western Pacific north of the equator and central Pacific south of the equator. However, the seasonal differences of zonal wind stress anomalies are underestimated among models, especially for strong El Niño events. The anomalous SLP in the Philippine Anticyclone region is also roughly half the magnitude observed. Another obvious difference between the observations and the CMIP5 models with SWS is the lack of simulated zonal offset of the zonal winds about the equator for strong El Niño. In particular, the positive zonal wind difference south of the equator is not offset to the east of the negative zonal wind difference above the equator as seen in observations.

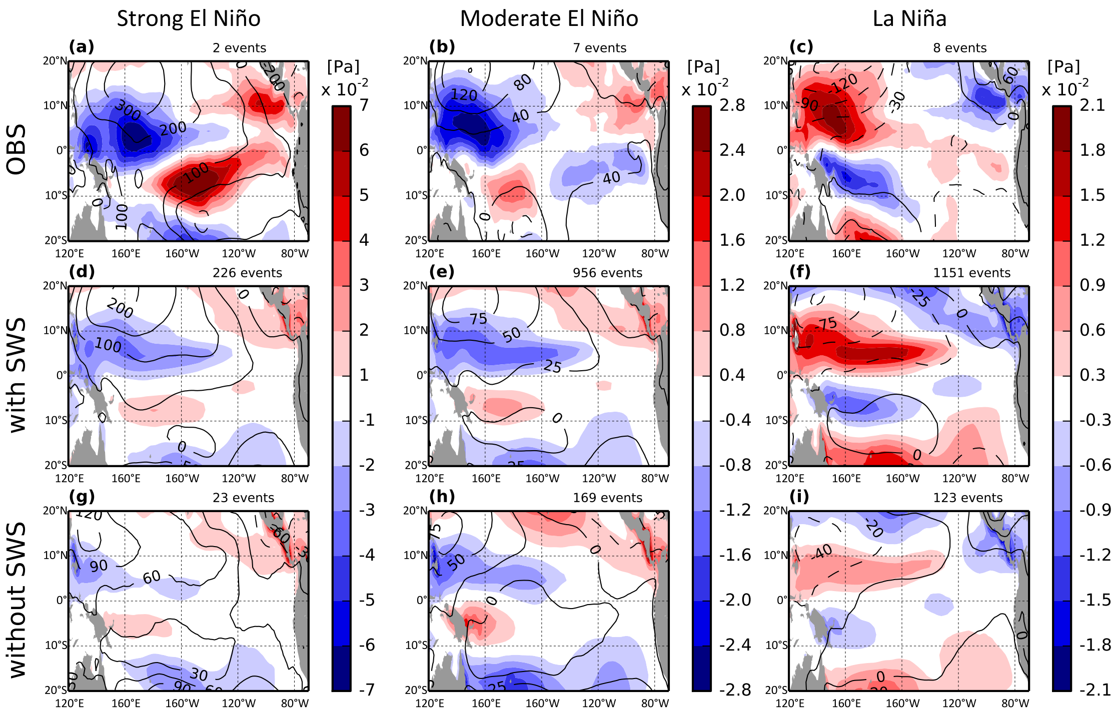

Figure 2.3: Zonal wind stress anomaly composites during FMA season minus that during ASO season (shading) and SLP anomaly (contours) for strong El Niño (a, d, g), moderate El Niño (b, e, h) and La Niña (c, f, i) for observations (a-c), models with SWS (d-f) and models without SWS (g-i). Note that negative contours are dashed; units for both variables are in Pa and that we employ different color bars to better highlight all events more clearly. The numbers on each panel indicate the number of the events falling within that category.

Even though most models without a SWS (according to the criterion we adopt) can simulate a SWS to some extent, albeit with much weaker magnitude, the meridional movement tends to be displaced too far to the west compared to the observations (Fig. 2.3g-i). Consequently, the Philippine Sea anticyclone (cyclone) is not as well developed during the simulated El Niño (La Niña). The westward extension of ENSO-related zonal wind stress anomalies found in the CMIP5 models, which is more pronounced in models without a SWS, is a common failure for most CGCMs (Kirtman et al. 2002; Zhang and Sun 2014).

2.4 Possible drivers of the SWS

2.4.1 The role of anomalies

It is generally accepted that the anomalous SST during ENSO events is intimately linked with rainfall and wind stress anomalies (e.g., Bjerknes 1969; Ropelewski and Halpert 1987; Philander 1990). Thus, in this section we explore both qualitatively and quantitatively (using linear regression) the relationship between the representation of SWS, the details of the SST anomalies, the accompanying precipitation and their climatology during boreal winter.

SST anomalies

It is well known that El Niño (La Niña) events are characterized by anomalously warm (cold) SST over the central-eastern equatorial Pacific (Fig. 2.4a-c). In particular, during strong El Niño events, the maximum SST anomalies are situated in the eastern equatorial Pacific (Fig. 2.4a), where the cold tongue is located (Larkin and Harrison 2005; Ashok et al. 2007; Kao and Yu 2009; Kug et al. 2009; Kim et al. 2009; Holland 2009). However, during moderate El Niño events the maximum SST anomalies are weaker and shifted to the west, while La Niña events generally mirror the moderate El Niño (Fig. 2.4b-c). This shift to the west of the maximum SST anomalies with weaker values off the South American coast for moderate El Niño is consistent with aspects of ENSO diversity described in the literature (Takahashi et al. 2011; Capotondi et al. 2015).

Both groups of CMIP5 models broadly reproduce SST anomaly patterns that are overall consistent with those observed, including most models producing La Niña and moderate El Niño events as approximate mirror images of each other (Fig.

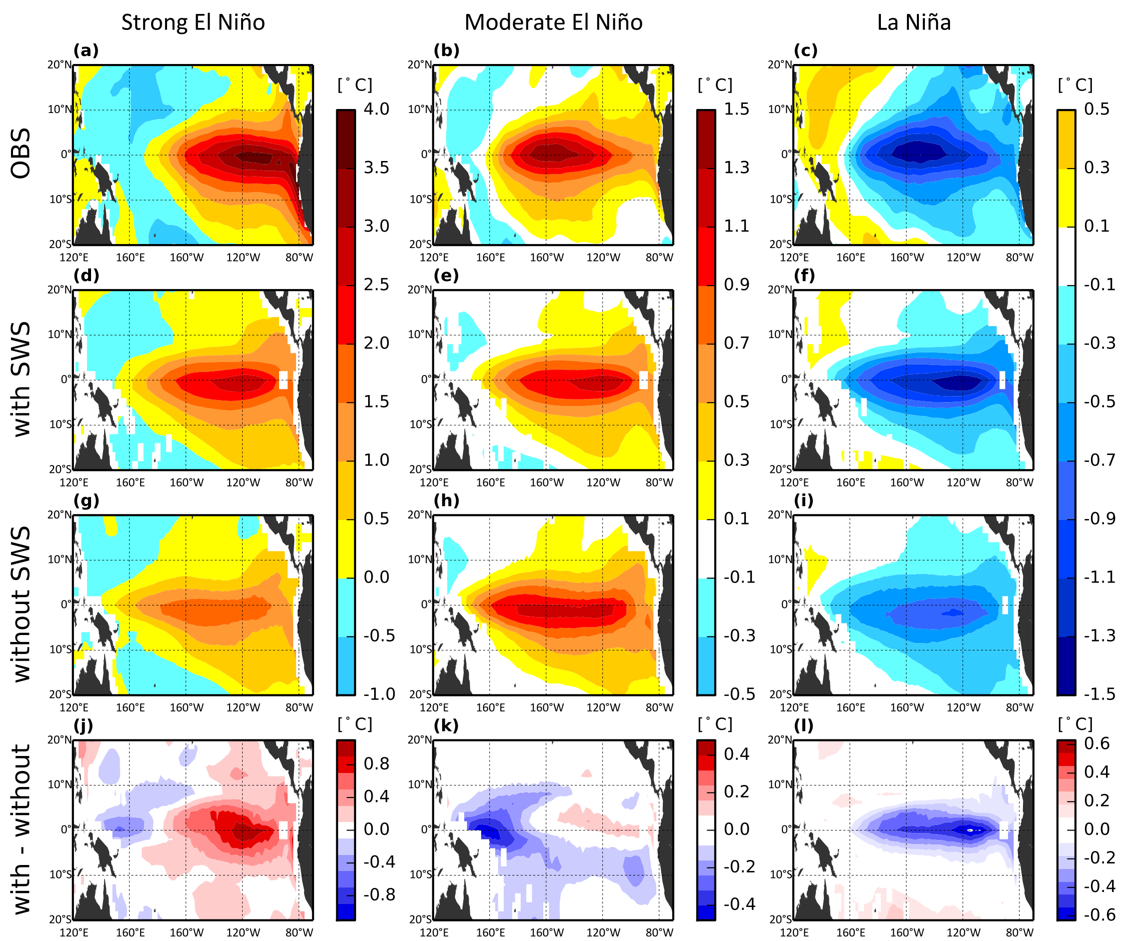

Figure 2.4: SST anomalies in DJF during strong El Niño (a, d, g, j), moderate El Niño (b, e, h, k) and La Niña (c, f, i, l) for observations (a-c), models with SWS (d-f), models without SWS (g-i) and the difference between models with and without SWS (j-l). Note the different color scales.

2.4e-f). However, it is noted that the models have been shown to underrepresent the observed ENSO diversity (e.g. Capotondi and Wittenberg (2013)), and here we highlight several other notable differences. Firstly, in contrast to the observations models that reproduce the SWS exhibit no significant differences in the location of SST anomalies between strong and moderate El Niño (Fig. 2.4d-e). These models also display a westward shift of the anomalous SST values during extreme El Niño events compared to observations. For instance, the anomalous 0.5 °C isotherm is shifted around 10 ° longitude when compared to that observed. Models without a SWS tend to underestimate the magnitude of the anomalous values of SST for La Niña and strong El Niño, whereas the amplitude is larger for moderate El Niño (Fig. 2.4g-i).

Here we calculate and display the ensemble mean SST anomaly differences between models with and without a SWS in an attempt to better understand the cause of the SWS (Fig. 2.4j, k). The differences between these two types of models (with and without the SWS) show warmer conditions over the eastern and colder over the western equatorial Pacific for El Niño events although the eastern Pacific difference is larger for the strong events and the western Pacific difference is larger for moderate events. We also find that the maximum event magnitude, identified with each model's SST anomaly in DJF, is statistically significantly related to the magnitude of the SWS during La Niña and strong El Niño events (Table 2.1). If we instead classify the event magnitude with the magnitude of the wind stress response (rather than SST magnitude) we find that the relationship between the event magnitude and the SWS decreases (increases) for La Niña (strong El Niño) (Table 2.1). We also find that the erroneous westward displacement of western edge of SST anomalies during extreme El Niño events is much more pronounced in models without a SWS, and it is also seen during moderate El Niño events in these models. However, the relationship between the extent of the westward shift of the SST anomaly edge and the magnitude of the SWS is only statistically significant for moderate El Niño events (Table 2.1). The shift towards the west of the SST anomaly edge has been related to the cold tongue bias, which is one of the long-standing problems among climate models (Kirtman et al. 2002; Capotondi et al. 2006) and still remains an issue in CMIP5 models (Brown et al. 2014; Kug et al. 2012; Capotondi and Wittenberg 2013; Ham et al. 2012; Ham and Kug 2015). Consistent with the westward bias, we also find a linear significant relationship between the SST bias in the equatorial Pacific cold tongue region (2 °S - 2 °N, 160 °E - 90 °W; Li et al. (2016)) and the SWS magnitude for moderate El Niño events (Table 2.1).

Table 2.1: Coefficients of determination (R^2) and correlation coefficient (r; shown in parentheses) between possible drivers of the SWS and the SWS index (defined in Sect. 2.3.1). Note that bold values indicate that the correlation is significant at the 95% confidence level. The meridional gradients are defined as the average over the equatorial region (5 °S-4 °N, 120 °E-160 °W) minus the average over the north off-equatorial region (5 °N-12 °N, 140 °E-160 °W). For climatological predictors, we focus on the DJF season, when the anomalous zonal winds are migrating southwards. The number of degrees of freedom is 28 for strong El Niño, and 32 for the other events.

Variable	Description	Strong El Niño	Moderate El Niño	La Niña
PR_{clim}	Meridional gradient of climatological precipitation during DJF	**0.160 (0.40)**	**0.396 (0.63)**	**0.262 (0.51)**
SST_{clim}	Meridional gradient of climatological SST during DJF	**0.293 (0.54)**	**0.428 (0.65)**	**0.397 (0.63)**
$TAUX_{clim}$	Meridional gradient of climatological zonal wind stress during DJF	**0.160 (0.40)**	**0.247 (0.50)**	**0.242 (0.49)**
PR_{anom}	Precipitation anomaly in DJF averaged over Eq. - 10 °N, 120 °E - 160 °E during ENSO	**0.294 (0.54)**	**0.518 (0.72)**	**0.333 (0.58)**
SST_{anom}	Equatorial (5 °S-5 °N) maximum SST anomaly in DJF during ENSO events averaged over 20 ° longitude with the maximum located in the centre of the selected region	**0.137 (0.37)**	0.026 (0.16)	**0.248 (0.50)**
$TAUX_{anom}$	Maximum zonal wind stress anomaly between 10 °S-10 °N averaged over Aug-Apr and 160 °E-120 °W during ENSO	**0.199 (0.45)**	**0.352 (0.59)**	**0.190 (0.44)**
CT	Annual mean climatology of SST over 2 °S - 2 °N, 150 °E - 110 °W (Cold tongue)	0.081 (0.29)	**0.141 (0.38)**	0.099 (0.32)
LON_{05}	Longitude of ±0.5 °C SST anomaly over the equator in DJF during ENSO years	0.097 (0.31)	**0.138 (0.37)**	0.068 (0.26)
ZRes	Zonal resolution of the atmosphere	0.113 (0.34)	0.068 (0.26)	0.098 (0.31)
MRes	Meridional resolution of the atmosphere	0.054 (0.23)	**0.119 (0.35)**	0.021 (0.15)

Precipitation anomalies

During strong El Niño events, the warm SST anomalies over the equatorial central and eastern Pacific lead to the equatorward displacement of the Intertropical Convergence Zone and South Pacific Convergence Zone resulting in positive precipitation anomalies over this region (Fig. 2.5a). In contrast, negative precipitation anomalies are robust to the north, south and west of this enhanced precipitation (Fig. 2.5a), showing that this is more a redistribution than an increase (Choi et al. 2015). This redistribution of precipitation during strong El Niño events is also seen in the CMIP5 models, however the magnitude of the model anomalies is much weaker, and this bias is more pronounced in models without the SWS. In fact, there is a statistically significant relationship between precipitation anomalies in the northwestern Pacific and the magnitude of the SWS (see yellow box in Fig. 2.5, Table 2.1). Consistent with the westward shift of the SST anomaly edge seen in both model groups (Fig. 2.4), the enhanced equatorial precipitation during strong El Niño events is also shifted to the west relative to observations (Fig. 2.5a-c) (Misra et al. 2007; Cai

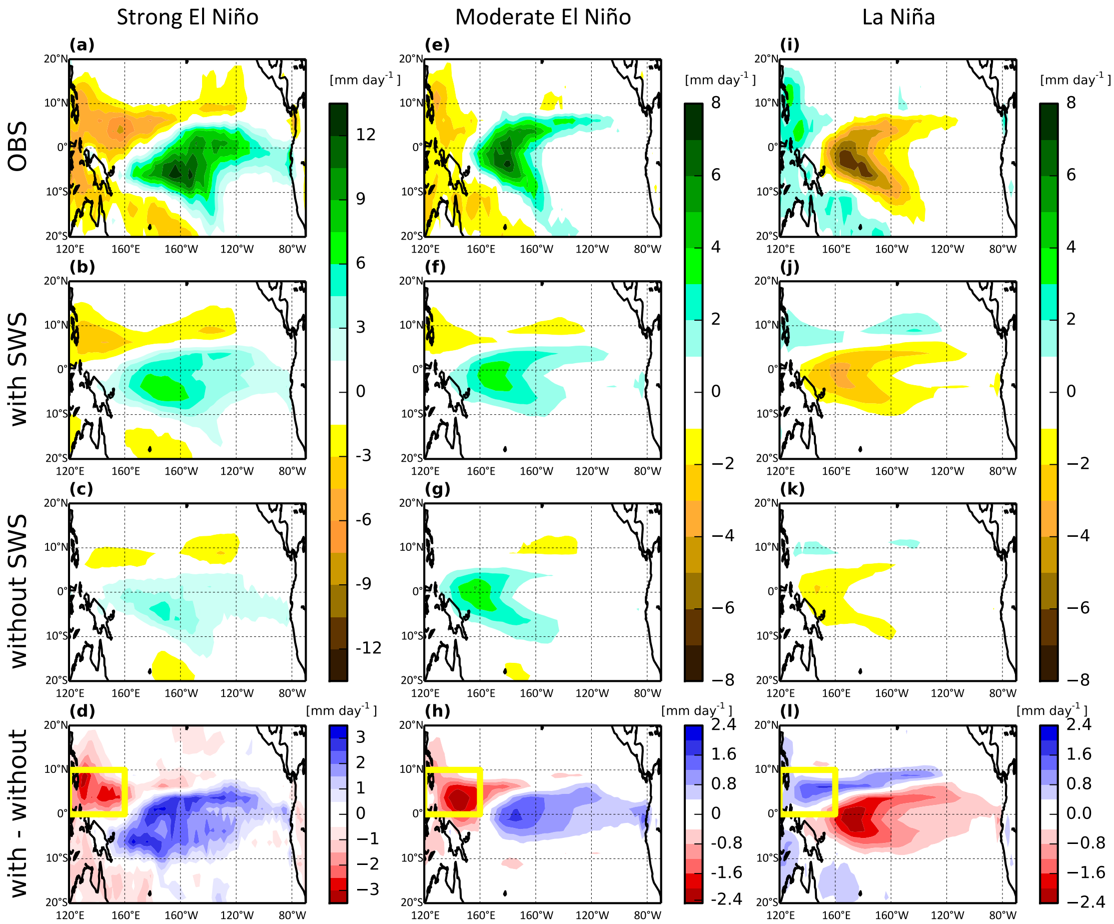

Figure 2.5: Precipitation anomalies in DJF during strong El Niño (a-d), moderate El Niño (e-h) and La Niña (i-l) for observations (a, e, i), models with SWS (b, f, j), models without SWS (c, g, k) and the difference between models with and without SWS (d, h, l). Note the different color scales. The yellow boxes indicate the area over which indices are calculated for use in the regression models carried out in Sect. 2.4c.

et al. 2012; Kug et al. 2012).

A similar pattern of precipitation is observed for moderate El Niño events (i.e., negative anomalous values of rainfall over the western tropical Pacific and positive over the central Pacific) (Fig. 2.5e), although the anomaly magnitude is around half that seen for strong El Niño events and no anomalies are observed over the eastern equatorial Pacific for moderate El Niño events consistent with the study of Cai et al. (2014). As for strong El Niño events, the models tend to simulate excessive precipitation anomalies over the western Pacific Warm Pool region, which is likely due to the westward shift of SST anomalies as this bias is more marked in models without a SWS (Fig. 2.5f-g). As a consequence, the difference map exhibits more (less) precipitation anomalies over the central-west (far west) equatorial Pacific (Fig. 2.5h). Again the northwestern Pacific changes are so robust that a statistically significant relationship between precipitation anomalies in the northwestern Pacific and the magnitude of the SWS also exists for moderate El Niño events (Table 2.1).

For observed La Niña events, there is a marked similarity with moderate observed El Niño events (Fig. 2.5e, i), although with opposite anomaly patterns, as expected, i.e. drier (wetter) conditions than normal over the central/western (far west) equatorial Pacific. As before, the CMIP5 models underestimate the magnitude of the anomalous rainfall during La Niña compared to observations, particularly those without a SWS (Fig. 2.5j-k). Focusing again on precipitation anomalies in the northwestern Pacific, a statistically significant relationship is found between the anomaly magnitude and the magnitude of the SWS during La Niña events (Table 2.1).

In short, we found that the magnitude of the anomalous values of equatorial SST, rainfall over the northwestern Pacific, and equatorial zonal wind are related to the magnitude of the SWS. As a consequence, models without a SWS show biases in both the magnitude (weaker) and location (westward) of SST and precipitation.

2.4.2 The role of the mean state

It has been suggested that climatological biases affect the fidelity of the simulation of ENSO in climate models (Wang and An 2002; Guilyardi 2006; Sun et al. 2009; Bellenger et al. 2014). Here, we analyze the climatological SST, precipitation and wind stress in the tropical Pacific to further examine if mean state biases might influence the ability of CMIP5 models to simulate the SWS during ENSO events. We chose to focus on the DJF period as this is when the surface winds are migrating southwards, but we also note that the differences between the CMIP5-with-SWS and CMIP5-without-SWS are very similar regardless of whether MAM or SON was selected (Fig. 2.6).

The tropical Pacific mean state during DJF is characterized by relatively cold SST in a band centered on the equator in the central and eastern Pacific, and the warmest temperatures in the west (Fig. 2.6a). These two regions are commonly referred to as the cold tongue and warm pool, respectively. The climatological precipitation during DJF exhibits two bands of heavy precipitation: the first extending across the central/eastern Pacific (i.e., the ITCZ); and the second extending southeast from near New Guinea to the southeastern Pacific (i.e., the SPCZ), with highest rainfall in the SPCZ (Fig. 2.6a). Consequently, minimum wind stress is observed in the SPCZ region, and the strongest easterly anomalies are found north and south of the ITCZ, converging in this area.

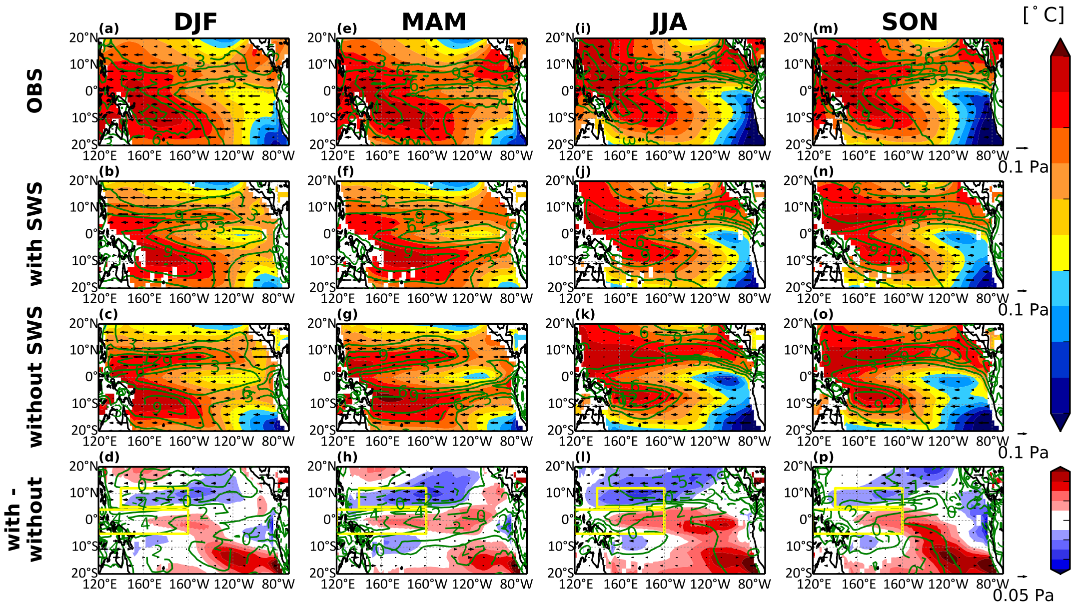

Figure 2.6: Climatological SST (shading), precipitation (green contours) and zonal wind stress (vectors) during DJF (a-d), MAM (e-h), JJA (i-l) and SON (m-p) for observations (a, e, i, m), the ensemble of models which display the SWS (b, f, j, n), the ensemble of models which do not display the SWS (c, g, k, o), and the difference between the ensemble mean of these (d, h, l, p). The two yellow boxes in the differences map indicate the southern (5 °S-4 °N, 120 °E-160 °W) and northern region (5 °N-12 °N, 140 °E-160 °W), where meridional gradients are carried out in Sect. 2.4.3.

To first order, the models (both with and without the SWS) appear to do a reasonable job capturing the main features of the observed spatial patterns of SST and precipitation described above (Fig. 2.6a-c). However, models without a SWS during ENSO events exhibit two notable differences compared to observations or models with a SWS: (1) larger rainfall in the ITCZ than in the SPCZ; and (2) SST underlying the ITCZ appear much warmer. Both changes are highlighted by looking at the differences between the models with and without the SWS (Fig. 2.6d). Precipitation differences of up to 4 mm day^{-1} are found, whereby the models with the SWS are wetter in the western equatorial Pacific and dryer in the northwestern Pacific. The rate of precipitation in these regions is significantly related to the magnitude of the SWS during all event types. Furthermore, the models with the SWS have cooler SST (up to 1.2 °C) underlying the ITCZ than those without, and they also have a less pronounced cold tongue bias in the central Pacific. It has been suggested that weaker gradients of SST facilitate shift in convection zones (Cai et al. 2014). Thus, we expect the meridional gradient of SST between the equator and north off-equator regions, which is weaker in models without a SWS, to favor the shift in convection zone from SPCZ to ITCZ in these models. This is supported by calculating the coefficient of determination between the meridional gradient of SST and the magnitude of the modeled SWS, as we find a statistically significant relationship in all event types (Table 2.1). Another feature revealed by Fig. 2.6d is that models without a SWS tend to also exhibit weaker north Pacific trade winds due to weaker zonal SST gradient.

2.4.3 Possible drivers of the SWS - evidence from a multi-linear regression

The results presented in Sect. 2.4.1 and 2.4.2 above suggest that the models mean climate and its representation of ENSO both impact the magnitude of the modeled SWS. In order to quantify the dependency of the SWS on these variables described above (Table 2.1), we conduct multiple-linear regressions (Wilks 2006) between the SWS, defined in Sect. 2.3.1, and a set of metrics each related to the possible driving mechanisms of the SWS, as listed in Table 2.1. As with the linear regressions presented in Table 2.1, each model's ENSO event composite mean is computed, then the relationship (regression) between the indices is computed across the ensemble of models. We emphasize that the purpose of this analysis is not to generate a set of SWS predictors. Rather, the intent is to gain insight into the SWS dynamics, by analyzing its possible link to mean state metrics and their ENSO-related values, along with the horizontal resolution in the atmospheric model.

Table 2.2: Multiple correlation (r) and squared multiple correlation (R^2) between the variables defined in Table 1 and the SWS index (defined in Sect. 2.3.1) and their root-mean-square error (RMSE). Note that bold values or variables indicate that the correlation coefficient are significant at the 95% confidence level. Each model's ENSO event composite mean is computed prior to the regression across the ensemble of models.

ENSO event	Predictors	R-squared (r)	RMSE (° lat)
Strong El Niño	PR_{clim}+SST_{clim}+$TAUX_{clim}$+PR_{anom}+SST_{anom}+$TAUX_{anom}$	0.393 (0.63)	3.4
	PR_{clim}+$\mathbf{SST}_{clim}$+$TAUX_{clim}$	**0.304 (0.55)**	4.3
	PR_{anom}+SST_{anom}+$TAUX_{anom}$	**0.301 (0.55)**	4.3
	SST_{clim}+PR_{anom}	**0.362 (0.60)**	5.7
Moderate El Niño	PR_{clim}+SST_{clim}+$TAUX_{clim}$+$\mathbf{PR}_{anom}$+SST_{anom}+$TAUX_{anom}$	**0.598 (0.77)**	4.2
	PR_{clim}+$\mathbf{SST}_{clim}$+$TAUX_{clim}$	**0.483 (0.70)**	5.4
	$\mathbf{PR}_{anom}$+SST_{anom}+$TAUX_{anom}$	**0.565 (0.75)**	5.8
	SST_{clim}+$\mathbf{PR}_{anom}$	**0.570 (0.76)**	7.1
La Niña	PR_{clim}+SST_{clim}+$TAUX_{clim}$+PR_{anom}+$\mathbf{SST}_{anom}$+$TAUX_{anom}$	**0.511 (0.72)**	3.6
	PR_{clim}+SST_{clim}+$TAUX_{clim}$	**0.368 (0.61)**	4.3
	$\mathbf{PR}_{anom}$+$\mathbf{SST}_{anom}$+$TAUX_{anom}$	**0.481 (0.69)**	4.9
	SST_{clim}+PR_{anom}	**0.394 (0.63)**	5.4

Given the large number of possible combinations of explanatory variables listed in Table 2.1, only those regressors with highest R-squared values are taken into account. These include the three climatological values in DJF and the three anomalous variables, each of which we consider to be physically linked with the SWS. For each type of event, there are 4 multiple-regression models, shown in Table 2.2, which consist of: (i) the 6 variables mentioned above; (ii) the 3 climatological values; (iii) the 3 anomalous values; and (iv) the meridional gradient of DJF climatological SST and rainfall anomaly in the northwestern Pacific, which have the highest correlation in the single linear regression (Table 2.1). The highest (significant) squared multiple correlations are up to 0.36, 0.60 and 0.51 for strong El Niño, moderate El Niño and La Niña, respectively.

Interestingly, the resulting correlation is not the sum of the individual correlations, which highlights that each of these variables is not linearly independent. For instance, the climatological meridional gradient of SST and the ENSO-related anomalous precipitation in the Northwest equatorial Pacific are linearly related (R-squared = 0.39, 0.46 and 0.46 for strong El Niño, moderate El Niño and La Niña, respectively). As the latter variable is also related to the Philippine anticyclone development (i.e., how well the SWS is simulated, Fig. 2.3), the meridional gradient of SST in each model is expected to be a potentially important driver for both precipitation in the Northwest equatorial Pacific and the SWS. It is also interesting to note that a large portion of the multilinear regression (R-squared) can be recovered when simply considering the climatological gradients of SST, precipitation and wind stress; and that this combined effect is not dissimilar to that which can be achieved with the meridional gradient of climatological SST alone. Again, we highlight the potential importance of the meridional gradient of climatological SST as a driver of the SWS. Further experimentation, however, is needed to better understand the dynamics behind this link. We note that the coefficients of these two explanatory variables are statistically significant in most of our regression models. In addition to these two variables, including the rest of regressors lead to increase the explained variance of the SWS for La Niña (from 39% to 51%), whereas no large contribution is found for strong El Niño (from 36% to 39%) and moderate El Niño (from 57% to 60%). We also notice that, given a variable, most (with the exception being SST anomalies) correlation coefficients are larger for moderate than for strong El Niño events (Table 2.1), which is consistent with the atmospheric nonlinear interaction between ENSO and the Pacific warm pool annual cycle (C-mode).

We emphasize that correlation of course, does not necessarily imply causality. The association between the SWS and the anomalous variables described above may simply indicate symptomatic changes, however we believe that this is unlikely to be the case for the climatological variables.

2.5 Seasonal synchronization and SWS

A well-known characteristic of ENSO events is their tendency to peak at the end of the calendar year, and as outlined in Sect. 2.1, previous studies have proposed that the SWS plays a significant role in El Niño phase-locking and therefore in the seasonal modulation of air-sea coupling strength. To further verify this hypothesis, we now examine the connection between ENSO seasonal synchronization and the SWS in the CMIP5 coupled models.

Figure 2.7 shows the composite Niño-3.4 region (defined in Sect. 2.2.3) SST anomaly evolution during a 13-month period (6 months before and 6 months after the peak) for the ensemble mean of CMIP5 models with SWS (CMIP5-with-SWS) and without SWS (CMIP5-without-SWS) versus observations for comparison. The maximum amplitude in CMIP5-with-SWS (2.2 °C) is roughly the same as the observed (2.1 °C) and larger than that seen in CMIP5-without-SWS (1.8 °C). A t-test is conducted to assess the statistical significance (at the 95% level) of the differences in the modeled composites and statistically significant differences are denoted by the gray shaded area in Fig. 2.7. It is found that for strong El Niño events, the CMIP5-with-SWS and CMIP5-without-SWS are significantly different during the development and mature phase. It is clear that the SST anomalies of the CMIP5-with-SWS models decay at a much faster rate than the CMIP5-without-SWS ensemble. To quantify the strength of this decay, we calculate the average

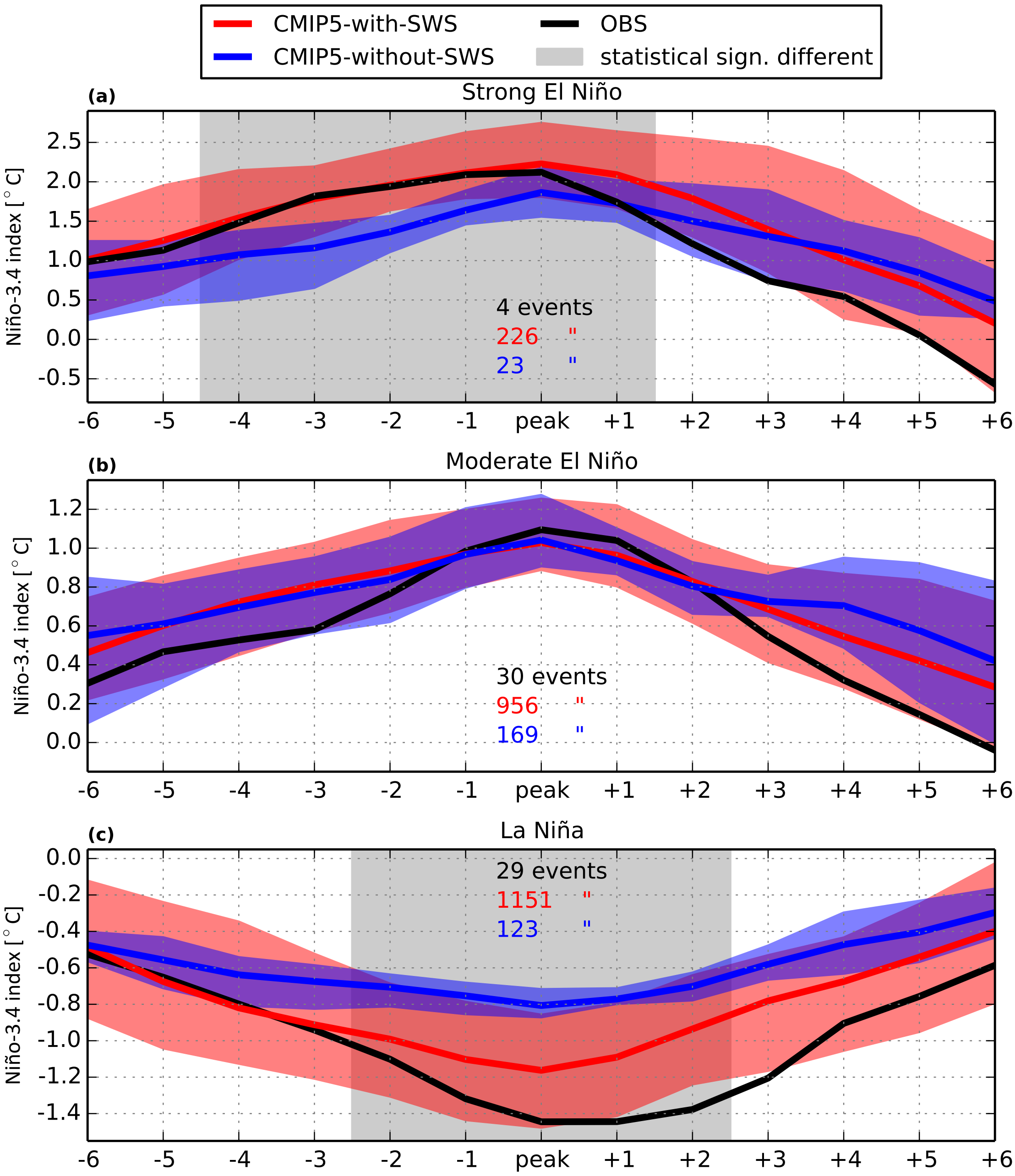

Figure 2.7: Composite mean of SST anomalies over the Niño-3.4 region during the 6-month period around the peaks of ENSO events. Black lines indicate the observed values; red (blue) lines represent the ensemble mean of CMIP5 models with (without) SWS. The red and blue shaded areas show the 5^{th} and 95^{th} percentile range, whereas gray shading indicate that the two ensemble means are different at the 95% level, after employing a t-test. Different y-axis temperature scales are employed in each panel.

of the monthly difference in the Niño-3.4 index between the peak of the event and 6 months after. The resulting average SST anomalies decay is -0.34 °C month $^{-1}$ in CMIP5-with-SWS, which is much stronger than the -0.23 °C month $^{-1}$ seen in CMIP5-without-SWS. It is interesting to note, however, that both values are lower than average SST anomalies decay observed during strong El Niño events (-0.45 °C month $^{-1}$).

For moderate El Niño events, in contrast, no statistically significant difference is seen between the two-modeled composite means throughout the whole period analyzed (Fig. 2.7b). The maximum values between CMIP5-with-SWS and CMIP5-without-SWS are approximately the same ($\sim$1 °C), which is somewhat expected given these events must fall within the range of 0.5 °C and 1.5 °C, and their decaying rate (-0.12 °C month $^{-1}$ and -0.10 °C month $^{-1}$, respectively) are also highly similar. As is the case for strong events, the decaying rate for moderate El Niño is underestimated compared with observations (-0.19 °C month $^{-1}$).

In contrast to moderate El Niño events, there is a statistically significant difference between the two composite means during the mature phase for La Niña events (Fig. 2.7c). In particular, the peak magnitude is higher (-1.2 °C) in CMIP5-with-SWS compared to CMIP5-without-SWS (-0.8 °C), and the peak in the latter set is much less pronounced. Additionally, the decay of SST anomalies following the event peak is larger in CMIP5-with-SWS (0.13 °C month $^{-1}$) compared to CMIP5-without-SWS (0.08 °C month $^{-1}$), with both values again lower than observed (0.14 °C month $^{-1}$).

We note that, given a certain magnitude of an ENSO event, its decaying rate is larger in CMIP5-with-SWS than that in CMIP5-without-SWS. Thus, the fact that the decay of SST anomalies is lower in CMIP5-without-SWS is not only owing to lower magnitude of the events but also the lack of the SWS.

To further elucidate this feature of ENSO phase locking in relation to the SWS, Fig. 2.8 shows the percentage of ENSO events peaking in each calendar month for models with and without SWS compared to observed. The four observed extreme El Niño (1888–89, 1902–03, 1982–83, 1997–98) all reached their maximum amplitude in NDJ (Fig. 2.8a). In comparison, in CMIP5-with-SWS, 60% of strong El Niño events peak during NDJ, consistent with observations, whereas only 28% strong El Niño events peak in NDJ in CMIP5-without-SWS. In addition, a relatively large proportion ($\sim$38%) of the modeled strong El Niño events peak erroneously during April–June in CMIP5-without-SWS. The number of strong events erroneously peaking during April–June is only 6% in models with a SWS. Such a clear difference between the CMIP5-with-SWS and CMIP5-without-SWS is not seen for moderate

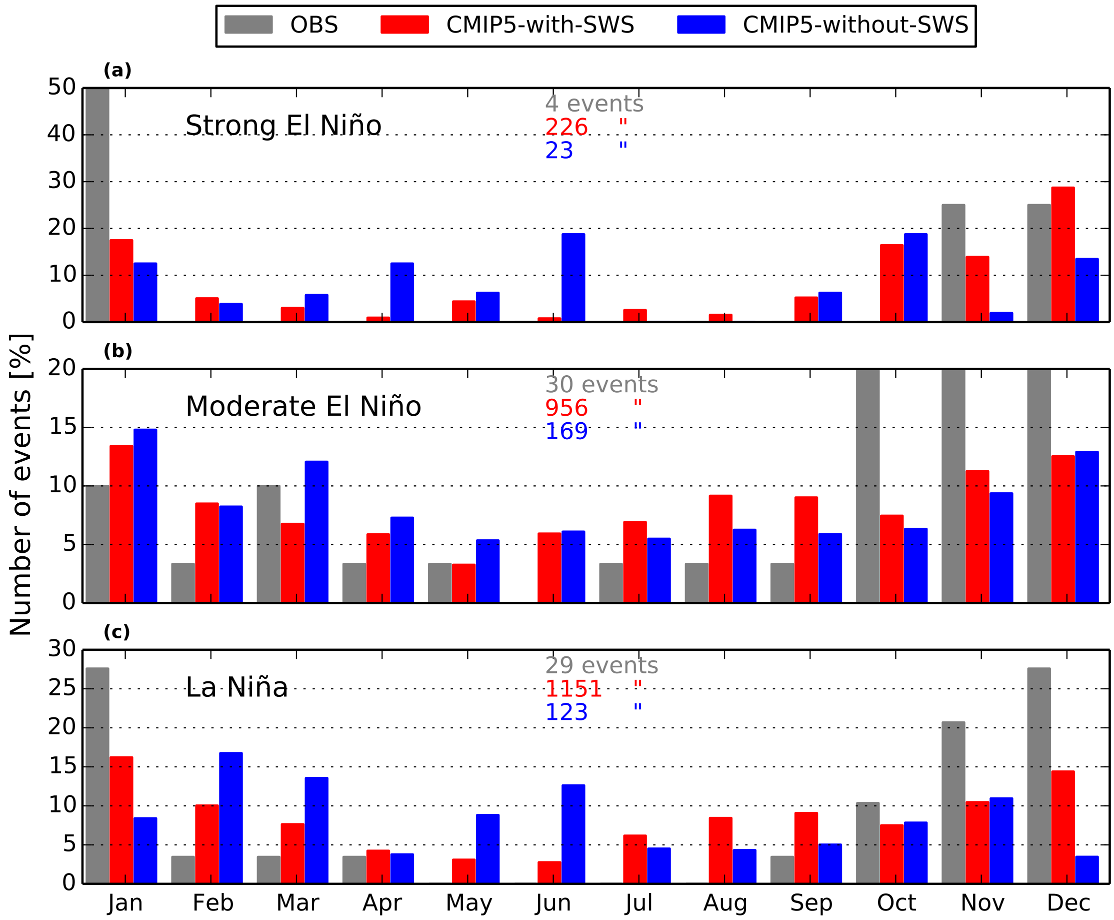

Figure 2.8: Percentage of strong El Niño (a), moderate El Niño (b) and La Niña events (c) with peaks occurring for each calendar month. Red (blue) bars refer to models with (without) SWS and gray bars the observed values.

El Niño events, as ∼30% of event peaks occur during October–December (OND) regardless of whether models accurately produce the SWS or not (Fig. 2.8b). In the observations, 60% of moderate El Niño events peak during OND, while 76% of La Niña events peaks during NDJ. Some CMIP5-with-SWS and CMIP5-without-SWS differences are found, with 41% and 23% of La Niña events, respectively, peaking in NDJ (Fig. 2.8c).

Finally, following Bellenger et al. (2014) where they pointed out a large spread in CMIP5 ensemble ENSO variability, we now explore whether this behaviour is partially due to how well models can reproduce the SWS. Figure 2.9 displays the standard deviation of the normalised Niño-3 index (i.e., SST anomalies averaged over 150 °W-90 °W, 5 °S-5 °N) for each calendar month in the observations and models, where the models are split into those with and without a realistic SWS for the three event types and the CMIP5 multi-model ensemble mean. The seasonal cycle in the observations shows a clear maximum of SST anomaly during November–January and a minimum during March–April. Although the CMIP5-with-SWS ensemble exhibits

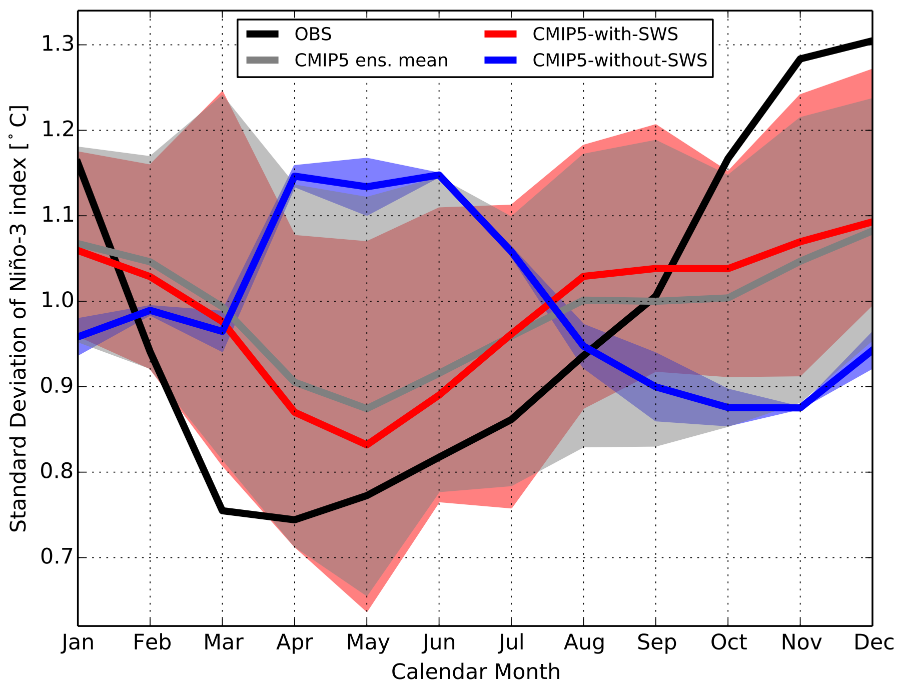

Figure 2.9: Standard deviation of Niño-3 SSTA stratified by calendar month from observations (black line), CMIP5 models with SWS for all three ENSO event types (red line), without SWS for none of the events (blue line) and all CMIP5 models (gray line). Thick lines represent the mean values, whereas the shaded areas show the 5^{th} and 95^{th} percentile range.

a large spread and a smaller range, there is a tendency for a boreal winter maximum, as observed, and a minimum around April–June, which lags that observed by one month. These two limit values occur during the opposite seasons in CMIP5-without-SWS ensemble, which is consistent with the tendency for some ENSO events to peak in the wrong time of the calendar year in those models, as described above. The multi-model ensemble mean is in close agreement with the CMIP5-with-SWS (Fig. 2.9). However, its spread is larger than CMIP5-with-SWS around April–June and August–December, coinciding with the maximum and minimum peaks in CMIP5-without-SWS, respectively.

Thus, in summary, ENSO phase-locking and its termination rates appear much more realistic in models with a SWS than models without a SWS for strong El Niño and La Niña events, especially for El Niño. However, as noted in the abstract, the models do underestimate the seasonal phase-locking tendency of ENSO events and this is only partially improved by focusing on the CMIP5 models which accurately reproduce the SWS. As to whether the improvements in SWS representation in the CMIP5 models with SWS is due to the more realistic synchronisation of ENSO events, we revert to past literature that shows that SWS can be generated for arbitrary frequencies of ENSO anomalies (Spencer 2004; Stuecker et al. 2015). Further to this, the study of Abellán and McGregor (2016) suggests that the SWS plays a crucial role in the synchronisation of ENSO events to the seasonal cycle.

2.5.1 WWV changes

It has been previously shown that variability in WWV, and hence heat content, in the tropical Pacific is related to the dynamics of the ENSO cycle (Wyrtki 1985; Cane and Zebiak 1985; Zebiak 1989; Springer et al. 1990; Jin 1997; Meinen and McPhaden 2000). In fact, the Recharge/Discharge Oscillator (RDO) theory proposes that warm water builds up in the equatorial Pacific prior to El Niño, as a consequence of equatorward transport of warm water. Then, the equatorial region is discharged of heat during El Niño, which ultimately sets up conditions favourable for the termination of the event. The fact that the SWS enhances the pre-event peak WWV recharge and the post-event peak WWV discharge effectively links the WWV with the seasonal cycle and provides a mechanism for the seasonal synchronisation of the events.

Thus, in order to understand why the CMIP5 models are underestimating this phase locking, in spite of realistically producing the SWS we focus on the WWV changes driven by the SWS. Changes in WWV are generated by transports that converge/diverge in the equatorial region and defined here as transport differences at 5 °S (V_{5S}) and 5 °N (V_{5N}), ($V_{5S} - V_{5N}$), which represents the convergent meridional transport. Now, rather than calculating total transports in each model, which would make it difficult to distinguish the role of the SWS, we seek to identify the transports and WWV changes related to the wind stress changes that occur during the SWS. Firstly, the wind stress changes that occur during the SWS are identified as the average wind stresses during the February–April (FMA) season minus the August–October (ASO) average wind stresses (as shown in Fig. 2.3). As Kug et al. (2003) and McGregor et al. (2014) demonstrated that the WWV changes generated by the SWS are largely forced by surface Ekman transport changes, here we simply calculate the SWS induced changes in WWV from the meridional Ekman transport of the SWS (Fig. 2.3). The Ekman transport is calculated by

$$V_E = -\frac{\tau_x}{f\rho}\Delta x \tag{2.1}$$

where τ_x is the zonal wind anomaly, f the Coriolis parameter, ρ the water density (1000 kg m^{-3}) and Δx the zonal resolution (in metres) so that the units of V_E are m^3 s^{-1} (Sverdrups). Note that this formulation calculates mass transport, regardless water temperature.

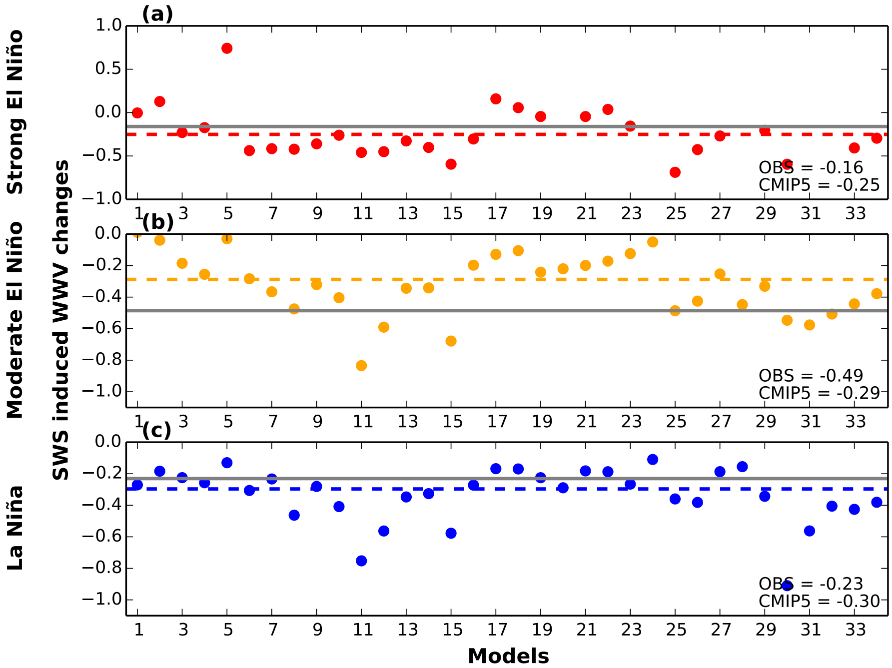

Figure 2.10: SWS-driven WWV changes (calculated as the WWV difference between FMA and ASO) divided by the total WWV changes (i. e. Sverdrup transport, calculated from the NDJ winds) during event years. Note that horizontal gray lines indicate the observed values. See the list of CMIP5 models used in Fig. 2.1 or 2.2.

It is worthwhile to note that the SWS induced WWV changes represent approximately 25–30% of the estimated total WWV changes in the CMIP5 models (estimated using NDJ Sverdrup transport during event years; Fig. 2.10). Thus the CMIP5 model results are consistent with the modelled results of McGregor et al. (2014) (their Fig. 7), which suggested that the SWS should play a prominent role in the termination of modeled ENSO events. We note that using Sverdrup transports to estimate WWV changes may overestimate the magnitude of the changes as the interior transports are often partially compensated by transports at the Pacific Ocean western boundary. We then seek to identify the relationship between these SWS induced WWV changes during ASO prior to the peak of the ENSO event and their relationship with the magnitude of the events, and SWS induced WWV changes during FMA after the event peak and their relationship with the decay of SST anomalies (event termination).

Figure 2.11 highlights a statistically significant linear relationship between the SWS induced WWV changes during ASO preceding the event peak and the magnitude of the ENSO event peak (SST anomalies during DJF) (Fig. 2.11a-c). This relationship is consistent with the RDO theory (Meinen and McPhaden 2000), which links the two metrics, however the recharging due to the SWS is distinct from that explicitly covered by the RDO theory. It is also revealed that models with weak

SWS (light green dots) tend to exhibit weak changes in WWV, although the relationship between the SWS and changes in WWV is significant only for La Niña (r = 0.43, Fig. 2.12). However, those models with strong SWS (dark green dots) do not necessarily show strong changes in WWV. This is not unexpected, as it is the magnitude and zonal extent of the wind changes that drives an oceanic response, not only the latitude of the maximum.

In order to understand how the SWS changes in WWV after the event peak (FMA during the decaying year) impact the SST anomalies decay of each event type, Figure 2.11 also displays the FMA WWV changes plotted against the post ENSO event peak SST anomalies decay. It is noteworthy that again a statistically significant relationship is found for ENSO events (Fig. 2.11d-f), reaching the maximum correlation for strong El Niño (r = 0.60). Thus, if the SWS induced discharge (recharge) of heat content for El Niño (La Niña) is large, the termination of the event tends to be more rapid than that with small WWV changes. It is interesting to note that multi-model mean WWV change for moderate El Niño is much lower than that observed, which may help to explain why these events are not as phase locked as the observations (Fig. 2.8b). It is also illustrated here the symmetries between La Niña and moderate El Niño events for values of the Niño-3.4 index, SST anomalies decay and WWV changes. Hence, this analysis highlights how the SWS modulates the evolution of the WWV changes in the equatorial Pacific Ocean, and effectively links these changes with the seasonal cycle: the recharge of the WWV occurs prior to the El Niño event (represented here in ASO season), whereas the discharged state is obtained after the peak (represented here in FMA season)

2.6 Summary and conclusions

The goal of our study was to address the following questions: (1) Do the CMIP5 models reproduce a realistic southward wind shift (SWS)? (2) What variables are related to the SWS in CMIP5 models? and (3) What is the role of the SWS in the seasonal synchronization of modeled ENSO events? Firstly, however, we define three ENSO event types: El Niño events are separated into strong and moderate categories while La Niña events have only the one category (see Sect. 2.2.3).

It was demonstrated that the magnitude of zonal wind stress anomaly during ENSO events is clearly underestimated and its spatial pattern extends too far into the western Pacific, although the latter has been incrementally improved in CMIP5 with respect to CMIP3 (Capotondi et al. 2006; Lee et al. 2013). In terms of capturing the SWS, it is encouraging that the vast majority (81−86%) of CMIP5 models

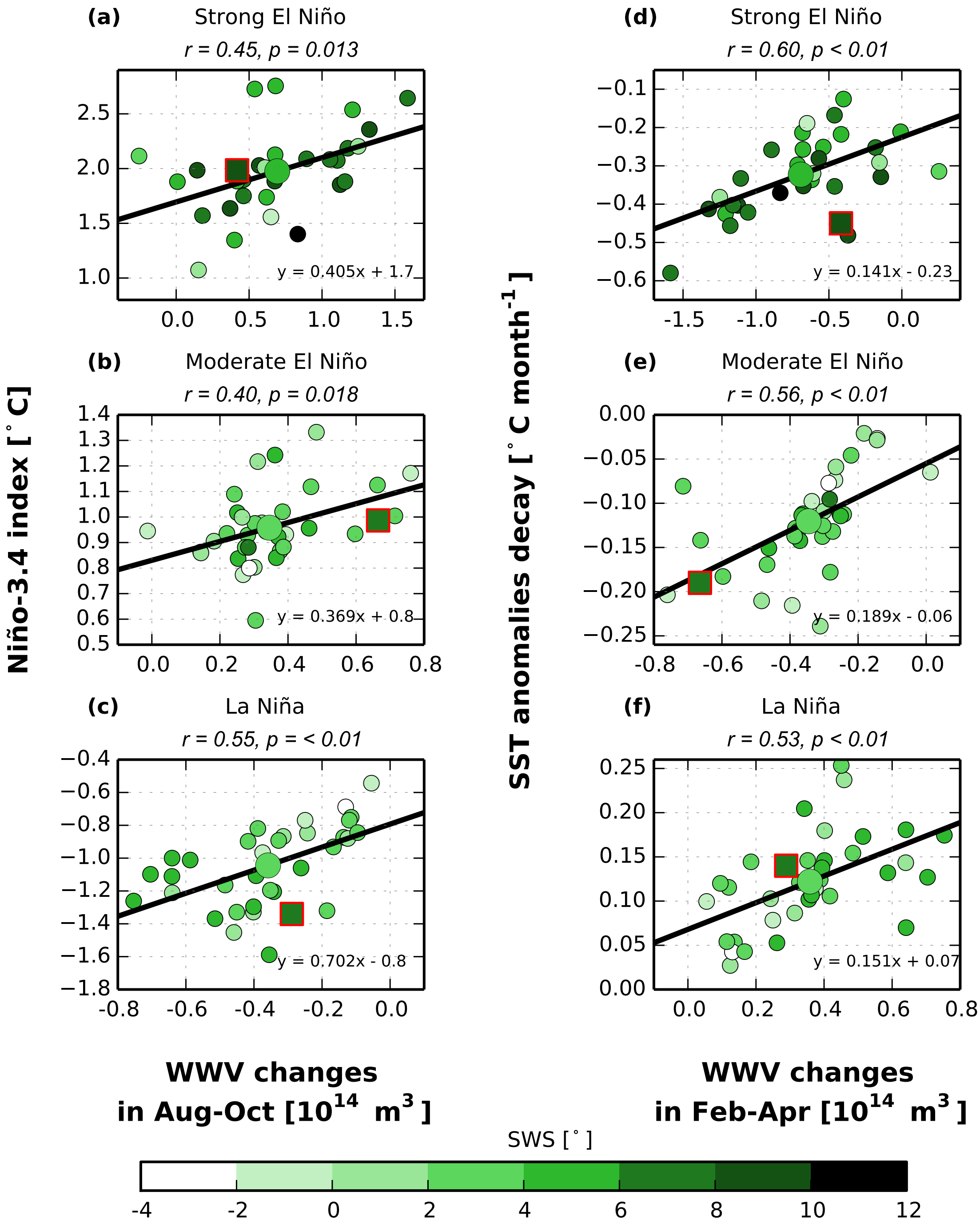

Figure 2.11: Scatter plots showing the modelled relationship between the magnitude of ENSO events in DJF and WWV changes in August–October (a-c) and between the termination rate (defined in Sect. 2.5) and WWV changes in February–April (d-f). Note that the colors of the dots indicate the intensity (in ° latitude) of the SWS and the slopes of the regression lines are multiplied by 10^{14}. The squares, with a red outline, represent the observed values whereas the big circles indicate the multi-model ensemble means. The average value in ASO and FMA [i.e., (ASO + FMA) /2] is subtracted for changes of WWV in both ASO and FMA in order to emphasize the role of the SWS in WWV changes. The spatial patterns of zonal wind stresses anomalies used to compute WWV changes are shown in Fig. 2.3.

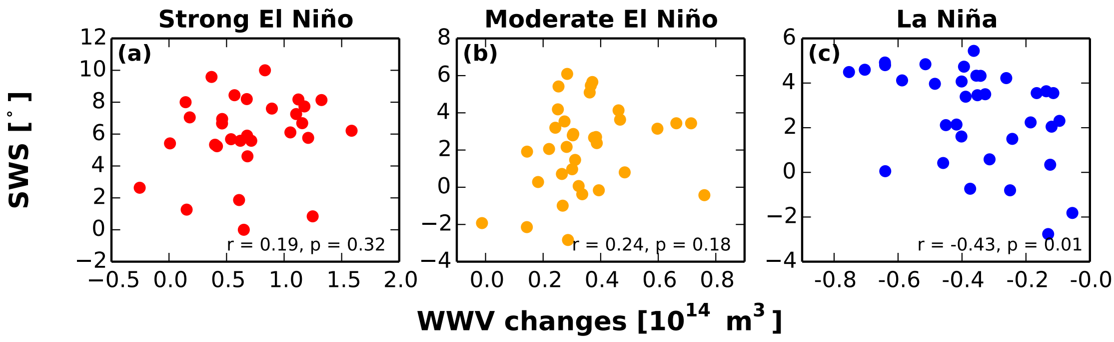

Figure 2.12: Scatter plots showing the modelled relationship between the magnitude of the SWS (in ° latitude) and WWV changes in ASO. As in Fig. 2.11, the average value in ASO and FMA [i.e., (ASO + FMA) /2] is subtracted.

successfully captures the observed SWS during some of the three types of ENSO events (strong El Niño, moderate El Niño and La Niña), with mean latitude biases of -1.4 °, 0.3 ° and -0.8 °, respectively (see Sect. 2.3.1 for SWS definition). We found in addition that 65% of models reproduce a SWS for all types of ENSO events, whereas only 2 out of 34 models (IPSL-CM5A-LR and IPSL-CM5A-MR) fail to simulate the SWS for all three event types.

In examining the factors that are related to the performance of CMIP5 models in simulating the SWS, we first classify the models according to their ability to represent the SWS during ENSO events and then make model ensembles with and without the SWS. We then composite means of SLP, precipitation and SST anomaly patterns. Our results indicate that most models have a problem reproducing the zonal location of the anomalies in zonal wind stress, precipitation and SST, as documented in past studies (e.g., Kug et al. 2012; Capotondi and Wittenberg 2013; Zhang and Sun 2014; Ham and Kug 2014; Taschetto et al. 2014). However, here we have demonstrated that these biases in models without a SWS are much larger than those in models with a SWS. Furthermore, the seasonal differences of zonal wind stress and SLP anomalies prior to the peak of the events (August–October) and after the mature phase (February–April) are underestimated in all of the CMIP5 models, however, this is most pronounced in CMIP5 models that do not accurately produce a SWS. It is also clear from our analyses that the anomalous values of SST and rainfall during the mature phase (DJF) of La Niña and strong El Niño are weaker in models having a poor simulation of the SWS compared to models with a SWS, whereas no striking difference is seen for moderate El Niño. To further explore differences between models with and without a SWS, we analyzed the climatological SST, precipitation and zonal wind during DJF over the tropical Pacific. It was shown that models without a SWS exhibit stronger ITCZ, warmer underlying SST and weaker trade winds over the north tropical Pacific compared to models with a

SWS, in addition to westward extension of the cold tongue.

To provide a more quantitative idea as to the relationship between the composite difference and the SWS, we assessed a set of multiple linear regression models of the SWS according to indices derived from fields mentioned above. Our results give a clear indication that the anomalous rainfall over the northwestern Pacific in DJF during ENSO events is strongly related the SWS; such that, larger negative (positive) precipitation anomalies over that region during El Niño (La Niña) events is strongly related to a strong SWS. Further, we find that the meridional gradient of mean state SST in this season is also strongly related to the magnitude of the modeled SWS. We expect this linkage between mean state and the SWS is because the weaker gradients of SST facilitate shift in convection zones (Cai et al. 2014). The amplitude of SST and surface wind stress anomalies also provides additional information about the SWS during ENSO events, which is consistent with the theory that the SWS is due to the nonlinear interaction between ENSO and the annual cycle (Stuecker et al. 2013).

In our study it was also noted that the magnitude of the event, in terms of SST anomalies, is larger and the termination is more rapid in models with a SWS compared to models without a SWS for La Niña and strong El Niño, more evident for the latter. These findings are consistent with those reported by Abellán and McGregor (2016), where they pointed out that the inclusion of the SWS in their simple model results in larger La Niña events and shorter El Niño events. In association, models that successfully reproduce the SWS, peaks of La Niña and strong El Niño match observations much better than models that do not accurately produce the SWS. However, for moderate El Niño, no statistically significant differences are found in the magnitude, seasonal synchronization or termination across SWS/non-SWS models. When models are classified by their ability to capture the SWS for all ENSO types, it is revealed that the seasonal cycle of the standard deviation of ENSO (a proxy for the phase locking of events) in the models without a SWS shows maximum and minimum anomalies during the opposite season compared to models with a SWS, and observations (i.e., minimum in April–June and maximum in November–January). While those model with the SWS are much more accurate in the representation of the seasonal synchronization, they underestimate their magnitude.

To gain insight into this, SWS-driven WWV changes were calculated during the lead up to ENSO peaks and after the event peaks. It was shown that statistically significant linear correlations exist between the SWS induced WWV changes in August–October and the magnitude of the event in DJF, and between the SWS induced WWV changes in February–April and the decay of event SST anomalies. We also find that the models dramatically underestimate the magnitude of SWS induced WWV changes during moderate El Niño events, which may explain why the SWS does not appear to impact the evolution of moderate events.

Thus, these results emphasize the importance of simulating the SWS for two overarching reasons: (1) this is associated with a decrease in some well known biases in both mean state and ENSO-driven anomalous values; and (2) this yields a better performance in the synchronization to the seasonal cycle of ENSO events, particularly important for ENSO teleconnections (e.g., Webster et al. 1998). It is interesting to note that although the majority of models can produce a SWS, they largely underestimate the seasonal phase-locking of ENSO. Thus, we highlight that while the SWS is an interesting metric to examine, it is also the magnitude and zonal extent of the wind changes that accompany this SWS that drives the changes in WWV. Further to this, there are likely more processes involved in the spring termination of ENSO events than considered here, such as the seasonally changing cloud feedbacks (Dommenget and Yu 2016; Rashid and Hirst 2015).

Part 3

Distinctive role of ocean advection anomalies in the development of the extreme 2015–16 El Niño

---

The material in this Part is based around the work submitted as:

E. Abellán, S. McGregor, M. H. England and A. Santoso, 2017. Distinctive role of ocean advection anomalies in the development of the extreme 2015–16 El Niño. *Climate Dynamics*, under review.

Abstract

The recent 2015–16 El Niño was of comparable magnitude to the two previous record-breaking events in 1997–98 and 1982–83. To better understand how this event became an extreme El Niño, we examine the underlying processes leading up to the peak of the event in comparison to those occurring in the 1997–98 and 1982–83 events. Differences in zonal wind stress anomalies are found to be an important factor. In particular, the persistent location of the zonal wind stress anomalies north of the equator during the two years prior to the 2015–16 peak contrasts the more symmetric pattern and shorter duration observed during the other two events. By using linear equatorially trapped wave theory, we determine the effect of these off-equatorial westerly winds on the amplitude of the forced oceanic Rossby and Kelvin wave response. We find a stronger upwelling projection onto the asymmetric Rossby wave during the 2-yr period prior to the peak of the most recent event compared to the two previous events, which might explain the long-lasting onset. Here we also examine the ocean advective heat fluxes in the surface mixed layer throughout the event development phase. We demonstrate that, although zonal advection becomes the main contributor to the heat budget across the three events, meridional and vertical advective fluxes are significantly larger in the most recent event compared to those in 1997–98 and 1982–83. We further highlight the key role of advective processes during 2014 in enhancing the sea surface temperature anomalies, which led to the big El Niño in the following year.

3.1 Introduction

The El Niño-Southern Oscillation (ENSO) is the most dominant mode of interannual climate variability; characterized by warming (El Niño) or cooling (La Niña) of the tropical central and eastern Pacific sea surface, and associated large-scale changes in sea level pressure, winds and convection (e.g., Rasmusson and Arkin 1985). The three strongest El Niño events ever observed - the 1982–83, 1997–98 and most recent 2015–16 event - all exhibited exceptional warming across the central-eastern equatorial Pacific (e.g. L'Heureux et al. 2016) (Fig. 3.1). This warming pushed the edge of the western Pacific warm-pool eastward, and as a consequence atmospheric convection also shifted from the western equatorial Pacific to the usually cold and dry equatorial central-eastern Pacific (Cai et al. 2014). Although all ENSO events, regardless of strength, can affect climate over many regions of the world (e.g. Philander 1990), the strongest El Niño events have been associated with

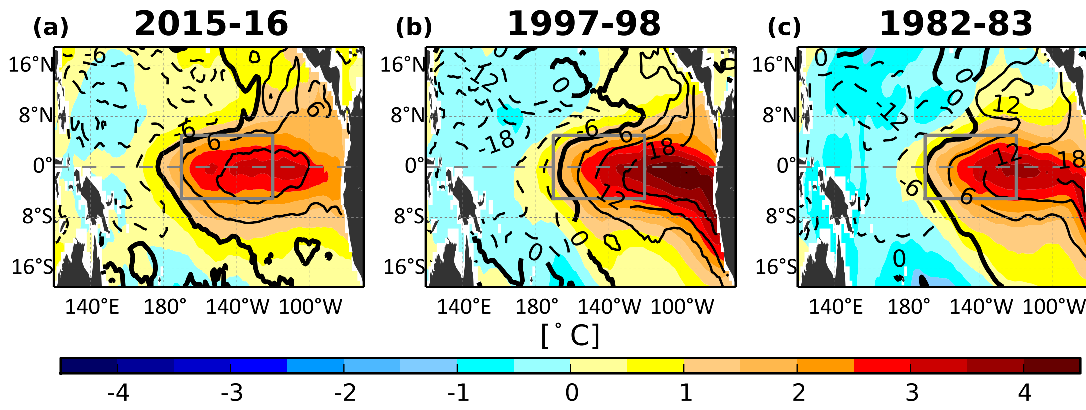

Figure 3.1: SST anomalies (shading) and SSH anomalies (contours) in NDJ during the 2015–16 (a), 1997–98 (b) and 1982–83 (c) El Niño events. Note that the contour interval is 6 cm, labels are in cm units and solid contours indicate positive values, bold line zero SSH anomaly, while dashed contours indicate negative values.The dashed gray line indicates the equator and the solid gray box represents the Niño-3.4 region. Datasets for SST: ERSST, HadISST, COBE, ERA-Interim. Datasets for SSH: GODAS, AVISO, PEODAS, ORA-S4.

the most significant natural disasters and socio-economic impact (Cai et al. 2014). Thus, it is of crucial importance to better understand the mechanisms controlling the evolution and intensity of these strong El Niño events.

It is well known that El Niño events are generally preceded by and coincide with anomalous westerly winds, which are considered a requirement to release the available energy stored in the anomalous warm water volume (WWV) (Kessler 2002; Philander and Fedorov 2003; Zavala-Garay et al. 2004; McGregor et al. 2016; Levine and McPhaden 2016). Westerly wind bursts (WWBs) preceding El Niño events have been shown to play an important role triggering El Niño events (Latif et al. 1988; Lengaigne et al. 2004), whereas the buildup of the WWV in the equatorial Pacific is considered a necessary precondition for the development of an El Niño (Wyrtki 1985; Meinen and McPhaden 2000; An and Kang 2001). The occurrence of strong WWBs in early 2014 (Menkes et al. 2014; Chen et al. 2015) led many seasonal forecast teams to warn of a possible El Niño event by the end of the year, while the coincident near record Pacific WWV anomalies in March led many experts to warn that the anticipated event may rival the catastrophic 1997–98 event (Ludescher et al. 2014; Tollefson 2014). However, the anticipated event never eventuated, as surface ocean warming ceased following the absence of westerly wind events from April to July 2014 (Menkes et al. 2014), signifying a lack of air-sea coupling (McPhaden 2015).

Recent studies by Hu and Fedorov (2016), and Levine and McPhaden (2016)

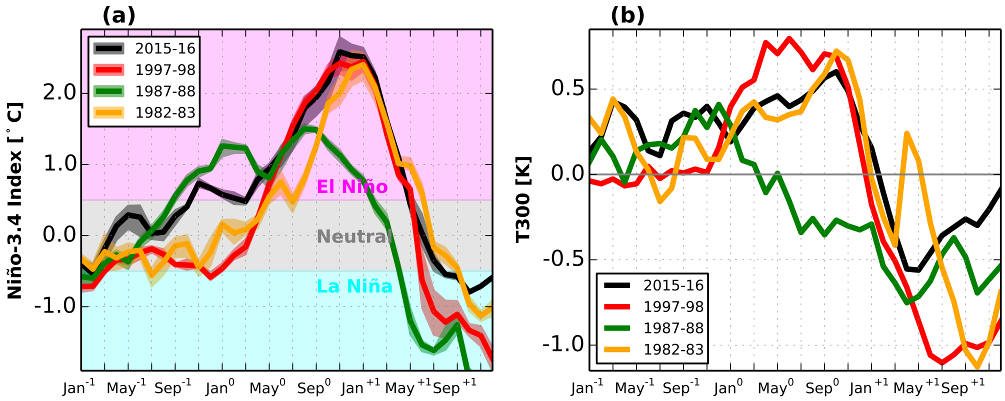

Figure 3.2: (a) Sea surface temperature anomalies in the Niño-3.4 region during the two years prior to the peak of strong El Niño event and one year afterward. Solid lines represent mean values of ERSST, HadISST, COBE and ERA-Interim whereas shaded areas represent the one standard deviation envelope of the observed SST. Note that shades in different colors have been used to indicate the three ENSO states. (b) Upper ocean heat content defined as depth averaged temperature in the upper 300 m (GODAS) over the region 5°S-5°N, 120°E-80°W, during the same period as (a).

have suggested that the easterly wind bursts that occurred in the boreal summer were responsible for halting the development of this event, with relatively dry atmospheric conditions despite higher than normal sea surface temperature (SST). Furthermore, after an initial Ekman induced discharge of WWV (McGregor et al. 2016), these easterlies would ultimately recharge equatorial heat content some months later (Jin 1997), priming the system for the 2015 El Niño (Levine and McPhaden 2016). Another recent study (Imada et al. 2016) suggested the subsurface cool anomalies in the South Pacific Ocean as one of the reasons for the failed materialization of an El Niño in 2014. Furthermore, after an initial Ekman induced discharge of WWV (McGregor et al. 2016), these easterlies would ultimately recharge equatorial heat content some months later(Jin 1997), priming the system for the 2015 El Niño (Levine and McPhaden 2016). During the first few months of 2015 a new episode of strong westerly wind bursts combined with an abundance of WWV, allowing El Niño conditions to rapidly re-intensify (McPhaden 2015) (Fig. 3.2).

The spatial patterns of SST anomalies around the peak of the strong El Niño events in 2015–16, 1997–98 and 1982–83 are comparable in magnitude along the central equatorial Pacific (Fig. 3.1 shading and Fig. 3.2) being 2.6±0.1, 2.4±0.1 and 2.3±0.2°C, respectively, in the Niño-3.4 region averaged during November-January (NDJ). Despite similar central Pacific event magnitudes, weaker warming off the west coast of South America is evident during 2015–16. Further, as pointed out by L'Heureux et al. (2016) and Xue and Kumar (2016), the 2015–16 SST anomalies in the western tropical Pacific were warmer. The evolution of SST anomalies (Fig. 3.2a) is clearly different across the three events, with values at the beginning of the El Niño years across the three events, being 0.58±0.04°C in January 2015, −0.46±0.05°C in January 1997 and 0.16±0.08°C in January 1982. Consistent with the weaker SST anomalies in the far eastern equatorial Pacific in the most recent event, the SSH anomalies also exhibit weaker values than the other two events.

The aim of this study is to investigate the physical mechanisms that controlled the development of the extreme El Niño event of 2015–16, and how they differed from the past two strongest El Niño events observed since the satellite era began in 1979. To this end, we first describe the datasets and analyses methods used in Sect. 3.2. In Sect. 3.3, we analyze zonal wind stress and sea surface height anomalies during the months prior to the peak of these strongest observed El Niño events. Based on both the results presented in Sect. 3.3 and the key role for ocean advection in generating ENSO SST anomalies along the equator in central and eastern equatorial Pacific (Wang and McPhaden 2000; Vialard et al. 2001), we examine the associated ocean advective fluxes during the events in Sect. 3.4. In Sect. 3.5 we compare the two-year warming phenomenon of 2014–2015–2016 with the 1986–1987–1988 event, which did not become a super El Niño. Finally, the main results are summarized and discussed in Sect. 3.6.

3.2 Datasets and methodology

3.2.1 Datasets

This study employs the National Centers for Environmental Prediction (NCEP) Global Ocean Data Assimilation System (GODAS; Behringer et al. (1998); Behringer and Xue (2004)), the European Centre for Medium-Range Weather Forecasts (ECMWF) Ocean Re-Analysis system 4 (ORA-S4; Balmaseda et al. (2013)) and the Predictive Ocean Atmosphere Model for Australia (POAMA) Ensemble Ocean Data Assimilation System (PEODAS; Yin et al. (2011)) to compute the advection terms in the heat budget equation in addition to the heating rate term. Multiple products were utilised here to validate the heat budget analysis, as suggested by Su et al. (2010), and provide a measure of the robustness of any results presented. The models have a horizontal resolution of $1\,^{\circ} \times 0.3\,^{\circ}$, $1\,^{\circ} \times 1\,^{\circ}$ and $2\,^{\circ} \times 0.5\,^{\circ}$, and vertical resolution of 10, 10, and 15 m, respectively. For all variables, anomalies are calculated by removing the long-term monthly climatology over the period 1980–2015. As there is no direct output of the vertical velocity field in ORA-S4, this variable is calculated from the horizontal currents by using the continuity equation.

The SST datasets used here are the Hadley Centre Sea Ice and Sea Surface Temperature dataset version 1 (HadISST1; Rayner et al. (2003)), the Extended Reconstructed Sea Surface Temperature version 3 (ERSSTv3; Smith et al. (2008)), the Centennial in situ Observation-Based Estimates of SST (COBE; Ishii et al. (2005)) and the Interim ECMWF Re-Analysis (ERA-Interim; Dee et al. (2011)). These reanalysis have a resolution of $1\,^\circ \times 1\,^\circ$, $2\,^\circ \times 2\,^\circ$, $1\,^\circ \times 1\,^\circ$ and $0.75\,^\circ \times 0.75\,^\circ$, respectively. Wind stress data are from the NCEP-National Center for Atmospheric Research (NCEP-NCAR) Reanalysis 1 (NCEP1; Kalnay et al. (1996)), PEODAS (Yin et al. 2011) and ERA-Interim (Dee et al. 2011) with resolutions of $2.5\,^\circ \times 2.5\,^\circ$, $2\,^\circ \times 0.5\,^\circ$ and $1.5\,^\circ \times 1.5\,^\circ$, respectively. We note here that the surface wind products selected for analysis are largely consistent with those used to force the ocean reanalysis data sets examined (GODAS and NCEP1, PEODAS with PEODAS and ORA-S4 with ERA-Interim). Surface wind stress data was only available for PEODAS dataset, which is made up of ERA-40 (Uppala et al. 2005) prior to 2002 and NCEP Reanalysis II (Kanamitsu et al. 2002) thereafter. For the other two datasets the surface winds were converted to wind stresses using the quadratic stress law (Wyrtki and Meyers 1976): $(\tau_x, \tau_y) = C_D \rho_a W(U, V)$ where U and V are the zonal and meridional surface winds (m s^{-1}) respectively; W denotes the surface wind speed (m s^{-1}), $C_D = 1.5 \times 10^{-3}$ is the dimensionless drag coefficient; and $\rho_a = 1.2$ kg m^{-3} represents the atmospheric density at the surface.

The SSH fields used in this study are from GODAS (Behringer et al. 1998; Behringer and Xue 2004), PEODAS (Yin et al. 2011), ORA-S4 (Balmaseda et al. 2013), whose resolutions are the same as for the heat budget variables, and the observed Archiving, Validation, and Interpretation of Satellite Oceanographic (AVISO), with $0.25\,^\circ \times 0.25\,^\circ$ of spatial resolution and daily temporal resolution. The global mean of the SSH products has been removed. As for the heat budget computation, the anomalous values of the rest of the variables are computed as the deviation of the 1980–2015 climatology.

Ideally, reanalysis with shorter timescales than a month might lead to resolve non-linear processes, such as vertical mixing or those arising from tropical instability waves. Hence, our heat content results must be viewed with this caveat in mind. However, we emphasize that in order to validate the heat budget analysis, as suggested by Su et al. (2010), multiple ocean assimilation data products have been used in this study.

3.2.2 Methodology

Kelvin-Rossby wave projections

To examine the effect of the westerly wind anomalies on the amplitude of the forced oceanic Rossby and Kelvin weave response, we use linear shallow water wave theory described in McGregor et al. (2016). The ocean model utilized here is a shallow-water model, which can produce observed variations of ocean heat content, sea surface heights (e.g., McGregor et al. 2012a,b) and Niño-3 and Niño-3.4 indexes (Abellán and McGregor 2016) reasonably well when the model is forced by wind stress anomalies.

It is shown that the Hermite functions provide the meridional structure of the oceanic Rossby and Kelvin wave response to the wind stress forcing (Clarke 2008). Thus, the amplitudes of these resulting Kelvin and Rossby waves are calculated by projecting the surface wind stress forcing onto the Hermite functions (Clarke 2008; McGregor et al. 2016). As the only eastward propagating waves available in this model are Kelvin waves, the Rossby wave mass transport at the western boundary must be balanced by the Kelvin wave mass transport (e.g., Kessler 1991).

Ocean heat advection analaysis

We consider the total mixed layer heat balance can be expressed as follows (e.g. Qiu 2000; Qu 2003; Du et al. 2005; Santoso et al. 2010; Cai et al. 2015):

$$\frac{\partial T}{\partial t} = \frac{Q_{net}}{\rho_o c_p h} - u\frac{\partial T}{\partial x} - v\frac{\partial T}{\partial y} - w\frac{\partial T}{\partial z} + Res \tag{3.1}$$

where T denotes the mixed layer temperature, which is a good proxy for SST, Q_{net} represents the net surface heat flux, ρ_a is the reference oceanic density (1026 kg m^{-3}), c_p is the specific heat capacity of seawater (3986 J kg^{-1} K^{-1}), h is the depth of the mixed layer, and $-\vec{u} \cdot \nabla T$ denotes the advective fluxes. The fifth term on the right-hand side of Eq. (3.1) Res indicates all remaining unresolved processes, including lateral diffusion, vertical mixing, and the shortwave radiation that escapes through the base of the mixed layer (Paulson and Simpson 1977; Santoso et al. 2010). This residual term also includes any unresolved processes that are not captured over the monthly time-scales of interest in this study, such as the impact of tropical instability waves. The focus of this work is instead on the monthly-evolving ocean advection terms in the heat budget equation (Eq. 3.1). For this reason, along with a lack of data for the surface air-sea heat flux term Q_{net} in some of the ocean reanalysis products used, we will focus in this study on the advective terms only. Previous studies have demonstrated the damping effect of the two terms Q_{net} and Res (e.g. (Wang and McPhaden 1999, 2001; Huang et al. 2010; Su et al. 2010). The mixed layer depth is assumed to be constant in our study and is taken to be 50 m as in several past studies (e.g. An and Jin 2004; Thual et al. 2011; Imada and Kimoto 2012; Hua and Yu 2015). This is motivated by the Cane and Zebiak model for ENSO (Zebiak and Cane 1987), which has been shown to give a reasonable representation of the mixed layer depth in the central Pacific (de Boyer Montégut et al. 2004; Lorbacher et al. 2006). Both horizontal and vertical potential-temperature gradients are estimated from first-order finite difference scheme.

The total oceanic advection of heat can be decomposed as:

$$\vec{u} \cdot \nabla T = \bar{u}T'_x + u'\bar{T}_x + u'T'_x + \bar{v}T'_y + v'\bar{T}_y + v'T'_y + \bar{w}T'_z + w'\bar{T}_z + w'T'_z \tag{3.2}$$

where u, v, w represent the zonal, meridional and vertical ocean current velocities, overbar denotes the monthly mean climatology, prime denotes the anomaly (relative to the monthly climatology) and the subscript denotes the partial derivative in that particular direction.

The use of multiple reanalysis products allows statistical significance to be evaluated in differentiating the processes between events. In order to achieve this, we use a *Student* t-test, in which the significance is determined at the 95% confidence level.

3.3 Evolution of zonal wind stress and sea surface height anomalies

3.3.1 Zonal wind stress anomalies

The anomalous westerly winds that precede El Niño events, as mentioned before, can be made up of higher frequency (intra-seasonal) bursts and a lower frequency and large-scale Bjerkness feedback component, a combination of which can be seen in the monthly latitude-time sections of the zonal wind stress (Fig. 3.3). Here, the 2015–16 event anomalous winds appear to be distinct from the earlier events in several other ways. As reported by L'Heureux et al. (2016), the 2015–16 event equatorial winds were weaker than those of the 1997–98 event. For instance, the zonal wind averaged between 5°S-5°N during the 12 months prior to the peak of the events are 0.68±0.24

and 1.23±0.02 × 10^{-2} N m^{-2}, respectively. Secondly, the wind anomalies in the 2015–16 event display much more asymmetry about the equator than the other two events, with the 2015–16 event primarily displaying westerly (easterly) anomalies north (south) of the equator. This characteristic can be also seen by the average values during the 12-month and 24-month periods in Fig. 3.4, where the maximum anomalies occur at 5°N in the 2015–16 event and only easterlies are found in the Southern Hemisphere, in contrast to the other two events in which westerlies are found in both hemispheres. To better illustrate these results, we consider an asymmetry index defined as the zonal wind in the Northern Hemisphere (0°-20°N) minus the Southern Hemisphere (20°S-0°) averaged over both, the 12-month and 24-month periods prior to the event peak. These indices, averaged across the 3 products and shown in Table 3.1, highlight the strong meridional asymmetry of the 2015–16 event (three times larger than that in the 1997–98 event), which is statistically significant. It should be noted that the main difference is in the Southern Hemisphere (Table 3.1), with easterly anomalous wind in the 2015–16 event and westerly (as in the Northern Hemisphere) in the other two events. This persistent maximum westerly wind anomaly location north of the equator is at least partly associated with highly unusual cyclone activity in the western Pacific (Boucharel et al. 2016a,b; Collins et al. 2015). This unusual cyclone activity has also been related to the substantially warmer SST anomalies over the north tropical Pacific (5°N-20°N) observed over the 2-yr period in the 2015–16 event (0.42±0.05°C) relative to 1997–98 (0.07±0.02°C) and 1982–83 (−0.06±0.03°C) (Fig. 3.5) (Murakami et al. 2017).

Another prominent feature revealed by Fig. 3.3 is that for the 2015–16 event, anomalous westerly winds persisted as far back as the beginning of 2014. This is distinct from the 1997–98 and 1982–83 events, which had the largest anomalous westerly winds only beginning some 12 months prior to the peak of the events. This difference in wind persistence could indicate the role of the 2014–15 “failed event” in contributing to the emergence of the 2015–16 El Niño. As such, our analysis below in distinguishing the dynamics of these events will consider the genesis of the events over both the 12 and 24-month periods prior to the peak of the events, indicating the monthly temporal evolution and the average over these two periods. Furthermore, the warming conditions over the central equatorial Pacific in early 2015 (Fig. 3.2a) suggest that the previous year should be taken into account as a possible explanation of the large event.

To further understand the ocean response to the relaxation of the easterly trade winds during the onset of El Niño events, we calculate the projection coefficients averaged over the whole basin for the eastward propagating equatorial Kelvin wave and the first six westward propagating equatorially trapped Rossby waves following

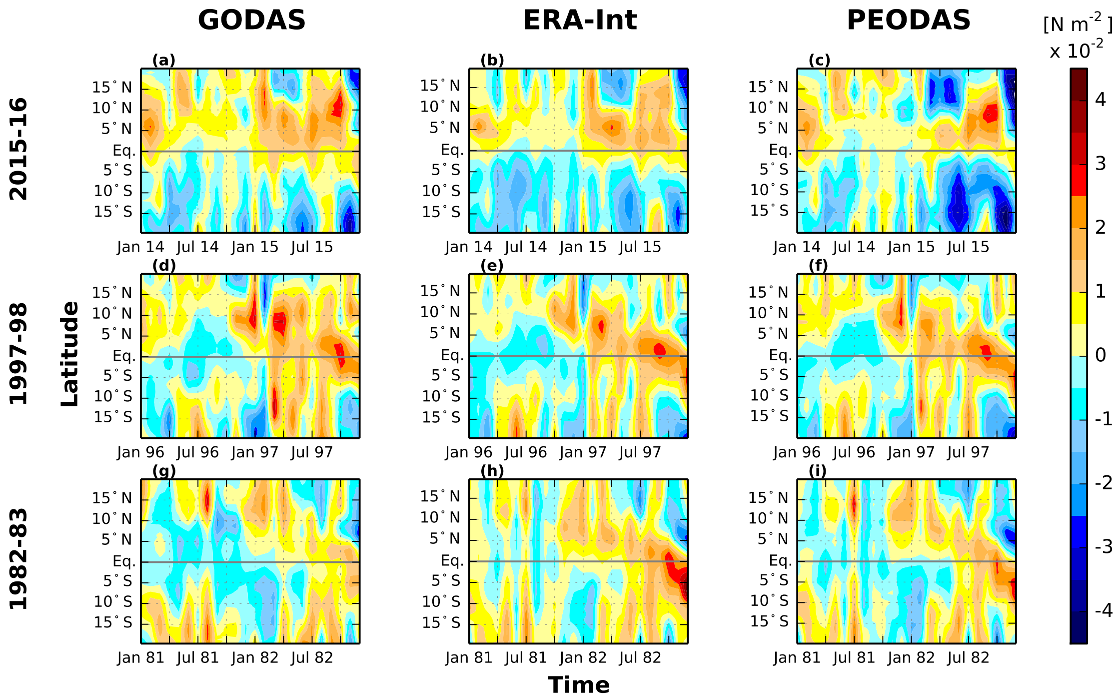

Figure 3.3: Zonal wind stress anomalies averaged over 120°E-80°W during the 2-yr period prior to the peak of the (a-c) 2015–16, (d-f) 1997–98, and (g-i) 1982–83 events. Note that gray horizontal lines indicate the equator. Datasets: GODAS, ERA-Interim and PEODAS.

Table 3.1: Basin-wide average zonal wind anomalies and their standard deviations in the Northern Hemisphere (Eq.-20°N) and the Southern Hemisphere (20°S-Eq.) and the asymmetry index defined in section 3.1 averaged over 12-month and 24-month periods prior to the event peaks. Units are expressed in $\times\ 10^{-2}$ N m^{-2}. Datasets: GODAS, ERA-Interim and PEODAS.

	-12 months			**-24 months**		
	2015–16	**1997–98**	**1982–83**	**2015–16**	**1997–98**	**1982–83**
Northern Hemisphere	0.35±0.36	0.64±0.19	0.29±0.08	0.39±0.19	0.46±0.09	0.17±0.08
Southern Hemisphere	-0.53±0.36	0.45±0.04	0.44±0.19	-0.49±0.16	0.16±0.02	0.30±0.13
Asymmetry index	0.85±0.03	0.17±0.17	-0.16±0.15	0.86±0.04	0.29±0.07	-0.13±0.05

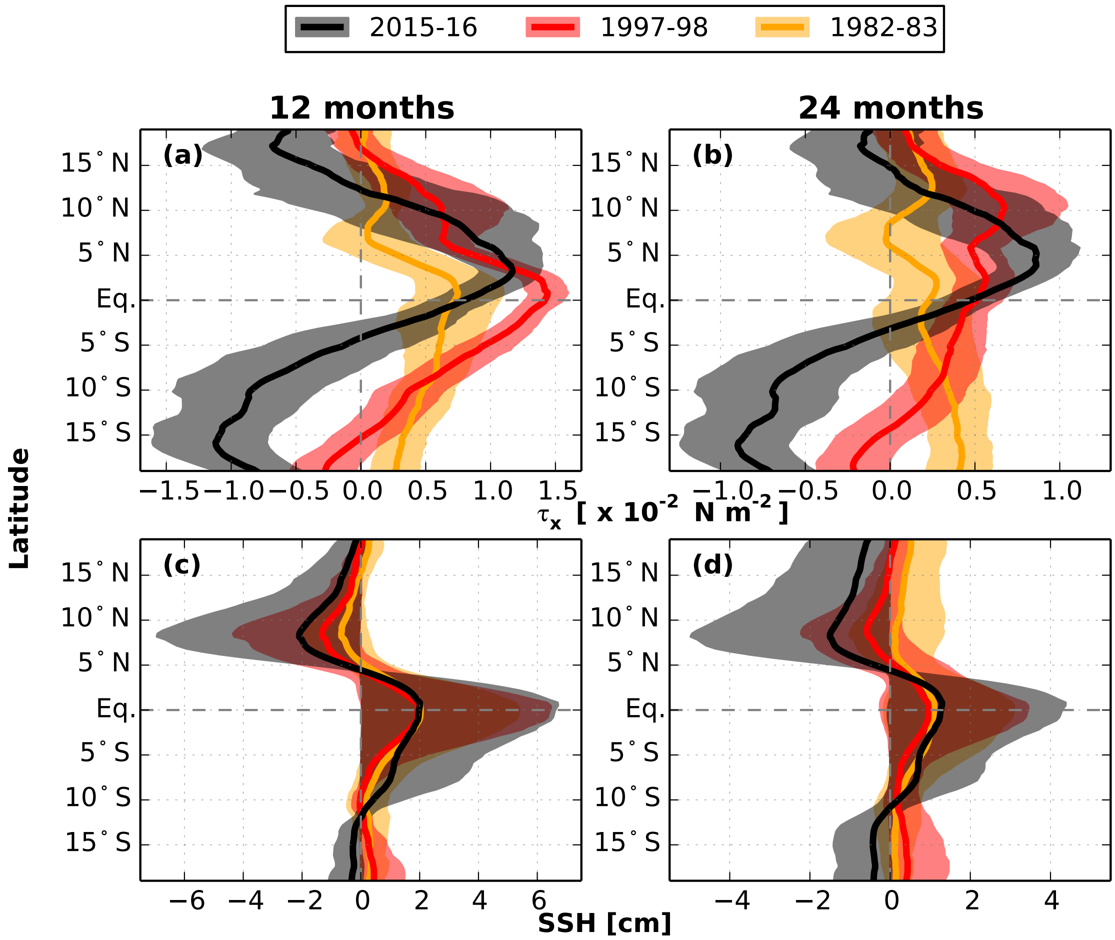

Figure 3.4: Zonal wind stress (a,b) and sea surface height (c,d) anomalies averaged over 120°E-80°W and during two periods (12 and 24 months prior to the peak of the events). Solid lines represent the mean values across the datasets: GODAS, PEODAS and ERA-Interim for τ_x; and GODAS, AVISO, PEODAS and ORA-S4 for SSH. The shaded areas show the 5th and 95th percentiles for every monthly value across all products.

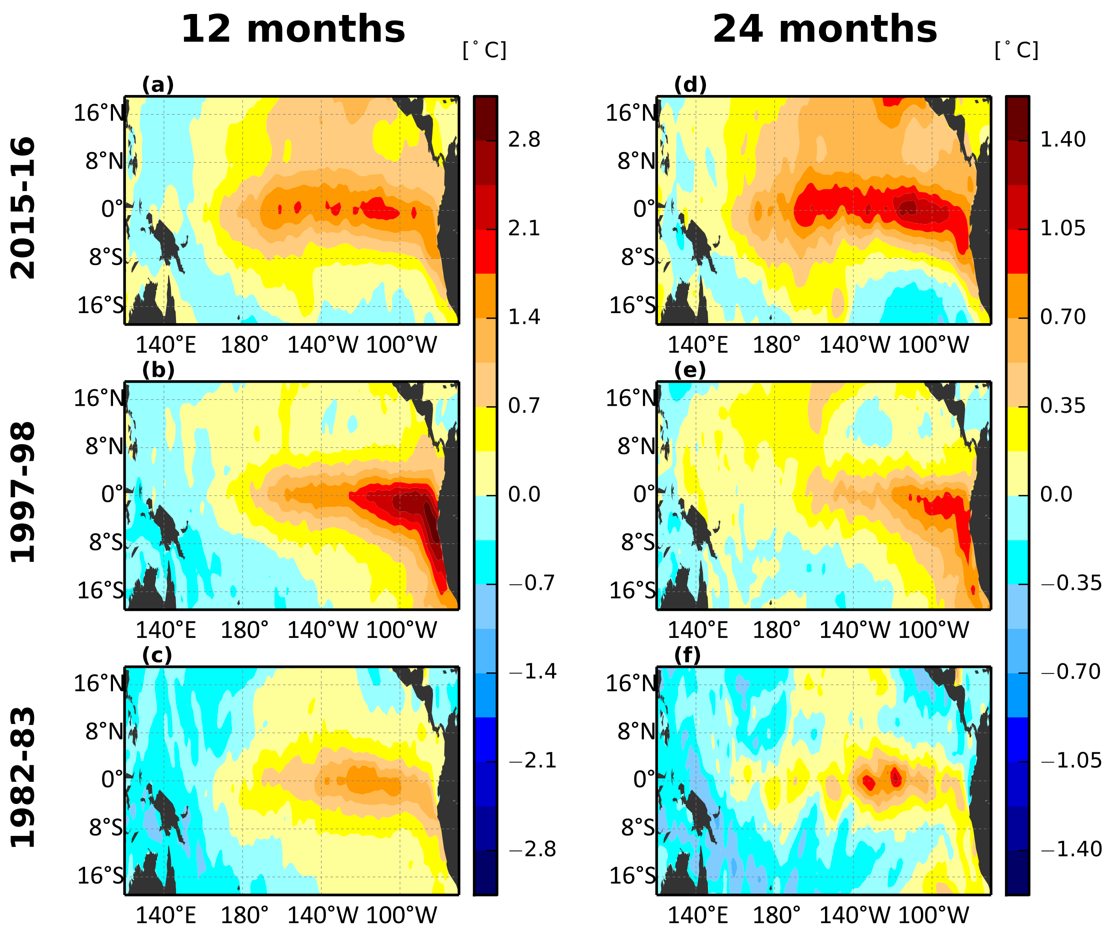

Figure 3.5: SST anomalies averaged over the 12-month (a-c) and 24-month (d-f) periods prior to the peak of the 2015–16 El Niño (a, d), 1997–98 El Niño (b, e), and 1982–83 El Niño (c, f) events. Data obtained from HadISST.

Table 3.2: Projections coefficient values of Kelvin and Rossby waves (see Fig. 3.6) averaged over 12- and 24-month periods prior to the even peaks and their standard deviations. Units are expressed in m. Dataset: GODAS, ERA-Interim and PEODAS.

		-12 months			**-24 months**		
		2015–16	**1997–98**	**1982–83**	**2015–16**	**1997–98**	**1982–83**
Kelvin wave		2.6±4.1	14.4±1.7	12.0±1.9	1.4±2.1	7.7±0.6	5.2±1.5
Rossby waves	N = 1	-14.5±3.1	-14.6±1.1	-2.7±5.5	-8.9±1.2	-1.8±1.6	2.2±3.1
	N = 2	-14.4±2.8	-7.1±1.4	-8.9±0.4	-9.4±2.3	-3.3±0.4	-6.2±0.5
	N = 3	-10.8±1.7	-7.4±1.8	-0.9±5.9	-6.6±2.0	-2.3±1.8	2.4±4.5
	N = 4	-13.8±2.7	-0.2±1.5	-3.6±4.1	-11.4±1.3	-1.1±1.3	-1.0±2.1
	N = 5	-4.6±2.4	-5.1±1.9	3.8±7.0	-2.6±1.7	-2.4±2.0	5.5±5.0
	N = 6	-4.7±2.5	-1.5±2.4	-1.7±4.9	-4.2±1.1	-1.9±1.6	0.4±3.1

the methodology detailed in McGregor et al. (2016). As defined by the Hermite functions solutions to the shallow-water model equations, Rossby waves with odd (even) numbers produce thermocline anomalies that are symmetric (asymmetric) structure about the equator (Kessler 1991; Fedorov and Brown 2009). The mode number also highlights several other key features of the Rossby waves, i) the higher the mode number, the slower and further away from the equator the main thermocline depth perturbation propagates; ii) even number Rossby waves do not generate an equatorial Kelvin wave upon impinging on the western boundary, and iii) the magnitude of the reflected Kelvin wave decreases as the odd order mode number increases (Kessler 1991). The excitation of strong downwelling Kelvin waves observed in May and July 1997 and August, October and December 1982 (Fig. 3.6a), as a result of strong westerly wind anomalies (e.g., McPhaden 1999), contribute to the exceptional strength of El Niño events in 1997–98 and 1982–83, respectively. However, the 2015–16 El Niño event exhibits a series of much weaker Kelvin waves and only one Kelvin wave in August 2015 whose magnitude is comparable to those of the preceding events. The first baroclinic mode n = 1 Rossby wave for the 2015–16 event also displays significantly weaker magnitudes during most of the 24-month period (Fig. 3.6b). Further to this, the 2015–16 event produces an upwelling projection occurring earlier than the other two events, which may impact the Kelvin wave projection since these waves would be reflected as upwelling Rossby waves, which would act to offset the downwelling Kelvin wave response. Interestingly, the downwelling Kelvin wave in April 2014 (Fig. 3.6a), had almost no upwelling n = 1 Rossby wave signal (Fig. 3.6b) and strong upwelling projection onto the n = 2 Rossby wave (Fig. 3.6c) (i.e, with no western boundary reflection), which might explain why the warming that started in 2014 was able to continue into 2015. Finally, the significantly stronger projection through much of the two years onto the asymmetric n = 4 Rossby wave in addition to the smaller Kelvin wave projection in the 2015–16 El Niño compared to the previous events (Table 3.2) are consistent with the asymmetric location of the westerly winds described above.

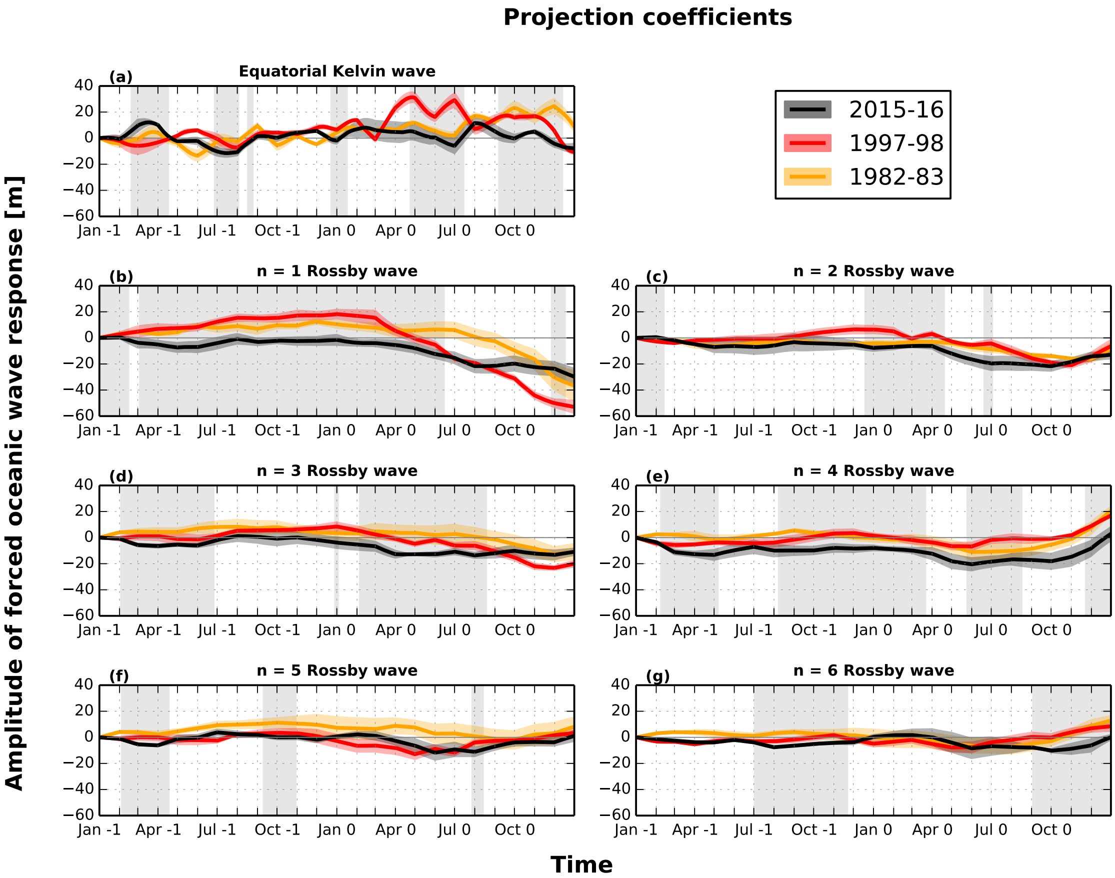

Figure 3.6: The time evolution of the forced basinwide projection coefficients for the equatorial Kelvin wave (a) and the first six Rossby waves (b-g). Note that thick lines represent the mean values averaged across the 3 reanalysis products (GODAS, PEODAS, ERA-Interim) and shading indicates one standard deviation. The gray shading indicates that the 2015–16 El Niño amplitudes are significantly different to the other two events. The amplitudes are taken positive (negative) for downwelling (upwelling) waves.

Table 3.3: Basin-wide average SSH anomalies in the north-off equatorial region (5°N-15°N) and the equatorial region (5°S-5°N) over 12-month and 24-month periods prior to the event peaks and their standard deviations. Units are expressed in cm. Dataset: GODAS, PEODAS, ORA-S4 and AVISO.

	-12 months			**-24 months**		
	2015–16	**1997–98**	**1982–83**	**2015–16**	**1997–98**	**1982–83**
North-off Equator	-4.95±0.54	-4.58±0.98	-1.66±0.31	-3.78±0.46	-2.63±0.96	0.15±0.33
Equator	4.67±1.29	5.63±0.51	4.28±0.67	3.28±0.88	2.77±0.09	2.41±0.48

3.3.2 Sea surface height anomalies

The basin-wide average SSH anomalies (Fig. 3.7) exhibit significantly (above the 95 % level) larger negative values along the north off-equatorial region (5-15°N) throughout the 2-yr period in the 2015–16 event compared to the 1997–98 and 1982–83 events (Table 3.3). This negative sea level pattern north of the equator is consistent with Ekman velocity anomalies (Fig. 3.8), given by the curl of the surface stress (Harrison 1989; Enriques and Friehe 1995):

$$w_E = \frac{1}{\rho f}\vec{k} \cdot (\nabla \times \tau) \tag{3.3}$$

where f is the Coriolis parameter, ρ is the seawater density, and k is the vertical unit vector. For instance, the Ekman suction in this region was significantly larger in the 2015–16 event averaged during the 2-yr period (2.6±0.9 cm day^{-1}) than that seen in 1997–98 (0.6±0.4 cm day^{-1}), occurring Ekman pumping in the 1982–83 (-0.2±0.1 cm day^{-1}).

The strong basin-wide average SSH anomalies along the north off-equatorial region (Fig. 3.4c-d) are also consistent with the basinwide projection onto Rossby waves, as the 2015–16 event displays a significantly stronger negative projection onto the asymmetric n = 4 Rossby waves observed over the entire two year period (Fig. 3.6e and Table 3.2).

Another striking feature of the basin-wide average SSH anomalies in the equatorial region is that the 2015–16 El Niño displays positive values between 5°S-5°N that persist throughout the whole 24-month period prior to the event peak. Although no statistically significant difference is found between the 24-month average of the 2015–16 El Niño and the other two events (Table 3.3), the earlier events exhibit positive anomalies largely during the 12-month period only that are more symmetrically distributed about the equator (Fig. 3.7). Again, the apparent 2-yr persistence of the equatorial positive SSH signal in the 2015–16 event and the larger upwelling in the northern region mentioned above point to the different dynamics from the past events.

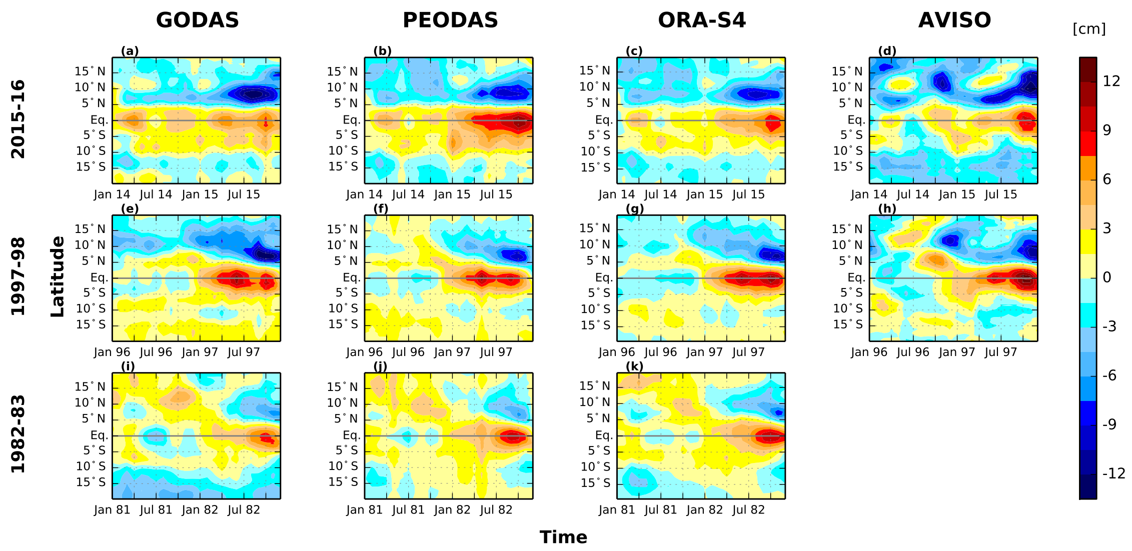

Figure 3.7: Sea surface height anomalies averaged over 120°E-80°W during the 2-yr period prior to the peak of the (a-d) 2015–16, (e-h) 1997–98, and (i-k) 1982–83 events. Note that gray horizontal lines indicate the equator. Data are obtained from reanalysis (GODAS, PEODAS and ORA-S4) and observations (AVISO).

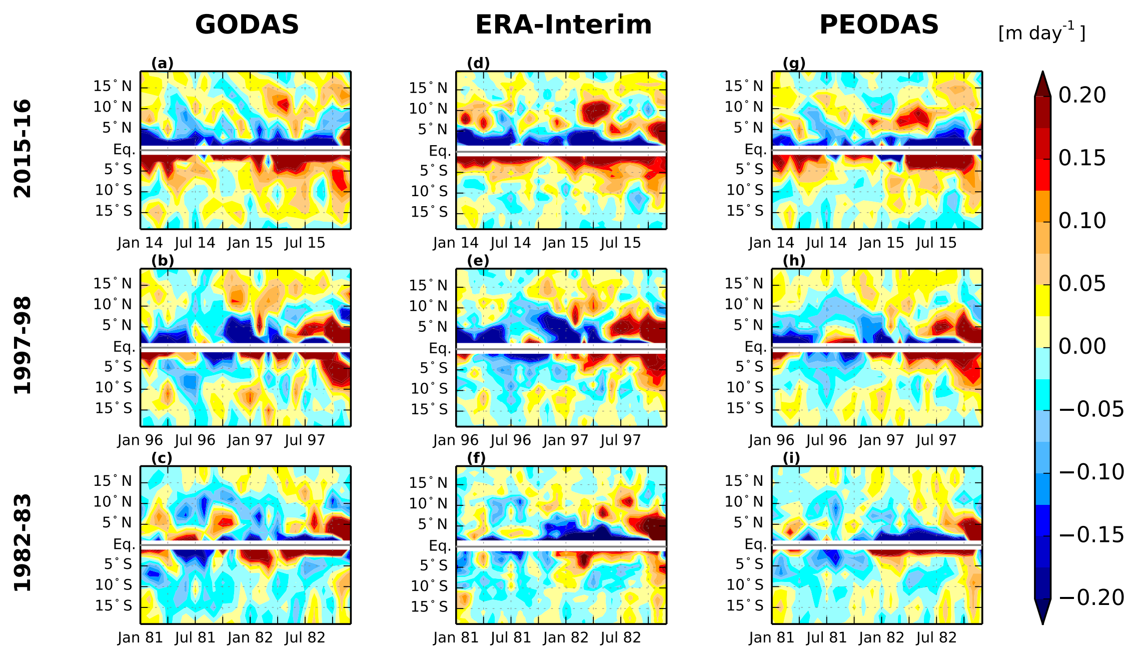

Figure 3.8: Ekman vertical velocity anomalies (in m day^{-1}) computed from wind stress over 120°E-80°W during the 2-yr period prior to the peak of the (a-c) 2015–16, (d-f) 1997–98, and (g-i) 1982–83 events. Note that positive velocities indicate upwelling and Ekman suction whereas negative values indicate downwelling and Ekman pumping. Datasets: GODAS, ERA-Interim and PEODAS.

3.4 Ocean advective heat fluxes

Previous studies (Wang and McPhaden 2000, 2001; Vialard et al. 2001; Huang et al. 2010) have shown the influence of ocean advection during the onset of El Niño events. To further reveal the distinction among the events arising from the processes described in Sect. 3.3, we expect to see some differences in the advective constituents shown in Eq. (3.2) that lead to the growth of SST anomalies over the Niño-3.4 region (170°W – 120°W and 5°S – 5°N) - a region which is used for ENSO operational forecast. We first examine the impact of both persistence and meridional asymmetry of westerly wind anomalies on the horizontal ocean currents anomalies (u' and v'). Figure 3.9 shows the time series of anomalous zonal and meridional ocean currents during the two years prior to the peak of the events averaged over the Niño-3.4 region. The zonal component of the 2015–16 El Niño event displays two clear eastward propagation periods in early 2014 and late 2014 as a consequence of westerly wind anomalies (Fig. 3.3a-c). These anomalous winds generate a zonal pressure gradient between the eastern and western tropical Pacific, which generates a meridional SSH gradient, being positive (negative) south (north) of the equator (Fig. 3.7), producing this eastward geostrophic current anomaly. The meridional asymmetry in the anomalous zonal winds seen in the 2015–16 El Niño event leads to a south-flowing ocean flow during the whole period prior to the event peak (Fig. 3.9b). This is a discernible difference compared to the 1997–98 and 1982–83 El Niño events, in which the meridional ocean current is near climatological values in 1996 and 1981, respectively.

We now explore how these dramatic differences of ocean currents between the most recent El Niño and the other two events described above influence the magnitude of the events. Monthly anomalies of each individual advection term of the heat budget equation (Eq. 3.2) during the 24-month period prior to the peak of the events over the Niño-3.4 region are shown in Fig. 3.10. As expected from the time series of Niño-3.4 index (Fig. 3.2a), the warming tendency in the 1997–98 and 1982–83 El Niño events occurs mainly during the 12 months before the maximum amplitude of the events (Fig. 3.10a). While the major heating during the 2015–16 El Niño event also occurs during this period, it is interesting to note two periods of warming tendency in 2014, consistent with the 2014–15 failed event. There is a marked similarity between this total heating time evolution (Fig. 3.10a) and the zonal advection of climatological temperature by anomalous current ($u'\bar{T}_x$, Fig. 3.10c), suggesting the important role of this term in El Niño development (Huang et al. 2010).

Here we aim to identify the dominant processes controlling the trajectory to-

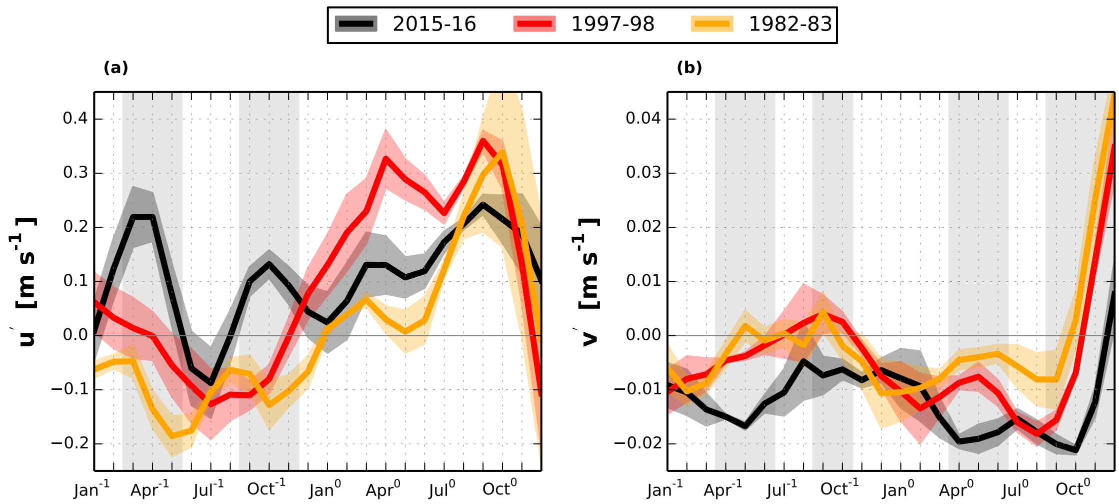

Figure 3.9: Time series of zonal (a) and meridional (b) ocean currents averaged over the Niño-3.4 region and integrated vertically over the mixed layer. The gray shading indicates that the 2015–16 El Niño values are significantly different to the other two events. Datasets: GODAS, PEODAS, ORA-S4.

ward anomalous warming by integrating the advection terms over 24 and 12 months (i.e., expressed in degree Celsius) leading up to the peak of each event, respectively referred to "year -1" and "year 0". This approach allows a gauge of the relevance of the 2014 conditions for the development of the 2015–16 El Niño.

Figure 3.11 shows that the advective terms overall contribution to the total heating rate during all three strong El Niño events. Note that Q_{net} and the Res terms not shown constitute cooling rates, as mentioned before. Integrated over both 12 months and 24 months, the anomalous heating of all events is most strongly attributed to $u'\bar{T}_x$, followed by $\bar{v}T'_y$ and to a lesser extent by $\bar{w}T'_z$ (terms 3, 5, and 8). These terms respectively refer to the zonal advection of climatological temperature by anomalous currents, the meridional advection of anomalous temperature by mean currents, and the vertical advection of anomalous temperature by mean upwelling. However, we note that, for the 1982–83 event, the heating contribution of $u'\bar{T}_x$ becomes small when integrated over the 24-month period, even displaying a weak damping effect in the GODAS reanalysis (Fig. 3.11d). This is mainly due to the fact that this term tended to cool SST during 1981 (Fig. 3.10c).

The total heating rate ($\partial T/\partial t$) integrated over 12 months prior to the peak of the 2015–16 event (2.0±0.1°C) is significantly weaker than that for the 1997–98 and 1982–83 events (3.0±0.4°C) (Fig. 3.11a). However, when integrated over 2 years, the heating rate for the 2015–16 event increases and becomes more comparable to the other two events in which the 1997–98 event shows a slight increase and the 1982–83 event a decrease (Fig. 3.11b). As demonstrated below, this reflects the

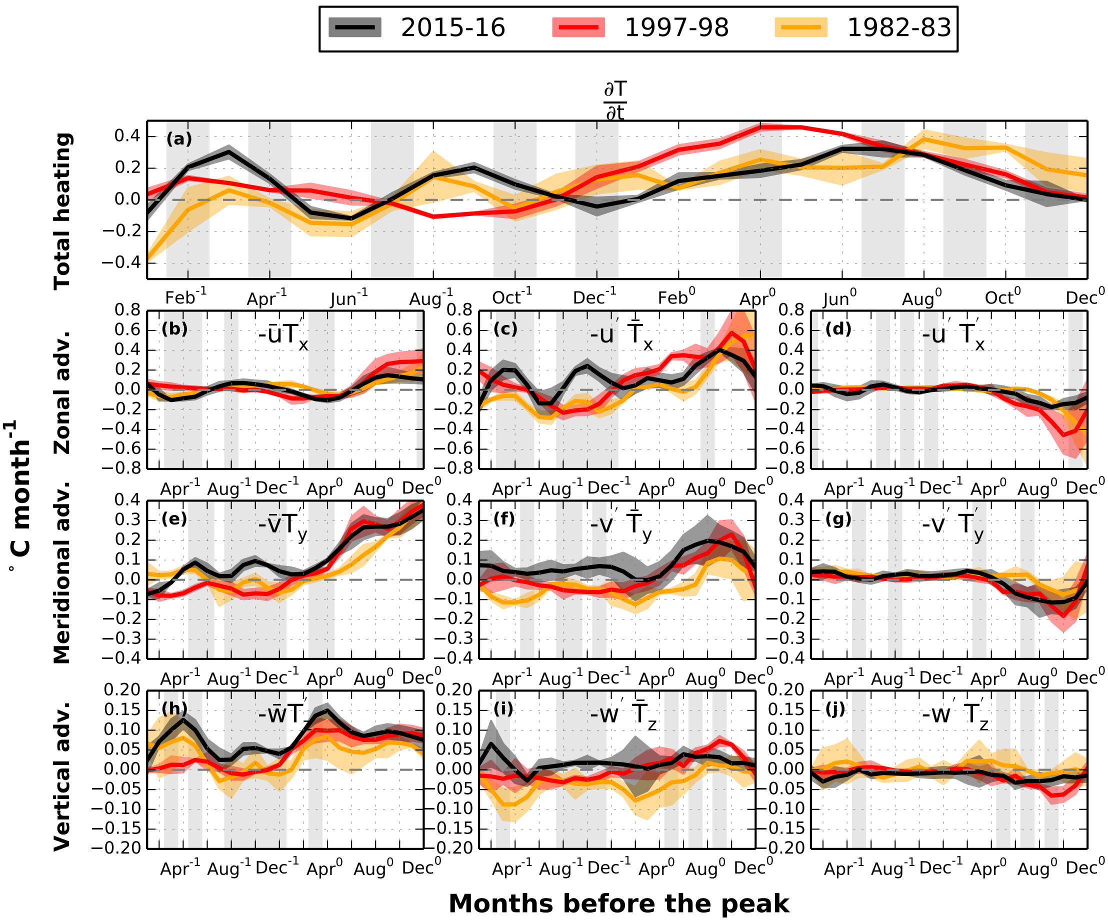

Figure 3.10: The time evolution of temperature budget anomalies of the strong El Niño events in the Niño-3.4 region for the total heating (a), zonal (b-d), meridional (e-g), and vertical (h-j) advection terms of the heat budget equation. A three-month running average is calculated. The events are averaged across the three datasets (GODAS, PEODAS and ORA-S4) and shown their standard deviation (shading). The gray shading indicates that the 2015–16 El Niño values are significantly different to the other two events. Different y-axis heating scales are employed in each direction of advective terms.

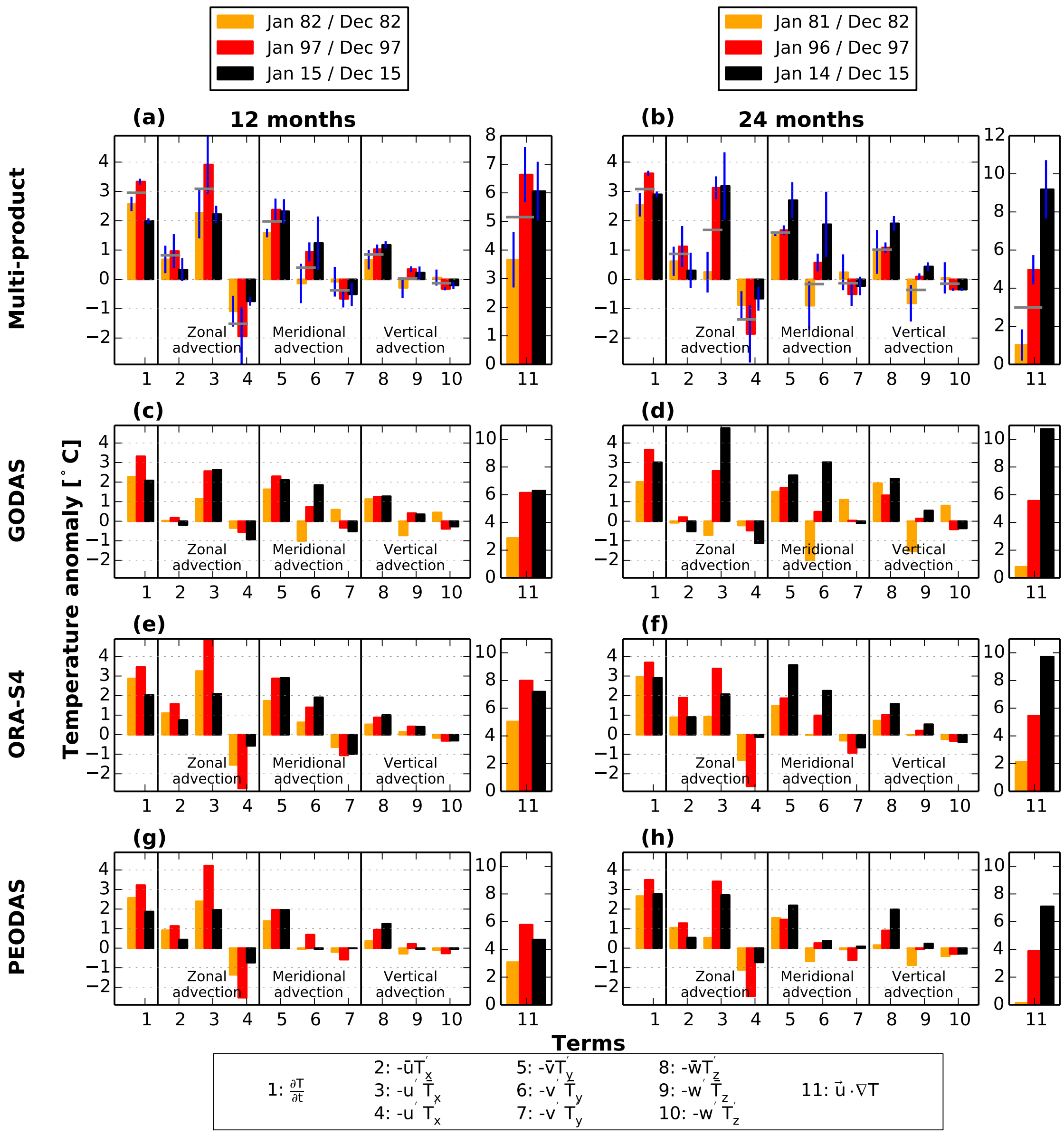

Figure 3.11: Contribution of each individual advection term of the heat budget equation and the total advective term integrated over (left column) 12 and (right column) 24 months before the peak, and averaged over the Niño-3.4 region, for all datasets (a, b), GODAS (c, d), ORA-S4 (e, f) and PEODAS (g, h). Orange, red and black shaded vertical bars represent the 1982–83, the 1997–98, and the 2015–16 El Niño events, respectively. The gray horizontal bars in panels (a) and (b) indicate the composite mean for each term across the 1982–83 and 1997–98 events, and the error bars represent the standard deviation across the three datasets for each event.

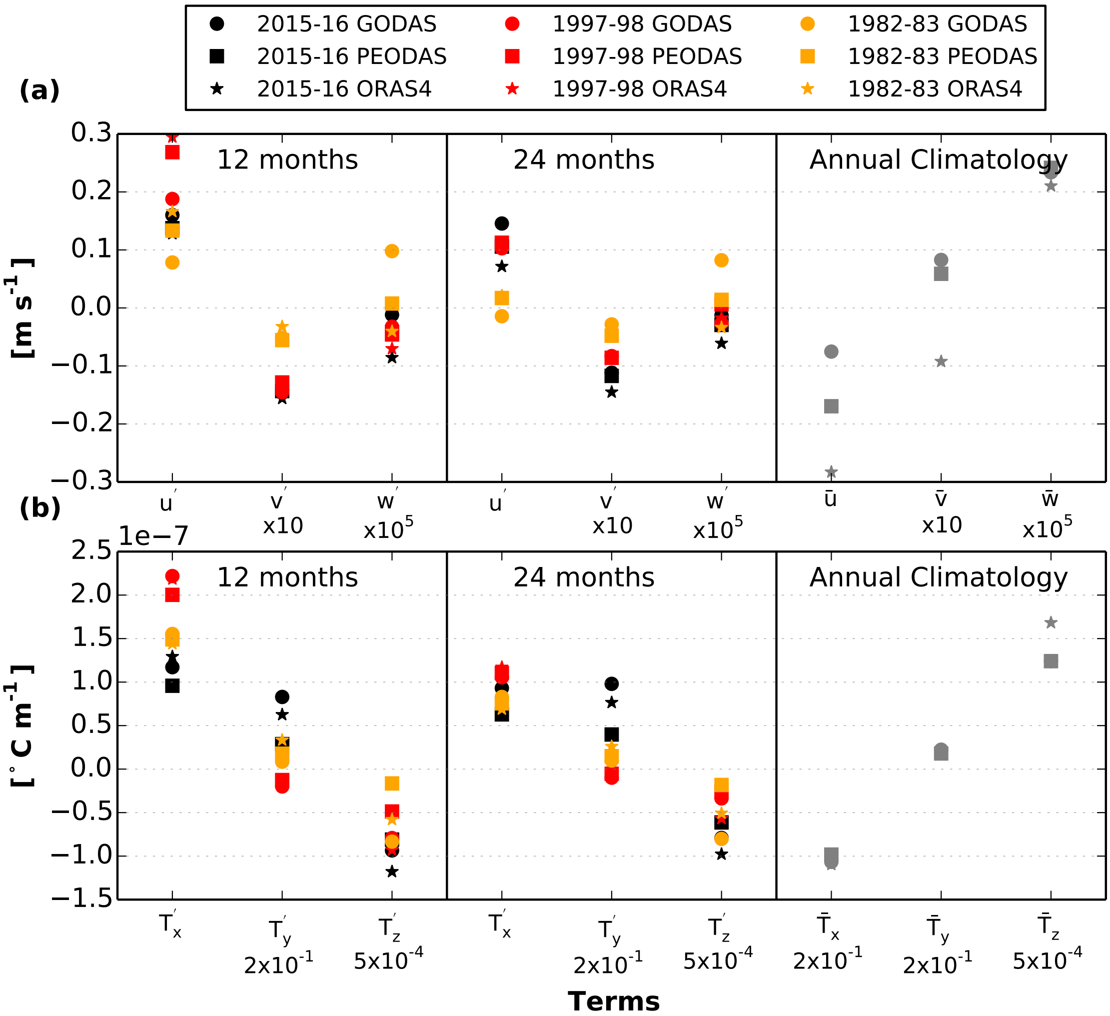

Figure 3.12: Averaged values of ocean currents (a) and temperature gradients (b) over the Niño-3.4 region during the 12-month and 24-month periods and annual mean climatology for each reanalysis product and each event. Note the different scale used for some terms.

importance of the 2014 ocean advection for the large magnitude of the 2015–16 El Niño. Focusing on the individual advection terms, there are no significant differences in the 12-month analysis between the 2015–16 event and past events, except for $u'\bar{T}_x$ when comparing the recent event to the 1997–98 event only. However, significant differences are found over the 24-month period in the $\bar{v}T_y'$, $v'\bar{T}_y$ and $\bar{w}T_z'$ terms, when comparing the 2015–16 event with the average of 1982–83 and 1997–98 events. The larger magnitude of $\bar{v}T_y'$, $v'\bar{T}_y$ and $\bar{w}T_z'$ indicate that these terms played a more prominent role in the growth of the 2015 El Niño with a notable contribution from the previous year. In particular, the sum of all advective terms contributes to much larger warming in the 2015–16 event (9.2±1.5°C) compared to the other two events (3.0±2.1°C).

It is worth emphasizing the large spread across the datasets in some terms of the heat budget analysis carried out in this study. For instance, the heating contribution of the main term ($u'\bar{T}_x$) varies between 2.1 °C in ORA-S4 and 4.8 °C in GODAS when integrated for the 24-month period in the 2015–16 event (Fig. 3.11d, f). Such a large spread is represented as a long error bar in Fig. 3.11b. To further examine the source of this big uncertainty, we decompose the advective terms into the single terms (i.e., velocities and gradients of temperature) for the two periods considered and annual mean climatological values (Fig. 3.12). The anomalous zonal current (u') for the 24-month period range between 0.07 and 0.15 m s^{-1} across the reanalysis products, being the minimum value around 50% less than the maximum value. However, the zonal climatological gradient of temperature ($\bar{T}_x$) for the same period is in the range -5.33×10^{-7} to -4.91×10^{-7} °C m^{-1}, which in this case is approximately 10% of difference between these two extreme values. We note that although the temperature gradients display uncertainties, they appear to be less important than the anomalous and climatological currents. In particular, the vertical velocity field exhibits the largest spread, with different sign for the 1982–83 event in both periods considered. It is noteworthy that in spite of the large spread across the three reanalysis products, the heat budget analyses derived from each product exhibit similar behaviour for the $\bar{v}T'_y$, $v'\bar{T}_y$ and $\bar{w}T'_z$ terms (Fig. 3.11c-h).

To further reveal the relative role of $\bar{v}T'_y$, $v'\bar{T}_y$ and $\bar{w}T'_z$ terms in the temporal evolution of the 2015–16 El Niño event (Fig. 3.2a), we now examine the temperature anomaly in the Niño-3.4 region integrated over the mixed layer that would occur if only the total advective terms were considered. This is done by integrating the variables forward in time starting from either January of year 0 (Fig. 3.13a) or January of year -1 (Fig. 3.13b), taking into account that the anomalous terms referred to the 2015–16 event (three members, one for each dataset) are computed as deviations from the 1997–98 and 1982–83 composite (six members). Comparing the anomalous three terms whose mean differences between the 2015–16 event and the other two events are significant ($\bar{v}T'_y$, $v'\bar{T}_y$ and $\bar{w}T'_z$), we find a positive contribution throughout the entire 2-yr period. However, $u'\bar{T}_x$ (orange line), which is a major heating term, particularly for the 2015–16 and 1997–98 events, leads to warming during year -1 and cooling during year 0. The cooling effect of this anomalous term is more evident when the integration starts instead in year 0 of the event (i.e. only the 12-month lead-in window), showing smaller values than what occurs for the 1997–98 and 1982–83 average. The anomalous all advective terms combined (red line) exhibit the major heating during year -1 whereas the increase in temperature is more gradual during year 0. Hence, the heating due to advection terms during the last event is not considered distinct when compared to past events over the 12-month period but it is distinct over the 24-month lead-in period.

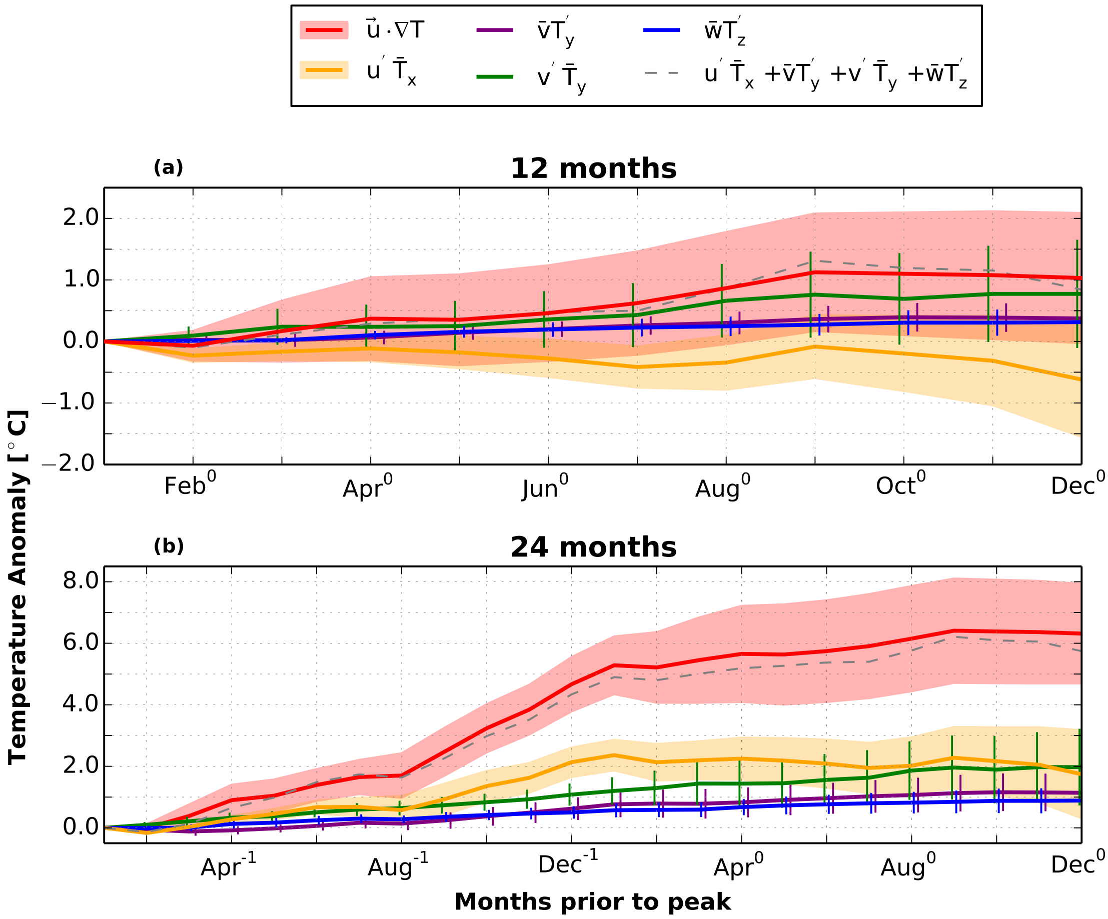

Figure 3.13: Temperature anomalies in the Niño-3.4 region integrated over the mixed layer according to all anomalous advective terms and those with statistically significant differences between the events starting from 0 anomaly at the beginning of (a) 12 months and (b) 24 months before the observed peak. Solid lines represent the mean across the three products (GODAS, PEODAS and ORA-S4), vertical lines and shading areas indicate the standard deviation across the three products. Note that these anomalous terms in 2015–16 event are computed as the deviation of the 1997–98 and 1982–83 average.

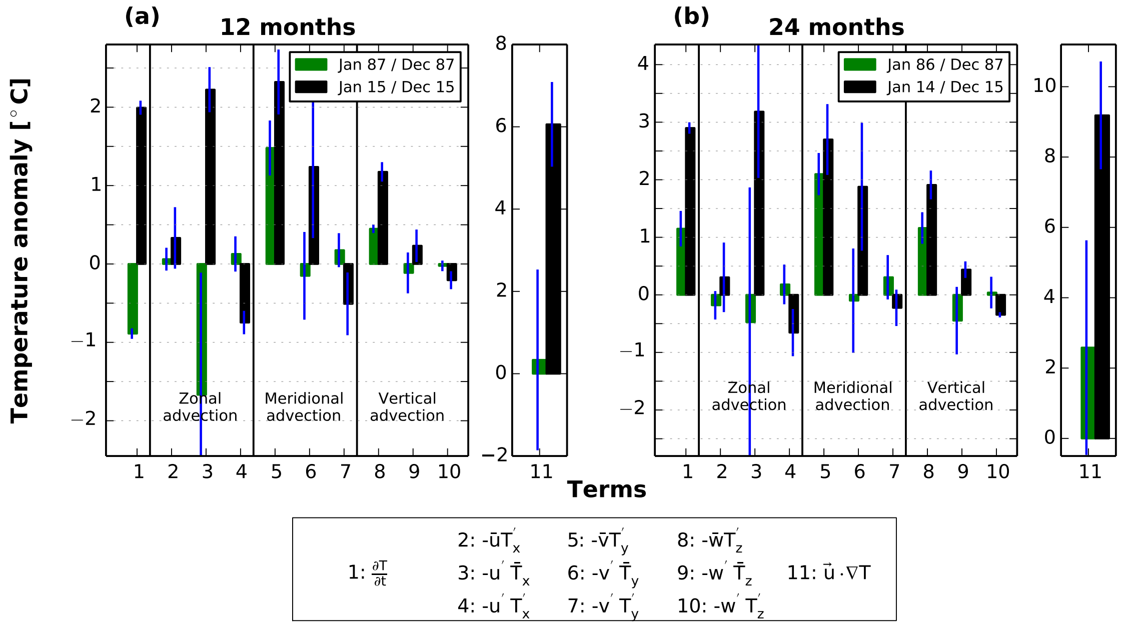

Figure 3.14: Contribution of each individual advection term of the heat budget equation and the total advective term integrated over time, summed up over (a) 12 and (b) 24 months before the peak, and averaged over the Niño-3.4 region. Green and black shaded vertical bars represent the 1987–88, and the 2015–16 El Niño events, respectively. The error bars represent the standard deviation across the three datasets. Datasets: GODAS, PEODAS, ORA-S4.

3.5 The 1987–88 El Niño

It is well known that one of the robust features of ENSO events is their tendency to peak near the end of the calendar year (e.g. Rasmusson and Carpenter 1982). However, the 1987–88 El Niño event evolved differently from the El Niño composite, where a second peak occurred in September 1987 after the first peak in January of the same year, which is the most common season (Fig. 3.2a). In view of the unique two-year warming phenomenon of 2014–2015–2016, we also conduct an additional analysis of the 1986–1987–1988 event examining the upper ocean heat content (T300) as a proxy for the warm water volume and the heat budget analysis.

The 2015–16 event displays a gradual increase of warm water volume, although with some fluctuations, during the two years prior to the peak. However, the 1987–88 event shows a dramatic fall after the first peak in early 1987 (Fig. 3.2b). This is consistent with the findings by Zhang and Endoh (1994) in which they found that the El Niño conditions in the eastern Pacific disappear in mid-1987 because of the increase in trade winds over this region, whereas warm conditions remain in the central and western Pacific until early 1988. To further elucidate why the 1987–88 event was not as strong as the 2015–16 event, we derive a heat budget for the Niño-

3.4 region during these two events (Fig. 3.14). We find that the zonal and meridional advection of climatological temperature by anomalous currents terms ($u'\bar{T}_x$ and $v'\bar{T}_y$) have opposite sign among these two events regardless the time period before their peaks. For instance, the first term is equal to $-0.5\pm2.3\,°C$ for the 1987–88 event and $3.2\pm1.2\,°C$ for the 2015–16 event. This difference in the first term might be related to the fact that there is a significant cooling in mid-1987 over the central Pacific (Fig. 3.2a) in response to strong westward surface zonal advection (Zhang and Endoh 1994). The much weaker meridional asymmetry in the westerly wind anomalies for the 1987–88 event (with asymmetry index = $-0.38\pm0.08 \times 10^{-2}$ N m^{-2} averaged over the 24-month period) leads to a poor contribution of $v'\bar{T}_y$ to the development of this event in contrast to the 2015–16 El Niño event.

3.6 Summary and conclusions

Aiming to explain the mechanisms responsible for the strong 2015–16 El Niño, we analyzed some climate variables such as SST, SSH and zonal wind stress during the months prior to the peak and compared with the patterns seen in the two strong events observed since 1979: the 1997–98 and 1982–83 events. While the magnitude of SST and SSH anomalies over the central equatorial Pacific are comparable across the 3 events, we found some obvious differences in the zonal wind stress anomalies that we now summarize below.

We found that the westerly wind stress anomalies are located either side of the equator in the previous extreme El Niño events, in contrast to the 2015–16 event, where anomalous winds are largely confined to the northern region of the tropical Pacific location. Another distinct feature of the most recent event is the early occurrence of these winds in the previous year (year -1), i.e., in early 2014, compared to the other two events in which they tend to concentrate in year 0 of the El Niño event.

Following McGregor et al. (2016), we solved the amplitude of the forced oceanic Rossby and Kelvin wave response by specifying the temporal and spatial structure of the observed wind stress (Clarke 2008). We suggested that the downwelling Kelvin wave in April 2014, which had nearly no upwelling n = 1 Rossby wave signal but strong upwelling projection onto the n = 2 Rossby wave, without western boundary reflection, might explain the long-lasting warming initiated in 2014 and continued during 2015. We further related both the stronger projection onto the n = 4 Rossby wave and the smaller downwelling Kelvin wave projection to the meridional asymmetry of the anomalous westerly winds.

Motivated by these results, we carried out an analysis of the heat budget evolution of the surface mixed layer during the 24 months leading up to the event peak by examining its time evolution and its average over two periods: 12-month and 24-month periods prior to the event peak. We found that the development of the recent event, in terms of the rate of change of SST, during the 12-month period prior to the peak is weaker than that for the other events. However, when the 24-month period is considered as the growing phase, then all three events show comparable values. Thus, this characteristic highlights that the physical processes occurring in 2014 play a key role in the large magnitude of the 2015–16 event that leads to warmer SST anomalies at the beginning of 2015 unlike near climatological values in early 1997 and 1982.

One of the similarities among the three events analyzed here is that the anomalous heating is mostly attributed to $u'\bar{T}_x$, followed by $\bar{v}T'_y$ and to a lesser extent by $\bar{w}T'_z$. However, we found three advective fluxes with significant differences between the 2015–16 event and past strong events ($\bar{v}T'_y$, $v'\bar{T}_y$ and $\bar{w}T'_z$) whose link with the physical processes described in Sect. 3.3 can be summarized as follows: (1) the long-lasting and equatorial asymmetry of zonal wind anomalies in the 2015–16 event produce a larger $v'\bar{T}_y$ compared to the other events attributed to the lack of equatorward current south of the equator; (2) these two distinct features of zonal wind are at least partly related to the warmer SST anomalies north of the equator (e.g. Murakami et al. 2017), which increase the importance of the $\bar{v}T'_y$; (3) finally, warmer ocean temperature anomalies underneath the mixed layer over the central equatorial Pacific (Fig. 3.15) would explain the larger values of $\bar{w}T'_z$ term. We suggest that the driver of this warmer subsurface temperature, supported by higher WWV (Fig. 3.2b), during the most recent event might be related to deeper basin-wide average thermocline depth due to the long duration of westerly wind anomalies through the 2-yr period. Interestingly, the contribution of $u'\bar{T}_x$, which is related to the thermocline depth variations and zonal SSH gradients by geostrophic balance, during the 1-yr period for the 2015–16 event is much weaker than that for the 1997–98 event. This result supports the findings presented recently by Paek et al. (2017), where they reported that the thermocline anomalies during the 2015–16 event are much weaker than those during the 1997–98 event, suggesting a stronger influence of Central Pacific El Niño dynamics on the 2015–16 event than on the 1997–98 event. In line with this, the smaller Kelvin wave projection that we found would suggest that the thermocline feedback would not be as large during the most recent event.

Our conclusions are reached by examining three different ocean reanalysis products, which show largely consistent behavior albeit considerable spread across products. Thus, our results must still be viewed with some degree of caution in light

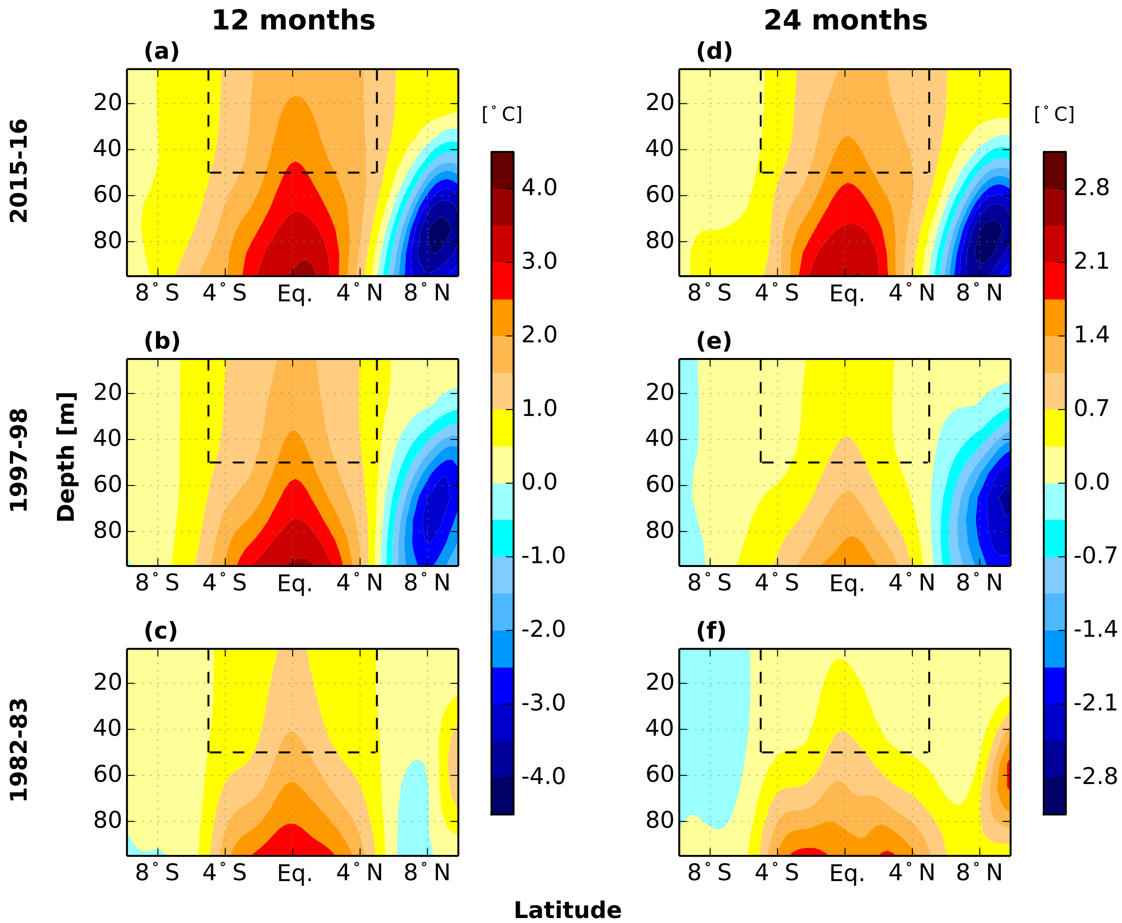

Figure 3.15: Vertical profile of anomalous potential temperature averaged over the Niño-3.4 region across latitude during both the 12-month (a–c) and 24-month (d–f) periods prior to the peak of the events. Note that black dashed lines represent the meridional (5°S-5°N) and vertical (50 m) domain considered in this study. Dataset: GODAS.

of uncertainty in the reanalysis products as well as the assumption of a constant mixed layer depth in the Niño-3.4 region. It should be noted that we expect more uncertainty from the reanalysis products compared to this assumption. By way of example, the difference in the magnitude of advective terms averaged over the nine terms and 24-month period for the 2015–16 El Niño event between mixed layer depth assumption of $h = 30$ m and $h = 50$ m is 0.18 °C, whereas the difference across the products for $h = 50$ m is 0.26 °C. Finally, here we emphasized that although strong El Niño events have some robust features, such as the tendency for their peak to occur during boreal winter, every event has a somewhat different character. In this regard, we have demonstrated that ocean advection plays a key role during the growth of strong El Niño events. We further contrasted the 2015–16 event with the 1987–88 event; both events were preceded by warm equatorial Pacific in the previous year but the 1987–88 event failed to peak as a strong event due to the weak ocean advection.

Our results reaffirm the need for adequate ocean observations are needed to more fully constrain reanalysis products and to better understand the mechanisms that control these variations across El Niño events, and in particular what makes these events grow in magnitude. This will ultimately help improve predictive skill for these significant and damaging climatic events.

Concluding Remarks

Summary of Thesis Findings

This thesis aimed to improve our understanding of the role of the movement of the westerly wind anomalies to the southern hemisphere during the mature phase of ENSO events. Previous work suggested that this shift in wind anomalies might explain the seasonal synchronization of ENSO events due to its role in making the thermocline depth return near normal values in the eastern equatorial Pacific (e.g., Harrison and Vecchi 1999; Vecchi and Harrison 2003, 2006; Lengaigne et al. 2006; Lengaigne and Vecchi 2010), changes in equatorial WWV (McGregor et al. 2012b, 2013) and interhemispheric exchanges of upper ocean mass (McGregor et al. 2014). Here we used both simple and more complex climate models to further investigate the relationship between this wind meridional movement and the tendency for ENSO peaks to occur at the end of the calendar year. We also examined the dynamics of this southward wind shift by analyzing the variables that determine its occurrence and magnitude. This work spans the first two Parts of the thesis (Part 1 and 2). In Part 3 we identified the mechanisms responsible for the strong 2015–16 El Niño, highlighting the main differences between past strong warm events. We briefly summarise the main findings of the thesis below, and finish with recommendations for future research.

Part 1 of this thesis sought to assess the role of the southward wind shift on both the seasonal synchronization as well as the duration of ENSO events by developing a hybrid coupled model capable of reproducing ENSO and this meridional movement of the winds. We found that the inclusion of this shift in our experiments leads to ENSO seasonal synchronization, with more abrupt termination of El Niño events (i.e., shorter duration) compared to those simulations without this shift. This is explained by the changes of the air-sea coupling strength throughout ENSO years: the strong coupling during boreal summer occurs when ENSO's anomalous wind stresses are largely symmetric about the equator, allowing the events to grow rapidly, whereas the weak coupling during boreal winter occurs when ENSO's anomalous wind stresses are largely asymmetric about the equator, which enhances the termination of the events. This result acts as a theoretical proof of the earlier work of Harrison and Vecchi (1999), Vecchi and Harrison (2003), Vecchi and Harrison (2006), and Lengaigne et al. (2006); and is conceptually consistent with the idealized results of Stein et al. (2014). We suggested that the effect of the meridional movement of the easterly wind during La Niña events is small, given the relatively minor southward wind shift that occurs compared to El Niño, playing a minimal role in the length of these events. However, we found that if this meridional movement was stronger than observed, La Niña events would be synchronised to the seasonal cycle. This implies that other mechanism may be responsible for making these events peak with the seasonal cycle. Furthermore, we demonstrated that the effective termination is carried out by two components: (1) the ocean dynamics of the traditional RDO mechanism (Jin 1997); and (2) the discharge of WWV due to the southward wind shift, and both must align to some degree to allow for an abrupt event termination.

The objective of Part 2 was to determine whether the CMIP5 models can reproduce a realistic southward wind shift, the variables related to this movement and its role in the seasonal synchronization of modeled ENSO events. This work extends on Part 1 in this regard by providing insight into dynamical aspects of the wind shift through more complex coupled general circulation models instead of an idealised model. We noted that most models are able to reproduce a southward wind shift during ENSO events. However, the magnitude of the zonal wind stress anomaly is clearly underestimated and located further west compared to the observations. We also demonstrated that biases in the zonal location of these anomalies along with precipitation and SST are more pronounced in models without a southward wind shift. Regarding the background state, models without a southward wind shift exhibit stronger ITCZ, warmer underlying SST and weaker trade winds over the north tropical Pacific during DJF compared to models with a southward wind shift. We also found that the anomalous rainfall over the northwestern Pacific in this season during ENSO events is one of the key variables related to the southward wind shift. Thus larger negative (positive) precipitation anomalies during El Niño (La Niña) events produce a stronger southward wind shift. Consistent with the results presented in Part 1, the magnitude of La Niña and strong El Niño as well as their termination appears to be more rapid in models with a southward wind shift, this being more evident for the latter. The phase locking of ENSO events in models without a southward wind shift is opposite to observations or models with a southward wind shift, which confirms the result of the idealised model in the role of this meridional wind movement in ENSO phase locking.

Part 3 of this thesis aimed to explain the mechanism responsible for the strong 2015–16 El Niño by analyzing some climate variables during the developing phase and comparing with the patterns seen in the two previous strong events observed since 1979: the 1997–98 and 1982–83 events. We found that the westerly wind stress anomalies are located about the equator in both hemispheres in the previous events in contrast to the northern region of the tropical Pacific location where the maximum anomalous zonal wind occurs during the 2015–16 event. Another distinct feature of the most recent event is the early occurrence of these winds in the previous year (year -1), i.e., in early 2014, compared to the other two events in which they tend to concentrate in year 0 of the El Niño event. To gain insight into this, a heat budget analysis of the surface mixed layer was carried out over the central equatorial Pacific throughout the event development phase. We found three advective fluxes with significant differences between the 2015–16 event and past strong events ($\bar{v}T'_y$, $v'\bar{T}_y$ and $\bar{w}T'_z$). The long duration and equatorial asymmetry of zonal wind anomalies in the 2015–16 event produce a larger $v'\bar{T}_y$ compared to the other events attributed to the lack of equatorward current south of the equator. These two distinct features of zonal wind are at least partly related to the warmer SST anomalies north of the equator, which increase the importance of the $\bar{v}T'_y$. Finally, warmer ocean temperature anomalies underneath the mixed layer over the central equatorial Pacific would explain the larger values of $\bar{w}T'_z$ term.

Future Perspectives

Although the work completed in this thesis goes one step further than previous studies in terms of the southward wind shift and its role in the termination of ENSO events, there are still some uncertainties and open questions. For instance, both the simple model used in Part 1 and the CMIP5 models analyzed in Part 2 show a weaker seasonal cycle of the standard deviation of SST anomalies in the Niño-3.4 region. Therefore, they underestimate the magnitude of the observed seasonal synchronization of ENSO events (Fig. 1.9 and 2.9), and display a 1-2 month delay in the minimum in boreal spring. This common feature of climate models should thus be examined.

While we demonstrated the key role of the meridional movement of the westerly wind anomalies in the termination of El Niño events, especially for large events, the role of the easterly wind anomalies in the termination of La Niña is still unclear. In our simple model experiment we found that La Niña events are synchronized to the seasonal cycle when the southward wind shift is strong, which is not consistent with the observations. Thus, we suggest that other mechanism/s might be responsible for synchronizing La Niña event peaks with the seasonal cycle.

Finally, under greenhouse-gas-induced warming conditions, shifts in convection zones, facilitated by weaker changes in SST gradients, might imply an increase in the frequency of extreme El Niño (Cai et al. 2014). Given the prominent role of the southward wind shift in hastening the termination of this type of ENSO event, future work could repeat the analysis carried out in Part 2 under different RCPs scenarios. This would allow investigation of the termination of strong El Niño events for future climate projections.

Bibliography

Abellán, E. and S. McGregor, 2016: The role of the southward wind shift in both, the seasonal synchronization and duration of enso events. *Clim. Dyn.*, **47**, 509–527.

An, S.-I. and F.-F. Jin, 2004: Nonlinearity and Asymmetry of ENSO. *J. Climate*, **17 (12)**, 2399–2412.

An, S.-I. and I.-S. Kang, 2001: Tropical Pacific basin-wide adjustment and oceanic waves. *Geophys. Res. Lett.*, **28**, 3975–3978.

An, S.-I. and B. Wang, 2000: Interdecadal Change of the Structure of the ENSO Mode and Its Impact on the ENSO Frequency. *J. Climate*, **13**, 2044–2055.

An, S.-I. and B. Wang, 2001: Mechanisms of Locking of the El Niño and La Niña Mature Phases to Boreal Winter. *J. Climate*, **14**, 2164–2176.

Annamalai, H., S. P. Xie, J. P. McCreary, and R. Murtugudde, 2005: Impact of Indian Ocean sea surface temperature on a developing El Niño. *J. Climate*, **18**, 302–319.

Ashok, K., S. K. Behera, S. A. Rao, H. Weng, and T. Yamagata, 2007: El Niño Modoki and its possible teleconnection. *J. Geophys. Res.*, **112**, C11 007.

Balmaseda, M. A., M. K. Davey, and D. L. T. Anderson, 1995: Decadal and seasonal dependence of ENSO prediction skill. *J. Climate*, **8**, 2705–2715.

Balmaseda, M. A., K. Mogensen, and A. T. Weaver, 2013: Evaluation of the ECMWF ocean reanalysis system ORAS4. *Quart. J. Roy. Meteor. Soc.*, **139**, 1132–1161.

Battisti, D. S., 1988: The dynamics and thermodynamics of a warming event in a coupled tropical atmosphere-ocean model. *J. Atmos. Sci.*, **45**, 2889–2919.

Battisti, D. S. and A. C. Hirst, 1989: Interannual variability in the tropical atmosphere-ocean system: Influences of the basic state, ocean geometry, and non-linearity. *J. Atmos. Sci.*, **46**, 1687–1712.

Behringer, D. W., M. Ji, and A. Leetmaa, 1998: An improved coupled model for ENSO prediction and implications for ocean initialization. Part I: The ocean data assimilation system. *Mon. Wea. Rev.*, **126**, 1013–1021.

Behringer, D. W. and Y. Xue, 2004: Evaluation of the global ocean data assimilation system at ncep. *Eighth symposium on integrated observing and assimilation system for atmosphere, ocean, and land surface, AMS 84th annual meeting*, Washington State Convention and Trade Center, Seattle, 11–15.

Bellenger, H., E. Guilyardi, J. Leloup, M. Lengaigne, and J. Vialard, 2014: ENSO representation in climate models: from CMIP3 to CMIP5. *Clim. Dyn.*, **42**, 1999–2018.

Benson, C. and E. J. Clay, 1998: The Impact of Drought on Sub-Saharan African Economies: A Preliminary Examination. *World Bank Technical Paper.*

Bjerknes, J., 1969: Atmospheric teleconnections from the equatorial Pacific. *Mon. Wea. Rev.*, **97**, 163–172.

Bjerkness, J., 1969: Climatological effects of orography and land–sea heating contrasts on the gravity wave–driven circulation of the mesosphere. *Mon. Wea. Rev.*, **60**, 103–118.

Boucharel, J., F.-F. Jin, M. H. England, B. Dewitte, I. Lin, H.-C. Huang, and M. A. Balmaseda, 2016a: Influence of oceanic intraseasonal Kelvin waves on the Eastern Pacific hurricane activity. *J. Climate*, **29**, 7941–7955.

Boucharel, J., F.-F. Jin, M. H. England, and I. I. Lin, 2016b: Modes of hurricane activity variability in the eastern Pacific: Implications for the 2016 season. *Geophys. Res. Lett.*, **43**, 11,358–11,366.

Bouma, M. J. and C. Dye, 1997: Cycles of malaria associated with El Niño in Venezuela. *JAMA*, **278**, 1772–1774.

Brown, J. N., C. Langlais, and C. Maes, 2014: Zonal structure and variability of the Western Pacific dynamic warm pool edge in CMIP5. *Clim. Dyn.*, **42**, 3061–3076.

Burgers, G. and D. B. Stephenson, 1999: The “normality” of El Niño. *Geophys. Res. Lett.*, **26**, 1027–1030.

Cai, W., et al., 2012: More extreme swings of the South Pacific convergence zone due to greenhouse warming. *Nature*, **488**, 365–369.

Cai, W., et al., 2014: Increasing frequency of extreme El Niño events due to greenhouse warming. *Nature Clim. Change*, **4**, 111–116.

Cai, W., et al., 2015: Increased frequency of extreme La Niña events under greenhouse warming. *Nature Clim. Change*, **5**, 132–137.

Cane, M. A., M. Münnich, and S. E. Zebiak, 1990: A Study of Self-Excited Oscillations of the Tropical Ocean-Atmosphere System. Part I: Linear Analysis. *J. Atmos. Sci.*, **47**, 1562–1577.

Cane, M. A. and S. Zebiak, 1985: A theory for El Niño and the Southern Oscillation. *Science*, **228**, 1084–1087.

Capotondi, A. and A. T. Wittenberg, 2013: ENSO diversity in climate models. *U.S. CLIVAR Variations*, **11**, 10–14.

Capotondi, A., A. T. Wittenberg, and S. Masina, 2006: Spatial and temporal structure of Tropical Pacific interannual variability in 20th century coupled simulations. *Ocean Model.*, **15**, 274–298.

Capotondi, A., et al., 2015: Understanding ENSO diversity. *Bull. Amer. Meteor. Soc.*, **96**, 921–938.

Chang, P., et al., 2006: Climate Fluctuations of Tropical Coupled Systems-The Role of Ocean Dynamics. *J. Climate*, **19**, 5122–5174.

Chen, D., et al., 2015: Strong influence of westerly wind bursts on El Niño diversity. *Nature Geosci*, **8**, 339–345.

Chen, S. S., R. A. Houze, and B. E. Mapes, 1996: Multiscale variability of deep convection in relation to large-scale circualtion in TOGA COARE. *J. Atmos. Sci.*, **53**, 1380–1409.

Chiodi, A. M. and D. E. Harrison, 2015: Equatorial Pacific easterly wind surges and the onset of La Niña events. *J. Climate*, **28**, 776–792.

Chiodi, A. M., D. E. Harrison, and G. A. Vecchi, 2014: Subseasonal atmospheric variability and El Niño waveguide warming: observed effects of the Madden-Julian Oscillation and westerly wind events. *J. Climate*, **27**, 3619–3642.

Choi, K. Y., G. A. Vecchi, and A. Wittenberg, 2013: ENSO transition, duration, and amplitude asymmetries: role of the nonlinear wind stress coupling in a conceptual model. *J. Climate*, **26**, 9462–9476.

Choi, K.-Y., G. A. Vecchi, and A. T. Wittenberg, 2015: Nonlinear Zonal Wind Response to ENSO in the CMIP5 Models: Roles of the Zonal and Meridional Shift of the ITCZ/SPCZ and the Simulated Climatological Precipitation. *J. Climate*, **28**, 8556–8573.

Chu, P. S., 1988: Extratropical forcing and the burst of equatorial westerlies in the western Pacific: a synoptic study. *J. Meteor. Soc. Japan*, **66**, 4549–4564.

Clarke, A., 2008: *An introduction to the dynamics of El Niño and the Southern Oscillation*, Vol. ISBN: 9780120885480. Academic Press, 324 pp.

Collins, J. M., P. J. Klotzbach, R. N. Maue, D. R. Roache, E. S. Blake, C. H. Paxton, and C. A. Mehta, 2015: The record-breaking 2015 hurricane season in the eastern North Pacific: An analysis of environmental conditions. *Geophys. Res. Lett.*, **43**, 9217–9224.

de Boyer Montégut, C., G. Madec, A. S. Fischer, A. Lazar, and D. Iudicone, 2004: Mixed layer depth over the global ocean: An examination of profile data and a profile-based climatology. *J. Geophys. Res. Oceans*, **109**, C12 003.

Dee, D. P. and S. P. Uppala, 2009: Variational bias correction of satellite radiance data in the ERA-Interim reanalysis. *Q. J. Roy. Meteor. Soc.*, **135**, 1830–1841.

Dee, D. P., et al., 2011: The ERA-Interim reanalysis: configuration and performance of the data assimilation system. *Quart. J. Roy. Meteor. Soc.*, **137**, 553–597.

Deser, C. and J. M. Wallace, 1987: El Niño and their relation to the Southern Oscillation: 1925-1986. *J. Geophys. Res.*, **92**, 14 189–14 196.

Deser, C., et al., 2012: ENSO and Pacific decadal variability in the Community Climate System Model version 4. *J. Climate*, **25**, 2622–2651.

Dilley, M. and B. N. Heyman, 1995: ENSO and disaster: Droughts, floods and El Niño/Southern Oscillation warm events. *Disasters*, **19**, 181–193.

DiNezio, P. N. and C. Deser, 2014: Nonlinear Controls on the Persistence of La Niña. *J. Climate*, **27**, 7335–7355.

Dommenget, D., T. Bayr, and C. Frauen, 2013: Analysis of the non-linearity in the pattern and time evolution of El Niño southern oscillation. *Clim. Dyn.*, **40**, 2825–2847.

Dommenget, D. and Y. Yu, 2016: The seasonally changing cloud feedbacks contribution to the ENSO seasonal phase-locking. *Clim. Dyn.*, **47**, 3661–3672.

Dong, B.-W., 2005: Asymmetry between El Niño and La Niña in a Global Coupled GCM with and Eddy-Permitting Ocean Resolution. *J. Climate*, **18**, 3373–3387.

Du, Y., T. Qu, G. Meyers, Y. Masumoto, and H. Sasaki, 2005: Seasonal heat budget in the mixed layer of the southeastern tropical Indian Ocean in a high-resolution ocean general circulation model. *J. Geophys. Res. Oceans*, **110**, C04 012.

Eisenman, I., L. Yu, and E. Tziperman, 2005: Westerly Wind Bursts: ENSO's tail rather than the dog? *J. Climate*, **18**, 5224–5238.

Enriques, A. and C. Friehe, 1995: Effects of Wind Stress and Wind Stress Curl Variability on Coastal Upwelling. *J. Phys. Oceanogr.*, **25**, 1651–1671.

Fasullo, J. and P. Webster, 2000: Atmospheric and surface variations during westerly wind bursts in the tropical western Pacific. *Quart. J. Roy. Meteor. Soc.*, **126**, 899–924.

Fedorov, A. and J. N. Brown, 2009: *Equatorial waves.* Encyclopedia of Ocean Sciences, pp. 3679-3695, Academic, San Diego, Calif.

Frauen, C. and D. Dommenget, 2010: El Niño and La Niña amplitude asymmetry caused by atmospheric feedbacks. *Geophys. Res. Lett.*, **37**, L18 801.

Galanti, E. and E. Tziperman, 2000: ENSO's phase locking to the seasonal cycle in the fast-SST, fast-wave, and mixed-mode regimes. *J. Atmos. Sci.*, **57**, 2936–2950.

Galanti, E., E. Tziperman, M. Harrison, A. Rosati, R. Giering, and Z. Sirkes, 2002: The equatorial thermocline outcropping - A seasonal control on the tropical Pacific Ocean-atmosphere instability strength. *J. Climate*, **15**, 2721–2739.

Gebbie, G., I. Eisenman, A. Wittenberg, and E. Tziperman, 2007: Modulation of westerly wind bursts by sea surface temperature: a semistochastic feedback for ENSO. *J. Atmos. Sci.*, **64**, 3281–3295.

Gebbie, G. and E. Tziperman, 2009: Predictability of SST-modulated westerly wind bursts. *J. Climate*, **22**, 3894–3909.

Giese, B. and D. Harrison, 1991: Eastern equatorial Pacific response to three composite westerly wind types. *J. Geophys. Res.*, **96**, 3239–3248.

Giese, B. and D. E. Harrison, 1990: Aspects of the Kelvin wave response to episodic wind forcing. *J. Geophys. Res.*, **95**, 7289–7312.

Goddard, L. and M. Dilley, 2005: El Niño: Catastrophe or Opportunity. *J. Climate*, **18**, 651–665.

Graham, N. and W. White, 1988: The El Niño cycle: A natural oscillator of the Pacific ocean-atmosphere system. *Science*, **240**, 1293–1302.

Grose, M. R., et al., 2014: Assessment of the CMIP5 global climate model simulations of the western tropical Pacific climate system and comparison to CMIP3. *Int. J. Climatol.*, **34**, 3382–3399.

Guilyardi, E., 2006: El Niño–mean state–seasonal cycle interactions in a multi-model ensemble. *Clim. Dyn.*, **26**, 329–348.

Guilyardi, E., H. Bellenger, M. Collins, S. Ferrett, W. Cai, and A. Wittenberg, 2012: A first look at ENSO in CMIP5. *CLIVAR Exchanges*, **17**, 29–32.

Ham, Y.-G., I.-S. Kang, D. Kim, and J.-S. Kug, 2012: El-Niño Southern Oscillation simulated and predicted in SNU coupled GCMs. *Clim. Dyn.*, **38**, 2227–2242.

Ham, Y.-G. and J.-S. Kug, 2014: ENSO phase-locking to the boreal winter in CMIP3 and CMIP5 models. *Clim. Dyn.*, **43**, 305–318.

Ham, Y.-G. and J.-S. Kug, 2015: Improvement of ENSO Simulation Based on Intermodel Diversity. *J. Climate*, **28**, 998–1015.

Ham, Y.-G., J.-S. Kug, D. Kim, Y.-H. Kim, and D.-H. Kim, 2013: What controls phase-locking of ENSO to boreal winter in coupled GCMs? *Clim. Dyn.*, **40**, 1551–1568.

Hannachi, A., D. Stephenson, and K. Sperber, 2003: Probability-based methods for quantifying nonlinearity in the ENSO. *Clim. Dyn.*, **20**, 241–256.

Hansen, J. W., A. W. Hodges, and J. W. Jones, 1998: ENSO influences on agriculture in the southeastern United States. *J. Climate*, **11**, 404–411.

Harrison, D., 1989: On Climatological Monthly Mean Wind Stress and Wind Stress Curl Fields over the World Ocean. *J. Climate*, **2**, 57–70.

Harrison, D. E., 1987: Monthly mean island surface winds in the central tropical Pacific and El Niño events. *Mon. Wea. Rev.*, **115**, 3133–3145.

Harrison, D. E. and A. M. Chiodi, 2009: Pre- and Post-1997/98 westerly wind events and equatorial Pacific cold tongue warming. *J. Climate*, **22**, 568–581.

Harrison, D. E. and B. S. Giese, 1991: Episodes of surface westerly winds as observed from islands in the western tropical Pacific. *J. Geophys. Res. Oceans*, **96**, 3221–3237.

Harrison, D. E. and N. K. Larkin, 1996: The COADS Sea Level Pressure Signal: A Near-Global El Niño Composite and Time Series View, 1946-1993. *J. Climate*, **9**, 3025–3055.

Harrison, D. E. and N. K. Larkin, 1998: Seasonal U.S. temperature and precipitation anomalies associated with El Niño: Historical results and comparison with 1997-1998. *Geophys. Res. Lett.*, **25**, 3959–3962.

Harrison, D. E. and D. S. Luther, 1990: Surface winds from tropical Pacific Islands-Climatological statistics. *J. Climate*, **3**, 251–271.

Harrison, D. E. and G. A. Vecchi, 1997: Surface westerly wind events in the tropical Pacific 1986-1995. *J. Climate*, **10**, 3131–3156.

Harrison, D. E. and G. A. Vecchi, 1999: On the termination of El Niño. *Geophys. Res. Lett.*, **26**, 1593–1596.

Hartten, L. M., 1996: Synoptic settings of westerly wind bursts. *J. Geophys. Res. Atmospheres*, **101 (D12)**.

Hirst, A., 1986: Unstable and damped equatorial modes in simple coupled ocean-atmosphere models. *J. Atmos. Sci.*, **43**, 606–632.

Hoerling, M., A. Kumar, and M. Zhong, 1997: El Niño, La Niña, and the nonlinearity of their Teleconnections. *J. Climate*, **10**, 1769–1786.

Holland, G. J., 2009: ENSO Warming Impacts. *Science*, **3**, 325–347.

Horii, T. and K. Hanawa, 2004: A relationship between timing of El Niño onset and subsequent evolution. *Geophys. Res. Lett.*, **31**, L06 304.

Hu, S. and A. V. Fedorov, 2016: Exceptionally strong easterly wind burst stalling El Niño of 2014. *Proceedings of the National Academy of Sciences*, **113**, 2005–2010.

Hua, L.-J. and Y.-Q. Yu, 2015: How are El Niño and La Niña events improves in an eddy-resolving ocean general circulation model? *Atmospheric and Oceanic Science Letters*, **8**, 245.

Huang, B., Y. Xue, D. Zhang, A. Kumar, and M. J. McPhaden, 2010: The NCEP GODAS Ocean Analysis of the Tropical Pacific Mixed Layer Heat Budget on Seasonal to Interannual Time Scales. *J. Climate*, **23**, 4901–4925.

Imada, Y. and M. Kimoto, 2012: Parameterization of Tropical Instability Waves and Examination of Their Impact on ENSO Characteristics. *J. Climate*, **25**, 4568–4581.

Imada, Y., H. Tatebe, M. Watanabe, M. Ishii, and M. Kimoto, 2016: South Pacific influence on the termination of El Niño in 2014. *Scientific Reports*, **6**.

Ishii, M., A. Shouji, S. Sugimoto, and T. Matsumoto, 2005: Objective analyses of sea-surface temperature and marine meteorological variables for the 20th century using ICOADS and the Kobe Collection. *Int. J. Climatol.*, **25**, 865–879.

Jin, F.-F., 1997: An equatorial ocean recharge paradigm for ENSO. Part I: Conceptual model. *J. Atmos. Sci.*, **54**, 811–829.

Jin, F.-F., S.-I. An, A. Timmermann, and J. Zhao, 2003: Strong El Niño events and nonlinear dynamic heating. *Geophys. Res. Lett.*, **30**, 1120.

Jin, F.-F., J. Neelin, and M. Ghil, 1994: El Niño on the devil's staircase: annual subharmonic steps to chaos. *Science*, **264**, 70–72.

Kalnay, E., et al., 1996: The NCEP/NCAR 40-Year Reanalysis Project. *Bull. Amer. Meteor. Soc.*, **77**, 437–471.

Kanamitsu, M., W. Ebisuzaki, J. Woollen, S. K. Yang, J. J. Hnilo, M. Fiorino, and G. L. Potter, 2002: NCEP-DOE AMIP-II Reanalysis (R-2). *Bull. Amer. Meteor. Soc.*, **83**, 1631–1643.

Kang, I.-S. and J.-S. Kug, 2002: El Niño and La Niña sea surface temperature anomalies: Asymmetry characteristics associated with their wind stress anomalies. *J. Geophys. Res.*, **107**, 4372.

Kao, H.-Y. and J.-Y. Yu, 2009: Contrasting Eastern-Pacific and Central-Pacific Types of ENSO. *J. Climate*, **22**, 615–632.

Keen, R. A., 1982: The role of cross-equatorial cyclone pairs in the Southern Oscillation. *Mon. Wea. Rev.*, **110**, 1405–1416.

Kerr, R. A., 1999: Atmospheric science: does a globe-girdling disturbance jigger El Niño? *Science*, **285**, 322–323.

Kessler, W. S., 1991: Can Reflected Extra-equatorial Rossby Waves Drive ENSO? *J. Phys. Oceanogr.*, **21**, 444–452.

Kessler, W. S., 2002: Is ENSO a cycle or a series of events? *Geophys. Res. Lett.*, **29**, 2125.

Kessler, W. S. and R. Kleeman, 2000: Rectification of the Madden-Julian Oscillation into the ENSO Cycle. *J. Climate*, **13**, 3560–3575.

Kim, H.-M., P. J. Webster, and J. A. Curry, 2009: Impact of Shifting Patterns of Pacific Ocean Warming on North Atlantic Tropical Cyclones. *Science*, **325**, 77–80.

Kirtman, B. P., 1997: Oceanic Rossby Wave Dynamics and the ENSO Period in a Coupled Model. *J. Climate*, **10**, 1690–1704.

Kirtman, B. P., Y. Fan, and E. K. Schneider, 2002: The COLA Global Coupled and Anomaly Coupled Ocean-Atmosphere GCM. *J. Climate*, **15**, 2301–2320.

Kleeman, R., 1993: On the dependence of hincast skill on ocean thermodynamics in a coupled ocean-atmosphere model. *J. Climate*, **6**, 2012–2033.

Kug, J.-S., Y.-G. Ham, J.-Y. Lee, and F.-F. Jin, 2012: Improved simulation of two types of El Niño in CMIP5 models. *Environ. Res. Lett.*, **7**, 034 002.

Kug, J.-S., F. Jin, and S.-I. An, 2009: Two types of El Niño events: Cold tongue El Niño and warm pool El Niño. *J. Climate*, **22**, 1499–1515.

Kug, J. S. and I. S. Kang, 2006: Interactive feedback between ENSO and the Indian Ocean. *J. Climate*, **19**, 1784–1801.

Kug, J.-S., I.-S. Kang, and S.-I. An, 2003: Symmetric and antisymmetric mass exchanges between the equatorial and off-equatorial Pacific associated with ENSO. *J. Geophys. Res.*, **108**, doi:10.1029/2002JC001671.

Larkin, N. K. and D. E. Harrison, 2002: ENSO warm (El Niño) and cold (La Niña) event lifecycles: ocean surface anomaly patterns, their symmetries, asymmetries, and implications. *J. Climate*, **15**, 1118–1140.

Larkin, N. K. and D. E. Harrison, 2005: On the definition of El Niño and associated seasonal average U.S. weather anomalies. *Geophys. Res. Lett.*, **32**, L13 705.

Latif, M., J. Biercamp, and H. von Storch, 1988: The response of a coupled ocean-atmosphere general circulation model to wind bursts. *J. Atmos. Sci*, **45**, 964–979.

Lee, T. and M. J. McPhaden, 2010: Increasing intensity of El Niño in the central-equatorial Pacific. *Geophys. Res. Lett.*, **37**, L14 603.

Lee, T., D. E. Waliser, J.-L. F. Li, F. W. Landerer, and M. M. Gierach, 2013: Evaluation of CMIP3 and CMIP5 Wind Stress Climatology Using Satellite Measurements and Atmospheric Reanalysis Products. *J. Climate*, **26**, 5810–5826.

Lengaigne, M., J. Boulanger, C. Meinkes, and H. Spencer, 2006: Influence of the seasonal cycle on the termination of El Niño events in a coupled general circulation model. *J. Climate*, **19**, 1850–1868.

Lengaigne, M., E. Guilyardi, J. P. Boulanger, C. Menkes, P. Delecluse, P. Inness, J. Cole, and J. Slingo, 2004: Triggering of El Niño by westerly wind events in a coupled general circulation model. *Clim. Dyn.*, **23**, 601–620.

Lengaigne, M. and G. A. Vecchi, 2010: Contrasting the termination of moderate and extreme El Niño events in Coupled General Circulation Models. *Clim. Dyn.*, **35**, 299–313.

Levine, A. F. Z. and M. J. McPhaden, 2016: How the July 2014 easterly wind burst gave the 2015–2016 El Niño a head start. *Geophys. Res. Lett.*, **43**, 6503–6510.

L'Heureux, M. L., et al., 2016: Observing and Predicting the 2015–16 El Niño. *Bull. Amer. Meteor. Soc.*, **0**, null.

Li, G., S.-P. Xie, Y. Du, and Y. Luo, 2016: Effects of excessive equatorial cold tongue bias on the projections of tropical Pacific climate change. Part I: the warming pattern in CMIP5 multi-model ensemble. *Clim. Dyn.*, **47**, 3817–3831.

Li, T. and B. Wang, 2005: A review on the western North Pacific monsoon: Synoptic-to-interannual variabilities. *Terr. Atmos. Oceanic Sci.*, **16**, 285–314.

Lorbacher, K., D. Dommenget, P. P. Niiler, and A. Kohl, 2006: Ocean mixed layer depth: A subsurface proxy of ocean-atmosphere variability. *J. Geophys. Res. Oceans*, **111**, C07 010.

Lorenz, E. N., 1956: *Empirical orthogonal functions and statistical weather prediction*. Sci. Rep. No. 1, Statistical Forecasting Project, M.I.T., Cambridge, MA, 48 pp.

Ludescher, J., A. Gozolchiani, M. I. Bogachev, A. Bunde, S. Havlin, and H. J. Schellnhuber, 2014: Very early warning of next El Niño. *Proceedings of the National Academy of Sciences*, **111**, 2064–2066.

Luther, D. S., D. E. Harrison, and R. A. Knox, 1983: Zonal winds in the central equatorial Pacific and El Niño. *Science*, **222**, 327–330.

Matsuno, T., 1966: Quasi-Geostrophic Motions in the Equatorial Area. *J. Meteorol. Soc. Jpn.*, **44**, 25–43.

McGregor, S., A. S. Gupta, and M. H. England, 2012a: Constraining wind stress products with sea surface height observations and implications for pacific ocean sea level trend attribution. *J. Climate*, **25**, 8164–8176.

McGregor, S., N. Ramesh, P. Spence, M. H. England, M. J. McPhaden, and A. Santoso, 2013: Meridional movement of wind anomalies during ENSO events and their role in event termination. *Geophys. Res. Lett.*, **40**, 749–754.

McGregor, S., P. Spence, F. U. Schwarzkopf, M. H. England, A. Santoso, W. S. Kessler, A. Timmermann, and C. W. Böning, 2014: ENSO-driven interhemispheric Pacific mass transports. *J. Geophys. Res. Oceans*, **119**, 6221–6237.

McGregor, S., A. Timmermann, F.-F. Jin, and W. S. Kessler, 2016: Charging El Niño with off-equatorial westerly wind events. *Clim. Dyn.*, **47**, 1111–1125.

McGregor, S., A. Timmermann, N. Schneider, M. F. Stuecker, and M. H. England, 2012b: The effect of the South Pacific Convergence Zone on the termination of El Niño events and the meridional asymmetry of ENSO. *J. Climate*, **25**, 5566–5586.

McPhaden, M. J., 1999: Genesis and evolution of the 1997-98 El Niño. *Science*, **283**, 950–954.

McPhaden, M. J., 2004: Evolution of the 2002/03 El Niño. *Bull. Amer. Meteor. Soc.*, **85**, 677–695.

McPhaden, M. J., 2015: Playing hide and seek with El Niño. *Nature Clim. Change*, **5**, 791–795.

McPhaden, M. J., S. E. Zebiak, and M. H. Glantz, 2006: ENSO as an integrating concept in earth science. *Science*, **314**, 1740–1745.

McPhaden, M. J. and X. Zhang, 2009: Asymmetry in zonal phase propagation of ENSO sea surface temperature anomalies. *Geophys. Res. Lett.*, **36**, L13 703.

Meehl, G. A., C. Covey, K. E. Taylor, T. Delworth, R. J. Stouffer, M. Latif, B. McAvaney, and J. F. B. Mitchell, 2007: The WCRP CMIP3 multimodel dataset: a new era in climate change research. *Bull. Amer. Meteor. Soc.*, **88**, 1383–1394.

Meinen, C. S. and M. J. McPhaden, 2000: Observations of warm water volume changes in the equatorial Pacific and their relationship to El Niño and La Niña. *J. Climate*, **13**, 3551–3559.

Menkes, C. E., M. Lengaigne, J. Vialard, M. Puy, P. Marchesiello, S. Cravatte, and G. Cambon, 2014: About the role of westerly wind events in the possible development of an El Niño in 2014. *Geophys. Res. Lett.*, **41**, 6476–6483.

Misra, V., et al., 2007: Validating and understanding the ENSO simulation in two coupled climate models. *Tellus A*, **59**, 292–308.

Monahan, A. H. and A. Dai, 2004: The spatial and temporal structure of ENSO nonlinearity. *J. Climate*, **17**, 3026–3036.

Murakami, H., et al., 2017: Dominant Role of Subtropical Pacific Warming in Extreme Eastern Pacific Hurricane Seasons: 2015 and the Future. *J. Climate*, **30**, 243–264.

Neale, R. B., J. H. Richter, and M. Jochum, 2008: The Impact of Convection on ENSO: From a Delayed Oscillator to a Series of Events. *J. Climate*, **21**, 5904–5924.

Neelin, J. D., D. S. Battisti, A. C. Hirst, F.-F. Jin, Y. Wakata, T. Yamagata, and S. E. Zebiak, 1998: ENSO theory. *J. Geophys. Res.*, **103**, 14 261–14 290.

Neelin, J. D., F.-F. Jin, and H.-H. Syu, 2000: Variations in ENSO Phase Locking. *J. Climate*, **13**, 2570–2590.

Obha, M. and H. Ueda, 2007: An impact of SST anomalies in the Indian Ocean in acceleration of the El Niño to La Niña transition. *J. Meteor. Soc. Japan*, **85**, 335–348.

Obha, M. and H. Ueda, 2009: Role of nonlinear atmospheric response to SST on the asymmetric transition process of ENSO. *J. Climate*, **22**, 177–192.

Ohba, M., D. Nohara, and H. Ueda, 2010: Simulation of asymmetric ENSO transition in WCRP CMIP3 multimodel experiments. *J. Climate*, **23**, 6051–6067.

Ohba, M. and H. Ueda, 2009: Role of Nonlinear Atmospheric Response to SST on the Asymmetric Transition Process of ENSO. *J. Climate*, **22**, 177–192.

Okumura, Y. M. and C. Deser, 2010: Asymmetry in the duration of El Niño and La Niña. *J. Climate*, **23**, 5826–5843.

Okumura, Y. M., O. Masamichi, D. Clara, and U. Hiroaki, 2011: A proposed mechanism for the asymmetric duration of El Niño and La Niña. *J. Climate*, **24**, 3822–3829.

Paek, H., J.-Y. Yu, and C. Qian, 2017: Why were the 2015/2016 and 1997/1998 extreme el Niños different? *Geophys. Res. Lett.*, **44**, 1848–1856.

Paulson, C. A. and J. J. Simpson, 1977: Irradiance Measurements in the Upper Ocean. *J. Phys. Oceanogr.*, **7**, 952–956.

Philander, S., T. Yamagata, and R. Pacanowski, 1984: Unstable air-sea interactions in the tropics. *J. Atmos. Sci.*, **41**, 604–613.

Philander, S. G., 1983: El Niño Southern Oscillation phenomena. *Nature*, **302**, 295–301.

Philander, S. G., 1990: *El Niño, La Niña, and the Southern Oscillation.* Academic Press, 293 pp.

Philander, S. G. and A. Fedorov, 2003: Is El Niño sporadic or cyclic? *Annual Review of Earth and Planetary Sciences*, **31**, 579–594.

Qiu, B., 2000: Interannual Variability of the Kuroshio Extension System and Its Impact on the Wintertime SST Field. *J. Phys. Oceanogr.*, **30**, 1486–1502.

Qu, T., 2003: Mixed layer heat balance in the western North Pacific. *J. Geophys. Res. Oceans*, **108**, 3242.

Quiños, J., V. González Carman, J. Zeballos, S. Purca, and H. Mianzan, 2010: Effects of El niño-driven environmental variability on black turtle migration to Peruvian foraging grounds. *Hydrobiologia*, **645**, 69–79.

Rashid, H. A. and A. C. Hirst, 2015: Investigating the mechanisms of seasonal ENSO phase locking bias in the ACCESS coupled model. *Clim. Dyn.*, **46**, 1075–1090.

Rasmusson, E. and T. Carpenter, 1982: Variations in tropical sea surface temperature and surface wind fields associated with the Southern Oscillation/El Niño. *Mon. Wea. Rev.*, **110**, 353–384.

Rasmusson, E. M. and P. A. Arkin, 1985: *Interannual climate variability associated with the El Niño - Southern Oscillation*, Elsevier Oceanography Series, Vol. 40. Elsevier.

Rayner, N. A., D. E. Parker, E. B. Horton, C. K. Folland, L. V. Alexander, D. P. Rowell, E. C. Kent, and A. Kaplan, 2003: Global analyses of sea surface temperature, sea ice, and night marine air temperature since the late nineteenth century. *J. Geophys. Res. Atmospheres*, **108**, 4407.

Rebert, J. P., J. R. Donguy, and G. Eldin, 1985: Relations between sea level, thermocline depth, heat content and dynamic height in the tropical Pacific Ocean. *J. Geophys. Res.*, **90**, 11 719–11 725.

Ren, H.-L., J. Zuo, F.-F. Jin, and M. F. Stuecker, 2016: ENSO and annual cycle interaction: the combination mode representation in CMIP5 models. *Clim. Dyn.*, **46**, 3753–3765.

Rodgers, K. B., P. Friederichs, and M. Latif, 2004: Tropical Pacific decadal variability and its relation to decadal modulations of ENSO. *J. Climate*, **17**, 3761–3774.

Ropelewski, C. F. and M. S. Halpert, 1987: Global and regional scale temperature patterns associated with the El Niño/Southern Oscillation. *Mon. Wea. Rev.*, **115**, 1606–1626.

Ropelewski, C. H. and S. Halpert, 1989: Precipitation patterns associated with the high index phase of the Southern Oscillation. *J. Climate*, **2**, 268–284.

Saba, V. S., G. L. Shillinger, A. M. Swithenbank, B. A. Block, J. R. Spotila, J. A. Musick, and F. V. Paladino, 2008: An oceanographic context for the foraging ecology of eastern Pacific leatherback turtles: Consequences of ENSO. *Deep Sea Res.*, **55**, 646–660.

Santoso, A., A. S. Gupta, and M. H. England, 2010: Genesis of Indian Ocean Mixed Layer Temperature Anomalies: A Heat Budget Analysis. *J. Climate*, **23**, 5375–5403.

Santoso, A., S. McGregor, F.-F. Jin, W. Cai, M. H. England, S.-I. An, M. J. McPhaden, and E. Guilyardi, 2013: Late-twentieth-century emergence of the El Niño propagation asymmetry and future projections. *Nature*, **504**, 126–130.

Schopf, P. S. and M. J. Suarez, 1988: Vacillations in a coupled ocean-atmosphere model. *J. Atmos. Sci.*, **45**, 549–566.

Smith, T. M., R. W. Reynolds, T. C. Peterson, and J. Lawrimore, 2008: Improvements to NOAA's Historical Merged Land-Ocean Surface Temperature Analysis (1880-2006). *J. Climate*, **21**, 2283–2296.

Smith, W. H. F. and D. T. Sandwell, 1997: Global sea floor topography from satellite altimetry and ship depth soundings. *Science*, **277**, 1956–1962.

Spencer, H., 2004: Role of the atmosphere in seasonal phase locking of El Niño. *Geophys. Res. Lett.*, **31**, L24 104.

Springer, S. R., M. J. McPhaden, and A. J. Busalacchi, 1990: Oceanic heat content variability in the tropical Pacific during the 1982-1983 El Niño. *J. Geophys. Res.*, **95**, 22 089 – 22 101.

Stein, K., A. Timmermann, and N. Schneider, 2014: ENSO seasonal synchronization theory. *J. Climate*, **27**, 5285–5310.

Stuecker, M. F., F.-F. Jin, A. Timmermann, and S. McGregor, 2015: Combination Mode Dynamics of the Anomalous Northwest Pacific Anticyclone. *J. Climate*, **28**, 1093–1111.

Stuecker, M. F., A. Timmermann, F. F. Jin, S. McGregor, and H. L. Ren, 2013: A combination mode of the annual cycle and the El Niño/Southern Oscillation. *Nat. Geosci.*, **6**, 540–544.

Su, J., R. Zhang, T. Li, X. Rong, J.-S. Kug, and C.-C. Hong, 2010: Causes of the El Niño and La Niña Amplitude Asymmetry in the Equatorial Eastern Pacific. *J. Climate*, **23**, 605–617.

Sun, D.-Z., Y. Yu, and T. Zhang, 2009: Tropical Water Vapor and Cloud Feedbacks in Climate Models: A Further Assessment Using Coupled Simulations. *J. Climate*, **22**, 1287–1304.

Takahashi, K. and B. Dewitte, 2015: Strong and moderate nonlinear El Niño regimes. *Clim. Dyn.*, **46**, 1627–1645.

Takahashi, K., A. Montecinos, K. Goubanova, and B. Dewitte, 2011: ENSO regimes: Reinterpreting the canonical and Modoki El Niño. *Geophys. Res. Lett.*, **38**, L10 704.

Taschetto, A. S., A. S. Gupta, N. C. Jourdain, A. Santoso, C. C. Ummenhofer, and M. H. England, 2014: Cold Tongue and Warm Pool ENSO Events in CMIP5: Mean State and Future Projections. *J. Climate*, **27**, 2861–2885.

Taylor, K. E., 2001: Summarizing multiple aspects of model performance in a single diagram. *J. Geophys. Res.*, **106**, 7183–7192.

Taylor, K. E., R. J. Stouffer, and G. A. Meehl, 2012: An overview of CMIP5 and the experiment design. *Bull. Amer. Meteor. Soc.*, **93**, 485–498.

Thual, S., B. Dewitte, S. An, and N. Ayoub, 2011: Sensitivity of ENSO to Stratification in a Recharge-Discharge Conceptual Model. *J. Climate*, **24**, 4332–4349.

Timmermann, A. and F.-F. Jin, 2002: Phytoplankton influences on tropical climate. *Geophys. Res. Lett.*, **29**, 2104.

Tollefson, J., 2014: El Niño test forecasters. *Nature*, **508**, 20–21.

Tomczak, M. and S. J. Godfrey, 1994: *Regional Oceanography: An Introduction*. Pergamon Press.

Torrence, C. and P. J. Webster, 1998: The annual cycle of persistence in the El Niño/Southern Oscillation. *Quart. J. Roy. Meteorol. Soc.*, **124**, 1985–2004.

Trenberth, K. E., 1997: The definition of El Niño. *Bull. Amer. Meteor. Soc.*, **78**, 2771–2777.

Trenberth, K. E., G. W. Branstator, D. Karoly, A. Kumar, N.-C. Lau, and C. Ropelewski, 1998: Progress during TOGA in understanding and modeling global teleconnections associated with tropical sea surface temperatures. *J. Geophys. Res.*, **103**, 14 291–14 324.

Trenberth, K. E. and D. P. Stepaniak, 2001: Indices of El Niño evolution. *J. Climate*, **14**, 1697–1701.

Twine, T. E., C. J. Kucharik, and J. A. Foley, 2005: Effects of El Niño-Southern Oscillation on the climate, water balance, and streamflow of the Mississippi River Basin. *J. Climate*, **18**, 4840–4861.

Tziperman, E., M. A. Cane, S. E. Zebiak, Y. Xue, and B. Blumenthal, 1998: Locking of El Niño's peak time to the end of the calendar year in the delayed oscillator picture of enso. *J. Climate*, **11**, 2191–2199.

Tziperman, E., E. Stone, M. Cane, and H. Jarosh, 1994: El Niño chaos: Overlapping of resonances between the seasonal cycle and the Pacific ocean-atmosphere oscillator. *Science*, **264**, 72–74.

Tziperman, E., S. Zebiak, and M. Cane, 1997: Mechanisms of seasonal - ENSO interaction. *J. Atmos. Sci.*, **54**, 61–71.

Uppala, S. M., et al., 2005: The ERA-40 re-analysis. *Quart. J. Roy. Meteorol. Soc.*, **131**, 2961–3012.

Vecchi, G. and D. Harrison, 2000: Tropical Pacific sea surface temperature anomalies, El Niño, and equatorial westerly wind events. *J. Climate*, **13**, 1814–1830.

Vecchi, G. and D. E. Harrison, 2003: On the termination of the 2002-03 El Niño event. *Geophys. Res. Lett.*, **30**, 1964.

Vecchi, G. A., 2006: The termination of the 1997-98 El Niño. Part II: Mechanisms of atmospheric change. *J. Climate*, **19**, 2647–2664.

Vecchi, G. A. and D. E. Harrison, 2006: The termination of the 1997-1998 El Niño. Part I: Mechanisms of oceanic change. *J. Climate*, **19**, 2633–2646.

Vecchi, G. A., A. Rosati, and D. E. Harrison, 2004: Setting the timing of El Niño termination. *Bull. Amer. Meteor. Soc.*, **85**, 1065–1066.

Verbickas, S., 1998: Westerly wind bursts in the tropical Pacific. *Weather*, **53**, 282–284.

Vialard, J., C. Menkes, J. Boulanger, P. Delecluse, E. Guilyardi, M. McPhaden, and G. Madec, 2001: A Model Study of Oceanic Mechanisms Affecting Equatorial Pacific Sea Surface Temperature during the 1997–98 El Niño. *J. Phys. Oceanogr.*, **31**, 1649–1675.

Voisin, N., A. F. Hamlet, L. P. Graham, D. W. Pierce, T. P. Barnett, and D. P. Lettenmaier, 2006: The role of climate forecasts in western U.S. power planning. *J. Appl. Meteorol.*, **45**, 653–673.

Wang, B. and S. An, 2002: A mechanism for decadal changes of ENSO behavior: roles of background wind changes. *Clim. Dyn.*, **18**, 475–486.

Wang, B., R. Wu, and X. Fu, 2000: Pacific-East Asian teleconnection: How does ENSO affect East Asian Climate? *J. Climate*, **13**, 1517–1536.

Wang, B., R. Wu, and R. Lukas, 1999: Roles of the western North Pacific wind variation in thermocline adjustment and ENSO phase transition. *J. Meteor. Soc. Japan*, **77**, 1–16.

Wang, B. and Q. Zhang, 2002: Pacific-East Asian Teleconnection. Part II: How the Philippine Sea Anomalous Anticyclone is Established during El Niño Development. *J. Climate*, **15**, 3252–3265.

Wang, C. and R. H. Weisberg, 2000: El Niño evolution relative to previous El Niño events. *J. Climate*, **13**, 488–501.

Wang, W. and M. J. McPhaden, 1999: The surface layer heat balance in the equatorial Pacific Ocean. Part I: Mean seasonal cycle. *J. Phys. Oceanogr.*, **29**, 1812–1831.

Wang, W. and M. J. McPhaden, 2000: The surface-layer heat balance in the equatorial Pacific Ocean. Part II: Interannual variability. *J. Phys. Oceanogr.*, **30**, 2989–3008.

Wang, W. and M. J. McPhaden, 2001: Surface Layer Temperature Balance in the Equatorial Pacific during the 1997-98 El Niño and 1998-99 La Niña. *J. Climate*, **14**, 3393–3407.

Wang, X., F.-F. Jin, and Y. Wang, 2003: A tropical ocean recharge mechanism for climate variability. Part I: Equatorial heat content changes induced by the off-equatorial wind. *J. Climate*, **16**, 3585–3598.

Webster, P. J., V. O. Magaña, T. N. Palmer, J. Shukla, R. A. Tomas, M. Yanai, and T. Yasunari, 1998: Monsoons: Processes, predictability, and the prospects for prediction. *J. Geophys. Res.*, **103**, 14 451–14 510.

Weisberg, R. H. and C. Wang, 1997: A western Pacific oscillator paradigm for the El Niño-Southern Oscillation. *Geophys. Res. Lett.*, **24**, 779–782.

Welch, B. L., 1947: The Generalization of 'Student's' Problem when Several Different Population Variances are Involved. *Biometrika*, **34**, 28–35.

Weng, H., K. Ashok, and S. K. Behera, 2007: Impacts of recent El Niño Modoki and dry/wet conditions in the Pacific rim during boreal summer. *Clim. Dyn.*, **29**, 113–129.

Wilks, D., 2006: *Statistical Methods in the Atmospheric Sciences*. 2d ed., 627 pp., Elsevier.

Wittenberg, A. T., 2004: Extended Wind Stress Analyses for ENSO. *J. Climate*, **17**, 2526–2540.

Wyrtki, K., 1975: El Niño - The dynamic response of the equatorial Pacific ocean to atmospheric forcing. *J. Phys. Oceanogr.*, **5**, 572–584.

Wyrtki, K., 1985: Water displacements in the Pacific and the genesis of El Niño cycles. *J. Geophys. Res.*, **90**, 7129–7132.

Wyrtki, K. and G. Meyers, 1976: The trade wind field over the Pacific Ocean. *J. Appl. Meteor.*, **15**, 698–704.

Xiao, H. and C. R. Mechoso, 2009: Seasonal cycle - El Niño relationship: validation of hypotheses. *J. Atmos. Sci.*, **66**, 1633–1653.

Xie, P. and P. A. Arkin, 1997: Global precipitation: a 17-year monthly analysis based on gauge observations, satellite estimates, and numerical model outputs. *Bull. Amer. Meteor. Soc.*, **78**, 2539–2558.

Xie, S. P., 1995: Interaction between the annual and interannual variations in the equatorial Pacific. *J. Phys. Oceanogr.*, **25**, 1930–1941.

Xue, Y. and A. Kumar, 2016: Evolution of the 2015/16 El Niño and historical perspective since 1979. *Science China Earth Sciences*, 1–17.

Yamanaka, G., T. Yasuda, Y. Fujii, and S. Matsumoto, 2009: Rapid termination of the 2006 El Niño and its relation to the Indian Ocean. *Geophys. Res. Lett.*, **36**, L07 702.

Yan, B. and R. Wu, 2007: Relative roles of different components of the basic state in the phase locking of El Niño mature phases. *J. Climate*, **20**, 4267–4277.

Yin, Y., O. Alves, and P. R. Oke, 2011: An Ensemble Ocean Data Assimilation System for Seasonal Prediction. *Mon. Wea. Rev.*, **139**, 786–808.

Yoo, S.-H., J. Fasullo, S. Yang, and C.-H. Ho, 2010: On the relationship between Indian Ocean sea surface temperature and the transition from El Niño to La Niña. *J. Geophys. Res.*, **115**, D15 114.

Yu, J. Y. and H. Y. Kao, 2007: Decadal changes of ENSO persistence barrier in SST and ocean heat content indices: 1958–2001. *J. Geophys. Res.*, **112**, D13 106.

Yu, L. and M. M. Rienecker, 1998: Evidence of an extratropical atmospheric influence during the onset of the 1997-98 El Niño. *Geophys. Res. Lett.*, **25**, 3537–3540.

Yu, L., R. A. Weller, and T. W. Liu, 2003: Case analysis of a role of ENSO in regulating the generation of westerly wind bursts in the western equatorial Pacific. *J. Geophys. Res.*, **108**, 3128.

Zavala-Garay, J., A. M. Moore, and R. Kleeman, 2004: Influence of stochastic forcing on ENSO prediction. *J. Geophys. Res.*, **109**, C1107.

Zebiak, S. E., 1989: Oceanic heat content variability and El Niño cycles. *J. Phys. Oceanogr.*, **19**, 475–483.

Zebiak, S. E. and M. A. Cane, 1987: A model of El Niño-Southern Oscillation. *Mon. Wea. Rev.*, **115**, 2262–2278.

Zelle, H., G. Appeldoorn, G. Burgers, and G. J. V. Oldenborgh, 2004: The relationship between sea surface temperature and thermocline depth in the eastern equatorial Pacific. *J. Phys. Oceanogr.*, **34**, 643–655.

Zhang, C., 1996: Atmospheric intraseasonal variability at the surface in the tropical western Pacific Ocean. *J. Atmos. Sci.*, **53**, 739–758.

Zhang, R.-H. and M. Endoh, 1994: Simulation of the 1986-1987 El Niño and 1988 La Niña events with a free surface tropical Pacific Ocean general circulation model. *J. Geophys. Res. Oceans*, **99**, 7743–7759.

Zhang, T. and D.-Z. Sun, 2014: ENSO Asymmetry in CMIP5 Models. *J. Climate*, **27**, 4070–4093.

Zhang, W., Y. Wang, F.-F. Jin, M. F. Stuecker, and A. G. Turner, 2015: Impact of different El Niño types on the El Niño/IOD relationship. *Geophys. Res. Lett.*, **42**, 8570–8576.

Appendix A

Published Article

A copy of the following published manuscript as it appears in the journal is included hereafter. This paper constitutes the material in Part 1.

Abellán, E. and S. McGregor, 2016. The role of the southward wind shift in both, the seasonal synchronization and duration of ENSO events. *Climate Dynamics*, **47**, 509-527, doi: 10.1007/s00382-015-2853-1

Clim Dyn (2016) 47:509–527
DOI 10.1007/s00382-015-2853-1

The role of the southward wind shift in both, the seasonal synchronization and duration of ENSO events

Esteban Abellán[1] · Shayne McGregor[1,2]

Received: 19 March 2015 / Accepted: 24 September 2015 / Published online: 30 October 2015

Abstract Near the end of the calendar year, when El Niño events typically reach their peak amplitude, there is a southward shift of the zonal wind anomalies, which were centred around the equator prior to the event peak. Previous studies have shown that ENSO's anomalous wind stresses, including this southward shift, can be reconstructed with the two leading EOFs of wind stresses over the tropical Pacific. Here a hybrid coupled model is developed, featuring a statistical atmosphere that utilises these first two EOFs along with a linear shallow water model ocean, and a stochastic westerly wind burst model. This hybrid coupled model is then used to assess the role of this meridional wind movement on both the seasonal synchronization as well as the duration of the events. It is found that the addition of the southward wind shift in the model leads to a Christmas peak in variance, similar to the observed timing, although with weaker amplitude. We also find that the added meridional wind movement enhances the termination of El Niño events, making the events shorter, while this movement does not appear to play an important role on the duration of La Niña events. Thus, our results strongly suggest that the meridional movement of ENSO zonal wind anomalies is at least partly responsible for seasonal synchronization of ENSO events and the duration asymmetry between the warm (El Niño) and cool (La Niña) phases.

✉ Esteban Abellán
esteban.abellan@unsw.edu.au

[1] ARC Centre of Excellence for Climate System Science and Climate Change Research Centre, University of New South Wales, Sydney, NSW, Australia

[2] School of Earth, Atmosphere and Environment, Monash University, Clayton, VIC, Australia

Keywords ENSO · Southward wind shift · Seasonal synchronization · HCM · Termination · Asymmetry

1 Introduction

The El Niño-Southern Oscillation (ENSO) phenomenon is the main driver of Earth's interannual climate variability (Neelin et al. 1998; McPhaden et al. 2006), leading to significant changes in the global atmospheric circulation (Ropelewski and Halpert 1989; Philander 1990; Trenberth et al. 1998; Wang et al. 2003). ENSO refers to a year-to-year recurring warming (El Niño) and cooling (La Niña) of the eastern and central tropical Pacific sea surface temperature (hereafter SST), and a related large-scale seesaw in atmospheric sea level pressure between the Australia-Indonesian region and the south-central tropical Pacific (Bjerkness 1969; Wyrtki 1975; Cane and Zebiak 1985; Graham and White 1988).

El Niño and La Niña events typically last for about a year and have an irregular period ranging between 2 and 7 years. As every winter or summer is different in the extratropics, ENSO events come in many different flavours (Trenberth and Stepaniak 2001). However, they generally follow a similar pattern of developing during boreal spring (MAM), peaking in boreal winter (DJF) and decay during boreal spring of the following year (Rasmusson and Carpenter 1982; Larkin and Harrison 2002; Chang and Coauthors 2006). Understanding the physical processes responsible of such seasonal synchronization is of central importance to predictions (Balmaseda et al. 1995; Torrence and Webster 1998), simulations (Ham et al. 2013) as well as impacts of ENSO, which depend on the characteristics of the events (Trenberth 1997).

However, the dynamics underlying ENSO synchronization to the annual cycle is not yet understood. Recently, Stein et al. (2014) classified existing theories into two possible categories: (1) frequency locking of ENSO, as a nonlinear oscillator, to periodic forcing by the annual cycle (e.g., Jin et al. 1994; Tziperman et al. 1994); or (2) the modulation of the stability of ENSO due to the seasonal variation of the background state of the equatorial Pacific (Philander et al. 1984; Hirst 1986). Their results suggest that the annual modulation of the coupled stability of the equatorial Pacific ocean-atmosphere system is by far the more likely mechanism generating the synchronization of ENSO events to the annual cycle (Stein et al. 2014). Thus, below we will provide a brief description of the main theories that fall into this category.

One of the earliest suggestions about the tendency of ENSO seasonal synchronization was reported by Philander (1983), who suggested the seasonal movement of the Pacific intertropical convergence zone (ITCZ), and its effect on the atmospheric heating, (i.e. the coupled instability strength) as the responsible for ENSO's onset, hence for such seasonal synchronization. Furthermore, Hirst (1986) noted that other seasonal climatological factors that might enhance the coupled instability of the system are strong zonal wind in July–August, shallow thermocline in September–October, large zonal equatorial SST gradient in September, and high SST over the central equatorial Pacific in May. Subsequently, Battisti (1988) added to the previous list the influence of some weakening of oceanic upwelling in the central Pacific during March–May and some strengthening of the coastal upwelling in the eastern Pacific during August–September. Tziperman et al. (1997) found that the dominant factor in determining the strength of the ocean-atmosphere instability to be due to the seasonal wind convergence (i.e., the ITCZ location), while Yan and Wu (2007) work suggested that the seasonal change in the mean SST is the predominating factor. The results of Galanti et al. (2002) were partly consistent with those of Hirst (1986), suggesting that the seasonal ocean-atmosphere coupling strength is influenced by the outcropping of the east Pacific thermocline during the second half of the year. Inter-basin teleconnections have also recently been implicated in the termination of ENSO events. As one example, some studies indicate that the basin warming of the tropical Indian Ocean is responsible for the weakening or reversal of equatorial westerly wind anomalies over the western Pacific at the mature phase of El Niño (Annamalai et al. 2005; Kug and Kang 2006; Obha and Ueda 2007, 2009; Yamanaka et al. 2009; Yoo et al. 2010). Finally, another mechanism, which involves meridional changes in the coupled ocean-atmosphere wind system and thought as a major negative feedback playing a role in the decay of El Niño events, will be emphasized below.

This paper focuses on the southward wind shift theory proposed by Harrison and Vecchi (1999) and Vecchi and Harrison (2003) as a major negative feedback involved in the phase synchronization between ENSO and the annual cycle. During El Niño events, the associated westerly wind anomalies are centred quite symmetric about the equator prior to the event peak (SON) whereas there is a shift of these anomalies towards south of the equator during the mature phase (DJF), with anomalous northerly winds developing north of the equator (Fig. 1). The magnitude of this southward wind shift appears to be dependent on the magnitude of the ENSO event, as suggested by Lengaigne et al. (2006). For instance, during DJF of strong El Niño events there is a strong southward movement along with movement towards east, with the maximum amplitude of the anomalous westerly winds shifting from date line in SON, to 160°W in DJF (Fig. 1 top). In contrast, during DJF of moderate El Niño events there is a much smaller southward wind shift, consistent with the findings of McGregor et al. (2013) who utilised multiple reanalysis products, and virtually no zonal movement of the anomalous westerlies (Fig. 1 middle). The zonal and meridional movement observed with easterly wind anomalies during La Niña events largely mirror for moderate El Niño events (Fig. 1 bottom), although with southerly winds developing north of the equator. These composite analyses shown in Fig. 1 are in broad agreement with those reported by Okumura and Deser (2010), where a different atmospheric reanalysis product was used.

This shift in wind anomalies has been studied by Harrison (1987), Harrison and Larkin (1998), Harrison and Vecchi (1999), Vecchi and Harrison (2003); and more recently it has been proposed to explain the seasonal synchronization since the resulting reduction of equatorial westerly wind anomalies has been shown to drive: (1) strong thermocline shoaling in the eastern equatorial Pacific (e.g., Harrison and Vecchi 1999; Vecchi and Harrison 2003, 2006; Lengaigne et al. 2006; Lengaigne and Vecchi 2009); (2) changes in equatorial warm water volume (WWV) (McGregor et al. 2012a, 2013) and (3) interhemispheric exchanges of upper ocean mass (McGregor et al. 2014). This shift has been linked to the southward displacement of the warmest SSTs and convection during DJF (Lengaigne et al. 2006; Vecchi 2006), and the associated minimal surface momentum damping of wind anomalies (McGregor et al. 2012a), both of which are due to the seasonal evolution of solar insolation. McGregor et al. (2013) also show that the discharging effect of the southward wind shift increases with increasing El Niño amplitude, while remaining relatively small regardless of La Niña amplitude. They suggest that this aspect may also help explain the ENSO phase duration asymmetry (i.e., why El Niño events have a shorter duration than La Niña events).

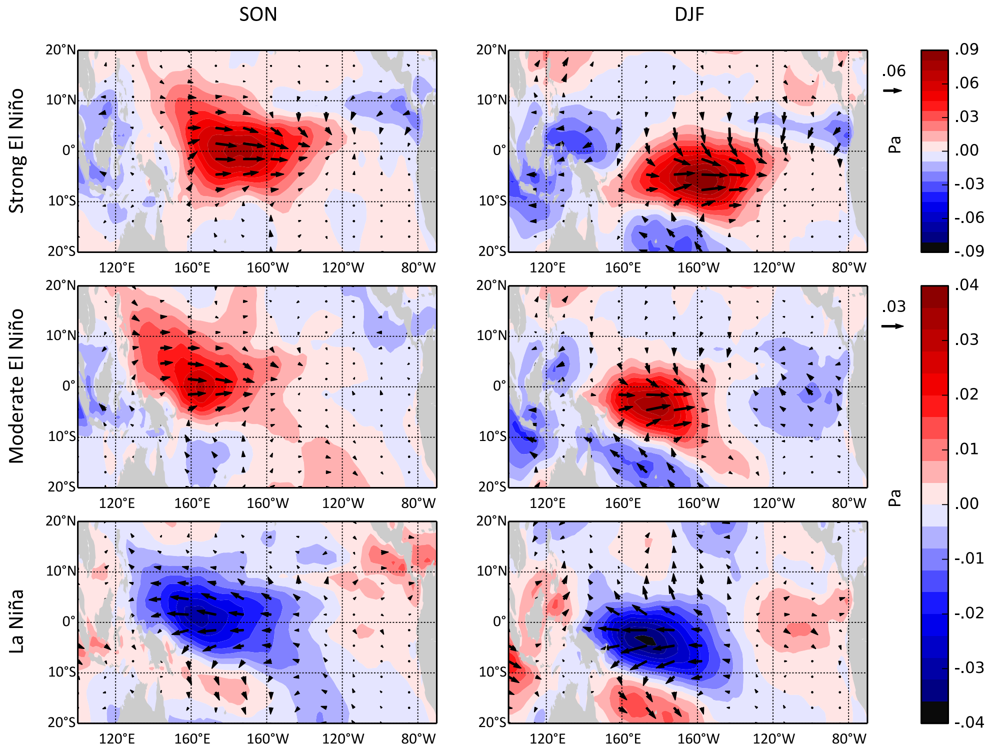

Fig. 1 Composites of wind stress anomalies during strong El Niño events (*top*), moderate-weak El Niño events (*middle*), and La Niña events (*bottom*). The anomalies are averaged from September to November during year 0 (*left*), and from December to February during year +1 (*right*). *Shading* indicates zonal components. Strong El Niño years: 1982/83 and 1997/98. Moderate-weak El Niño years: 1987/88, 1991/92, 1994/95, 2002/03, 2004/05, 2006/07 and 2009/10. La Niña years: 1984/85, 1988/89, 1995/96,1999/00, 2000/01, 2007/08, 2010/11 and 2011/12. See Sect. 2.1 for the ENSO definition

The purpose of this study is to single out the meridional wind movement of ENSO winds from the other possible mechanisms detailed above, and identify its role in the synchronization of ENSO events to the seasonal cycle. We also examine whether the ENSO phase asymmetry observed in this shift can account for the fact that La Niña events tend to persist for longer periods than El Niño (Okumura et al. 2011). Specifically, a simple hybrid coupled model (HCM), which utilises a statistical atmospheric that is able to function with and without the southward wind shift, is developed. We find that this meridional wind movement plays a crucial role in the seasonality of ENSO events since its inclusion in the model results in a moderate synchronization of modeled ENSO events to the seasonal cycle with maximum of SST anomalies (SSTA hereafter) in November–January. Additionally, we show that the duration of warm events is influenced by this shift, with the meridional wind movement favouring the early termination, while the duration of cool events appears to be marginally dependent on whether and how the shift is included in the model.

The rest of the paper is organized as follows. In the next section we shall present the SST dataset used and the two leading empirical orthogonal functions (EOFs) of wind stresses over the tropical Pacific, Sect. 3 describes the 3-component hybrid coupled model developed in this study. Sections 4 and 5 present our experiment results, with the large 1997/98 El Niño and 4-member ensemble of 100-year runs respectively, carried out with and without this southward wind shift and how sensitive the response of thermocline depth and, consequently, SSTA result. Finally, a discussion of the major findings is presented in Sect. 6.

2 Data

2.1 SST data

This study employs the monthly Niño-3.4 and Niño-3 indexes (namely SSTA averaged in the region 5°S–5°N, 170°W–120°W, and 5°S–5°N, 150°W–90°W, respectively) derived from extended reconstructed SST (ERSST v3b) dataset (Smith et al. 2008) for the period 1979–2013 when wind stress data are required (Sects. 1 and 2) and for the period 1880–2013 when wind stresses are not required (Sect. 5). It is important to mention that the anomalies were computed with respect to a 1971–2000 monthly climatology. Here, we define an ENSO event when Niño-3.4 index is either above 0.5 °C (warm events) or below −0.5 °C (cool events) for at least 5 consecutive months after a 3-month binomial filter applied, as in Deser and Coauthors (2012) to reduce month-to-month noise. Strong El Niño events are identified when their peak magnitudes are greater than 2.0 °C, as Lengaigne et al. (2006). Further, this El Niño classification according to their magnitudes has been used in numerous other studies (e.g., Lengaigne and Vecchi 2009; Takahashi et al. 2011; Chen et al. 2015)

It is also worth noting that the results of the southward wind shift during ENSO events are qualitatively similar if we instead differentiate between Eastern Pacific (EP) and Central Pacific (CP) type ENSO events rather than event magnitude, consistent with McGregor et al. (2013).

2.2 Wind stress decomposition

In order to determine the dominant patterns associated with interannual wind changes, an empirical orthogonal function (EOF) analysis of wind stresses over the tropical Pacific (10°S–10°N and 100°E–70°W) is performed. Observational wind data is taken from the European Centre for Medium-Range Weather Forecasts (ECMWF) Interim Reanalysis (ERA-interim) (Dee and Uppala 2009). We first obtain the daily average wind data that span the period 1979–2013, the surface winds are then converted to wind stresses using the quadratic stress law (Wyrtki and Meyers 1976):

$$(\tau_x, \tau_y) = C_D \rho_a W(U, V) \tag{1}$$

where U and V are the zonal and meridional surface winds (m s^{-1}) respectively; W denotes the surface wind speed (m s^{-1}), $C_D = 1.5 \times 10^{-3}$ is the dimensionless drag coefficient; and $\rho_a = 1.2$ kg m^{-3} represents the atmospheric density at the surface. The monthly mean wind stresses are calculated from the daily wind stresses and wind stress anomalies are computed by removing the monthly climatology of the entire 35-year of record.

As in previous studies (McGregor et al. 2012a, 2013; Stuecker et al. 2013), the global spatial patterns of the first two EOFs are obtained by regressing the associated principal component (PC) time series onto the anomalous wind stress at each spatial location. The first EOF (EOF1), which accounts for 33 % of the equatorial region variance, features positive zonal wind anomalies in the western-central tropical Pacific (i.e., anomalous Walker circulation) that have their maximum amplitude south of the equator (Fig. 2a). It is clear that EOF1 represents ENSO variability since the correlation coefficient between this leading PC time series and SSTA averaged over the Niño-3 region (5°S–5°N and 150°–90°W) is 0.76.

Regarding the second mode (EOF2), which explains 16 % of the equatorial region variance, the associated regression patterns are largely meridionally asymmetric featuring a prominent anticyclonic circulation in the western north Pacific region (Fig. 2b) consistent with the Philippine Anticyclone (e.g., Wang et al. 1999). Furthermore, EOF2 captures westerlies located south of the equator, around the same region as the maximum anomalies during DJF of El Niño events (Fig. 1 top). As it will be shown later in this section, this second mode is related to the southward wind shift, although as expected by the definition of the EOF

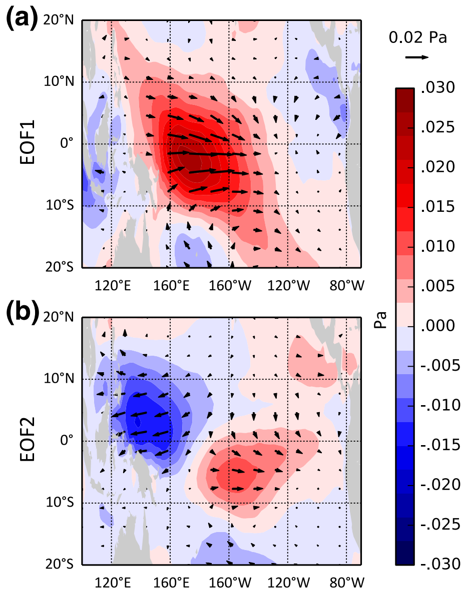

Fig. 2 The spatial pattern of surface wind stresses from **a** EOF1 and **b** and EOF2, which account for approximately 33 and 16 % of the total variance over the tropical Pacific region, respectively. The *shading contours* represent the zonal components

analysis (e.g., Lorenz 1956), there is only a weak linear relationship (r = 0.20) between the EOF2 time series (PC2) and ENSO (Niño-3 index). Interestingly however, PC2 has been linked to ENSO (McGregor et al. 2012a) as well as shown to play a prominent role in the recharge/discharge of equatorial region WWV (McGregor et al. 2013) and inter-hemispheric exchanges (McGregor et al. 2014).

Composites of PC1 around ENSO events reveal that event development occurs from Mar^0–May^0, and reaches the maximum amplitude near the end of the calendar year (Fig. 3). It is worthwhile to note the subtle differences between strong and moderate or weak El Niño events, where the maximum PC1 amplitudes in strong warm events tend to be stronger that seen during moderate events and zero values during moderate events are reached around 3 months before in strong events.

The composite of PC2 for warm events reveals a striking difference between the two types magnitudes of El Niño. For instance, PC2 during strong events changes sign dramatically around the mature phase (moderate negative prior and strong positive after), while PC2 values during moderate events tend to be negative prior to the mature phase and remain roughly zero thereafter (Fig. 3a). The evolution of PC2 during La Niña events is roughly mirrors that of moderate El Niño events, displaying positive values prior to event peak, which remain approximately zero thereafter (Fig. 3b).

These EOF results are consistent with the composites of wind stress anomalies shown in Fig. 1. For instance, PC1

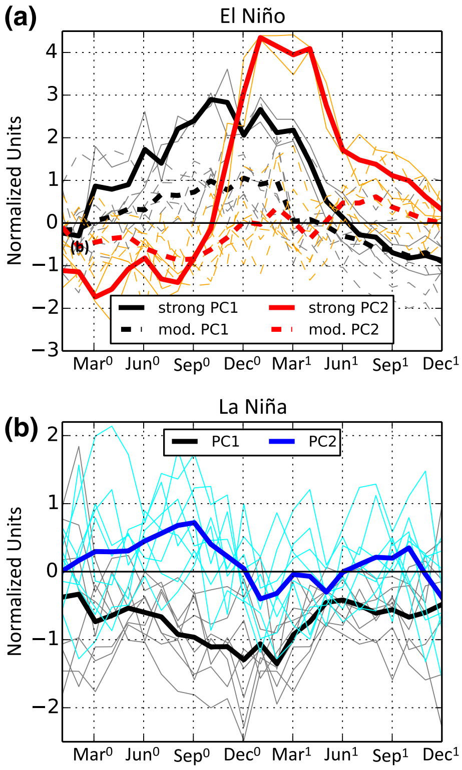

Fig. 3 Time series of the wind stresses PC1 and PC2 overlaid from Jan^0 to Dec^1 for **a** El Niño and **b** La Niña during 1979–2013. Each of the events is represented by an *individual line*, and the *thick lines* represent the mean values. Note the different scaling of the y-axes

(PC2) is positive (negative) during SON for El Niño events leading to westerly anomalies that are quasi-symmetric around the equator since the EOF2 anomalies of wind stress are positive over the Philippine region. If we analyse what occurs during DJF, we find that the maximum westerly anomalies in strong El Niño events are shifted southeastward towards the same area represented by the westerlies in the EOF2 pattern (Fig. 2b), consistent with the high positive values of PC2. During SON in both moderate El Niño and all La Niña events, PC1 and PC2 display anomalies of the same sign which ensures that the anomalies are largely symmetric about the equator, consistent with the observed composites (Fig. 1). The pattern observed for both moderate El Niño and all La Niña events during DJF (Fig. 1) is quite similar to EOF1 (Fig. 2a), which is in good agreement with PC2 values shown to be close to zero (Fig. 3). Therefore, in agreement with the previous studies of McGregor et al. (2012a, 2013) the combination of these two leading EOFs can be viewed to represent this southward shift of zonal wind stress anomalies during both El Niño and La Niña. It is worth emphasizing that McGregor et al. (2013) utilised eight global wind products, ERA-interim among others, finding a very similar spatial patterns and temporal variability for the two leading EOF modes amongst all data sets (see their Fig. S1 and Table S1).

3 Coupled model description

In this section, we describe the components of the hybrid coupled model which has been developed in this project with the objective of exploring the role of the southward wind shift in the synchronization of ENSO events to the seasonal cycle.

3.1 Ocean model

The ocean model utilised here is a shallow-water model (SWM), whose name refers to the fact that the horizontal scale of the planetary scale waves (100–1000 km) is much larger than the vertical scale (ocean depth ~4 km), which allows the Navier-Stokes equations to be simplified considerably. It is a linear reduced-gravity model resolved on a 1° × 1° spatial grid for the low- to mid-latitude global ocean between 57°S–57°N and 0°–360°E. The density structure of the $1\frac{1}{2}$-layer baroclinic system consists of a well mixed active upper layer of uniform density overlaying a deep motionless lower layer of larger uniform density. These ocean density layers are separated by an interface (the pycnocline) that provides a good approximation of the thermocline. This is a crucial consequence as it allows us to quantify the upper-ocean heat content (e.g. Rebert et al. 1985), i.e., the warm-water volume (Meinen and McPhaden 2000), and provide an estimate of equatorial SSTA (e.g., Kleeman 1993; Zelle et al. 2004).

The ocean dynamics are described by the linear reduced-gravity form of the shallow-water equations detailed below [Eqs. (2)–(4)]:

$$u_t - fv + g'\eta_x = \frac{\tau^x}{\rho H} + F_m \tag{2}$$

$$v_t + fu + g'\eta_y = \frac{\tau^y}{\rho H} + F_m \tag{3}$$

$$g'\eta_t + c_1^2(u_x + v_y) = 0 \tag{4}$$

where u and v are the eastward and northward components of velocity respectively (m s^{-1}), t is time (s), H represents the mean pycnocline depth, $H = 300$ m (Tomczak and Godfrey 1994, p. 37), f (s^{-1}) is the Coriolis parameter, ρ is the ocean water density, $\rho = 1000$ kg m^{-3}, and F_m the bottom friction per unit mass. The reduced gravity, g', reflects the density difference between the upper and lower layers. We use the typical value of $g' = 0.026$ m s^{-2} (Tomczak and Godfrey 1994, p. 37). The corresponding first baroclinic mode gravity wave speed, $c_1 = \sqrt{g'H}$), is 2.8 m s^{-1}. The long Rossby wave speed C_R (m s^{-1}) is given by the equation, $C_R = \beta(c_1^2/f^2)$, where β (m^{-1} s^{-1}) is the derivative of f northward.

The model time step is 2 h and Fischer's (1965) numerical scheme is utilized for model time stepping. Motion in the upper layer is driven by the applied wind stresses (per unit density), τ (m^2 s^{-2}), which are anomalies from long-term monthly means (i.e., seasonal cycle removed). The associated response of the ocean is displayed by the vertical displacement of the thermocline, η (m), and the horizontal velocity components (u and v) of the flow velocity. This model formulation permits Ekman pumping and both Rossby and Kelvin wave propagation along the thermocline to be generated with appropriate large-scale wind stress forcing. It also includes realistic continental boundaries that were calculated as the location where the bathymetric dataset of Smith and Sandwell (1997) has a depth of less than the model mean thermocline depth of 300 m.

Regarding the calculation eastern-central Pacific SSTA, we utilise a simplified version Kleeman's (1993) SST equation by applying the thermocline anomaly term only. Kleeman (1993) shows that this single term is primarily responsible for hindcast skill in ENSO predictions. Thus, while being the simplest scheme, it contains the essential physics required to produce realistic SSTA. Hence, the equatorial SSTA depends only on the thermocline depth anomaly. Changes in the SSTA on the equator are modeled by the equation

$$T_t = \alpha(x)\eta(x) - \epsilon T \tag{5}$$

where T is the SSTA at time t, ϵ is the Newtonian cooling coefficient, $\epsilon = 2.72 \times 10^{-7}$ s^{-1}, x is the longitude and α is a longitude-dependent parameter that relates the modeled oceanic thermocline depth displacement η along the equator to the SSTA, being $\alpha = 3.4 \times 10^{-8}$ °C m^{-1}s^{-1} in the eastern Pacific and reducing linearly west of 140°W to a minimum of $\alpha/5$ at the western equatorial boundary at 120°E. Such a difference reflects the fact that the equatorial thermocline depth anomalies display a tighter connection with SSTA in the east than the west (Zelle et al. 2004). For the rest of latitudes, a fixed meridional structure that decays away from the equator with an e-folding radius of 10° is assumed. Taking into account the non-linear relationship between central Pacific zonal wind stress anomalies and Niño-3 index as reported by Frauen and Dommenget (2010), the parameter α is reduced by 20 % for negative SSTA in Niño-3 region. In addition, a threshold of 37.5 m is set on the maximum absolute depth of equatorial thermocline anomalies in order to prevent runaway coupled instability.

It is also worthwhile to mention that the use of this simplified SST equation implies that each of these HCMs can generate only EP El Niño and La Niña events, i.e. only one EOF of SSTA. Therefore, the results of these HCM simulations will not distinguish between EP-CP event differences. It has been documented in several studies that this ocean model can produce observed variations of ocean heat content and sea surface heights reasonably well (e.g., McGregor et al. 2012a, b). Furthermore, a validation of this ocean model was carried out by simply forcing the model with ERA-interim monthly wind stress anomalies over 1979–2013. The modeled Niño-3 and Niño-3.4 indexes were then compared with those observed during the same period revealing correlation coefficients of 0.83 and 0.82, respectively (statistically significant above the 99 % level).

3.2 Statistical atmospheric model

The statistical atmosphere has been constructed by the two leading EOFs of wind stresses over the tropical Pacific. It has been shown above that the linear combination of both EOFs can reproduce quite well the southward shift of the maximum westerly wind anomalies and its related seasonal weakening of equatorial westerly wind anomalies, both of which have been proposed to contribute to the transition between El Niño and La Niña (e.g., Harrison and Vecchi 1999; Vecchi and Harrison 2003, 2006; Lengaigne et al. 2006; McGregor et al. 2012a, 2013).

The statistical atmospheric model is coupled to the ocean SWM to produce three hybrid coupled models (HCM): HCM1 consists of EOF1 only (i.e., no meridional wind movement); HCM1+2 and HCM1+2$_S$ include both EOF1 and EOF2 (i.e., they both produce meridional wind movement). In all cases, the EOF1 coupling is achieved by modelling the EOF1 surface wind stress response by:

$$(\tau_1^x, \tau_1^y) = PC1(t) \times (EOF1^x, EOF1^y) \tag{6}$$

where $PC1$ is approximated by the modeled Niño-3 index. The close relationship between these two variables was noted earlier.

The method used to calculate PC2 in HCM1+2 is a least squares second-order polynomial fit from PC1 for each calendar month (month),

$$(\tau_2^x, \tau_2^y) = PC2(PC1, month) \times (EOF2^x, EOF2^y) \tag{7}$$

where we use the two closest months to our month of interest (e.g., data taken for February, includes January and March also) in order to obtain a smooth transition of PC2 values from one month to another (Fig. 4). The second-degree polynomial function is of the form,

$$PC2 = a \cdot PC1^2 + b \cdot PC1 \tag{8}$$

where a and b depend on calendar month. The small independent term is set to zero in order to remove any seasonal cycle in EOF2. A full list of quadratic polynomial

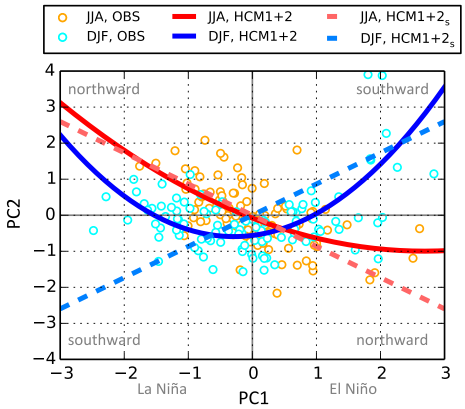

Fig. 4 Scatterplot of the wind stress PC2 against PC1 based on the observations (1979–2013) for two 3-month periods: June–August (*orange dots*); and December–February (*light blue dots*). The underlying solid (*dashed*) lines represent the regression used in HCM1+2 (HCM1+2$_S$). See text for the description of the two hybrid coupled model represented in this panel. The directions indicated on the corners in *gray mark* the direction of the meridional movement of ENSO wind anomalies

coefficients as well as their correlation coefficients and RMSE for each calendar month are given in Table 1.

The method used to calculate PC2 in HCM1+2$_S$, on the other hand, is based on a climate mode that emerges through the atmospheric non-linear interaction between ENSO and the annual cycle known as C-mode (Stuecker et al. 2013, 2015). Here PC2 wind stresses are calculated by,

$$(\tau_2^x, \tau_2^y) = PC2_S \times (EOF2^x, EOF2^y) \tag{9}$$

where $PC2_S = PC1(t) \times \cos(\omega_a\, month - \varphi)$ refers to PC2 simple, which comes from the lowest-order term of the atmospheric nonlinearity. Here ω_a denotes the angular frequency of the annual cycle, $\omega_a = 2\pi/12$ rad month^{-1} and φ represents a one-month phase shift, $\varphi = 2\pi/12$ rad. How well observed data fit this HCM for each calendar month is indicated by RMSE and correlation coefficients in Table 1.

It is clear that the relationship between PC1 and PC2 values depends strongly on calendar month (Fig. 4). The relationship between the pair is quasi-linear during JJA, with increasing values of PC1 being related to decreasing values of PC2. The relationship during DJF, on the other hand, displays a clear non-linearity with PC2 values increasing for increasing positive values of PC1, while the PC2 amplitude also appears to increase for decreasing negative values of PC1. Thus, the seasonal difference between the relationship between PC1 and PC2 is most pronounced for strong El Niño events (high values of PC1). Such behaviour is represented reasonably well by the HCM1+2 configuration (Fig. 4); for instance, for strong El Niño events ($2 <$ PC1< 3), PC2 prior to the event peak (JJA) has values around minus unity, while around the event peak (DJF) PC2 is between two and three, which is consistent with the sign change shown in Fig. 3a. Interestingly, however, such a strong seasonal change is not observed in moderate El Niño events (PC1 ~1) and La Niña events (PC1< 0), which is consistent with the ENSO phase and type asymmetry reported by Lengaigne et al. (2006). This ENSO phase and type non-linearity is not represented, however, in HCM1+2$_S$ where the relationship between PC2 and PC1 is linear regardless the calendar month (Fig. 4). Thus, the HCM1+2 simulations only have a weak southward wind shift during La Niña events, while the HCM1+2$_S$ simulations have a strong southward wind shift and the magnitude of the easterlies are also stronger.

Reconstructing PC2 with the polynomial fit of HCM1+2 and comparing with PC2 from the observations reveals a correlation coefficient of 0.61, while doing the same analysis for the HCM1+2$_S$ reconstructed PC2, reveals a correlation coefficient of 0.42. Thus, here we consider HCM1+2 as the more realistic experimental set up and HCM1+2$_S$ as the idealized southward wind shift, with RMSE 0.66 and 0.70 in JJA; and 0.83 and 1.20 in DJF, respectively (see Table 1 for the rest of calendar months). However, due to lack of data for strong negative SSTA over the eastern

Table 1 Polynomial parameters of $PC2 = a \cdot PC1^2 + b \cdot PC1$ used in HCM1+2 simulations for each calendar month as well as correlation coefficient and root mean squared error (RMSE) of HCM1+2 and HCM1+2$_S$

Parameter	Jan	Feb	Mar	Apr	May	Jun	Jul	Aug	Sep	Oct	Nov	Dec
a	0.38	0.46	0.49	0.53	0.30	0.13	0.13	0.09	0.14	0.18	0.17	0.27
b	0.22	0.17	0.11	−0.06	−0.19	−0.47	−0.68	−0.70	−0.62	−0.48	−0.20	0.03
r(HCM1+2)	0.70	0.71	0.58	0.46	0.24	0.36	0.61	0.69	0.71	0.61	0.40	0.56
RMSE(HCM1+2)	0.83	0.89	1.05	1.05	0.98	0.79	0.66	0.61	0.56	0.61	0.77	0.85
r(HCM1+2$_S$)	0.42	0.45	0.33	0.18	−0.01	0.34	0.59	0.68	0.66	0.47	0.14	0.24
RMSE(HCM1+2$_S$)	1.20	1.27	1.30	1.18	1.00	0.80	0.70	0.69	0.69	0.71	0.84	1.05

Note that the highest (lowest) values of RMSE are obtained around March (September) in both simulations, with differences roughly 30 % between HCM1+2 and HCM1+2$_S$ during January–February, being the former with lower values for all calendar months, although no significant difference is seen between the two HCMs during May–August. However, the strongest (weakest) relationship between PC2 and PC1 are obtained during boreal winter and summer (spring and autumn) for both HCMs equatorial Pacific for our analysis period, we take both methods into consideration in order to examine the sensitivity of the HCM results.

3.3 Westerly wind burst model

Westerly wind activity has been shown to play an important role in the onset of El Niño events (Latif et al. 1988; Kerr 1999; Lengaigne et al. 2004; McPhaden 2004). These wind events, known as westerly wind bursts (WWB), force downwelling Kelvin waves, which propagate to the eastern equatorial Pacific and ultimately act to warm SST there, potentially initiating the event (e.g., Giese and Harrison 1990, 1991). Equatorial westerly wind activity has been associated with tropical cyclones (Keen 1982), cold surges from midlatitudes (Chu 1988), the convectively active phase of the Madden–Julian oscillation (Chen et al. 1996; Zhang 1996), or a combination of all three (Yu and Rienecker 1998).

Although different definitions have been proposed to diagnose WWB from observations (e.g., Harrison and Vecchi 1997; Yu et al. 2003; Eisenman et al. 2005), there is a broad agreement that it can be represented roughly by a Gaussian shape in both space and time,

$$u_{\mathrm{wwb}}(x,y,t) = Aexp\left(-\frac{(t-T_0)^2}{T^2} - \frac{(x-x_0)^2}{L_x^2} - \frac{(y-y_0)^2}{L_y^2}\right) \tag{10}$$

where x_0 (160°) and y_0 (0°) are the central longitude and latitude of the wind event, T_0 (10 days) is the time of peak wind, A is the peak wind speed, T (10 days) represents the event duration, and L_x (20°) and L_y (9°) are the spatial scales. The values of these parameters are set here to obtain realistic values of wind stresses over the western Pacific (Niño-4 region). In regards to their frequency, Eisenman et al. (2005) found and average of 3.1 westerly wind events (WWEs) per year during 1990–2004, Gebbie et al. (2007) identified an average of 3.6 WWEs per year during 1979–2002 and Verbickas (1998) found 3.8 WWEs per year during 1979–1997.

In Sect. 5 we incorporate WWB into the HCM by utilising the WWB equation above, and having the probability of a WWB beginning on any given day set a fixed parameter which depends on the simulation set up. This means that we have WWBs that are purely stochastic, with the different parameter choice simply modulating the rate of WWB occurrence and their magnitude. Although it has been increasingly recognized that WWB are partially modulated by the SST field and partially dependent upon stochastic processes in the atmosphere (e.g., Kessler and Kleeman 2000; Eisenman et al. 2005; Gebbie et al. 2007), here WWB are represented by purely stochastic way due to the simplicity of our SSTA formulation (Gebbie and Tziperman 2009). Nevertheless, this paper is not about the response of El Niño events to different flavours of WWB. Rather, the intent of this paper is to focus on the role of the southward wind shift on the termination of ENSO events.

4 Response of the hybrid coupled models to observed WWBs

This first experiment is initiated by forcing all three hybrid coupled model versions with ERA-interim wind stress anomalies during the 16-month period (January 1996–April 1997). These are the anomalous wind stresses prior to the 1997/98 extreme El Niño, that contain numerous WWBs thought to initiate the event (McPhaden 1999). Each models statistical atmosphere and WWB components are inactive during this initial forcing period, and after this forcing period only the statistical atmospheric component is activated. Each of these simulations is then run for ten years after coupling, although SSTA in Niño-3 region are only plotted until December 2000 in Fig. 5 because the remaining evolution lacks importance.

Visual analysis of the model SSTA reveals, (1) that in its current configuration all three model versions are in a damped oscillatory state, and (2) that all three model versions do a reasonable job reproducing the 1997/98 El Niño peak. This last point is not noted to suggest predictive skill; it is the difference between each of these three model configurations that is of interest. First of all, the El Niño peak magnitudes in HCM1+2 and HCM1+2$_S$ are stronger than in HCM1. Secondly, normal values (i.e. SSTA = 0 °C) after the warm event are reached up to 3 months earlier in HCM1+2 compared to HCM1 and HCM1+2$_S$. This suggests that the addition of EOF2 in HCM1+2 allows El Niño events to terminate more abruptly, while it also makes

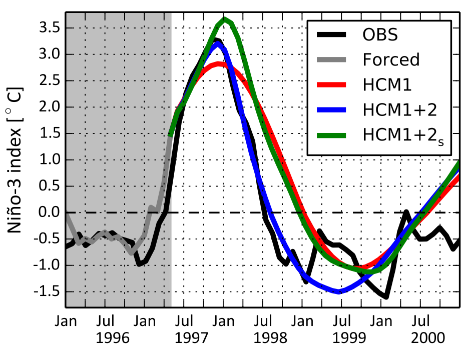

Fig. 5 Time series of SSTA in Niño-3 region for the period 1996–2000 in observations (*black line*), forced run (*gray line*) with wind stress anomalies observed during 16-month period, and coupled runs to HCM1 (*red line*), HCM1+2 (*blue line*), and HCM1+2$_S$ (*green line*)

the HCM1+2 temperature evolution more consistent with that observed (Fig. 5). Due to the huge growth of the event in HCM1+2$_S$, its effective termination occurs at similar time to HCM1 although the rate change of the SSTA of HCM1+2$_S$ is as strong as that seen in HCM1+2.

Such differences among the three HCM time series are due to the fact that the both magnitude and spatial distribution of zonal wind stresses are distinct. Figure 6 displays contour maps of zonal wind stress anomalies during ASO of 1997 (left column) and FMA of 1998 (right column) for the observations and the three HCM simulations. The magnitudes of western equatorial Pacific westerlies during the growth phase (ASO) in simulations with EOF2 (HCM1+2 and HCM1+2$_S$) are stronger than in that with EOF1 only (Fig. 6), and consistent with expectations the subsequent eastern equatorial Pacific warming is stronger (e.g., Vecchi and Harrison 2000). After the mature of phase of the large 1997/98 El Niño, however, the maximum peaks of westerlies in HCM1+2 and HCM1+2$_S$ are moved to central Pacific as observed (Fig. 6) and more importantly shifted south of the equator (~5°S). It is worth highlighting that the southward wind shift that occurs within this period is linearly related to the NDJ discharge of heat content (McGregor et al. 2013). Thus, the HCM1+2 and HCM1+2$_S$ simulations are expected to discharge equatorial heat content much faster than HCM1, which has a fixed structure, ultimately leading to the more abrupt termination of the El Niño event, as shown here.

4.1 Perpetual month experiments

Previous literature (e.g., Zebiak and Cane 1987) has suggested that the seasonal changes of the Pacific's background state may be considered as a seasonal modulation of the coupling strength between the ocean and the atmosphere. Here, we will not be considering the changes in background state explicitly, rather we will be considering changes in the surface wind response to ENSO (the southward wind shift) which can be deemed a product of the background state changes (e.g., Vecchi and Harrison 2006; McGregor et al. 2012a). Thus, in order to further examine the variability of the background stability in each calendar month, we have run a series of 12 perpetual month experiments with HCM1+2, in which the relationship between PC1 and PC2 was fixed to a given calendar month (i.e., PC2 is a function of PC1 only, while the coefficients which would vary with month are fixed to the prescribed month regardless the current calendar month of the simulations). Each of these 12 experiments (one for each calendar month) are initiated by forcing with wind stress anomalies observed from ERA-interim during a 16-month period (January 1996–April 1997). As above, each models statistical atmosphere and WWB components are inactive during this initial forcing period, and after this forcing period only the statistical atmospheric component is activated.

Here, as in Tziperman et al. (1997), we think of the amplitude of the resulting El Niño event as a rough measure of the coupling strength, or stability or the background state where a higher amplitude El Niño indicates more unstable background state or stronger coupling strength. In Fig. 7a we present the Niño-3 index and WWV anomaly, where WWV is defined as the volume of water above the thermocline between 5°S–5°N and 120°E–80°W, from the two most extreme calendar months (January and July) of HCM1+2. It is noted that January has the weakest

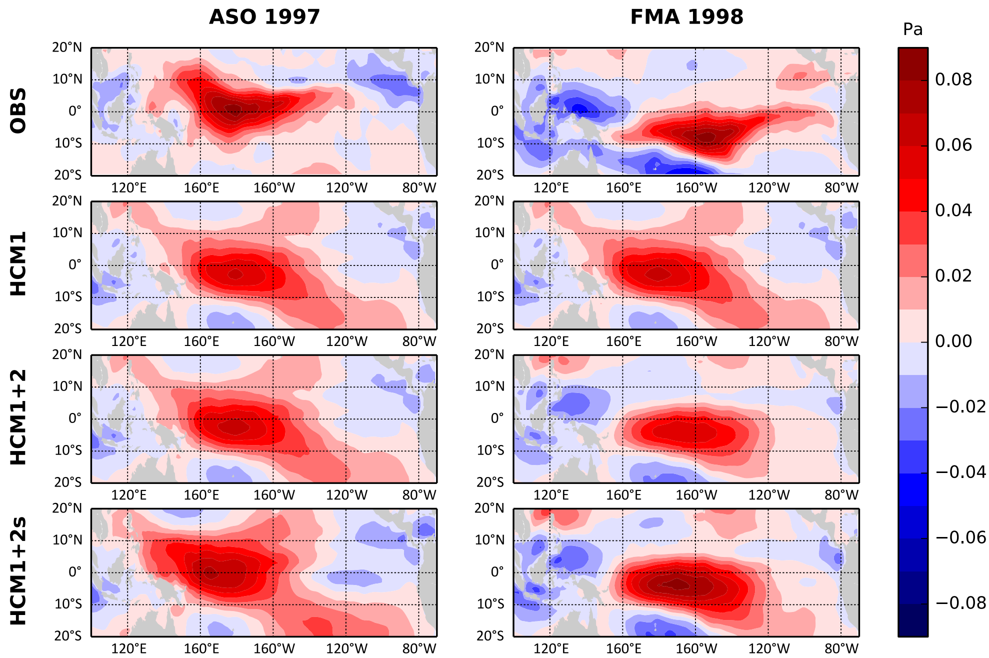

Fig. 6 Zonal surface wind stress anomalies (Pa) during ASO in 1997 (*left*) and FMA in 1998 (*right*) from observations (*top panels*), HCM1 (*second line*), HCM1+2 (*third line*) and HCM1+2$_S$ (*bottom panels*)

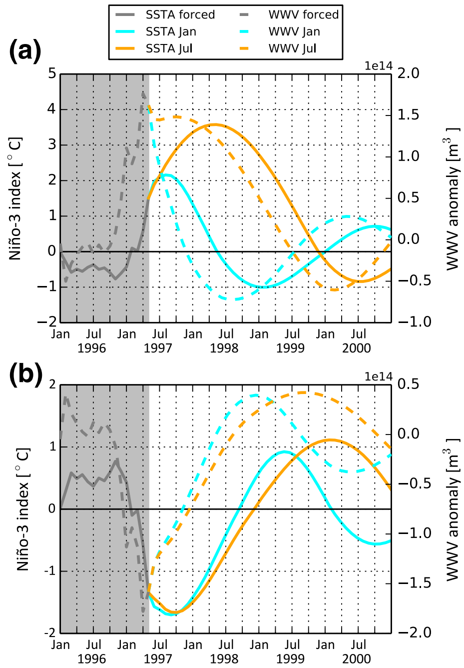

Fig. 7 **a** Time series of the SSTA in Niño-3 region (*solid lines*) and warm water volume anomalies integrated over 5°S–5°N and 120°E–80°W (*dashed lines*) for the period 1996–2000 in forced run (*gray lines*) with wind stress anomalies observed during the first 16 months and then coupled to HCM1+2 fixing the configuration of EOF2 at two calendar months, January (*light blue*) and July (*orange*). **b** The same as **a** but multiplying the wind stress anomalies during the forced period by minus one

ocean-atmosphere coupling (most stable conditions) and July has the strongest ocean-atmosphere coupling (most unstable conditions) (Fig. 7a). As a consequence, the duration of the resulting El Niño event in HCM1+2 is much longer when EOF2 is fixed in July (~2.5 years) than in January (~1 year) (Fig. 7a). It is also interesting to note that upon coupling, the perpetual January HCM1+2 simulation instantaneously begins to discharge WWV, while the perpetual July HCM1+2 simulation after a brief initial adjustment maintains WWV for a further 6–9 months.

These changes in coupling strength are consistent with PC2 and PC1 values in January and July shown in Fig. 4, where ENSO's winds (reconstructed with EOF1 and EOF2) are largely symmetric about the equator in July and display a strong asymmetry (southward shift) in January. Further to this, the SSTA and WWV changes displayed are consistent with our expectations based on previous studies, whereby the southward wind shift acts to enhance the discharge WWV (e.g., McGregor et al. 2014), which is shown to set up conditions favourable for the termination of ENSO warm events (Jin 1997; Meinen and McPhaden 2000).

As a demonstration of the ENSO phase non-linearity of HCM1+2 we repeated the above perpetual month experiments, however, this time simply multiplying the zonal winds forcing by minus one. Using the amplitude of the resulting La Niña event as a rough measure of the coupling strength, we find virtually no difference between the perpetual January and July experiments in SSTA or WWV (Fig. 7b). It is also interesting to note that the absolute value of SSTA does not get as large for La Niña events as it does for El Niño events, which is a reflection of the differing relationship between thermocline depth and SST reported in Sect. 3.1.

4.2 Seasonal synchronization

Previous studies (e.g., Harrison and Vecchi 1999; McGregor et al. 2012a) and the results above suggest that the southward wind should play a prominent role in the synchronization of ENSO events to the seasonal cycle. The goal of this set of experiments is to demonstrate, in an idealised setting, the southward wind shift role in the DJF event peak and, hence, the synchronization of ENSO events to the seasonal cycle.

To this end, four experiments are conducted, all of which are initiated by forcing with wind stress anomalies observed from ERA-interim during the 16-month period between January 1996 and April 1997. As above, each models statistical atmosphere and WWB components are inactive during this initial forcing period, and after this forcing period only the statistical atmospheric component is activated. What differs between each of the experiments, however, is the calendar month each of the two HCMs (HCM1 and HCM1+2) is initialised in when activated. The four runs for each HCM are initiated in February, May, August and November. Also, unlike in the perpetual month experiments, the calendar month is not held fixed at the initialization month, meaning

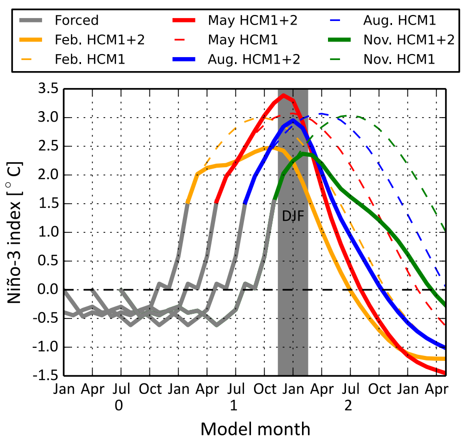

Fig. 8 Time series of the SSTA in Niño-3 region forcing the model during a 16-month period (*gray lines*) and then coupled to HCM1+2 (*solid lines*) and HCM1 (*dashed lines*) by starting in different calendar months: February (*orange*), May (*red*), August (*blue*) and November (*green*)

that the month does evolve with time after initialisation. This basically acts as a shift in timing of the applied wind stress forcing, which is representative of El Niño event triggering WWBs occurring at different times of the year.

Figure 8 depicts the Niño-3 index time series for the experiment described above. As expected for HCM1, each simulation produces a similar pattern for all runs with the maximum SSTA being reached roughly 7 months after coupling and termination occurring roughly 12 months after that (Fig. 8). As the coupling shifts to later in the calendar year in the HCM1+2 simulations, however, the wind stresses become less symmetric about the equator, thus the maximum amplitude of the events gets smaller. The most significant feature, however, is that each of the simulations reach their SSTA peak during DJF regardless the calendar month when the model coupling is initiated. Thus, this set of experiments demonstrates that the monthly varying coupling strength produced by the southward wind shift acts to synchronize the modeled ENSO event to the seasonal cycle.

5 Response of the hybrid coupled models to stochastic WWBs

In this section, we conduct a 4-member ensemble of 100-year simulations utilising: (1) four amplitudes of WWB (8, 10, 12 and 14 m s^{-1}), (2) three probabilities of occurrence of a WWB (2.50, 3.75 and 5.00 WWBs yr^{-1}), and (3) for each of the three HCM (HCM1, HCM1+2 and HCM1+2_S), giving 144 ensemble simulations. Each of the four ensemble members for each choice of WWB amplitude, occurrence probability and HCM version differ only in the set of random numbers used to set the timing of occurrence of the WWBs.

5.1 Seasonal synchronization

Here we aim too more fully understand the role of the EOF2 (i.e. the southward wind shift during El Niño events) in the synchronization of ENSO to the seasonal cycle. The tendency of seasonal synchronization of ENSO events can be seen in the observations, after normalization of Niño-3 index time series, in maximum peak (1.3 °C) in the standard deviation in December and minimum (0.75 °C) in April (Fig. 9). Thus, we present the standard deviation of the SSTA in the central-eastern Pacific (Niño-3 region) for each calendar month and for all runs of the ensemble (Fig. 9).

All HCM1 simulations, i.e. without EOF2, have standard deviations that are roughly constant throughout the year. That is, they do not show any synchronization to the annual cycle. The simulations including EOF2, on the other hand, do exhibit seasonal preference in the standard deviation, although there are some differences when compared to

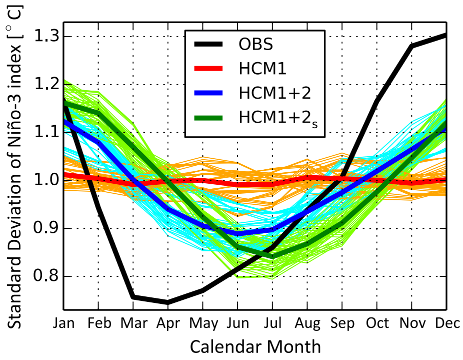

Fig. 9 Monthly standard deviation of Niño-3 SSTA from observations (*black line*), and all simulations: HCM1 (*red*), HCM1+2 (*blue*) and HCM1+2_S (*green*). *Thin lines* represent individual simulations and *thick lines* indicate the mean of each HCM

that observed. For instance, the HCM1+2 ensemble mean features a boreal winter maximum (1.1 °C) standard deviation and a boreal summer minimum (0.9 °C). Comparing this with observations reveals that the model displays a smaller range, and that the maximum lags that observed by approximately 1 month, while the minimum in June lags that observed by 2 months (Fig. 9). The HCM1+2_S ensemble mean displays a boreal winter (January) maximum of 1.2 °C, which lags that observed by one month, and a boreal summer minimum (0.85 °C) that lags by 3 months as that observed, and again exhibiting a weaker range of variability (Fig. 9). Therefore, the correlation coefficient between HCM1+2 and observations is higher ($r = 0.73$) than that between HCM1+2_S and observations ($r = 0.45$).

To characterize the seasonality of the standard deviation throughout the year, here we use the correlation coefficient between the modeled and observed monthly standard deviation of Niño-3 index, defined as phase-locking performance index (PP) by Ham and Kug (2014), as well as the ratio of the maximum and minimum modeled monthly standard deviation. These two parameters in addition to the standard deviation of SSTA in Niño-3 region are plotted in Fig. 10 as a function of the magnitude and probability of WWB.

As expected, the standard deviation increases for both magnitude and number of WWE per year higher for all simulations (Fig. 10a–c). However, it is noteworthy that the standard deviations in HCM1 simulations are slightly higher than the others for the same magnitude and probability values as a result of longer duration of warm events, as we shall present in Sect. 5.3. On average, the observed standard deviation (0.84 °C for the period 1880–2013 and 0.87 °C for the period 1979–2013) falls in the bottom left hand corner of the modeled standard deviations (Fig. 10a–c).

The PP indices in the HCM1 ensemble are roughly 0 regardless of the WWB parameters (Fig. 10d). The HCM1+2 and HCM1+2_S correlation coefficients,

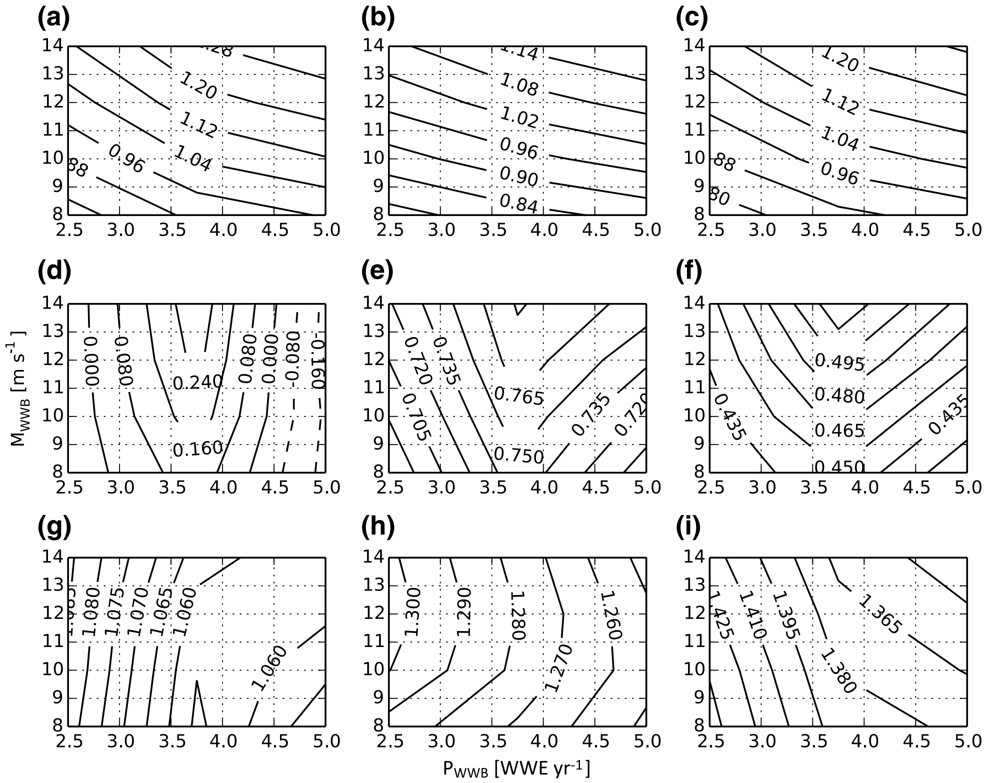

Fig. 10 Standard deviation of Niño-3 index (**a**–**c**), correlation coefficient between monthly standard deviation of Niño-3 index modeled and observed (**d**–**f**), and division of maximum by minimum monthly standard deviation of Niño-3 index (**g**–**i**) for HCM1 (*left*), HCM1+2 (*middle*) and HCM1+2_S (*right*) simulations as function of magnitude and probability of WWB

however, do appear to depend on both WWB parameters. For instance, the greatest values in both simulations are obtained with the probability of 3.5–4 WWB yr^{-1} and WWB magnitudes between 12 and 14 m s^{-1} (Fig. 10e, f). Regarding the amplitude of the seasonal cycle, i.e. rate of maximum and minimum values of monthly standard deviation, there is a clear increase trend towards few WWE in all simulations (Fig. 10g–i), although values in HCM1 are roughly 1. Therefore, the high frequency of WWE might neutralize the role of the southward wind shift and hence the ENSO seasonal synchronization when EOF2 is added in the model. In all cases, the modeled amplitudes are lower than the observed one (1.74 for the period 1880–2013 and 1.97 for the period 1979–2013).

5.2 ENSO peak time

To further verify how the addition of EOF2 in HCM1+2 and HCM1+2_S can influence the seasonality of El Niño and La Niña event peaks separately, we construct a histogram displaying the number of El Niño and La Niña event peaks for each calendar month and compare them against those observed and in the HCM1 ensemble (Fig. 11). It is worthwhile to mention that the modeled Niño-3.4 data had the long term mean removed and the resulting time series was also smoothed with a 3-month binomial filter to be consistent with the observed. Here we identify ENSO events for which the anomalous Niño-3.4 index exceeds one standard deviation, following Okumura and Deser (2010), however rather than focusing only on the December values our events must exceed this threshold for at least 5 consecutive months.

As expected, most observed peaks of both El Niño and La Niña events tend to occur toward the end of a calendar year from November to January (Fig. 11a). In sharp contrast, but not surprisingly, peaks in HCM1 are distributed all year round and there is no marked difference between warm and cold events (Fig. 11b) for the entire ensemble. The lack of seasonal synchronization in HCM1 is expected, as it has no mechanism incorporated to link its ENSO phase to the seasonal cycle.

As shown above the simulations including EOF2, HCM1+2 and HCM1+2_S, do display a synchronization to the seasonal cycle which is similar to that observed (Fig. 9). Looking at the number of El Niño event peaks for each calendar month in HCM1+2 and HCM1+2_S, both show that most El Niño event peaks occur between November and January (Fig. 11c, d) consistent with that seen in

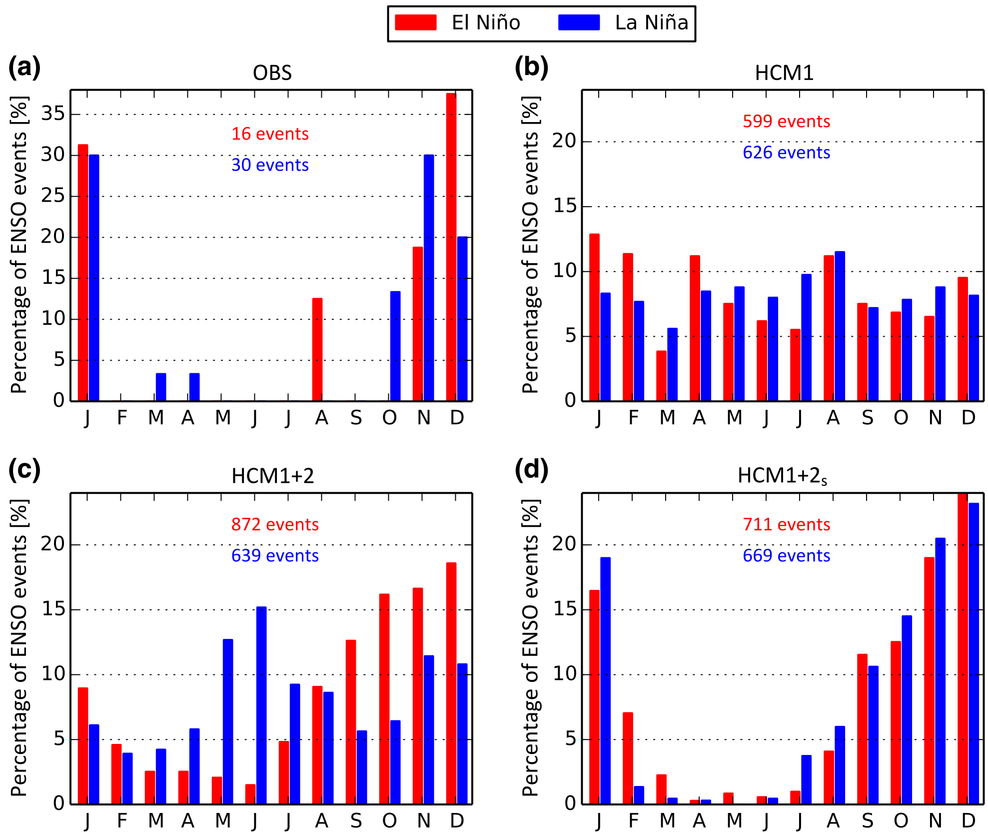

Fig. 11 Monthly peaks of El Niño (*red*) and La Niña (*blue*) events in observations (**a**) and the three different versions of HCM: HCM1 (**b**), HCM1+2 (**c**), and HCM1+2$_S$ (**d**). Note that number of El Niño and La Niña events is indicated in *red* and *blue*, respectively, at the *top* of each panel

the observations (Fig. 11a). However, there are some clear differences between HCM1+2 and HCM1+2$_S$ and with the observations, when looking at the number of La Niña event peaks for each calendar month. For instance, while both HCM1+2$_S$ and the observations show that most La Niña event peaks occur between November and January, the HCM1+2 simulations suggest that most La Niña peaks occur during two periods of time in May–August and November–December. This difference helps to explain the weaker range of monthly ENSO variability seen in HCM1+2 compared to that seen in HCM1+2$_S$ (Fig. 9).

Bearing in mind that both HCM1+2 and HCM1+2$_S$ incorporate EOF2 (the southward wind shift), their differences must be due to the relationship between PC1 and PC2 for La Niña (negative PC1 values) events (Fig. 4). During JJA of a moderate La Niña type event (PC1∼−1.5), PC2 from both HCMs display positive PC2 values that indicates the northward location of the related anomalous wind stresses. During DJF, on the other hand, HCM1+2$_S$ displays strong negative values of PC2 (∼−1), which indicates the southward location of the anomalous wind stresses and higher magnitude of these anomalies. As shown above, this southward wind shift would enhance the recharge of heat, acting to terminate the event and leading to its apparent synchronization with the seasonal cycle. HCM1+2, however, still displays positive values (although smaller than in JJA), indicating that the anomalous wind stresses still remain in a northward location relative to the wind stresses of EOF1 (Fig. 2a). Thus, the relatively minor southward wind shift that occurs in HCM1+2 during La Niña events does not act to synchronize the events to the seasonal cycle.

5.3 Duration asymmetry

It is generally accepted that there is an asymmetry in the duration of the two phases of ENSO events, with La Niña events lasting longer than El Niño events (Larkin and Harrison 2002; McPhaden and Zhang 2009; Obha and Ueda 2009; Okumura and Deser 2010; Okumura et al. 2011; DiNezio and Deser 2014). Given that McGregor et al. (2013) proposed that the asymmetries in the southward wind shift (e.g., El Niño event magnitude is strongly related to the extent of the meridional wind movement, while the meridional wind movement during La Niña events remains relatively small

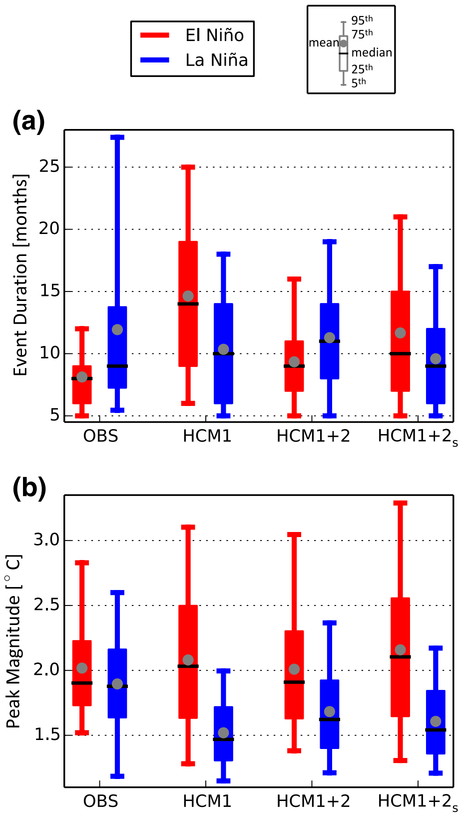

Fig. 12 Box plots of duration (**a**) and peak magnitude (**b**) of El Niño (*red*) and La Niña (*blue*) events for observations and the three different versions of HCM (HCM1, HCM1+2 and HCM1+2S). *Boxes* indicate the 25th and 75th values and caps the 5th and 95th ones. Medians (means) values are highlighted by *solid black lines* (*gray circles*). Note that the magnitudes of La Niña peaks are multiplied by minus one

regardless of the event magnitude) may play a role in this asymmetric duration, here we examine the ensemble of HCM simulations in an attempt to validate this proposal.

The boxplots in Fig. 12a, b show the range in durations and magnitudes, respectively, of El Niño and La Niña events, with the event duration defined as the number of months of normalized Niño-3.4 index (Sect. 5.2) exceeds one standard deviation, while the magnitude is defined at the event peak which follows the definition of Sect. 5.2. To determine whether the mean differences are significant in the duration and magnitude of events amongst the HCMs, we perform a Welch's *t* test (Welch 1947), which does not assume equal population variance. We also assess how these duration changes play out temporally by compositing the ensemble Niño-3.4 indexes during the 3-year period (12 and 24 months before and after the peaks, respectively) around the event peak (Fig. 13) for all simulations and those observed for comparison.

The boxplot of El Niño event duration (Fig. 12a) and composite of these events for HCM1 (Fig. 13a) reveals events that extend out to over two years and that are on average 6 months longer that observed. This duration difference comes about in spite of HCM1 event magnitudes having no significant differences when compared to observed event amplitude (Fig. 12b). Interestingly, the HCM1 composite reveals that a cool state generally follows El Niño events by 18 months (Fig. 13a), giving the modeled ENSO a 3-year period. This suggests that the boreal summer peak of La Niña events in the HCM1+2 ensemble could simply reflect that warm events are forced to peak in boreal winter via EOF2, while the trailing cool event peak (which has minimal meridional wind movement) is largely only reliant on the ocean dynamical negative feedbacks of the HCM1 simulation. We also note that all versions of the HCM generate warm events stronger than cold events as observed (Fig. 12b) (Hoerling et al. 1997; Burgers and Stephenson 1999; Timmermann and Jin 2002; Jin et al. 2003; Hannachi et al. 2003; An and Jin 2004; Monahan and Dai 2004; Rodgers et al. 2004; Dong 2005).

Comparing the duration of El Niño events of HCM1+2 and HCM1+2S with those of HCM1, we find that the inclusion of EOF2 in the HCMs (i.e., HCM1+2 and HCM1+2S) results in warm events having a significantly shorter duration (Fig. 12a; Table 2). For instance, El Niño events in HCM1+2 are on average 5 months shorter than those of HCM1, while the events of HCM1+2S are on average 3 months shorter. This result is consistent with the results of Sect. 4, shown in Figs. 5 and 8. The HCM1+2 composite on average matches the observed composite very well during event build-up, peak and through the early stages of decay (Fig. 13c). In fact, the average El Niño duration in HCM1+2 and observations are not significantly different (Table 2). The HCM1+2S composite also matches the observed composite reasonably well in the months close to the events peak (Fig. 13e). It is noticeable, however, that both the average duration and magnitude of the events in HCM1+2S are significantly longer/larger than those observed (Table 2; Fig. 12), which is consistent with the results of Sect. 4 (Fig. 5). The largest differences between the composites of the HCMs that include EOF2 (HCM1+2 and HCM1+2S) and the observations come about around the trailing minimum peak, as there is clearly not as strong of a tendency in both of the HCMs for La Niña events to follow 12 months after El Niño events as the La Niña events tend to follow by 18 months (Fig. 13c, e).

Unlike warm event duration, the cool event duration response of the HCM simulations which include EOF2 depends on how the southward wind shift (EOF2) has been added. For instance, La Niña events in HCM1+2 (HCM1+2S) are significantly longer (shorter) than in HCM1. However, the three mean values are only slightly different (10.4, 11.3 and 9.6 months for HCM1, HCM1+2 and HCM1+2S respectively). In regards to their magnitudes, the inclusion of the southward wind shift in both

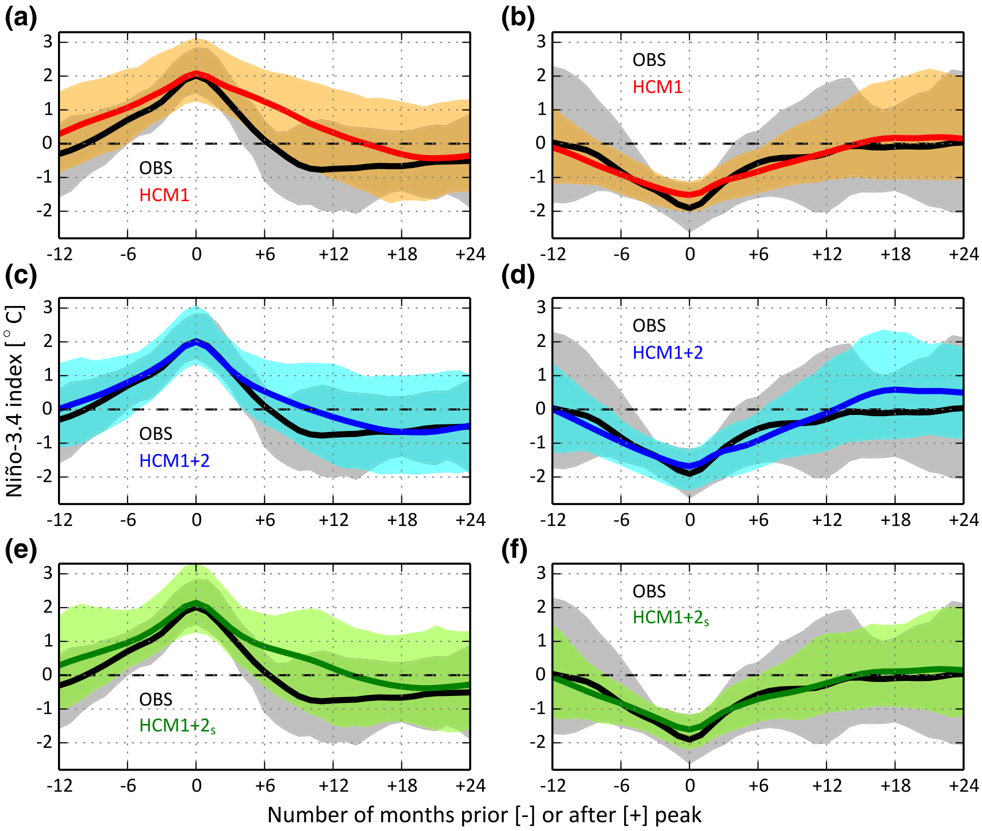

Fig. 13 Composites of time series of SSTA in Niño-3.4 region during 12 (24) months prior (after) peaks for El Niño (**a**, **c**, **e**) and La Niña (**b**, **d**, **f**). The *shaded* areas represent the 5th and 95th envelopes of values. *Solid lines* indicate the mean values

Table 2 Differences between the mean values of ENSO duration (above diagonal) in months and magnitude (below diagonal) in Kelvin amongst observations and all HCMs. Note that values are the result of the subtraction between each column and each row

	EN obs	LN obs	EN HCM1	LN HCM1	EN HCM1+2	LN HCM1+2	EN HCM1+2$_S$	LN HCM1+2$_S$
LN HCM1+2$_S$	**−1.5**	*2.3*	**5.1**	**0.8**	*−0.2*	**1.7**	**2.0**	–
EN HCM1+2$_S$	**−3.5**	0.3	**3.0**	**−1.3**	**−2.3**	−0.4	–	**0.6**
LN HCM1+2	**−3.2**	0.7	**3.4**	**−0.9**	−1.9	–	**−0.5**	**0.1**
EN HCM1+2	*−1.2*	*2.6*	**5.3**	**1.0**	–	**0.3**	**−0.2**	**0.4**
LN HCM1	**−2.2**	1.6	**4.3**	–	**−0.5**	**−0.2**	**−0.6**	**−0.1**
EN HCM1	**−6.5**	*−2.7*	–	**0.6**	**0.1**	**0.4**	**−0.1**	**0.5**
LN obs	**−3.8**	–	**−0.2**	**0.4**	−0.1	**0.2**	**−0.3**	**0.3**
EN obs	–	0.1	−0.1	**0.5**	0.0	**0.3**	−0.1	**0.4**

Bold (italic) values indicate that the difference is significant at the 95 % (90 %) level, as judged by a Welch's *t* test

HCM1+2 and HCM1+2$_S$) makes La Niña events significantly larger than in HCM1 (Table 2).

6 Discussion and conclusions

In this work we examine the role of the southward movement of ENSO's anomalous zonal winds that occurs near the end of the calendar year, when ENSO events typically reach their peak amplitude. It is shown (Figs. 1, 2, 3) that the combination of the two leading EOF of tropical Pacific wind stresses captures this meridional wind movement, consistent with previous studies (e.g., McGregor et al. 2012a). With the aim of investigating how this meridional wind movement can influence both the seasonal synchronization and duration of ENSO events, a series of hybrid coupled models (HCMs) were constructed: HCM1 (which includes EOF1 only, i.e. no southward wind shift); HCM1+2 and HCM1+2$_S$ (which both including EOF2, while the monthly coefficients are realistic and idealized, respectively).

We found that the variation of the air–sea coupling intensity from month to month, due to the meridional movement of ENSO winds, leads to synchronization of ENSO events with the seasonal cycle. It was shown in Sect. 4 (our idealised 1997/98 perturbation experiments) that the strong coupling during boreal summer occurs when ENSO's anomalous wind stresses are largely symmetric about the equator, while the weaker coupling during the boreal winter occurs when ENSO's anomalous wind stresses are largely asymmetric and the wind stress maximum is located between ∼ 5° and 7°S. The strong coupling in boreal summer allows ENSO events to grow rapidly throughout this period. Therefore, as demonstrated in Fig. 8, WWB that occur just prior to this strong coupling are the best placed to generate large ENSO events. On the other hand, the weak coupling during boreal winter limits growth and tends to discharge WWV, which enhances the termination the event. It is worth pointing out that in these idealized experiments no WWB activity occurs after the initial forcing. Thus, this result acts as a theoretical proof of the earlier work of Harrison and Vecchi (1999), Vecchi and Harrison (2003, 2006) and Lengaigne et al. (2006); and is conceptually consistent with the idealised results of Stein et al. (2014). Furthermore, it is in good agreement with that reported by Horii and Hanawa (2004), in which they noted that warm events that do not develop until late summer-fall tend to be weaker and persist longer into the second year.

In Sect. 5 we constructed three ensembles of simulations, each using a different version of the HCM, where the ensemble members differ in the timing, magnitude and probabilities of WWB. The purpose of these simulations was to more fully understand the effect of EOF2 in the tendency for ENSO events to be synchronized with the seasonal cycle. As expected, the HCM1 simulations do not exhibit any seasonal preference in the timing of ENSO events; in other words, they do not show any synchronization of ENSO events to the annual cycle. Furthermore, the duration of El Niño events are much longer (up to 6 months on average) that those observed, resulting in higher variability of SSTA over the eastern equatorial Pacific.

The realistic inclusion of EOF2 (HCM1+2), which reproduces strong (weak) southward shift of westerlies (easterlies) in DJF during El Niño (La Niña) years as observations, leads to ENSO seasonal synchronization, although the annual amplitude is weaker than that observed. Such difference (also seen in HCM1+2_S) might be associated with the stochastic WWBs, which were found to reduce the interannual variability compared to semistochastic WWBs (Gebbie et al. 2007). It is shown that El Niño events terminate abruptly in HCM1+2 after peaking near the end of the calendar year, which results in the events being significantly shorter than those of HCM1 ensemble. The minimal meridional wind movement during La Niña phases leaves the termination of these events to rely solely on the modeled oceanic wave adjustment. Therefore, cool events reach their peak amplitude at the wrong time of the year (Fig. 11c), while the relative symmetry of the wind stresses about the equator allows the events to grow larger than those of HCM1. The resulting La Niña events are on average also significantly longer than those in HCM1, however the mean difference between these two distributions is less than one month (Table 2).

The inclusion of EOF2 with idealised coefficients (HCM1+2_S) also results in synchronization of ENSO to the annual cycle with seasonal amplitude weaker than that observed, but also stronger than that produced in HCM1+2. The minimum variance, however, is lagged by 3 months compared to the observations. In this case, the positive EOF2 values during El Niño years in JJA acts to charge the equatorial region WWV while also making the associated westerlies more symmetric around the equator, which allows the event to grow larger, while the strong southward wind shift in DJF, similar to HCM1+2, enhances the termination of the warm events in the following months. Interestingly, the linearity of the simple southward shift allows this HCM to produce a strong southward shift of anomalous easterlies near the end of the calendar year during La Niña years (Fig. 4). This strong shift acts to synchronize the La Niña event peak to the seasonal cycle (Fig. 11d), consistent with the observations.

The clear difference between HCM1+2 and HCM1+2_S highlighted above is in the role of the EOF2 in the synchronization of La Niña events. HCM1+2 suggests that the effect of EOF2 is small during La Niña events, as such it does not act to synchronize the events to the annual cycle and the modeled cool events peak at the wrong time of the year. HCM1+2_S, on the other hand, has a strong role making the events peak at the right time of the year. While the resulting La Niña events do have a more realistic end of calendar year peak, it should be noted that the strong role of EOF2 during these events is not consistent with the observations (see Fig. 4). This implies that one of the other mechanism discussed in the introduction may be responsible for synchronizing the La Niña event peak with the seasonal cycle. However, it is worthwhile to note that there is very little data for large La Niña events so the composites are based largely around smaller magnitude events, thus the role of the southward wind shift in the duration of La Niña events is still unclear.

What has also become apparent from our study, however, is that the characteristics of WWB also have the potential to be incredibly important. In particular, the best correlation coefficients between the monthly standard deviation of Niño-3 index modeled and observed are obtained with 3.5–4.0 WWB yr^{-1} (Fig. 10e, f), probabilities consistent with that found in observations (e.g., Gebbie et al. 2007). In relation to the seasonal amplitude, higher values are reached for a lower frequency of WWB (Fig. 10h, i), suggesting that higher frequency WWBs (in the absence of any seasonality in the burst themselves) act to damp the seasonal variance changes. This result is in good agreement with previous studies, for instance Neelin et al. (2000), in which it was suggested that the atmospheric stochastic forcing might be a candidate for altering this ENSO's seasonal synchronization. This importance is perhaps most clearly apparent looking at the peak month of the El Niño event (Fig. 11c), as in the absence of WWB around the peak time all events appear to peak in DJF (Fig. 8). This suggests that while the meridional movement of winds leads to a rapid termination of El Niño events, as shown here, the effective termination of an event is also reliant on the ocean dynamics of the traditional RDO mechanism (Jin 1997). Thus, the enhanced termination of ENSO events due to the southward shift and its changes in coupling strength might be not enough to overcome poorly timed WWBs. This finding supports the earlier study of Gebbie et al. (2007), where the modeled seasonal synchronization displays a strong sensitivity of the timing of triggering WWBs.

Thus, despite the simplicity of the HCMs used in this work, we found that the southward shift of El Niño-related westerly plays a key role in having El Niño event peaks in the boreal winter, supporting previous studies (e.g., Harrison and Vecchi 1999; Vecchi and Harrison 2003; McGregor et al. 2012a; Stuecker et al. 2013). This shift also acts to shorten the modeled duration of El Niño events, while our results suggest that it plays a minimal role in the length of La Niña events. Although not mentioned as such, this shift is apparent in the Harrison and Vecchi (1997) analysis of WWEs, where they identified a clear seasonal preference for WWEs to occur north (south) of the equator during July–November (December–March) (see their Figs. 22, 23). This movement of WWBs may have the effect of enhancing the seasonal synchronization affects of the southward wind shift. Furthermore, in this study it is demonstrated that the effective termination is carried out by two components: (1) the ocean dynamics of the traditional RDO mechanism (Jin 1997); and (2) the discharge of WWV due to the southward wind shift, and both must align to some degree to allow for an abrupt event termination.

Acknowledgments This study was supported by the Australian Research Council's (ARC) through grant number DE130100663, with additional support coming via the ARC Centre of Excellence for Climate System Science. The authors would also like to thank the editor and one anonymous reviewer for the constructive comments and suggestions, which substantially improved this manuscript.

References

An SI, Jin FF (2004) Nonlinearity and asymmetry of ENSO. J Clim 17:2399–2412

Annamalai H, Xie SP, McCreary JP, Murtugudde R (2005) Impact of Indian Ocean sea surface temperature on a developing El Niño. J Clim 18:302–319

Balmaseda MA, Davey MK, Anderson DLT (1995) Decadal and seasonal dependence of ENSO prediction skill. J Clim 8:2705–2715

Battisti DS (1988) The dynamics and thermodynamics of a warming event in a coupled tropical atmosphere-ocean model. J Atmos Sci 45:2889–2919

Bjerkness J (1969) Climatological effects of orography and land-sea heating contrasts on the gravity wave-driven circulation of the mesosphere. Mon Wea Rev 60:103–118

Burgers G, Stephenson DB (1999) The "normality" of El Niño. Geophys Res Lett 26:1027–1030

Cane MA, Zebiak S (1985) A theory for El Niño and the Southern Oscillation. Science 228:1084–1087

Chang P (2006) Climate fluctuations of tropical coupled systems—the role of ocean dynamics. J Clim 19:5122–5174

Chen D, Lian T, Fu C, Cane MA, Tang Y, Murtugudde R, Song X, Wu Q, Zhou L (2015) Strong influence of westerly wind bursts on El Niño diversity. Nat Geosci 8:339–345

Chen SS, Houze RA, Mapes BE (1996) Multiscale variability of deep convection in relation to large-scale circulation in TOGA COARE. J Atmos Sci 53:1380–1409

Chu PS (1988) Extratropical forcing and the burst of equatorial westerlies in the western Pacific: a synoptic study. J Meteorol Soc Jpn 66:4549–4564

Dee DP, Uppala SP (2009) Variational bias correction of satellite radiance data in the ERA-Interim reanalysis. Q J R Meteorol Soc 135:1830–1841

Deser C et al. (2012) ENSO and Pacific decadal variability in the Community Climate System Model version 4. J Clim 25:2622–2651. doi:10.1175/JCLI-D-11-00301.1

DiNezio PN, Deser C (2014) Nonlinear controls on the persistence of La Niña. J Clim 27:7335–7355

Dong BW (2005) Asymmetry between El Niño and La Niña in a global coupled GCM with and eddy-permitting ocean resolution. J Clim 18:3084–3098

Eisenman I, Yu L, Tziperman E (2005) Westerly wind bursts: ENSO's tail rather than the dog? J Clim 18:5224–5238

Frauen C, Dommenget D (2010) El Niño and La Niña amplitude asymmetry caused by atmospheric feedbacks. Geophys Res Lett 37:L18801. doi:10.1029/2010GL044444

Galanti E, Tziperman E, Harrison M, Rosati A, Giering R, Sirkes Z (2002) The equatorial thermocline outcropping—a seasonal control on the tropical Pacific Ocean-atmosphere instability strength. J Clim 15:2721–2739

Gebbie G, Tziperman E (2009) Predictability of SST-modulated westerly wind bursts. J Clim 22:3894–3909

Gebbie G, Eisenman I, Wittenberg A, Tziperman E (2007) Modulation of westerly wind bursts by sea surface temperature: a semi-stochastic feedback for ENSO. J Atmos Sci 64:3281–3295

Giese B, Harrison D (1991) Eastern equatorial Pacific response to three composite westerly wind types. J Geophys Res 96:3239–3248

Giese B, Harrison DE (1990) Aspects of the Kelvin wave response to episodic wind forcing. J Geophys Res 95:7289–7312

Graham N, White W (1988) The El Niño cycle: a natural oscillator of the Pacific ocean-atmosphere system. Science 240:1293–1302

Ham YG, Kug JS (2014) ENSO phase-locking to the boreal winter in CMIP3 and CMIP5 models. Clim Dyn 43:305–318

Ham YG, Kug JS, Kim D, Kim YH, Kim DH (2013) What controls phase-locking of ENSO to boreal winter in coupled GCMs? Clim Dyn 40:1551–1568

Hannachi A, Stephenson D, Sperber K (2003) Probability-based methods for quantifying nonlinearity in the ENSO. Clim Dyn 20:241–256
Harrison DE (1987) Monthly mean island surface winds in the central tropical Pacific and El Niño events. Mon Wea Rev 115:3133–3145
Harrison DE, Larkin NK (1998) Seasonal U.S. temperature and precipitation anomalies associated with El Niño: historical results and comparison with 1997–1998. Geophys Res Lett 25:3959–3962
Harrison DE, Vecchi GA (1997) Surface westerly wind events in the tropical Pacific 1986–1995. J Clim 10:3131–3156
Harrison DE, Vecchi GA (1999) On the termination of El Niño. Geophys Res Lett 26:1593–1596
Hirst A (1986) Unstable and damped equatorial modes in simple coupled ocean-atmosphere models. J Atmos Sci 43:606–632
Hoerling M, Kumar A, Zhong M (1997) El Niño, La Niña, and the nonlinearity of their teleconnections. J Clim 10:1769–1786
Horii T, Hanawa K (2004) A relationship between timing of El Niño onset and subsequent evolution. Geophys Res Lett 31:L06304. doi:10.1029/2003GL019239
Jin FF (1997) An equatorial ocean recharge paradigm for ENSO. Part I: conceptual model. J Atmos Sci 54:811–829
Jin FF, Neelin J, Ghil M (1994) El Niño on the devil's staircase: annual subharmonic steps to chaos. Science 264:70–72
Jin FF, An SI, Timmermann A, Zhao J (2003) Strong El Niño events and nonlinear dynamic heating. Geophys Res Lett 30:1120. doi: 10.1029/2002GL016356
Keen RA (1982) The role of cross-equatorial cyclone pairs in the Southern Oscillation. Mon Wea Rev 110:1405–1416
Kerr RA (1999) Atmospheric science: does a globe-girdling disturbance jigger El Niño? Science 285:322–323
Kessler WS, Kleeman R (2000) Rectification of the Madden–Julian Oscillation into the ENSO Cycle. J Clim 13:3560–3575
Kleeman R (1993) On the dependence of hincast skill on ocean thermodynamics in a coupled ocean-atmosphere model. J Clim 6:2012–2033
Kug JS, Kang IS (2006) Interactive feedback between ENSO and the Indian Ocean. J Clim 19:1784–1801
Larkin NK, Harrison DE (2002) ENSO warm (El Niño) and cold (La Niña) event lifecycles: ocean surface anomaly patterns, their symmetries, asymmetries, and implications. J Clim 15:1118
Latif M, Biercamp J, von Storch H (1988) The response of a coupled ocean-atmosphere general circulation model to wind bursts. J Atmos Sci 45:964–979
Lengaigne M, Vecchi GA (2009) Contrasting the termination of moderate and extreme El Niño events in coupled general circulation models. Clim Dyn. doi:10.1007/s00382-009-2562-3
Lengaigne M, Guilyardi E, Boulanger JP, Menkes C, Delecluse P, Inness P, Cole J, Slingo J (2004) Triggering of El Niño by westerly wind events in a coupled general circulation model. Clim Dyn 23:601–620
Lengaigne M, Boulanger J, Meinkes C, Spencer H (2006) Influence of the seasonal cycle on the termination of El Niño events in a coupled general circulation model. J Clim 19:1850–1868
Lorenz EN (1956) Empirical orthogonal functions and statistical weather prediction. Science report no. 1, statistical forecasting project. MIT Press, Cambridge, MA, 48 pp
McGregor S, Timmermann A, Schneider N, Stuecker MF, England MH (2012) The effect of the South Pacific Convergence Zone on the termination of El Niño events and the meridional asymmetry of ENSO. J Clim 25:5566–5586
McGregor S, Gupta AS, England M (2012b) Constraining wind stress products with sea surface height observations and implications for Pacific ocean sea level trend attribution. J Clim 25:8164–8176
McGregor S, Ramesh N, Spence P, England MH, McPhaden MJ, Santoso A (2013) Meridional movement of wind anomalies during ENSO events and their role in event termination. Geophys Res Lett 40:749–754
McGregor S, Spence P, Schwarzkopf FU, England MH, Santoso A, Kessler WS, Timmermann A, Böning CW (2014) ENSO-driven interhemispheric Pacific mass transports. J Geophys Res Oceans. doi:10.1002/2014JC010286
McPhaden MJ (1999) Genesis and evolution of the 1997–98 El Niño. Science. doi:10.1126/science.283.5404.950
McPhaden MJ (2004) Evolution of the 2002/03 El Niño. Bull Am Meteorol Soc 85:677–695
McPhaden MJ, Zhang X (2009) Asymmetry in zonal phase propagation of ENSO sea surface temperature anomalies. Geophys Res Lett 36:L13703. doi:10.1029/2009GL038774
McPhaden MJ, Zebiak SE, Glantz MH (2006) ENSO as an integrating concept in earth science. Science 314:1740–1745
Meinen CS, McPhaden MJ (2000) Observations of warm water volume changes in the equatorial Pacific and their relationship to El Niño and La Niña. J Clim 13:3551–3559
Monahan AH, Dai A (2004) The spatial and temporal structure of ENSO nonlinearity. J Clim 17:3026–3036
Neelin JD, Battisti DS, Hirst AC, Jin FF, Wakata Y, Yamagata T, Zebiak SE (1998) ENSO theory. J Geophys Res 103:14261–14290
Neelin JD, Jin FF, Syu HH (2000) Variations in ENSO phase locking. J Clim 13:2570–2590
Obha M, Ueda H (2007) An impact of SST anomalies in the Indian Ocean in acceleration of the El Niño to La Niña transition. J Meteorol Soc Jpn 85:335–348
Obha M, Ueda H (2009) Role of nonlinear atmospheric response to SST on the asymmetric transition process of ENSO. J Clim 22:177–192
Okumura YM, Deser C (2010) Asymmetry in the duration of El Niño and La Niña. J Clim 23:5826–5843
Okumura YM, Masamichi O, Clara D, Hiroaki U (2011) A proposed mechanism for the asymmetric duration of El Niño and La Niña. J Clim 24:3822–3829
Philander S, Yamagata T, Pacanowski R (1984) Unstable air–sea interactions in the tropics. J Atmos Sci 41:604–613
Philander SG (1983) El Niño Southern Oscillation phenomena. Nature 302:295–301. doi:10.1038/302295a0
Philander SG (1990) El Niño, La Niña, and the Southern Oscillation. Academic Press, Waltham
Rasmusson E, Carpenter T (1982) Variations in tropical sea surface temperature and surface wind fields associated with the Southern Oscillation/El Niño. Mon Wea Rev 110:353–384
Rebert JP, Donguy JR, Eldin G (1985) Relations between sea level, thermocline depth, heat content and dynamic height in the tropical Pacific Ocean. J Geophys Res 90:11,719–11,725
Rodgers KB, Friederichs P, Latif M (2004) Tropical Pacific decadal variability and its relation to decadal modulations of ENSO. J Clim 17:3761–3774
Ropelewski CH, Halpert S (1989) Precipitation patterns associated with the high index phase of the southern oscillation. J Clim 2:268–284
Smith TM, Reynolds RW, Peterson TC, Lawrimore J (2008) Improvements to NOAA's historical merged land-ocean surface temperature analysis (1880–2006). J Clim 21:2283–2296
Smith WHF, Sandwell DT (1997) Global sea floor topography from satellite altimetry and ship depth soundings. Science 277:1956–1962
Stein K, Timmermann A, Schneider N (2014) ENSO seasonal synchronization theory. J Clim 27:5285–5310
Stuecker MF, Timmermann A, Jin FF, McGregor S, Ren HL (2013) A combination mode of the annual cycle and the El Niño/Southern Oscillation. Nat Geosci 6:540–544

Stuecker MF, Jin FF, Timmermann A, McGregor S (2015) Combination mode dynamics of the anomalous northwest Pacific anticyclone. J Clim 28:1093–1111
Takahashi K, Montecinos A, Goubanova K, Dewitte B (2011) ENSO regimes: Reinterpreting the canonical and Modoki El Niño. Geophys Res Lett 38:L10704
Timmermann A, Jin FF (2002) Phytoplankton influences on tropical climate. Geophys Res Lett 29: doi:10.1029/2002GL015434
Tomczak M, Godfrey SJ (1994) Regional oceanography: an introduction. Pergamon Press, Oxford
Torrence C, Webster PJ (1998) The annual cycle of persistence in the El Niño/Southern Oscillation. Q J R Meteorol Soc 124:1985–2004
Trenberth KE (1997) The definition of El Niño. Bull Am Meteorol Soc 78:2771–2777
Trenberth KE, Stepaniak DP (2001) Indices of El Niño evolution. J Clim 14:1697–1701
Trenberth KE, Branstator GW, Karoly D, Kumar A, Lau NC, Ropelewski C (1998) Progress during TOGA in understanding and modeling global teleconnections associated with tropical sea surface temperatures. J Geophys Res 103:14291–14324
Tziperman E, Stone E, Cane M, Jarosh H (1994) El Niño chaos: Overlapping of resonances between the seasonal cycle and the Pacific ocean-atmosphere oscillator. Science 264:72–74
Tziperman E, Zebiak S, Cane M (1997) Mechanisms of seasonal–ENSO interaction. J Atmos Sci 54:61–71
Vecchi G, Harrison D (2000) Tropical Pacific sea surface temperature anomalies, El Niño, and equatorial westerly wind events. J Clim 13:1814–1830
Vecchi G, Harrison DE (2003) On the termination of the 2002–03 El Niño event. Geophys Res Lett 30:1964
Vecchi GA (2006) The termination of the 1997–98 El Niño. Part II: Mechanisms of atmospheric change. J Clim 19:2647–2664
Vecchi GA, Harrison DE (2006) The termination of the 1997–1998 El Niño. Part I: mechanisms of oceanic change. J Clim 19:2633–2646
Verbickas S (1998) Westerly wind bursts in the tropical Pacific. Weather 53:282–284
Wang B, Wu R, Lukas R (1999) Roles of the western North Pacific wind variation in thermocline adjustment and ENSO phase transition. J Meteorol Soc Jpn 77:1–16
Wang X, Jin FF, Wang Y (2003) A tropical ocean recharge mechanism for climate variability. Part I: equatorial heat content changes induced by the off-equatorial wind. J Clim 16:3585–3598
Welch BL (1947) The generalization of 'Student's' problem when several different population variances are involved. Biometrika 34:28–35
Wyrtki K (1975) El Niño—the dynamic response of the equatorial Pacific ocean to atmospheric forcing. J Phys Oceanogr 5:572–584
Wyrtki K, Meyers G (1976) The trade wind field over the Pacific Ocean. J Appl Meteorol 15:698–704
Yamanaka G, Yasuda T, Fujii Y, Matsumoto S (2009) Rapid termination of the 2006 El Niño and its relation to the Indian Ocean. Geophys Res Lett 36:L07702. doi:10.1029/2009GL037298
Yan B, Wu R (2007) Relative roles of different components of the basic state in the phase locking of El Niño mature phases. J Clim 20:4267–4277
Yoo SH, Fasullo J, Yang S, Ho CH (2010) On the relationship between Indian Ocean sea surface temperature and the transition from El Niño to La Niña. J Geophys Res. doi:10.1029/2009JD012978
Yu L, Rienecker MM (1998) Evidence of an extratropical atmospheric influence during the onset of the 1997–98 El Niño. Geophys Res Lett 25:3537–3540
Yu L, Weller RA, Liu TW (2003) Case analysis of a role of ENSO in regulating the generation of westerly wind bursts in the western equatorial Pacific. J Geophys Res 108:3128. doi:10.1029/2002JC001498
Zebiak SE, Cane MA (1987) A model of El Niño-Southern Oscillation. Mon Wea Rev 115:2262–2278
Zelle H, Appeldoorn G, Burgers G, Oldenborgh GJV (2004) The relationship between sea surface temperature and thermocline depth in the eastern equatorial Pacific. J Phys Oceanogr 34:643–655
Zhang C (1996) Atmospheric intraseasonal variability at the surface in the tropical western Pacific Ocean. J Atmos Sci 53:739–758

Appendix B

Published Article

A copy of the following published manuscript as it appears in the journal is included hereafter. This paper constitutes the material in Part 2.

Abellán, E., S. McGregor, and M. England, 2017. Analysis of the Southward Wind Shift of ENSO in CMIP5 Models. *J. Climate*, **30**, 2415-2435, doi: 10.1175/JCLI-D-16-0326.1

Analysis of the Southward Wind Shift of ENSO in CMIP5 Models

ESTEBAN ABELLÁN

ARC Centre of Excellence for Climate System Science, and Climate Change Research Centre, University of New South Wales, Sydney, New South Wales, Australia

SHAYNE MCGREGOR

School of Earth, Atmosphere and Environment, Monash University, Clayton, Victoria, Australia

MATTHEW H. ENGLAND

ARC Centre of Excellence for Climate System Science, and Climate Change Research Centre, University of New South Wales, Sydney, New South Wales, Australia

(Manuscript received 20 April 2016, in final form 7 December 2016)

ABSTRACT

During the mature phase of El Niño–Southern Oscillation (ENSO) events there is a southward shift of anomalous zonal winds (SWS), which has been suggested to play a role in the seasonal phase locking of ENSO. Motivated by the fact that coupled climate models tend to underestimate this feature, this study examines the representation of the SWS in phase 5 of the Coupled Model Intercomparison Project (CMIP5). It is found that most models successfully reproduce the observed SWS, although the magnitude of the zonal wind stress anomaly is underestimated. Several significant differences between the models with and without the SWS are identified including biases in the magnitude and spatial distribution of precipitation and sea surface temperature (SST) anomalies during ENSO. Multiple-linear regression analysis suggests that the climatological meridional SST gradient as well as anomalous ENSO-driven convective activity over the northwest Pacific both might play a role in controlling the SWS. While the models that capture the SWS also simulate many more strong El Niño and La Niña events peaking at the correct time of year, the overall seasonal synchronization is still underestimated in these models. This is attributed to underestimated changes in warm water volume (WWV) during moderate El Niño events so that these events display relatively poor seasonal synchronization. Thus, while the SWS is an important metric, it is ultimately the magnitude and zonal extent of the wind changes that accompany this SWS that drive the changes in WWV and prime the system for termination.

1. Introduction

One of the key features of El Niño–Southern Oscillation (ENSO) events is their tendency to mostly peak in boreal winter (i.e., November to January; Rasmusson and Carpenter 1982). It is widely understood that the interaction of ENSO with the annual cycle is the main reason for this apparent seasonal synchronization (e.g., Philander 1983; Zebiak and Cane 1987; Battisti and Hirst 1989; Xie 1995; Tziperman et al. 1997, 1998; Neelin et al. 2000; An and Wang 2000). However, the exact mechanisms are not yet fully understood, with several potential mechanisms proposed linking ENSO and the annual cycle (e.g., Philander 1983; Philander et al. 1984; Zebiak and Cane 1987; Cane et al. 1990; Jin et al. 2003; Dommenget and Yu 2016). Despite this ongoing scientific debate, the southward wind shift (SWS) has been increasingly recognized as one of the major negative feedbacks involved in ENSO seasonal phase locking and termination (Harrison and Vecchi 1999; Vecchi and Harrison 2003; Lengaigne et al. 2006; Lengaigne and Vecchi 2009; McGregor et al. 2012a, 2013, 2014; Stuecker et al. 2013; Abellán and McGregor 2016); the climate dynamics linking the SWS to seasonal phase locking will be described below.

During El Niño (La Niña) events, the associated westerly (easterly) wind anomalies are quite symmetric about the equator prior to the event peak (SON); these then move south of the equator (5°–10°S) during the

Corresponding author e-mail: Esteban Abellán, esteban.abellan@unsw.edu.au

DOI: 10.1175/JCLI-D-16-0326.1

mature phase (DJF). This wind shift has been linked to the southward displacement of the Pacific's warmest sea surface temperatures (SST) and convection during DJF (Lengaigne et al. 2006; Vecchi 2006) and the associated minimum of wind speed climatology (McGregor et al. 2012a), both of which are due to the seasonal evolution of solar radiation. Recently, the SWS has been ascribed to a climate mode generated in response to nonlinear atmospheric interaction between ENSO SST and the annual cycle of the Pacific warm pool (Stuecker et al. 2013, 2015). This nonlinear interaction produced a climate mode, which is characterized as a combination mode (C-mode), that is responsible for the seasonally synchronized time evolution of the antisymmetric component of the Indo-Pacific atmospheric circulation during ENSO events (Stuecker et al. 2015). In terms of its consequences, the SWS has been shown to 1) make the thermocline depth in the eastern equatorial Pacific return to normal values (e.g., Harrison and Vecchi 1999; Vecchi and Harrison 2003, 2006; Lengaigne et al. 2006), 2) play a crucial role in the discharge process of the warm water volume (WWV) during El Niño events (McGregor et al. 2012a, 2013), and 3) transfer mass between the Northern and Southern Hemisphere during El Niño events (McGregor et al. 2014). Recently, Abellán and McGregor (2016) utilized a simple coupled model to demonstrate that the SWS during El Niño events plays a crucial role in the synchronization of the events with the annual cycle as well as a rapid termination of these events.

Apart from observational analysis (Harrison and Vecchi 1999; Vecchi and Harrison 2003), forced model studies (Spencer 2004; Vecchi and Harrison 2006; Vecchi 2006), and coupled model experiments (Vecchi et al. 2004; Lengaigne et al. 2006; Xiao and Mechoso 2009), the SWS has also been analyzed in phase 3 of the Coupled Model Intercomparison Project (CMIP3; Meehl et al. 2007). For example, Lengaigne and Vecchi (2009) considered the SWS as a precondition for the termination of El Niño owing to a shoaling of the eastern equatorial Pacific thermocline through eastward-propagating Kelvin pulses. Recently, Ren et al. (2016) found that the CMIP5 models with better performance in simulating the ENSO mode also tend to simulate a more realistic C-mode, related to the SWS as mentioned before (Stuecker et al. 2013, 2015). Additionally, the seasonal synchronization of ENSO in CMIP5 has been documented in numerous studies, showing a large model spread in this regard (Bellenger et al. 2014) and a clear dependency of this unique feature of ENSO on convective parameters (Ham et al. 2013). However, no study has yet undertaken a thorough evaluation of the representation of the SWS in state-of-the-art coupled general circulation models participating in the CMIP5 (Taylor et al. 2012); this is the overarching goal of the present study. We also investigate the dynamics underlying the SWS in CMIP5 models in addition to elucidating its link with the seasonal synchronization of ENSO events.

The rest of this paper is organized as follows. We begin in section 2 by providing a description of the datasets, CMIP5 models, and analysis method used in this study. In section 3, we evaluate how well the zonal wind stress and, in particular, the SWS are captured by CMIP5 models. An analysis of precipitation and SST anomalies during ENSO events as possible drivers of the SWS along with their mean state and multiple-linear regression analysis are then carried out in section 4. In section 5 we examine whether there is a relationship between the SWS, the peak time of these events, and the WWV changes. The final section presents a summary highlighting the main findings.

2. Models and methods

a. CMIP5 models

We focus our analyses on the historical runs by 34 CMIP5 CGCMs. A list with the official model names utilized is displayed in Fig. 1. Further information on individual models is available online (at http://www-pcmdi.llnl.gov/; Taylor et al. 2012). Although the exact duration of the simulations varies slightly from model to model, generally the historical run was carried out including solar, volcanic, and anthropogenic forcing from 1850 to 2005. Here, to avoid models with large ensemble numbers biasing the results, only one ensemble member ("r1i1p1") run for each model is used.

The models were chosen based on the availability of model output required for this study. However, the CSIRO Mk3.6 model was excluded owing to a poor simulation of equatorial SST through ENSO phases (Brown et al. 2014; Grose et al. 2014) showing more variability in the western than in the eastern Pacific (Guilyardi et al. 2012), in stark contrast to observations.

b. Observational data

For comparison with the model results, observed atmospheric and oceanic data are used. The SST dataset is the Extended Reconstructed Sea Surface Temperature, version 3b (ERSST.v3b; Smith et al. 2008), with a $2° \times 2°$ resolution. Both the surface wind stress and mean sea level pressure data are obtained from the European Centre for Medium-Range Weather Forecasts (ECMWF) interim reanalysis (ERA-Interim; Dee et al. 2011) with a $1.5° \times 1.5°$ resolution. In light of the large differences seen

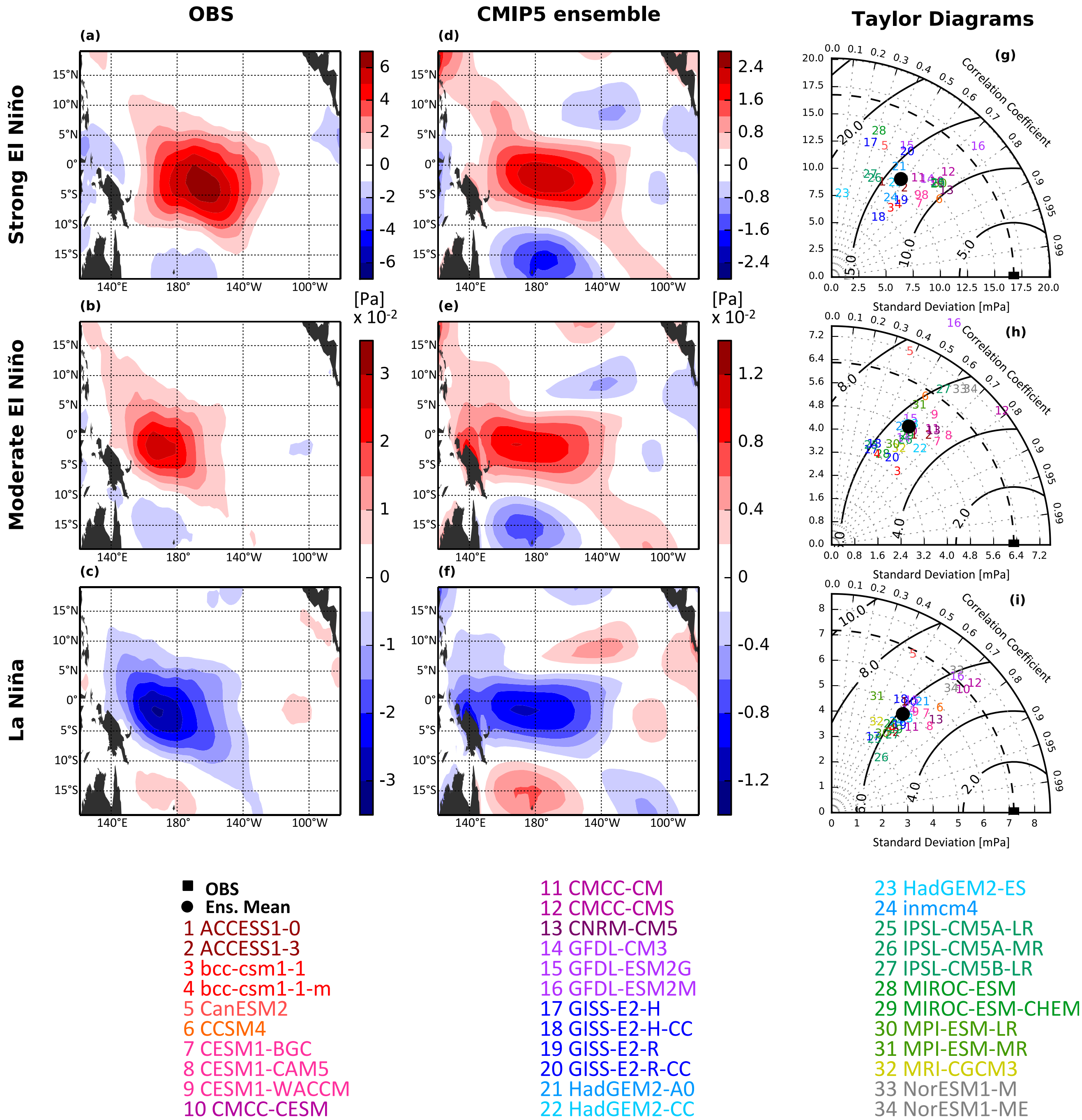

FIG. 1. Composite mean values of zonal wind stress anomalies during (a),(d),(g) strong El Niño, (b),(e),(h) moderate El Niño, and (c),(f),(i) La Niña for the period September^0–February^1, where 0 means the year during which an event develops and 1 means the decaying year, for (a)–(c) observations, (d)–(f) ensemble mean, and (g)–(i) all CMIP5 models. Note the different color bars for the observations and CMIP5 models. Taylor diagrams are obtained by calculating the standard deviation and correlation between each model and observations for the whole domain shown in the left panels.

across observation wind products (e.g., Wittenberg 2004; McGregor et al. 2012b), McGregor et al. (2013) utilized eight global wind products, ERA-Interim among others, finding similar spatial patterns and temporal variability for the meridional wind shift. Precipitation data are taken from the Climate Prediction Center (CPC) Merged Analysis of Precipitation (CMAP; Xie and Arkin 1997), having a horizontal resolution of 2.5° × 2.5°.

In this study, we consider the period from 1880 to 2014 for SST and the period 1979–2014 for all other datasets, with a monthly temporal resolution adopted throughout. The anomalies for the observed variables are defined as the deviations from the 1979–2014 climatological mean.

c. Methodology

Anomalies of all CMIP5 fields are calculated by removing the long-term monthly climatology over the entire period available for each model, whereas the period used to calculate the observed long-term monthly climatology is as discussed above in section 2b. Prior to the calculations, a 3-month binomial filter was applied to all wind stress data (including both the observed and CMIP5 modeled) in order to reduce month-to-month noise, as described in Deser et al. (2012). Both model data and observations were linearly detrended to approximately account for model drift and the impacts of global warming, to first order. Model outputs were examined at native grid resolution and then later interpolated to the same grid as the observations, to facilitate comparison with the measurement record and assessment of the multimodel means.

It has been shown that the dynamics of extreme El Niño events are different from moderate events (e.g., Dommenget et al. 2013; Santoso et al. 2013; Cai et al. 2014, 2015; Capotondi et al. 2015; Takahashi and Dewitte 2015). Therefore, here we classify El Niño events according to the magnitude of SST anomalies within the region 5°S–5°N, 170°–120°W (hereafter the Niño-3.4 index), while La Niña events only have the one category. Specifically, 1) strong El Niño events are identified when the Niño-3.4 index exceeds 1.5°C, 2) moderate El Niño events when the index is greater than 0.5°C but less than or equal to 1.5°C, and 3) La Niña events when the index is less than −0.5°C, for at least 5 consecutive months in all three cases. Following this criterion, we find in the observations two strong El Niño events (1982/83 and 1997/98), seven moderate El Niño events (1987/88, 1991/92, 1994/95, 2002/03, 2004/05, 2006/07, and 2009/10), and eight La Niña events (1984/85, 1988/89, 1995/96, 1999/2000, 2000/01, 2007/08, 2010/11, and 2011/12) during the period 1979–2014. It is worth pointing out that there are four CMIP5 models (GISS-E2-R-CC, INM-CM4.0, MIROC-ESM, and MRI-CGCM3) that are not capable of simulating strong El Niño events, according to our definition. We note that as ENSO events typically peak near the end of the calendar year, here we composite during DJF regardless of event peak.

3. Wind stress during ENSO

Ocean surface wind stress (hereafter wind stress) is an important variable in the coupled system as it indicates the exchange of momentum between the ocean and atmosphere (Lee et al. 2013). Furthermore, the spatial structure of anomalies during ENSO is considered an important factor in setting the ENSO time scale (e.g., Kirtman 1997; Wang et al. 1999; An and Wang 2000; Capotondi et al. 2006; Neale et al. 2008; Kug et al. 2009). Figures 1a–c show the composite of zonal wind stress anomalies for the period September (0) to February (1) for observed strong El Niño, moderate El Niño, and La Niña events, respectively. The spatial pattern of the observed zonal wind stress anomalies displays westerlies (easterlies) during El Niño (La Niña) with maximum Pacific anomaly located between the equator and 5°S. However, two distinct features between the strong El Niño events and the other two types of ENSO events can be clearly seen: 1) different magnitude (i.e., twice as strong for strong El Niño events) and 2) westward shift of maximum zonal wind stress anomalies during La Niña and moderate El Niño events (by about 30° compared to the strong El Niño pattern), which are almost mirror images. Previous studies have demonstrated that these wind stress differences (i.e., magnitude and location) have been associated with the nonlinear characteristics of the atmospheric response to the SST anomalies of the opposite sign (i.e., via atmospheric convection; Kang and Kug 2002; Ohba and Ueda 2009; Frauen and Dommenget 2010).

Although the zonal distribution of CMIP5 ensemble mean zonal wind stress anomalies are qualitatively similar to those observed, some differences can be seen (Figs. 1a–f): (i) the magnitude of the CMIP5 ensemble mean anomalous wind stress for each ENSO event type is much weaker (up to 50%–60%) than the observations for its corresponding event type, which is consistent with the results of Bellenger et al. (2014); (ii) the multimodel mean CMIP5 simulated equatorial winds are not as broad meridionally as those observed (i.e., the CMIP5 ensemble mean winds only extend to approximately 3°N and 7°S; cf. Figs. 1d–f), which can impact the period of ENSO (Capotondi et al. 2006); and (iii) the anomalous wind stresses have a larger longitudinal span than the observations, consistent with the earlier study of Lee et al. (2013).

To further assess the skill of the CMIP5 ensemble set in simulating the observed spatial pattern of anomalies of zonal wind stress during ENSO events, we present Taylor diagrams (Taylor 2001) in Figs. 1g–i for the three types of ENSO events. Generally speaking, the CMIP5 models produce reasonable correlations when compared with the observations, with average spatial correlation values of 0.58, 0.55, and 0.59 for strong El Niño, moderate El Niño, and La Niña events, respectively. In regard to the standard deviation of zonal wind stress patterns, most of the CMIP5 models have less variance (11.0, 4.9, and 4.8 mPa as mean values) than that seen in the observations (16.8, 6.3, and 6.2 mPa for strong

El Niño, moderate El Niño, and La Niña, respectively). The fact that the magnitude of simulated zonal wind stress is weaker than observed (Fig. 1), with a reduced meridional width, might explain the low standard deviation of the associated composite spatial maps.

a. The southward wind shift

As mentioned in the introduction, the SWS refers to a meridional movement of the anomalous wind stresses during the ENSO event mature phase (i.e., boreal winter). In particular, the maximum of these anomalies is located at (or slightly north of) the equator during August–October (ASO), while the magnitude of the wind stress is increased (decreased) south (north) of the equator during November–January (NDJ), such that the maximum zonal wind stress occurs south of the equator during February–April (FMA; e.g., Harrison and Vecchi 1999; McGregor et al. 2013). Here we define the SWS as the difference in latitude of the maximum zonal wind stress anomalies between ASO and FMA, averaged over 160°E–120°W. It is worth emphasizing that other factors, such as the strength and meridional width of the anomalies, also impact the oceanic response to the SWS. However, none of these changes are of interest if the model does not first produce the SWS. Thus, here we have chosen to focus our SWS definition on changes in the latitude of the wind stress anomalies, but we also note that the oceanic impact of the SWS is discussed in section 5 of this study. The magnitude of the observed SWS is 9.0°, 6.0°, and 7.5° for strong El Niño, moderate El Niño, and La Niña events, respectively.

Figure 2 displays the latitude of the maximum westerly (easterly) anomalies from August to April during El Niño (La Niña) years averaged zonally over the western and central Pacific. We note that these latitudes are calculated based on the composite mean zonal wind stress for each model. Here and in the rest of the paper we divide the CMIP5 models into two categories: models with SWS and those without SWS. This classification is based on the ability of each model to realistically reproduce an SWS during the three types of ENSO events, with the magnitude of the shift required to be at least 66.6% of the observed SWS.

The majority of the models simulate realistic SWS during at least one of the three types of defined ENSO events. In fact, two-thirds of the CMIP5 models analyzed (22 out of 34) can reproduce the SWS for all three types of events analyzed. It is also clear that the multimodel ensemble mean of models with SWS (MME with SWS) is comparable with observations (Figs. 2a–c). It is interesting to note that MME with SWS indicates stronger SWS for strong El Niño events (reaching the maximum of westerly anomalies up to 6°S in March) than that for moderate El Niño or La Niña (located at 4°S in the same month), which is also seen in observations. There are 4 (out of 30) models that do not capture the SWS during strong El Niño (Fig. 2d), while there are 6 and 4 (out of 34) models that do not reproduce the SWS during moderate El Niño and La Niña, respectively (Figs. 2e,f). The multimodel ensemble average of these models (i.e., MME without SWS) exhibit latitude of maximum zonal wind stress roughly constant (and south of the equator) throughout the 9-month period. It is also worth mentioning that two models (IPSL-CM5A-LR and IPSL-CM5A-MR) are not able to simulate the SWS for any type of ENSO event. The study of Bellenger et al. (2014) analyzes various other ENSO metrics and also concludes that the ENSO in these last two models exhibits poor agreement with observations.

b. SWS spatial characteristics

To highlight the SWS we present composite maps of the zonal wind stress and sea level pressure (SLP) anomaly difference between FMA and ASO for the observations and the CMIP5 models with and without SWS and for the three types of ENSO events (Fig. 3). The observational differences during strong El Niño events show several clear structures over the tropics: 1) easterly differences in the western Pacific north of the equator, 2) westerly differences over the central Pacific south of the equator, and 3) high positive anomalous SLP observed over the northwestern Pacific representing a large-scale low-level anticyclone (Fig. 3a). All of these features are consistent with the representation of this southward wind shift by an empirical orthogonal function (EOF) analysis (McGregor et al. 2013) and the C-mode, which emerges from the seasonal modulation of ENSO-related atmospheric anomalies (Stuecker et al. 2013). It is noted that the high SLP anomalies in the northwest are generally referred to as the Philippine Sea anticyclone (e.g., Harrison and Larkin 1996; Wang et al. 1999, 2000; Wang and Zhang 2002; Li and Wang 2005). Values in the center of the Philippine Sea anticyclone during strong El Niño years (~3 hPa), as shown in Fig. 3a, are larger than the amplitude of the local annual variation (~2 hPa) (Wang and Zhang 2002).

The observed zonal wind stress differences for moderate El Niño show a similar dipole structure to those for strong El Niño, although both easterly and westerly differences in the tropical Pacific are shifted westward, and their magnitudes are much weaker (Fig. 3b). Furthermore, the longitudinal offset of the winds north and south of the equator is reduced. Not surprisingly, the development of the Philippine Sea anticyclone is also more modest because of its link to the El Niño amplitude (Wang and Zhang 2002; Stuecker et al. 2015).

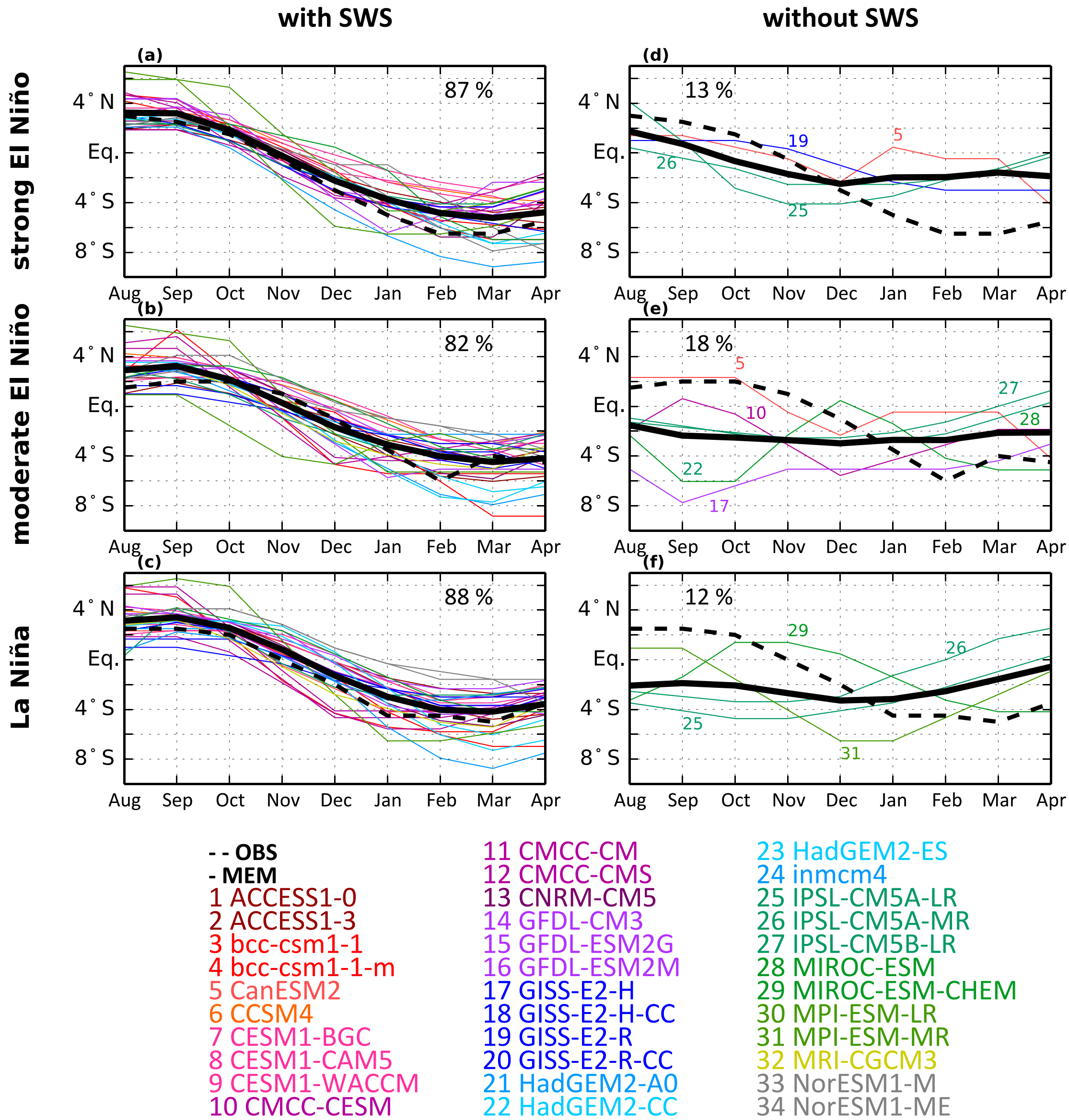

FIG. 2. Latitude of anomalous zonal wind stress maximum averaged over 160°E–120°W during ENSO events, for the period August^0–April^1. A 3-month running mean is applied; for instance, the value for August is the average of July, August, and September and so forth. Simulations are divided into models (a)–(c) with SWS and (d)–(f) without SWS for (a),(d) strong El Niño, (b),(e) moderate El Niño, and (c),(f) La Niña. See section 3a for SWS classification.

In contrast, the La Niña phase during FMA–ASO leads to an anomalous cyclone developing over the Philippine Sea reversing both its sign and the pattern of zonal wind anomalies (i.e., westerly seasonal difference north of the equator and easterly south of the equator; Fig. 3c). Unlike warm events, these two regions of opposite zonal wind stress anomalies north and south of the equator are centered at roughly the same longitude. Further to this, their magnitudes are weaker than those for moderate El Niño events.

In qualitative agreement with observations, models with SWS display anomaly differences between FMA and ASO with patterns similar to those observed (Figs. 3d–f). This includes positive (negative) anomalous SLP over the Philippine Sea region during El Niño (La Niña) events and pronounced differences in zonal wind stresses in the western Pacific north of the equator and central Pacific south of the equator. However, the seasonal differences of zonal wind stress anomalies are underestimated among models, especially for strong El Niño events. The anomalous SLP in the Philippine anticyclone region is also roughly half the magnitude observed. Another obvious difference between the observations and the CMIP5 models with SWS is the lack of simulated zonal offset of the zonal winds about the equator for strong El Niño. In particular, the positive zonal wind difference south of the

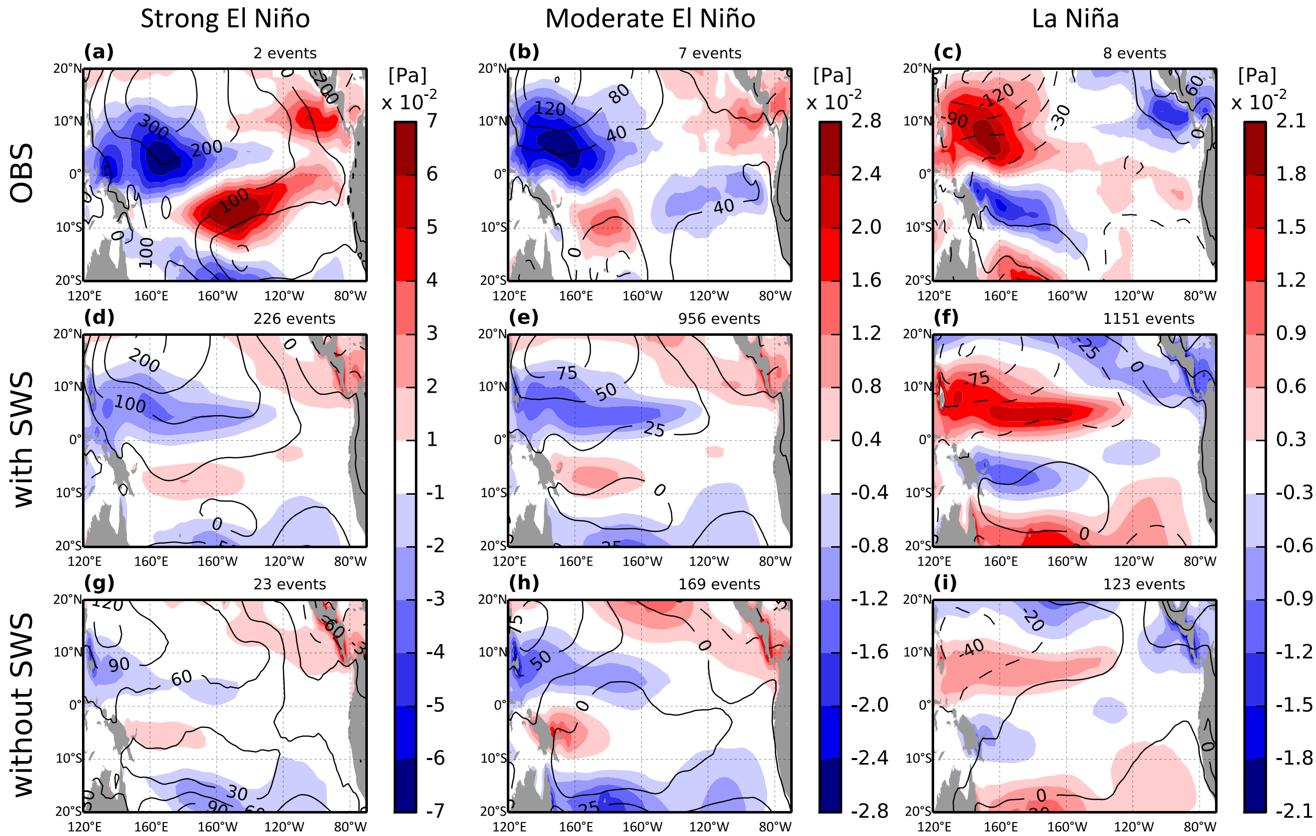

FIG. 3. Zonal wind stress anomaly composites during FMA season minus that during ASO season (shading) and SLP anomaly (contours) for (a),(d),(g) strong El Niño, (b),(e),(h) moderate El Niño, and (c),(f),(i) La Niña for (a)–(c) observation, (d)–(f) models with SWS, and (g)–(i) models without SWS. Note that negative contours are dashed; units for both variables are in Pa and that we employ different color bars to better highlight all events more clearly. The numbers in each panel indicate the number of the events falling within that category.

equator is not offset to the east of the negative zonal wind difference above the equator as seen in observations.

Even though most models without an SWS (according to the criterion we adopt) can simulate an SWS to some extent, albeit with much weaker magnitude, the meridional movement tends to be displaced too far to the west compared to the observations (Figs. 3g–i). Consequently, the Philippine Sea anticyclone (cyclone) is not as well developed during the simulated El Niño (La Niña). The westward extension of ENSO-related zonal wind stress anomalies found in the CMIP5 models, which is more pronounced in models without an SWS, is a common failure for most CGCMs (Kirtman et al. 2002; Zhang and Sun 2014).

4. Possible drivers of the SWS

a. *The role of anomalies*

It is generally accepted that the anomalous SST during ENSO events is intimately linked with rainfall and wind stress anomalies (e.g., Bjerknes 1969; Ropelewski and Halpert 1987; Philander 1990). Thus, in this section we explore both qualitatively and quantitatively (using linear regression) the relationship between the representation of SWS, the details of the SST anomalies, the accompanying precipitation, and their climatology during boreal winter.

1) SST ANOMALIES

It is well known that El Niño (La Niña) events are characterized by anomalously warm (cold) SST over the central-eastern equatorial Pacific (Figs. 4a–c). In particular, during strong El Niño events, the maximum SST anomalies are situated in the eastern equatorial Pacific (Fig. 4a), where the cold tongue is located (Larkin and Harrison 2005; Ashok et al. 2007; Kao and Yu 2009; Kug et al. 2009; Kim et al. 2009; Holland 2009). However, during moderate El Niño events the maximum SST anomalies are weaker and shifted to the west, while La Niña events generally mirror the moderate El Niño (Figs. 4b,c). This shift to the west of the maximum SST anomalies with weaker values off the South American coast for moderate El Niño is consistent with aspects of ENSO diversity described in the literature (Takahashi et al. 2011; Capotondi et al. 2015).

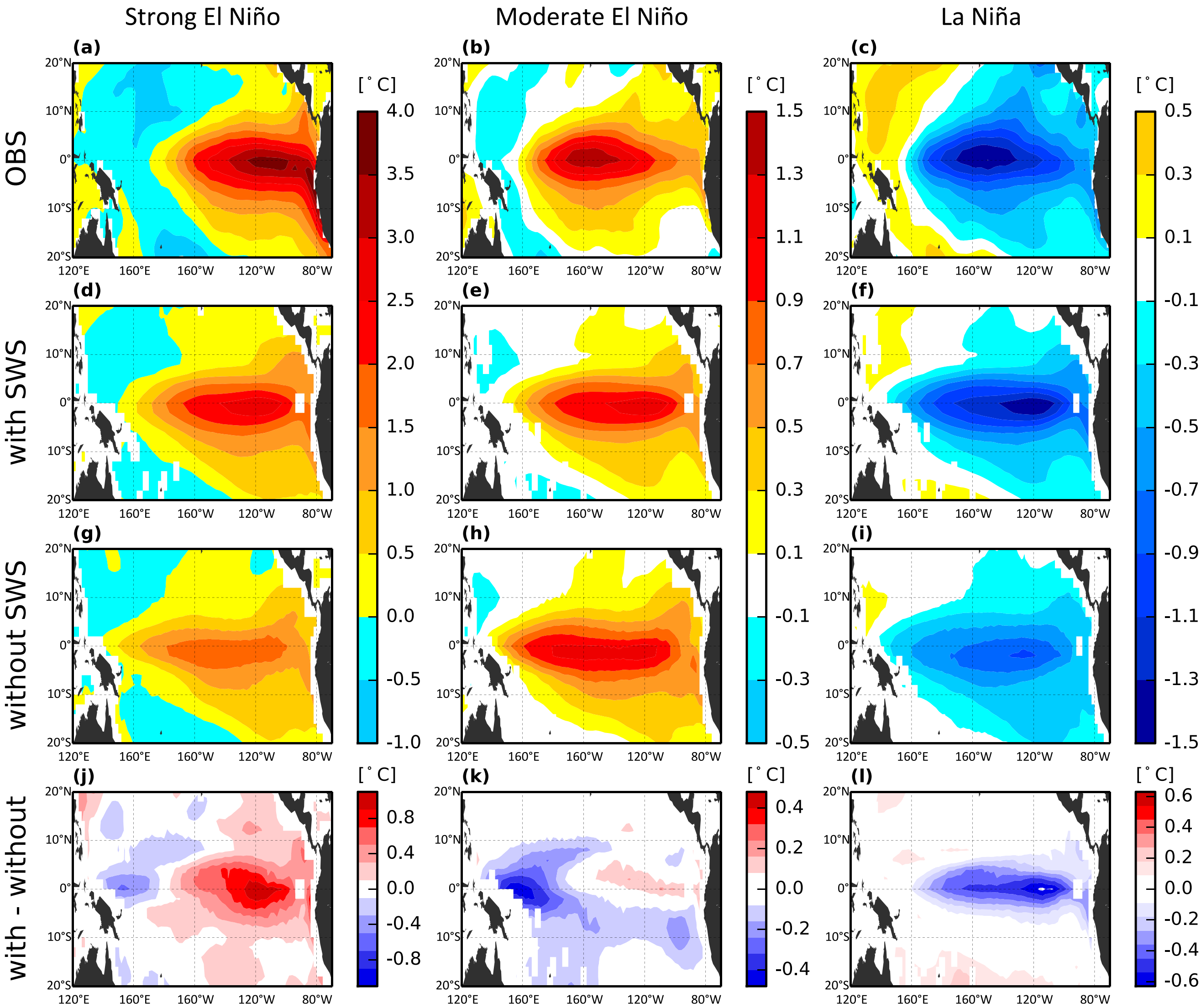

FIG. 4. SST anomalies in DJF during (a),(d),(g),(j) strong El Niño, (b),(e),(h),(k) moderate El Niño, and (c),(f),(i),(l) La Niña for (a)–(c) observations, (d)–(f) models with SWS, (g)–(i) models without SWS, and (j)–(l) the difference between models with and without SWS. Note the different color scales.

Both groups of CMIP5 models broadly reproduce SST anomaly patterns that are overall consistent with those observed, including most models producing La Niña and moderate El Niño events as approximate mirror images of each other (Figs. 4e,f). However, it is noted that the models have been shown to underrepresent the observed ENSO diversity (e.g., Capotondi and Wittenberg 2013), and here we highlight several other notable differences. First, in contrast to the observations, models that reproduce the SWS exhibit no significant differences in the location of SST anomalies between strong and moderate El Niño (Figs. 4d,e). These models also display a westward shift of the anomalous SST values during extreme El Niño events compared to observations. For instance, the anomalous 0.5°C isotherm is shifted around 10° longitude when compared to that observed. Models without an SWS tend to underestimate the magnitude of the anomalous values of SST for La Niña and strong El Niño, whereas the amplitude is larger for moderate El Niño (Figs. 4g–i).

Here we calculate and display the ensemble mean SST anomaly differences between models with and without an SWS in an attempt to better understand the cause of the SWS (Figs. 4j,k). The differences between these two types of models (with and without the SWS) show warmer conditions over the eastern and colder over the western equatorial Pacific for El Niño events, although the eastern Pacific difference is larger for the strong events and the western Pacific difference is larger for moderate events. We also find that the maximum event

TABLE 1. Coefficients of determination R^2 and correlation coefficient r (shown in parentheses) between possible drivers of the SWS and the SWS index (defined in section 3a). Note that bold values indicate that the correlation is significant at the 95% confidence level. The meridional gradients are defined as the average over the equatorial region (5°S–4°N, 120°E–160°W) minus the average over the north off-equatorial region (5°–12°N, 140°E–160°W). For climatological predictors, we focus on the DJF season, when the anomalous zonal winds are migrating southward. The number of degrees of freedom is 28 for strong El Niño and 32 for the other events.

Variable	Description	Strong El Niño	Moderate El Niño	La Niña
PR_{clim}	Meridional gradient of climatological precipitation during DJF	**0.160 (0.40)**	**0.396 (0.63)**	**0.262 (0.51)**
SST_{clim}	Meridional gradient of climatological SST during DJF	**0.293 (0.54)**	**0.428 (0.65)**	**0.397 (0.63)**
$TAUX_{clim}$	Meridional gradient of climatological zonal wind stress during DJF	**0.160 (0.40)**	**0.247 (0.50)**	**0.242 (0.49)**
PR_{anom}	Precipitation anomaly in DJF averaged over 0°–10°N, 120°E–160°E during ENSO	**0.294 (0.54)**	**0.518 (0.72)**	**0.333 (0.58)**
SST_{anom}	Equatorial (5°S–5°N) maximum SST anomaly in DJF during ENSO events averaged over 20° longitude with the maximum located in the center of the selected region	**0.137 (0.37)**	0.026 (0.16)	**0.248 (0.50)**
$TAUX_{anom}$	Maximum zonal wind stress anomaly between 10°S and 10°N averaged over August–April and 160°E–120°W during ENSO	**0.199 (0.45)**	**0.352 (0.59)**	**0.190 (0.44)**
CT	Annual mean climatology of SST over 2°S–2°N, 150°E–110°W (cold tongue)	0.081 (0.29)	**0.141 (0.38)**	0.099 (0.32)
LON_{05}	Longitude of ±0.5°C SST anomaly over the equator in DJF during ENSO years	0.097 (0.31)	**0.138 (0.37)**	0.068 (0.26)
ZRes	Zonal resolution of the atmosphere	0.113 (0.34)	0.068 (0.26)	0.098 (0.31)
MRes	Meridional resolution of the atmosphere	0.054 (0.23)	**0.119 (0.35)**	0.021 (0.15)

magnitude, identified with each model's SST anomaly in DJF, is statistically significantly related to the magnitude of the SWS during La Niña and strong El Niño events (Table 1). If we instead classify the event magnitude with the magnitude of the wind stress response (rather than SST magnitude) we find that the relationship between the event magnitude and the SWS decreases (increases) for La Niña (strong El Niño) (Table 1). We also find that the erroneous westward displacement of western edge of SST anomalies during extreme El Niño events is much more pronounced in models without an SWS, and it is also seen during moderate El Niño events in these models. However, the relationship between the extent of the westward shift of the SST anomaly edge and the magnitude of the SWS is only statistically significant for moderate El Niño events (Table 1). The shift toward the west of the SST anomaly edge has been related to the cold tongue bias, which is one of the longstanding problems among climate models (Kirtman et al. 2002; Capotondi et al. 2006) and still remains an issue in CMIP5 models (Brown et al. 2014; Kug et al. 2012; Capotondi and Wittenberg 2013; Ham et al. 2012; Ham and Kug 2015). Consistent with the westward bias, we also find a linear significant relationship between the SST bias in the equatorial Pacific cold tongue region (2°S–2°N, 160°E–90°W; Li et al. 2016) and the SWS magnitude for moderate El Niño events (Table 1).

2) Precipitation anomalies

During strong El Niño events, the warm SST anomalies over the equatorial central and eastern Pacific lead to the equatorward displacement of the intertropical convergence zone and South Pacific convergence zone resulting in positive precipitation anomalies over this region (Fig. 5a). In contrast, negative precipitation anomalies are robust to the north, south, and west of this enhanced precipitation (Fig. 5a), showing that this is more a redistribution than an increase (Choi et al. 2015). This redistribution of precipitation during strong El Niño events is also seen in the CMIP5 models; however, the magnitude of the model anomalies is much weaker, and this bias is more pronounced in models without the SWS. In fact, there is a statistically significant relationship between precipitation anomalies in the northwestern Pacific and the magnitude of the SWS (see yellow box in Fig. 5; Table 1). Consistent with the westward shift of the SST anomaly edge seen in both model groups (Fig. 4), the enhanced equatorial precipitation during strong El Niño events is also shifted to the west relative to observations (Figs. 5a–c) (Misra et al. 2007; Cai et al. 2012; Kug et al. 2012).

A similar pattern of precipitation is observed for moderate El Niño events (i.e., negative anomalous values of rainfall over the western tropical Pacific and positive over the central Pacific) (Fig. 5e), although the anomaly magnitude is around half that seen for strong El Niño events and no anomalies are observed over the eastern equatorial Pacific for moderate El Niño events consistent with the study of Cai et al. (2014). As for strong El Niño events, the models tend to simulate excessive precipitation anomalies over the western Pacific warm pool region, which is likely due to the westward shift of SST anomalies as this bias is more marked in

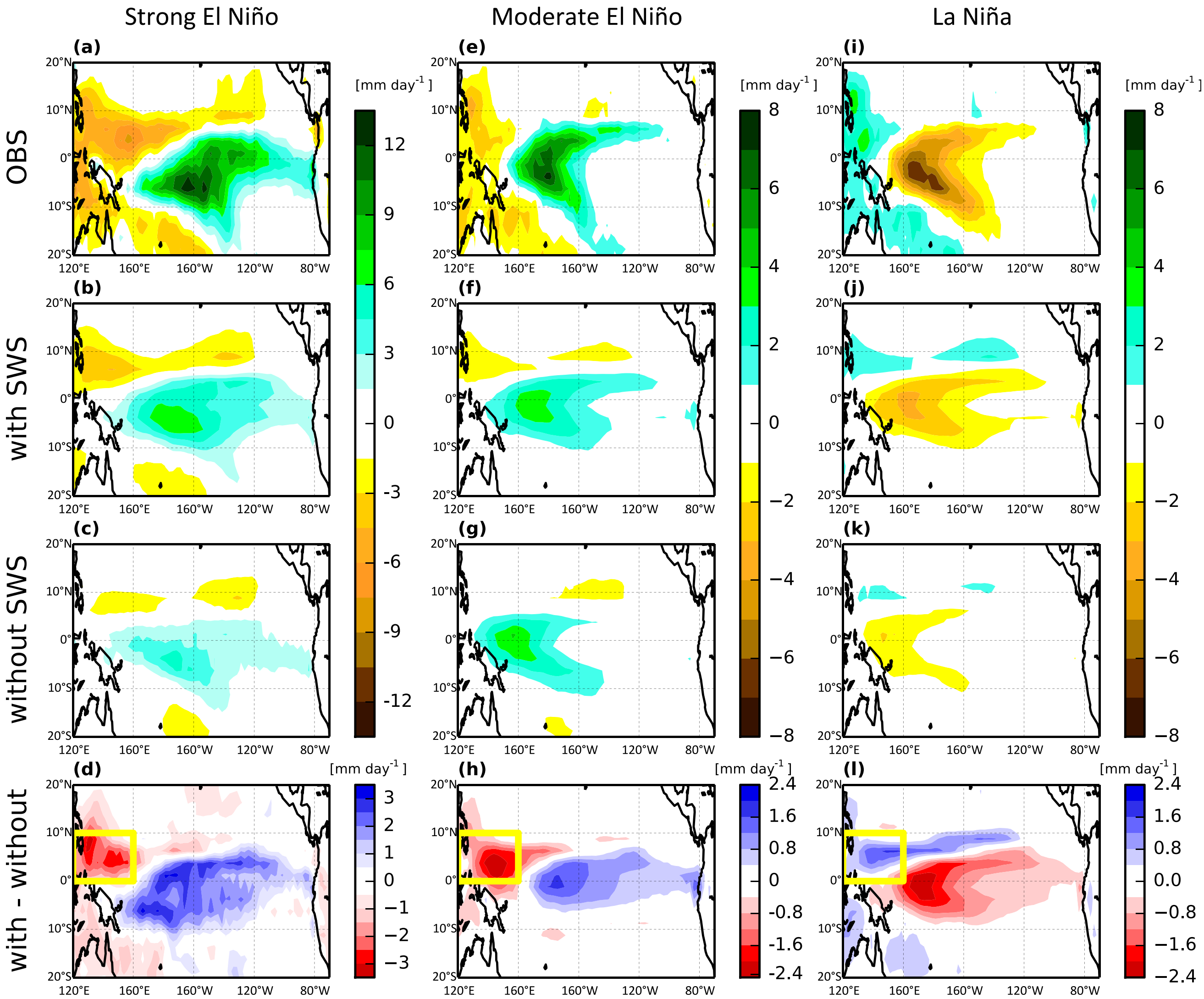

FIG. 5. Precipitation anomalies in DJF during (a)–(d) strong El Niño, (e)–(h) moderate El Niño, and (i)–(l) La Niña for (a),(e),(i) observations, (b),(f),(j) models with SWS, (c),(g),(k) models without SWS, and (d),(h),(l) the difference between models with and without SWS. Note the different color scales. The yellow boxes indicate the area over which indices are calculated for use in the regression models carried out in section 4c.

models without an SWS (Figs. 5f,g). As a consequence, the difference map exhibits more (less) precipitation anomalies over the central-west (far west) equatorial Pacific (Fig. 5h). Again the northwestern Pacific changes are so robust that a statistically significant relationship between precipitation anomalies in the northwestern Pacific and the magnitude of the SWS also exists for moderate El Niño events (Table 1).

For observed La Niña events, there is a marked similarity with moderate observed El Niño events (Figs. 5e,i), although with opposite anomaly patterns, as expected [i.e., drier (wetter) conditions than normal over the central/western (far west) equatorial Pacific]. As before, the CMIP5 models underestimate the magnitude of the anomalous rainfall during La Niña compared to observations, particularly those without an SWS (Figs. 5j,k). Focusing again on precipitation anomalies in the northwestern Pacific, a statistically significant relationship is found between the anomaly magnitude and the magnitude of the SWS during La Niña events (Table 1).

b. *The role of the mean state*

It has been suggested that climatological biases affect the fidelity of the simulation of ENSO in climate models (Wang and An 2002; Guilyardi 2006; Sun et al. 2009; Bellenger et al. 2014). Here, we analyze the climatological SST, precipitation, and wind stress during DJF in the tropical Pacific to further examine if mean state biases might influence the ability of CMIP5 models to simulate the SWS during ENSO events. We chose to

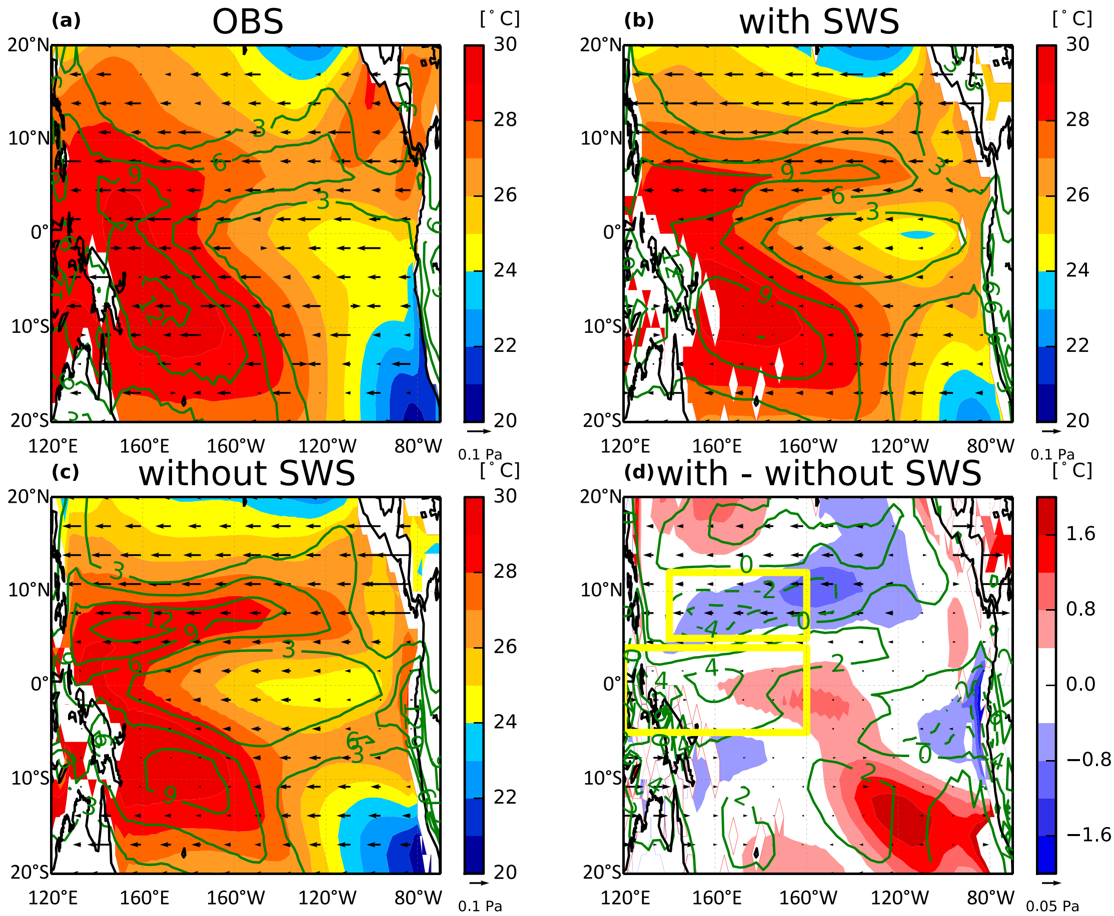

FIG. 6. Climatological SST (shading), precipitation (green contours), and zonal wind stress (vectors) during DJF for (a) observations, (b) the ensemble of models that display the SWS, (c) the ensemble of models that do not display the SWS, and (d) the difference between the DJF ensemble mean of these. The two yellow boxes in (d) indicate the southern (5°S–4°N, 120°E–160°W) and northern region (5°–12°N, 140°E–160°W), where meridional gradients are carried out in section 4c.

focus on the DJF period as this is when the surface winds are migrating southward, but we also note that the differences between the CMIP5 with SWS and CMIP5 without SWS are very similar regardless of whether MAM or ASO was selected (not shown).

The tropical Pacific mean state is characterized by relatively cold SST in a band centered on the equator in the central and eastern Pacific, and the warmest temperatures in the west (Fig. 6a). These two regions are commonly referred to as the cold tongue and warm pool, respectively. The climatological precipitation during DJF exhibits two bands of heavy precipitation: the first extending across the central-eastern Pacific (i.e., the ITCZ) and the second extending southeast from near New Guinea to the southeastern Pacific (i.e., the SPCZ), with highest rainfall in the SPCZ (Fig. 6a). Consequently, minimum wind stress is observed in the SPCZ region, and the strongest easterly anomalies are found north and south of the ITCZ, converging in this area (total winds not shown).

To first order, the models (both with and without the SWS) appear to do a reasonable job capturing the main features of the observed spatial patterns of SST and precipitation described above (Figs. 6a–c). However, models without an SWS during ENSO events exhibit two notable differences compared to observations or models with an SWS: 1) larger rainfall in the ITCZ than in the SPCZ and 2) SST underlying the ITCZ appear much warmer. Both changes are highlighted by looking at the differences between the models with and without the SWS (Fig. 6d). Precipitation differences of up to 4 mm day^{-1} are found, whereby the models with the SWS are wetter in the western equatorial Pacific and drier in the northwestern Pacific. The rate of precipitation in these regions is significantly related to the magnitude of the SWS during all event types. Furthermore, the models with the SWS have cooler SST (up to 1.2°C) underlying the ITCZ than those without, and they also have a less pronounced cold tongue bias in the central Pacific. It has

TABLE 2. Multiple correlation r and squared multiple correlation R^2 between the variables defined in Table 1 and the SWS index (defined in section 3a) and their root-mean-square error (RMSE). Note that bold values or variables indicate that the correlation coefficients are significant at the 95% confidence level. Each model's ENSO event composite mean is computed prior to the regression across the ensemble of models.

ENSO event	Predictors	R squared (r)	RMSE (° lat)
Strong El Niño	PR_{clim} + SST_{clim} + $TAUX_{clim}$ + PR_{anom} + SST_{anom} + $TAUX_{anom}$	0.393 (0.63)	3.4
	PR_{clim} + $\mathbf{SST}_{clim}$ + $TAUX_{clim}$	**0.304 (0.55)**	4.3
	PR_{anom} + SST_{anom} + $TAUX_{anom}$	**0.301 (0.55)**	4.3
	SST_{clim} + PR_{anom}	**0.362 (0.60)**	5.7
Moderate El Niño	PR_{clim} + SST_{clim} + $TAUX_{clim}$ + $\mathbf{PR}_{anom}$ + SST_{anom} + $TAUX_{anom}$	**0.598 (0.77)**	4.2
	PR_{clim} + $\mathbf{SST}_{clim}$ + $TAUX_{clim}$	**0.483 (0.70)**	5.4
	$\mathbf{PR}_{anom}$ + SST_{anom} + $TAUX_{anom}$	**0.565 (0.75)**	5.8
	SST_{clim} + $\mathbf{PR}_{anom}$	**0.570 (0.76)**	7.1
La Niña	PR_{clim} + SST_{clim} + $TAUX_{clim}$ + PR_{anom} + $\mathbf{SST}_{anom}$ + $TAUX_{anom}$	**0.511 (0.72)**	3.6
	PR_{clim} + SST_{clim} + $TAUX_{clim}$	**0.368 (0.61)**	4.3
	$\mathbf{PR}_{anom}$ + $\mathbf{SST}_{anom}$ + $TAUX_{anom}$	**0.481 (0.69)**	4.9
	SST_{clim} + PR_{anom}	**0.394 (0.63)**	5.4

been suggested that weaker gradients of SST facilitate a shift in convection zones (Cai et al. 2014). Thus, we expect the meridional gradient of SST between the equator and north off-equator regions, which is weaker in models without an SWS, to favor the shift in convection zone from SPCZ to ITCZ in these models. This is supported by calculating the coefficient of determination between the meridional gradient of SST and the magnitude of the modeled SWS, as we find a statistically significant relationship in all event types (Table 1). Another feature revealed by Fig. 6d is that models without an SWS tend to also exhibit weaker North Pacific trade winds owing to weaker zonal SST gradient.

c. Possible drivers of the SWS—Evidence from a multilinear regression

The results presented in sections 4a and 4b above suggest that the model's mean climate and its representation of ENSO both impact the magnitude of the modeled SWS. To quantify the dependency of the SWS on these variables described above (Table 1), we conduct multiple-linear regressions (Wilks 2006) between the SWS, defined in section 3a, and a set of metrics each related to the possible driving mechanisms of the SWS, as listed in Table 1. As with the linear regressions presented in Table 1, each model's ENSO event composite mean is computed, then the relationship (regression) between the indices is computed across the ensemble of models. We emphasize that the purpose of this analysis is not to generate a set of SWS predictors. Rather, the intent is to gain insight into the SWS dynamics, by analyzing its possible link to mean state metrics and their ENSO-related values, along with the horizontal resolution in the atmospheric model.

Given the large number of possible combinations of explanatory variables listed in Table 1, only those regressors with the highest R squared values are taken into account. These include the three climatological values in DJF and the three anomalous variables, each of which we consider to be physically linked with the SWS. For each type of event, there are four multiple-regression models, shown in Table 2, which consist of (i) the six variables mentioned above, (ii) the three climatological values, (iii) the three anomalous values, and (iv) the meridional gradient of DJF climatological SST and rainfall anomaly in the northwestern Pacific, which have the highest correlation in the single linear regression (Table 1). The highest (significant) squared multiple correlations are up to 0.36, 0.60, and 0.51 for strong El Niño, moderate El Niño, and La Niña, respectively.

Interestingly, the resulting correlation is not the sum of the individual correlations, which highlights that each of these variables is not linearly independent. For instance, the climatological meridional gradient of SST and the ENSO-related anomalous precipitation in the northwest equatorial Pacific are linearly related (R squared = 0.39, 0.46, and 0.46 for strong El Niño, moderate El Niño, and La Niña, respectively). As the latter variable is also related to the Philippine anticyclone development (i.e., how well the SWS is simulated; Fig. 3), the meridional gradient of SST in each model is expected to be a potentially important driver for both precipitation in the northwest equatorial Pacific and the SWS. It is also interesting to note that a large portion of the multilinear regression (R squared) can be recovered when simply considering the climatological gradients of SST, precipitation, and wind stress and that this combined effect is not dissimilar to that which can be achieved with the meridional gradient of climatological SST alone. Again, we highlight the potential importance of the meridional gradient of climatological SST as a driver of the SWS. Further experimentation, however, is needed to better understand the dynamics behind this link. We note that the coefficients of these two explanatory variables are statistically significant in most of our regression models. In addition to these two variables, including the rest of the regressors leads to an increase in the explained variance of the SWS for La Niña (from 39% to 51%), whereas no large contribution is found for strong El Niño (from 36% to 39%) and moderate El Niño (from 57% to 60%). We also notice that, given a variable, most (with the exception being SST anomalies) correlation coefficients are larger for moderate than for strong El Niño events (Table 1), which is consistent with the atmospheric nonlinear interaction between ENSO and the Pacific warm pool annual cycle (C-mode).

We emphasize that correlation, of course, does not necessarily imply causality. The association between the SWS and the anomalous variables described above may simply indicate symptomatic changes; however, we believe that this is unlikely to be the case for the climatological variables.

5. Seasonal synchronization and SWS

A well-known characteristic of ENSO events is their tendency to peak at the end of the calendar year, and as outlined in section 1, previous studies have proposed that the SWS plays a significant role in El Niño phase locking and therefore in the seasonal modulation of air–sea coupling strength. To further verify this hypothesis, we now examine the connection between ENSO seasonal synchronization and the SWS in the CMIP5 coupled models.

Figure 7 shows the composite Niño-3.4 region (defined in section 2c) SST anomaly evolution during a 13-month period (6 months before and 6 months after the peak) for the ensemble mean of CMIP5 models with SWS (CMIP5 with SWS) and without SWS (CMIP5 without SWS) versus observations for comparison. The maximum amplitude in CMIP5 with SWS (2.2°C) is roughly the same as the observed (2.1°C) and larger than that seen in CMIP5 without SWS (1.8°C). A *t* test is conducted to assess the statistical significance (at the 95% level) of the differences in the modeled composites, and statistically significant differences are denoted by the gray shaded area in Fig. 7. It is found that for strong El Niño events, the CMIP5 with- SWS and CMIP5 without SWS are significantly different during the development and mature phase. It is clear that the SST anomalies of the CMIP5-with-SWS models decay at a much faster rate than the CMIP5-without-SWS ensemble. To quantify the strength of this decay, we calculate the average of the monthly difference in the Niño-3.4 index between the peak of the event and 6 months after. The resulting average SST anomaly decay is -0.34°C month^{-1} in CMIP5 with SWS, which is much stronger than the -0.23°C month^{-1} seen in CMIP5 without SWS. It is interesting to note, however, that both values are lower than average SST anomalies decay observed during strong El Niño events (-0.45°C month^{-1}).

For moderate El Niño events, in contrast, no statistically significant difference is seen between the two modeled composite means throughout the whole period analyzed (Fig. 7b). The maximum values between CMIP5 with SWS and CMIP5 without SWS are approximately the same (~1°C), which is somewhat expected given these events must fall within the range of 0.5° and 1.5°C, and their decaying rates (-0.12° and -0.10°C month^{-1}, respectively) are also highly similar. As is the case for strong events, the decaying rate for moderate El Niño is underestimated compared with observations (-0.19°C month^{-1}).

In contrast to moderate El Niño events, there is a statistically significant difference between the two composite means during the mature phase for La Niña events (Fig. 7c). In particular, the peak magnitude is higher (-1.2°C) in CMIP5 with SWS compared to CMIP5 without SWS (-0.8°C), and the peak in the latter set is much less pronounced. Additionally, the decay of SST anomalies following the event peak is larger in CMIP5 with SWS (0.13°C month^{-1}) compared to CMIP5 without SWS (0.08°C month^{-1}), with both values again lower than observed (0.14°C month^{-1}).

We note that, given a certain magnitude of an ENSO event, its decaying rate is larger in CMIP5 with SWS than that in CMIP5 without SWS. Thus, the fact that the decay of SST anomalies is lower in CMIP5 without SWS is owing to not only the lower magnitude of the events but also the lack of the SWS.

To further elucidate this feature of ENSO phase locking in relation to the SWS, Fig. 8 shows the percentage of ENSO events peaking in each calendar month for models with and without SWS compared to observed. The four observed extreme El Niño (1888/89, 1902/03, 1982/83, and 1997/98) all reached their maximum amplitude in NDJ (Fig. 8a). In comparison, in CMIP5 with SWS, 60% of strong El Niño events peak during NDJ, consistent with observations, whereas only 28% strong El Niño events peak in NDJ in CMIP5 without SWS. In addition, a relatively large proportion (~38%) of the modeled strong El Niño events peak erroneously during April–June in CMIP5 without SWS. The number of strong events erroneously peaking during April–June is only 6% in models with an SWS. Such a clear difference between the CMIP5 with SWS

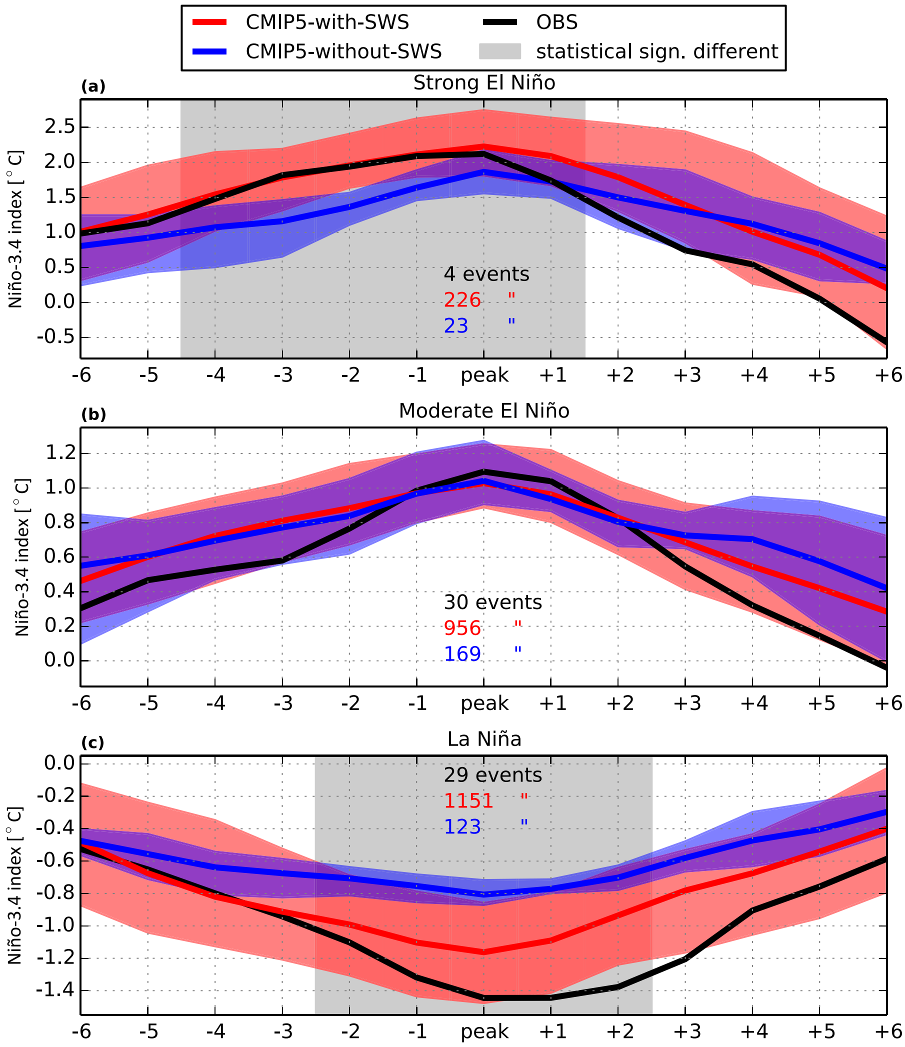

FIG. 7. Composite mean of SST anomalies over the Niño-3.4 region during the 6-month period around the peaks of ENSO events. Black lines indicate the observed values; red (blue) lines represent the ensemble mean of CMIP5 models with (without) SWS. The red and blue shaded areas show the 5th- and 95th-percentile range, whereas gray shading indicates that the two ensemble means are different at the 95% level, after employing a *t* test. Different *y*-axis temperature scales are employed in each panel.

and CMIP5 without SWS is not seen for moderate El Niño events, as ~30% of event peaks occur during October–December (OND) regardless of whether models accurately produce the SWS (Fig. 8b). In the observations, 60% of moderate El Niño events peak during OND, while 76% of La Niña events peak during NDJ. Some CMIP5-with-SWS and CMIP5-without-SWS differences are found, with 41% and 23% of La Niña events, respectively, peaking in NDJ (Fig. 8c).

Finally, following Bellenger et al. (2014), where they pointed out a large spread in CMIP5 ensemble ENSO variability, we now explore whether this behavior is partially due to how well models can reproduce the SWS. Figure 9 displays the standard deviation of the normalized Niño-3 index (i.e., SST anomalies averaged over 5°S–5°N, 150°–0°W) for each calendar month in the observations and models, where the models are split into those with and without a realistic SWS for the three event types and the CMIP5 multimodel ensemble mean. The seasonal cycle in the observations shows a clear maximum of SST anomaly during November–January and a minimum during March–April. Although the CMIP5-with-SWS ensemble exhibits a large spread and a smaller range, there is a tendency for a boreal winter maximum, as observed, and a minimum around April–June, which lags that observed by one month. These two limit values occur during the opposite seasons in CMIP5-without-SWS ensemble, which is consistent

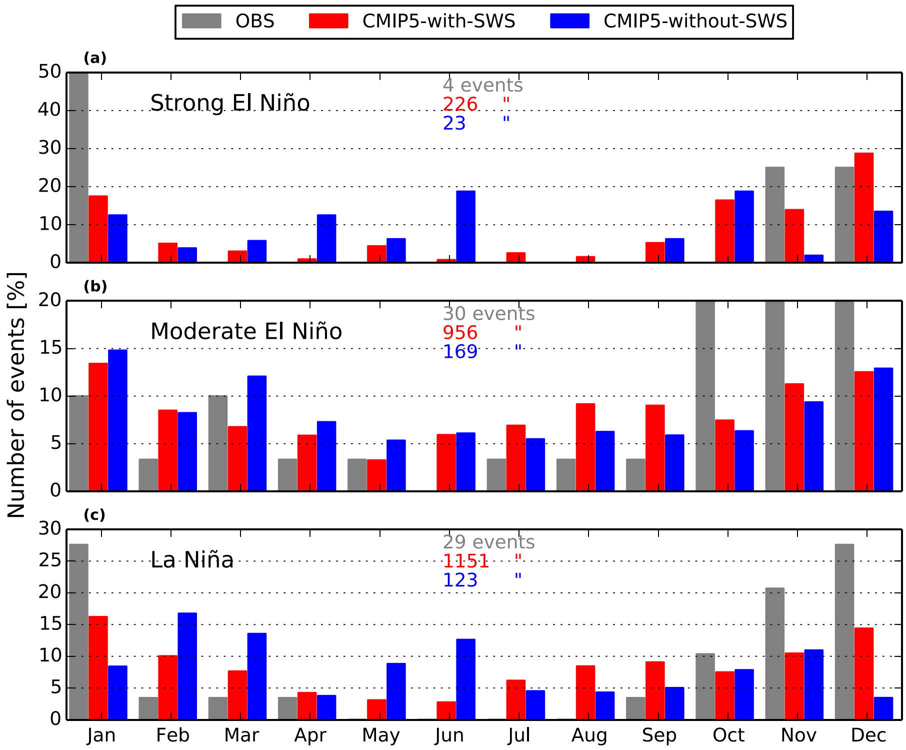

FIG. 8. Percentage of (a) strong El Niño events, (b) moderate El Niño, and (c) La Niña with peaks occurring for each calendar month. Red (blue) bars refer to models with (without) SWS and gray bars the observed values.

with the tendency for some ENSO events to peak in the wrong time of the calendar year in those models, as described above. The multimodel ensemble mean is in close agreement with the CMIP5 with SWS (Fig. 9). However, its spread is larger than CMIP5 with SWS around April–June and August–December, coinciding with the maximum and minimum peaks in CMIP5 without SWS, respectively.

Thus, in summary, ENSO phase locking and its termination rates appear much more realistic in models with an SWS than models without an SWS for strong El Niño and La Niña events, especially for El Niño. However, as noted in the abstract, the models do underestimate the seasonal phase-locking tendency of ENSO events, and this is only partially improved by focusing on the CMIP5 models that accurately reproduce the SWS. As to whether the improvements in SWS representation in the CMIP5 models with SWS is due to the more realistic synchronization of ENSO events, we revert to past literature that shows that SWS can be generated for arbitrary frequencies of ENSO anomalies (Spencer 2004; Stuecker et al. 2015). Further to this, the study of Abellán and McGregor (2016) suggests that the SWS plays a crucial role in the synchronization of ENSO events to the seasonal cycle.

a. WWV changes

It has been previously shown that variability in WWV, and hence heat content, in the tropical Pacific is related to the dynamics of the ENSO cycle (Wyrtki 1985; Cane

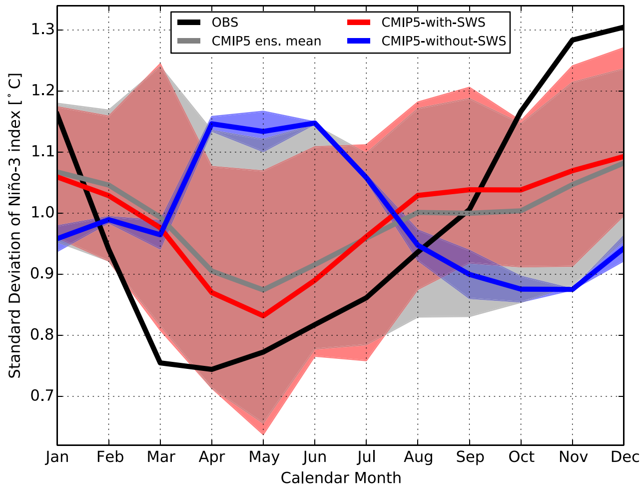

FIG. 9. Standard deviation of Niño-3 SSTA stratified by calendar month from observations (black line), CMIP5 models with SWS for all three ENSO event types (red line), without SWS for none of the events (blue line), and all CMIP5 models (gray line). Thick lines represent the mean values, whereas the shaded areas show the 5th- and 95th-percentile range.

and Zebiak 1985; Zebiak 1989; Springer et al. 1990; Jin 1997; Meinen and McPhaden 2000). In fact, the recharge/discharge oscillator (RDO) theory proposes that warm water builds up in the equatorial Pacific prior to El Niño, as a consequence of equatorward transport of warm water. Then, the equatorial region is discharged of heat during El Niño, which ultimately sets up conditions favorable for the termination of the event. The fact that the SWS enhances the pre-event peak WWV recharge and the postevent peak WWV discharge effectively links the WWV with the seasonal cycle and provides a mechanism for the seasonal synchronization of the events.

Thus, in order to understand why the CMIP5 models are underestimating this phase locking, in spite of realistically producing the SWS we focus on the WWV changes driven by the SWS. Changes in WWV are generated by transports that converge/diverge in the equatorial region and defined here as transport differences at 5°S (V_{5S}) and 5°N (V_{5N}), ($V_{5S} - V_{5N}$), which represents the convergent meridional transport. Now, rather than calculating total transports in each model, which would make it difficult to distinguish the role of the SWS, we seek to identify the transports and WWV changes related to the wind stress changes that occur during the SWS. First, the wind stress changes that occur during the SWS are identified as the average wind stresses during the FMA season minus the ASO average wind stresses (as shown in Fig. 3). As McGregor et al. (2014) demonstrated that the WWV changes generated by the SWS are largely forced by surface Ekman transport changes, here we simply calculate the SWS induced changes in WWV from the meridional Ekman transport of the SWS (Fig. 3). It is worthwhile to note that the SWS-induced WWV changes represent approximately 25%–30% of the estimated total WWV changes in the CMIP5 models (estimated using NDJ Sverdrup transport during event years; not shown). Thus the CMIP5 model results are consistent with the modeled results of McGregor et al. (2014, their Fig. 7), which suggested that the SWS should play a prominent role in the termination of modeled ENSO events. We note that using Sverdrup transports to estimate WWV changes may overestimate the magnitude of the changes as the interior transports are often partially compensated by transports at the Pacific Ocean western boundary. We then seek to identify the relationship between these SWS-induced WWV changes during ASO prior to the peak of the ENSO event and their relationship with the magnitude of the events, as well as SWS-induced WWV changes during FMA after the event peak and their relationship with the decay of SST anomalies (event termination).

Figure 10 highlights a statistically significant linear relationship between the SWS-induced WWV changes during ASO preceding the event peak and the magnitude of the ENSO event peak (SST anomalies during DJF) (Figs. 10a–c). This relationship is consistent with the RDO theory (Meinen and McPhaden 2000), which links the two metrics; however, the recharging due to the SWS is distinct from that explicitly covered by the RDO theory. It is also revealed that models with weak SWS (light green dots) tend to exhibit weak changes in WWV, although the relationship between the SWS and changes in WWV is significant only for La Niña (r = 0.43; not shown). However, those models with strong SWS (dark green dots) do not necessarily show strong changes in WWV. This is not unexpected, as it is the magnitude and zonal extent of the wind changes that drives an oceanic response, not only the latitude of the maximum.

To understand how the SWS changes in WWV after the event peak (FMA during the decaying year) impact the SST anomalies decay of each event type, Fig. 10 also displays the FMA WWV changes plotted against the post-ENSO-event peak SST anomaly decay. It is noteworthy that again a statistically significant relationship is found for ENSO events (Figs. 10d–f), reaching the maximum correlation for strong El Niño (r = 0.60). Thus, if the SWS-induced discharge (recharge) of heat content for El Niño (La Niña) is large, the termination of the event tends to be more rapid than that with small WWV changes. It is interesting to note that multimodel mean WWV change for moderate El Niño is much lower than that observed, which may help to explain why these events are not as phase locked as the observations (Fig. 8b). Also illustrated here are the symmetries between La Niña and moderate El Niño events for values of the Niño-3.4 index, SST anomaly decay, and WWV changes. Hence, this analysis highlights how the SWS modulates the evolution of the WWV changes in the equatorial Pacific Ocean and effectively links these changes with the seasonal cycle; the recharge of the WWV occurs prior to the El Niño event (represented here in ASO season), whereas the discharged state is obtained after the peak (represented here in FMA season).

6. Summary and conclusions

The goal of our study was to address the following questions: 1) Do the CMIP5 models reproduce a realistic southward wind shift (SWS)? 2) What variables are related to the SWS in CMIP5 models? 3) What is the role of the SWS in the seasonal synchronization of modeled ENSO events? First, however, we define three ENSO event types: El Niño events are separated into strong and moderate categories while La Niña events have only the one category (see section 2c).

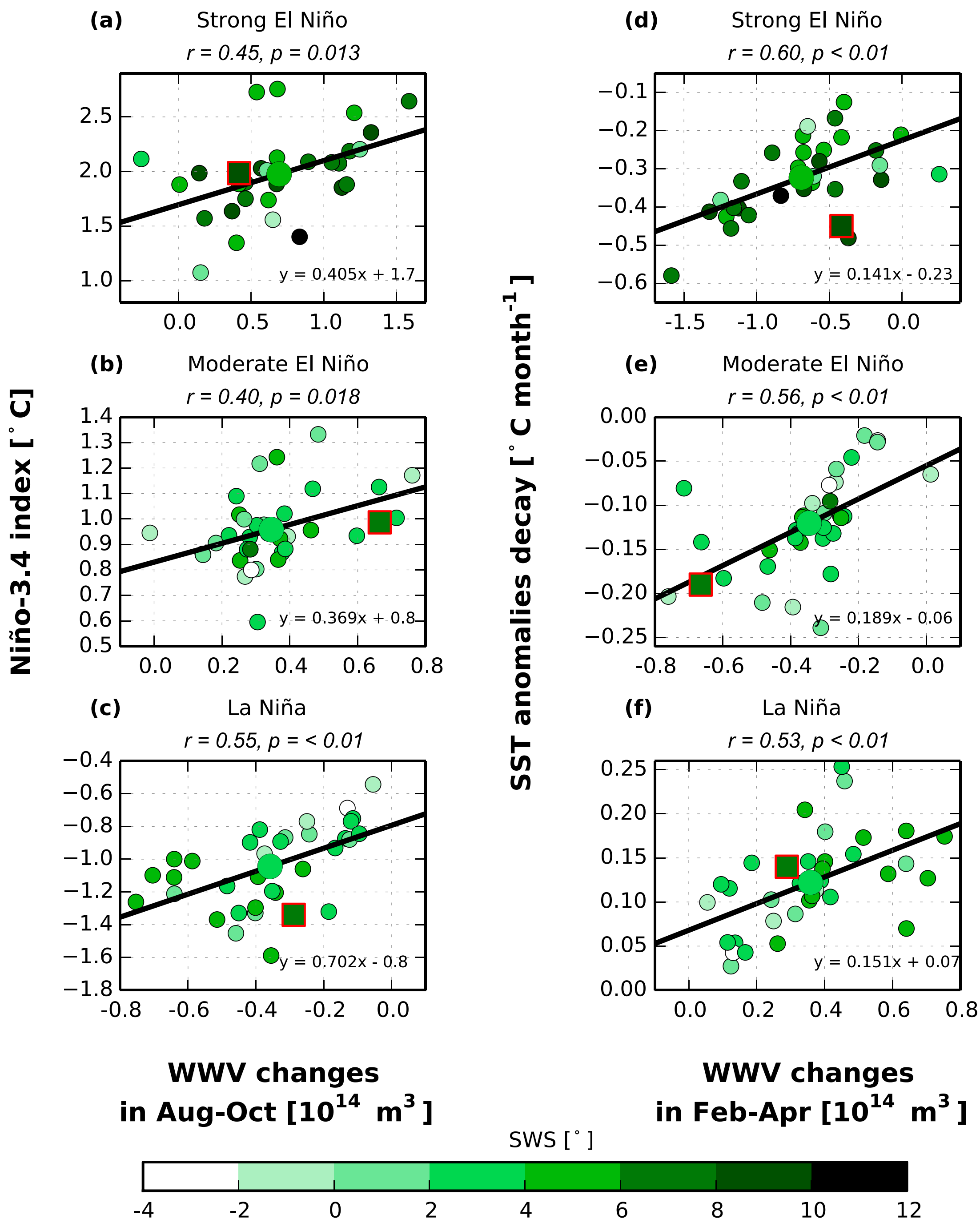

FIG. 10. Scatterplots showing the modeled relationship (a)–(c) between the magnitude of ENSO events in DJF and WWV changes in August–October and (d)–(f) between the termination rate (defined in section 5) and WWV changes in February–April. Note that the colors of the dots indicate the intensity (in ° latitude) of the SWS and the slopes of the regression lines are multiplied by 10^{14}. The squares, with a red outline, represent the observed values, whereas the big circles indicate the multimodel ensemble means. The average value in ASO and FMA [i.e., (ASO + FMA)/2] is subtracted for changes of WWV in both ASO and FMA in order to emphasize the role of the SWS in WWV changes. The spatial patterns of zonal wind stresses anomalies used to compute WWV changes are shown in Fig. 3.

It was demonstrated that the magnitude of zonal wind stress anomaly during ENSO events is clearly underestimated and its spatial pattern extends too far into the western Pacific, although the latter has been incrementally improved in CMIP5 with respect to CMIP3 (Capotondi et al. 2006; Lee et al. 2013). In terms of capturing the SWS, it is encouraging that the vast majority (81%–86%) of CMIP5 models successfully captures the observed SWS during some of the three types of ENSO events (strong El Niño, moderate El Niño, and La Niña), with mean latitude biases of −1.4°, 0.3°, and −0.8°, respectively (see section 3a for SWS definition). We found in addition that 65% of models reproduce an SWS for all types of ENSO events, whereas only 2 out of 34 models (IPSL-CM5A-LR and IPSL-CM5A-MR) fail to simulate the SWS for all three event types.

In examining the factors that are related to the performance of CMIP5 models in simulating the SWS, we first classify the models according to their ability to represent the SWS during ENSO events and then make model ensembles with and without the SWS. We then composite means of SLP, precipitation, and SST anomaly patterns. Our results indicate that most models have a problem reproducing the zonal location of the anomalies in zonal wind stress, precipitation, and SST, as documented in past studies (e.g., Kug et al. 2012; Capotondi and Wittenberg 2013; Zhang and Sun 2014; Ham and Kug 2014; Taschetto et al. 2014). However, here we have demonstrated that these biases in models without an SWS are much larger than those in models with an SWS. Furthermore, the seasonal differences of zonal wind stress and SLP anomalies prior to the peak of the events (August–October) and after the mature phase (February–April) are underestimated in all of the CMIP5 models; however, this is most pronounced in CMIP5 models that do not accurately produce an SWS. It is also clear from our analyses that the anomalous values of SST and rainfall during the mature phase (DJF) of La Niña and strong El Niño are weaker in models having a poor simulation of the SWS compared to models with an SWS, whereas no striking difference is seen for moderate El Niño. To further explore differences between models with and without an SWS, we analyzed the climatological SST, precipitation, and zonal wind during DJF over the tropical Pacific. It was shown that models without an SWS exhibit stronger ITCZ, warmer underlying SST, and weaker trade winds over the north tropical Pacific compared to models with an SWS, in addition to westward extension of the cold tongue.

To provide a more quantitative idea as to the relationship between the composite difference and the SWS, we assessed a set of multiple-linear regression models of the SWS according to indices derived from fields mentioned above. Our results give a clear indication that the anomalous rainfall over the northwestern Pacific in DJF during ENSO events is strongly related the SWS, such that larger negative (positive) precipitation anomalies over that region during El Niño (La Niña) events are strongly related to a strong SWS. Further, we find that the meridional gradient of mean state SST in this season is also strongly related to the magnitude of the modeled SWS. We expect this linkage between mean state and the SWS is due to the weaker gradients of SST facilitate shift in convection zones (Cai et al. 2014). The amplitude of SST and surface wind stress anomalies also provides additional information about the SWS during ENSO events, which is consistent with the theory that the SWS is due to the nonlinear interaction between ENSO and the annual cycle (Stuecker et al. 2013).

In our study it was also noted that the magnitude of the event, in terms of SST anomalies, is larger and the termination is more rapid in models with an SWS compared to models without an SWS for La Niña and strong El Niño, more evident for the latter. These findings are consistent with those reported by Abellán and McGregor (2016), where they pointed out that the inclusion of the SWS in their simple model results in larger La Niña events and shorter El Niño events. In association, models that successfully reproduce the SWS, peaks of La Niña, and strong El Niño match observations much better than models that do not accurately produce the SWS. However, for moderate El Niño, no statistically significant differences are found in the magnitude, seasonal synchronization, or termination across SWS/non-SWS models. When models are classified by their ability to capture the SWS for all ENSO types, it is revealed that the seasonal cycle of the standard deviation of ENSO (a proxy for the phase locking of events) in the models without an SWS shows maximum and minimum anomalies during the opposite season compared to models with an SWS and observations (i.e., minimum in April–June and maximum in November–January). While those models with the SWS are much more accurate in the representation of the seasonal synchronization, they underestimate their magnitude.

To gain insight into this, SWS-driven WWV changes were calculated during the lead-up to ENSO peaks and after the event peaks. It was shown that statistically significant linear correlations exist between the SWS-induced WWV changes in August–October and the magnitude of the event in DJF and between the SWS-induced WWV changes in February–April and the decay-of-event SST anomalies. We also find that the models dramatically underestimate the magnitude of SWS-induced WWV changes during moderate El Niño events, which may explain why the SWS does not appear to impact the evolution of moderate events.

Thus, these results emphasize the importance of simulating the SWS for two overarching reasons: 1) this is associated with a decrease in some well-known biases in both mean state and ENSO-driven anomalous values, and 2) this yields a better performance in the synchronization to the seasonal cycle of ENSO events, particularly important for ENSO teleconnections (e.g., Webster et al. 1998). It is interesting to note that although the majority of models can produce an SWS, they largely underestimate the seasonal phase locking of ENSO. Thus, we highlight that while the SWS is an interesting metric to examine, it is also the magnitude and zonal extent of the wind changes that accompany this SWS that drives the changes in WWV. Further to this, there are likely more processes involved in the spring termination of ENSO events than considered here, such as the seasonally changing cloud feedbacks (Dommenget and Yu 2016; Rashid and Hirst 2015).

Acknowledgments. This study was supported by the Australian Research Council (ARC) through Grant DE130100663, with additional support coming via the ARC Centre of Excellence for Climate System Science. We also acknowledge the World Climate Research Programme's Working Group on Coupled Modelling, which is responsible for CMIP, for producing and making available their model output. This work was undertaken with the assistance of resources from the National Computational Infrastructure (NCI), which is supported by the Australian Government. CMAP Precipitation and ERSST data were provided by the NOAA/OAR/ESRL PSD, Boulder, Colorado, and ERA-Interim data by ECMWF. The authors would also like to thank three anonymous reviewers for their comments and suggestions, which helped substantially improve the paper.

REFERENCES

Abellán, E., and S. McGregor, 2016: The role of the southward wind shift in both, the seasonal synchronization and duration of ENSO events. *Climate Dyn.*, **47**, 509–527, doi:10.1007/s00382-015-2853-1.

An, S.-I., and B. Wang, 2000: Interdecadal change of the structure of the ENSO mode and its impact on the ENSO frequency. *J. Climate*, **13**, 2044–2055, doi:10.1175/1520-0442(2000)013<2044:ICOTSO>2.0.CO;2.

Ashok, K., S. K. Behera, S. A. Rao, H. Weng, and T. Yamagata, 2007: El Niño Modoki and its possible teleconnection. *J. Geophys. Res.*, **112**, C11007, doi:10.1029/2006JC003798.

Battisti, D. S., and A. C. Hirst, 1989: Interannual variability in the tropical atmosphere-ocean system: Influences of the basic state, ocean geometry, and nonlinearity. *J. Atmos. Sci.*, **46**, 1687–1712, doi:10.1175/1520-0469(1989)046<1687:IVIATA>2.0.CO;2.

Bellenger, H., E. Guilyardi, J. Leloup, M. Lengaigne, and J. Vialard, 2014: ENSO representation in climate models: From CMIP3 to CMIP5. *Climate Dyn.*, **42**, 1999–2018, doi:10.1007/s00382-013-1783-z.

Bjerknes, J., 1969: Atmospheric teleconnections from the equatorial Pacific. *Mon. Wea. Rev.*, **97**, 163–172, doi:10.1175/1520-0493(1969)097<0163:ATFTEP>2.3.CO;2.

Brown, J. N., C. Langlais, and C. Maes, 2014: Zonal structure and variability of the western Pacific dynamic warm pool edge in CMIP5. *Climate Dyn.*, **42**, 3061–3076, doi:10.1007/s00382-013-1931-5.

Cai, W., and Coauthors, 2012: More extreme swings of the South Pacific convergence zone due to greenhouse warming. *Nature*, **488**, 365–369, doi:10.1038/nature11358.

——, and Coauthors, 2014: Increasing frequency of extreme El Niño events due to greenhouse warming. *Nat. Climate Change*, **4**, 111–116, doi:10.1038/nclimate2100.

——, and Coauthors, 2015: Increased frequency of extreme La Niña events under greenhouse warming. *Nat. Climate Change*, **5**, 132–137, doi:10.1038/nclimate2492.

Cane, M. A., and S. Zebiak, 1985: A theory for El Niño and the Southern Oscillation. *Science*, **228**, 1084–1087, doi:10.1126/science.228.4703.1085.

——, M. Münnich, and S. E. Zebiak, 1990: A study of self-excited oscillations of the tropical ocean–atmosphere system. Part I: Linear analysis. *J. Atmos. Sci.*, **47**, 1562–1577, doi:10.1175/1520-0469(1990)047<1562:ASOSEO>2.0.CO;2.

Capotondi, A., A. T. Wittenberg, and S. Masina, 2006: Spatial and temporal structure of tropical Pacific interannual variability in 20th century coupled simulations. *Ocean Modell.*, **15**, 274–298, doi:10.1016/j.ocemod.2006.02.004.

——, and ——, 2013: ENSO diversity in climate models. *U.S. CLIVAR Variations*, **11**, 10–14.

——, and Coauthors, 2015: Understanding ENSO diversity. *Bull. Amer. Meteor. Soc.*, **96**, 921–938, doi:10.1175/BAMS-D-13-00117.1.

Choi, K.-Y., G. A. Vecchi, and A. T. Wittenberg, 2015: Nonlinear zonal wind response to ENSO in the CMIP5 models: Roles of the zonal and meridional shift of the ITCZ/SPCZ and the simulated climatological precipitation. *J. Climate*, **28**, 8556–8573, doi:10.1175/JCLI-D-15-0211.1.

Dee, D. P., and Coauthors, 2011: The ERA-Interim reanalysis: Configuration and performance of the data assimilation system. *Quart. J. Roy. Meteor. Soc.*, **137**, 553–597, doi:10.1002/qj.828.

Deser, C., and Coauthors, 2012: ENSO and Pacific decadal variability in the Community Climate System Model version 4. *J. Climate*, **25**, 2622–2651, doi:10.1175/JCLI-D-11-00301.1.

Dommenget, D., and Y. Yu, 2016: The seasonally changing cloud feedbacks contribution to the ENSO seasonal phase-locking. *Climate Dyn.*, **47**, 3661–3672, doi:10.1007/s00382-016-3034-6.

——, T. Bayr, and C. Frauen, 2013: Analysis of the non-linearity in the pattern and time evolution of El Niño Southern Oscillation. *Climate Dyn.*, **40**, 2825–2847, doi:10.1007/s00382-012-1475-0.

Frauen, C., and D. Dommenget, 2010: El Niño and La Niña amplitude asymmetry caused by atmospheric feedbacks. *Geophys. Res. Lett.*, **37**, L18801, doi:10.1029/2010GL044444.

Grose, M. R., and Coauthors, 2014: Assessment of the CMIP5 global climate model simulations of the western tropical Pacific climate system and comparison to CMIP3. *Int. J. Climatol.*, **34**, 3382–3399, doi:10.1002/joc.3916.

Guilyardi, E., 2006: El Niño–mean state–seasonal cycle interactions in a multi-model ensemble. *Climate Dyn.*, **26**, 329–348, doi:10.1007/s00382-005-0084-6.

——, H. Bellenger, M. Collins, S. Ferrett, W. Cai, and A. Wittenberg, 2012: A first look at ENSO in CMIP5. *CLIVAR Exchanges*, No. 17, International CLIVAR Project Office, Southampton, United Kingdom, 29–32.

Ham, Y.-G., and J.-S. Kug, 2014: ENSO phase-locking to the boreal winter in CMIP3 and CMIP5 models. *Climate Dyn.*, **43**, 305–318, doi:10.1007/s00382-014-2064-1.

——, and ——, 2015: Improvement of ENSO simulation based on intermodel diversity. *J. Climate*, **28**, 998–1015, doi:10.1175/JCLI-D-14-00376.1.

——, I.-S. Kang, D. Kim, and J.-S. Kug, 2012: El Niño Southern Oscillation simulated and predicted in SNU coupled GCMs. *Climate Dyn.*, **38**, 2227–2242, doi:10.1007/s00382-011-1171-5.

——, J.-S. Kug, D. Kim, Y.-H. Kim, and D.-H. Kim, 2013: What controls phase-locking of ENSO to boreal winter in coupled GCMs? *Climate Dyn.*, **40**, 1551–1568, doi:10.1007/s00382-012-1420-2.

Harrison, D. E., and N. K. Larkin, 1996: The COADS sea level pressure signal: A near-global El Niño composite and time series view, 1946–1993. *J. Climate*, **9**, 3025–3055, doi:10.1175/1520-0442(1996)009<3025:TCSLPS>2.0.CO;2.

——, and G. A. Vecchi, 1999: On the termination of El Niño. *Geophys. Res. Lett.*, **26**, 1593–1596, doi:10.1029/1999GL900316.

Holland, G. J., 2009: ENSO warming impacts. *Science*, **3**, 325–347, doi:10.1088/1748-9326/7/3/034002.

Jin, F.-F., 1997: An equatorial ocean recharge paradigm for ENSO. Part I: Conceptual model. *J. Atmos. Sci.*, **54**, 811–829, doi:10.1175/1520-0469(1997)054<0811:AEORPF>2.0.CO;2.

——, S.-I. An, A. Timmermann, and J. Zhao, 2003: Strong El Niño events and nonlinear dynamic heating. *Geophys. Res. Lett.*, **30**, 1120, doi:10.1029/2002GL016356.

Kang, I.-S., and J.-S. Kug, 2002: El Niño and La Niña sea surface temperature anomalies: Asymmetry characteristics associated with their wind stress anomalies. *J. Geophys. Res.*, **107**, 4372, doi:10.1029/2001JD000393.

Kao, H.-Y., and J.-Y. Yu, 2009: Contrasting eastern-Pacific and central-Pacific types of ENSO. *J. Climate*, **22**, 615–632, doi:10.1175/2008JCLI2309.1.

Kim, H.-M., P. J. Webster, and J. A. Curry, 2009: Impact of shifting patterns of Pacific Ocean warming on North Atlantic tropical cyclones. *Science*, **325**, 77–80, doi:10.1126/science.1174062.

Kirtman, B. P., 1997: Oceanic Rossby wave dynamics and the ENSO period in a coupled model. *J. Climate*, **10**, 1690–1704, doi:10.1175/1520-0442(1997)010<1690:ORWDAT>2.0.CO;2.

——, Y. Fan, and E. K. Schneider, 2002: The COLA global coupled and anomaly coupled ocean–atmosphere GCM. *J. Climate*, **15**, 2301–2320, doi:10.1175/1520-0442(2002)015<2301:TCGCAA>2.0.CO;2.

Kug, J.-S., F. Jin, and S.-I. An, 2009: Two types of El Niño events: Cold tongue El Niño and warm pool El Niño. *J. Climate*, **22**, 1499–1515, doi:10.1175/2008JCLI2624.1.

——, Y.-G. Ham, J.-Y. Lee, and F.-F. Jin, 2012: Improved simulation of two types of El Niño in CMIP5 models. *Environ. Res. Lett.*, **7**, 034002, doi:10.1088/1748-9326/7/3/034002.

Larkin, N. K., and D. E. Harrison, 2005: On the definition of El Niño and associated seasonal average U.S. weather anomalies. *Geophys. Res. Lett.*, **32**, L13705, doi:10.1029/2005GL022738.

Lee, T., D. E. Waliser, J.-L. F. Li, F. W. Landerer, and M. M. Gierach, 2013: Evaluation of CMIP3 and CMIP5 wind stress climatology using satellite measurements and atmospheric reanalysis products. *J. Climate*, **26**, 5810–5826, doi:10.1175/JCLI-D-12-00591.1.

Lengaigne, M., and G. A. Vecchi, 2009: Contrasting the termination of moderate and extreme El Niño events in coupled general circulation models. *Climate Dyn.*, **35**, 299–313, doi:10.1007/s00382-009-0562-3.

——, J. Boulanger, C. Meinkes, and H. Spencer, 2006: Influence of the seasonal cycle on the termination of El Niño events in a coupled general circulation model. *J. Climate*, **19**, 1850–1868, doi:10.1175/JCLI3706.1.

Li, G., S.-P. Xie, Y. Du, and Y. Luo, 2016: Effects of excessive equatorial cold tongue bias on the projections of tropical pacific climate change. Part I: The warming pattern in CMIP5 multi-model ensemble. *Climate Dyn.*, **47**, 3817–3831, doi:10.1007/s00382-016-3043-5.

Li, T., and B. Wang, 2005: A review on the western North Pacific monsoon: Synoptic-to-interannual variabilities. *Terr. Atmos. Ocean. Sci.*, **16**, 285–314, doi:10.3319/TAO.2005.16.2.285(A).

McGregor, S., A. Timmermann, N. Schneider, M. F. Stuecker, and M. H. England, 2012a: The effect of the South Pacific convergence zone on the termination of El Niño events and the meridional asymmetry of ENSO. *J. Climate*, **25**, 5566–5586, doi:10.1175/JCLI-D-11-00332.1.

——, A. S. Gupta, and M. H. England, 2012b: Constraining wind stress products with sea surface height observations and implications for Pacific Ocean sea level trend attribution. *J. Climate*, **25**, 8164–8176, doi:10.1175/JCLI-D-12-00105.1.

——, N. Ramesh, P. Spence, M. H. England, M. J. McPhaden, and A. Santoso, 2013: Meridional movement of wind anomalies during ENSO events and their role in event termination. *Geophys. Res. Lett.*, **40**, 749–754, doi:10.1002/grl.50136.

——, P. Spence, F. U. Schwarzkopf, M. H. England, A. Santoso, W. S. Kessler, A. Timmermann, and C. W. Böning, 2014: ENSO-driven interhemispheric Pacific mass transports. *J. Geophys. Res. Oceans*, **119**, 6221–6237, doi:10.1002/2014JC010286.

Meehl, G. A., C. Covey, K. E. Taylor, T. Delworth, R. J. Stouffer, M. Latif, B. McAvaney, and J. F. B. Mitchell, 2007: The WCRP CMIP3 multimodel dataset: A new era in climate change research. *Bull. Amer. Meteor. Soc.*, **88**, 1383–1394, doi:10.1175/BAMS-88-9-1383.

Meinen, C. S., and M. J. McPhaden, 2000: Observations of warm water volume changes in the equatorial Pacific and their relationship to El Niño and La Niña. *J. Climate*, **13**, 3551–3559, doi:10.1175/1520-0442(2000)013<3551:OOWWVC>2.0.CO;2.

Misra, V., and Coauthors, 2007: Validating and understanding the ENSO simulation in two coupled climate models. *Tellus*, **59A**, 292–308, doi:10.1111/j.1600-0870.2007.00231.x.

Neale, R. B., J. H. Richter, and M. Jochum, 2008: The impact of convection on ENSO: From a delayed oscillator to a series of events. *J. Climate*, **21**, 5904–5924, doi:10.1175/2008JCLI2244.1.

Neelin, J. D., F.-F. Jin, and H.-H. Syu, 2000: Variations in ENSO phase locking. *J. Climate*, **13**, 2570–2590, doi:10.1175/1520-0442(2000)013<2570:VIEPL>2.0.CO;2.

Ohba, M., and H. Ueda, 2009: Role of nonlinear atmospheric response to SST on the asymmetric transition process of ENSO. *J. Climate*, **22**, 177–192, doi:10.1175/2008JCLI2334.1.

Philander, S., 1983: El Niño Southern Oscillation phenomena. *Nature*, **302**, 295–301, doi:10.1038/302.295a0.

——, 1990: *El Niño, La Niña, and the Southern Oscillation*. Academic Press, 293 pp.

——, T. Yamagata, and R. Pacanowski, 1984: Unstable air–sea interactions in the tropics. *J. Atmos. Sci.*, **41**, 604–613, doi:10.1175/1520-0469(1984)041<0604:UASIIT>2.0.CO;2.

Rashid, H. A., and A. C. Hirst, 2015: Investigating the mechanisms of seasonal ENSO phase locking bias in the ACCESS coupled model. *Climate Dyn.*, **46**, 1075–1090, doi:10.1007/s00382-015-2633-y.

Rasmusson, E., and T. Carpenter, 1982: Variations in tropical sea surface temperature and surface wind fields associated with the Southern Oscillation/El Niño. *Mon. Wea. Rev.*, **110**, 354–384, doi:10.1175/1520-0493(1982)110<0354:VITSST>2.0.CO;2.

Ren, H.-L., J. Zuo, F.-F. Jin, and M. F. Stuecker, 2016: ENSO and annual cycle interaction: The combination mode representation in CMIP5 models. *Climate Dyn.*, **46**, 3753–3765, doi:10.1007/s00382-015-2802-z.

Ropelewski, C. F., and M. S. Halpert, 1987: Global and regional scale temperature patterns associated with the El Niño/Southern Oscillation. *Mon. Wea. Rev.*, **115**, 1606–1626, doi:10.1175/1520-0493(1987)115<1606:GARSPP>2.0.CO;2.

Santoso, A., S. McGregor, F.-F. Jin, W. Cai, M. H. England, S.-I. An, M. J. McPhaden, and E. Guilyardi, 2013: Late-twentieth-century emergence of the El Niño propagation asymmetry and future projections. *Nature*, **504**, 126–130, doi:10.1038/nature12683.

Smith, T. M., R. W. Reynolds, T. C. Peterson, and J. Lawrimore, 2008: Improvements to NOAA's historical merged land–ocean surface temperature analysis (1880–2006). *J. Climate*, **21**, 2283–2296, doi:10.1175/2007JCLI2100.1.

Spencer, H., 2004: Role of the atmosphere in seasonal phase locking of El Niño. *Geophys. Res. Lett.*, **31**, L24104, doi:10.1029/2004GL021619.

Springer, S. R., M. J. McPhaden, and A. J. Busalacchi, 1990: Oceanic heat content variability in the tropical Pacific during the 1982–1983 El Niño. *J. Geophys. Res.*, **95**, 22 089–22 101, doi:10.1029/JC095iC12p22089.

Stuecker, M. F., A. Timmermann, F. F. Jin, S. McGregor, and H. L. Ren, 2013: A combination mode of the annual cycle and the El Niño/Southern Oscillation. *Nat. Geosci.*, **6**, 540–544, doi:10.1038/ngeo1826.

——, F.-F. Jin, A. Timmermann, and S. McGregor, 2015: Combination mode dynamics of the anomalous northwest Pacific anticyclone. *J. Climate*, **28**, 1093–1111, doi:10.1175/JCLI-D-14-00225.1.

Sun, D.-Z., Y. Yu, and T. Zhang, 2009: Tropical water vapor and cloud feedbacks in climate models: A further assessment using coupled simulations. *J. Climate*, **22**, 1287–1304, doi:10.1175/2008JCLI2267.1.

Takahashi, K., and B. Dewitte, 2015: Strong and moderate non-linear El Niño regimes. *Climate Dyn.*, **46**, 1627–1645, doi:10.1007/s00382-015-2665-3.

——, A. Montecinos, K. Goubanova, and B. Dewitte, 2011: ENSO regimes: Reinterpreting the canonical and Modoki El Niño. *Geophys. Res. Lett.*, **38**, L10704, doi:10.1029/2011GL047364.

Taschetto, A. S., A. S. Gupta, N. C. Jourdain, A. Santoso, C. C. Ummenhofer, and M. H. England, 2014: Cold tongue and warm pool ENSO events in CMIP5: Mean state and future projections. *J. Climate*, **27**, 2861–2885, doi:10.1175/JCLI-D-13-00437.1.

Taylor, K. E., 2001: Summarizing multiple aspects of model performance in a single diagram. *J. Geophys. Res.*, **106**, 7183–7192, doi:10.1029/2000JD900719.

——, R. J. Stouffer, and G. A. Meehl, 2012: An overview of CMIP5 and the experiment design. *Bull. Amer. Meteor. Soc.*, **93**, 485–498, doi:10.1175/BAMS-D-11-00094.1.

Tziperman, E., S. Zebiak, and M. Cane, 1997: Mechanisms of seasonal–ENSO interaction. *J. Atmos. Sci.*, **54**, 61–71, doi:10.1175/1520-0469(1997)054<0061:MOSEI>2.0.CO;2.

——, M. A. Cane, S. E. Zebiak, Y. Xue, and B. Blumenthal, 1998: Locking of El Niño's peak time to the end of the calendar year in the delayed oscillator picture of ENSO. *J. Climate*, **11**, 2191–2199, doi:10.1175/1520-0442(1998)011<2191:LOENOS>2.0.CO;2.

Vecchi, G., 2006: The termination of the 1997–98 El Niño. Part II: Mechanisms of atmospheric change. *J. Climate*, **19**, 2647–2664, doi:10.1175/JCLI3780.1.

——, and D. E. Harrison, 2003: On the termination of the 2002–03 El Niño event. *Geophys. Res. Lett.*, **30**, 1964, doi:10.1029/2003GL017564.

——, and ——, 2006: The termination of the 1997–1998 El Niño. Part I: Mechanisms of oceanic change. *J. Climate*, **19**, 2633–2646, doi:10.1175/JCLI3776.1.

——, A. Rosati, and D. E. Harrison, 2004: Setting the timing of El Niño termination. *Bull. Amer. Meteor. Soc.*, **85**, 1065–1066.

Wang, B., and S. An, 2002: A mechanism for decadal changes of ENSO behavior: Roles of background wind changes. *Climate Dyn.*, **18**, 475–486, doi:10.1007/s00382-001-0189-5.

——, and Q. Zhang, 2002: Pacific–East Asian teleconnection. Part II: How the Philippine Sea anomalous anticyclone is established during El Niño development. *J. Climate*, **15**, 3252–3265, doi:10.1175/1520-0442(2002)015<3252:PEATPI>2.0.CO;2.

——, R. Wu, and R. Lukas, 1999: Roles of the western North Pacific wind variation in thermocline adjustment and ENSO phase transition. *J. Meteor. Soc. Japan*, **77**, 1–16.

——, ——, and X. Fu, 2000: Pacific–East Asian teleconnection: How does ENSO affect East Asian climate? *J. Climate*, **13**, 1517–1536, doi:10.1175/1520-0442(2000)013<1517:PEATHD>2.0.CO;2.

Webster, P. J., V. O. Magaña, T. N. Palmer, J. Shukla, R. A. Tomas, M. Yanai, and T. Yasunari, 1998: Monsoons: Processes, predictability, and the prospects for prediction. *J. Geophys. Res.*, **103**, 14 451–14 510, doi:10.1029/97JC02719.

Wilks, D., 2006: *Statistical Methods in the Atmospheric Sciences*. 2nd ed. Elsevier, 627 pp.

Wittenberg, A. T., 2004: Extended wind stress analyses for ENSO. *J. Climate*, **17**, 2526–2540, doi:10.1175/1520-0442(2004)017<2526:EWSAFE>2.0.CO;2.

Wyrtki, K., 1985: Water displacements in the Pacific and the genesis of El Niño cycles. *J. Geophys. Res.*, **90**, 7129–7132, doi:10.1029/JC090iC04p07129.

Xiao, H., and C. R. Mechoso, 2009: Seasonal cycle–El Niño relationship: Validation of hypotheses. *J. Atmos. Sci.*, **66**, 1633–1653, doi:10.1175/2008JAS2870.1.

Xie, P., and P. A. Arkin, 1997: Global precipitation: A 17-year monthly analysis based on gauge observations, satellite estimates, and numerical model outputs. *Bull. Amer. Meteor. Soc.*, **78**, 2539–2558, doi:10.1175/1520-0477(1997)078<2539:GPAYMA>2.0.CO;2.

Xie, S. P., 1995: Interaction between the annual and interannual variations in the equatorial Pacific. *J. Phys. Oceanogr.*, **25**, 1930–1941, doi:10.1175/1520-0485(1995)025<1930:IBTAAI>2.0.CO;2.

Zebiak, S. E., 1989: Oceanic heat content variability and El Niño cycles. *J. Phys. Oceanogr.*, **19**, 475–483, doi:10.1175/1520-0485(1989)019<0475:OHCVAE>2.0.CO;2.

——, and M. A. Cane, 1987: A model of El Niño–Southern Oscillation. *Mon. Wea. Rev.*, **115**, 2262–2278, doi:10.1175/1520-0493(1987)115<2262:AMENO>2.0.CO;2.

Zhang, T., and D.-Z. Sun, 2014: ENSO asymmetry in CMIP5 models. *J. Climate*, **27**, 4070–4093, doi:10.1175/JCLI-D-13-00454.1.